ETH zürich

Diss. ETH No. 29543

Phase Dynamics and Andreev Bound State Spectroscopy in Planar Josephson Junctions

Daniel Z. Haxell

Diss. ETH No. 29543

Phase dynamics and Andreev bound state spectroscopy in planar Josephson junctions

A thesis submitted to attain the degree of

DOCTOR OF SCIENCES of ETH ZURICH

(Dr. sc. ETH Zurich)

presented by

Daniel Zachary Haxell

MPhys, University of Oxford

born on 08.08.1997

accepted on the recommendation of

Prof. Dr. Klaus Ensslin, examiner
Dr. Fabrizio Nichele, co-examiner
Prof. Dr. Werner Wegscheider, co-examiner
Prof. Dr. Christian Schönenberger, co-examiner

2023

Abstract

Josephson junctions (JJs) are an integral component in quantum computing, low temperature electronics, and fundamental physics research. Hybrid superconductor-semiconductor JJs in two-dimensional materials have recently emerged as a paradigm for novel applications, harnessing gate-tunable supercurrents and strong spin-orbit coupling in a scalable platform. In this thesis, we present a detailed study of planar JJs in an InAs/Al heterostructure, when subjected to bias currents, microwave irradiation and in-plane magnetic fields.

First, we investigate the stochastic dynamics of the superconducting-to-resistive transition of planar JJs and superconducting quantum interference devices (SQUIDs). We find that dynamics at low temperature are dominated by quantum fluctuations in the superconducting phase, which suppress the switching current to values less than half of the critical current. Phase dynamics are altered in a SQUID, such that the switching current of a JJ is more than doubled in a SQUID relative to being in isolation. Moderate damping leads to phase diffusion at higher temperatures, with a transition temperature that is tunable with gate voltages, magnetic fields and fluxes threading the SQUID.

In a second experiment, we perform tunnelling spectroscopy measurements on a planar JJ irradiated by a microwave signal. Replicas in the conductance spectrum are shown to be consistent with photon assisted tunnelling (PAT) between the spectroscopic probe and Andreev bound states (ABSs) in the junction, rather than due to novel light-matter coupling in the form of Floquet-Andreev states. By tuning the tunnel-barrier transparency and Fermi energy with gate voltages, in addition to complementary current-phase relation (CPR) measurements, signatures unique to PAT are identified. Further, microwave-induced distortions to the CPR are shown to be consistent with a non-equilibrium occupation of ABSs, without invoking Floquet states.

Finally, supercurrent and tunnelling spectroscopy measurements are performed on planar JJs in an in-plane magnetic field. Phase shifts in the CPR are reported relative to a phase reference, in devices with different superconducting lead sizes to investigate orbital effects. At low fields, we observe gate-dependent phase shifts of up to $\varphi_0 = 0.5\pi$, consistent with a Zeeman field coupling to highly-transmissive ABSs via Rashba spin-orbit interaction. A distinct phase shift at larger fields is concomitant with a switching current minimum and a closing and reopening of the superconducting gap. These signatures of a phase transition, which might resemble a topological transition, scale with the superconducting lead size indicating the crucial role of orbital effects in planar JJs.

Our results give a new baseline understanding of planar JJs in InAs/Al heterostructures, and elucidate the interplay of Zeeman, spin-orbit and orbital effects in magnetic fields. This guides towards improved realisations of gate-tunable qubits, superconducting electronics and novel states of matter in hybrid superconductor-semiconductor materials.

Zusammenfassung

Josephson-Kontakte (engl. Josephson-junctions, JJ) sind ein wesentlicher Bestandteil von Quantencomputern, in der Tieftemperaturelektronik und sind Gegenstand der physikalischen Grundlagenforschung. Aktuelle Ergebnisse haben gezeigt, dass hybride Supraleiter-Halbleiter JJs in zweidimensionalen Materialen eine vielversprechende und skalierbare Plattform für zukünftige Anwendungen darstellen, insbesondere aufgrund der starken Spin-Bahn Kopplung und weil der Suprastrom gesteuert werden kann. Die vorliegende Arbeit stellt eine detaillierte Studie von planaren InAs/Al JJs in Abhängigkeit von Bias-Strom, Mikrowellenstrahlung und Magnetfeld dar.

Zuerst untersuchen wir die stochastische Dynamik des Supraleiter-Normalleiter Übergangs planarer JJs und supraleitender Quanteninterferenzgeräte (engl. superconducting quantum interference devices, SQUIDs). Es stellt sich heraus, dass Quantenfluktuationen in der supraleitenden Phase die Dynamik bei tiefen Temperaturen dominieren und den Umschaltstrom auf weniger als den halben kritischen Strom reduzieren. Wird ein JJ in ein SQUID integriert, ändert sich die Phasendynamik, wodurch sich der Umschaltstrom im Vergleich zum isolierten JJ mehr als verdoppelt. Eine moderate Dämpfung führt zu Phasendiffusion bei höheren Temperaturen. Die Übergangstemperatur hängt von Gate-Spannung, Magnetfeld und magnetischem Fluss durch das SQUID ab.

Im zweiten Experiment führen wir Tunnelspektroskopie an einem planaren JJ bei Bestrahlung mit Mikrowellen durch. Die Struktur des Tunnelspektrums deutet auf Photonen-gestütztes Tunneln (engl. photon assisted tunnelling, PAT) zwischen der Spektroskopie-Sonde und gebundenen Andreev Zuständen (engl. Andreev bound states, ABS) hin, anstelle einer neuartigen Licht-Materie Kopplung in Form von Floquet-Andreev Zuständen. Durch Steuerung der Transparenz der Tunnelbarriere und der Fermi-Energie durch die Gate-Spannung, sowie mittels zusätzlicher Messungen der Strom-Phasen-Beziehung (engl. current-phase relation, CPR), finden sich Merkmale die eindeutig auf PAT hinweisen. Des Weiteren zeigen wir, dass Verzerrungen der CPR durch Mikrowellenstrahlen als Folge einer Nichtgleichgewichtsbesetzung der ABS verstanden werden können, ohne das Auftreten von Floquet-Zuständen.

Zuletzt Messen wir den Suprastrom und das Tunnelspektrum von planaren JJs unter dem Einfluss eines Magnetfeldes parallel zur Probenebene. Um orbitale Effekte zu untersuchen, werden Phasenverschiebungen in der CPR bei Proben mit unterschiedlichen Längen der supraleitenden Kontakte relativ zu einer absoluten Phasenreferenz gemessen. Unter dem Einfluss kleiner Magnetfelder können Phasenverschiebungen in Abhängigkeit der Gate-Spannung von bis zu $\varphi_0 = 0.5\pi$ beobachtet werden. Diese können durch den Zeeman-Effekt hochtransmissiver ABSs und Rashba Spin-Bahn-Kopplung erklärt werden. Eine klare Verschiebung der Phase bei hohen Feldern tritt begleitend mit einem Minimum im Umschaltstrom und dem Schliessen und erneuten Öffnen der supraleitenden

Energielücke auf. Diese Signaturen eines Phasenübergangs, welche einem topologischen Übergang ähneln könnten, skalieren mit der Länge der supraleitenden Kontakte. Dies unterstreicht die wichtige Rolle orbitaler Effekte in planaren JJs.

Unsere Ergebnisse zeigen ein neues, grundlegendes Verständnis von planaren JJs in InAs/Al Heterostrukturen auf und beleuchten das Zusammenspiel von Zeeman-Effekt, Spin-Bahn Kopplung und orbitalen Effekten im Magnetfeld. Diese Erkenntnisse werden zur Optimierung Gate-gesteuerter Qubits und supraleitender Elektronik, sowie zur Erforschung neuartiger Zustände in hybriden Supraleiter-Halbleiter Materialien beitragen.

Translated by Nele Harnack and Markus Ritter.

Contents

1 Introduction

In 1962, Brian Josephson predicted that a dissipationless supercurrent can flow between two superconductors separated by a thin insulating layer [1]. Such a Josephson junction was experimentally realised the following year [2–4], demonstrating a current without voltage bias. This prompted an explosion of activity over the following decades, where Josephson junctions were applied to large-scale superconducting circuits [5–7], including rapid single-flux-quantum logic [8, 9] and the Josephson field-effect transistor [10–13]; as sensors for ultra-low magnetic fields [14–17] and weak electromagnetic radiation [18, 19]; as microwave receivers [20–22], mixers [23–25] and amplifiers [26–28]; and to define the volt using fundamental constants [29–31]. Today, Josephson junctions are also at the forefront of quantum computing in the form of superconducting qubits [32], with implementations including flux qubits [33–35], fluxonium [36, 37], parity-protected qubits [38–40] and the industry-leading transmon [41–43].

Superconductor-insulator-superconductor junctions, as originally proposed by Josephson and realised in the years after, suffer from a lack of tunability. Supercurrents can be tuned via magnetic fluxes in a superconducting quantum interference device (SQUID) [44, 45], but flux control requires passing currents into cryogenic environments, which can be detrimental for large-scale devices. An alternative is to replace the insulator in the junction with a semiconductor, such that the dissipationless properties of the superconductor are combined with the tunability of the semiconductor. These hybrid materials were first realised in 1974 using thinned Si wafers [46], before signatures of a gate-tunable supercurrent were shown in an InAs two-dimensional electron gas in 1985 [47]. However, device performance was limited by material quality over the next 30 years, until the advent of clean hybrid interfaces from *in situ* superconductor deposition, first demonstrated in nanowires [48, 49] and then in two-dimensional electron gases [50]. This fostered a wave of research into hybrid devices over the last decade, leading to direct applications of hybrid junctions as gate-tunable transmons [51–58] and magnetic-field-compatible qubits [57, 59–62], as well as promising approaches to parity-protection [63–66].

High quality interfaces in hybrid materials also allow novel functionalities, due to the presence of localised current-carrying states with discrete energies below the superconducting gap: Andreev bound states [67]. These states open up new possibilities for defining qubits, such as by occupying Andreev levels with electron pairs [68–72] or single quasiparticles with different spins [73–80]. Phase transitions can also emerge in hybrid junctions, by coupling to ferromagnetic materials [81–86] or to an external

magnetic field [87–90]. The resulting shift in the ground state from 0 to π-phase forms the basis for a $\pi-$junction, which can be utilised in superconducting electronics [91–96]. The properties of hybrid junctions become richer with the inclusion of spin-orbit coupling, which enables spin-dependent transport [73, 74, 97–100], non-reciprocal supercurrents [101–103] and anomalous phase shifts [104–109]. Hybrid junctions have also been proposed as a platform for band engineering via light-matter coupling [110–114], or to host topological phases [115–124] for fault-tolerant quantum computation [125–129].

In this context, a detailed study of hybrid Josephson junctions is required to understand their properties, and ultimately establish their viability for technological applications. This thesis is a thorough investigation of Josephson junctions defined in a planar InAs/Al heterostructure, and their response to bias currents, microwave irradiation and large in-plane magnetic fields. The work presented in this thesis was performed in the Alternative Qubits group at IBM Research Europe – Zurich. Growth of the material used throughout this thesis was performed by the Advanced Semiconductor Quantum Materials group at ETH Zurich. The thesis will be structured as follows:

In **Chapter 2**, we review the basic theoretical concepts which are crucial to understand the results presented in this thesis. We begin by discussing the material properties of semiconductors, superconductors and hybrid interfaces, before introducing Josephson junctions and their response to a current bias, microwave drive and magnetic field. The composition and characterisation of the InAs/Al heterostructure is described in **Chapter 3**, along with the methods to fabricate devices and the measurement techniques used to obtain the results presented in subsequent chapters. In **Chapter 4**, the dynamics of the superconducting-to-resistive transition are investigated in planar Josephson junctions under a current bias, showing that their switching current is very susceptible to fluctuations in the superconducting phase. **Chapter 5** extends the analysis of phase dynamics to the case of a superconducting quantum interference device (SQUID), where we demonstrate an increase in the switching current of junctions in a SQUID relative to the same junction measured in isolation. In **Chapter 6**, we present tunnelling spectroscopy measurements on a planar Josephson junction under microwave irradiation, and show that the conductance response is consistent with photon assisted tunnelling in the spectroscopic probe rather than light-matter coupling to states in the junction. In **Chapter 7** we present phase shifts in planar Josephson junctions subjected to an in-plane magnetic field, and describe them using the interplay of Zeeman, orbital and spin-orbit effects. We summarise our results in **Chapter 8** and propose future avenues of research, both for the projects described in this thesis and the overall field of hybrid Josephson junctions.

2 Theoretical Background

The combined topics of Josephson junctions and superconductor-semiconductor materials have been subject to a vast amount of research in the last 60 years. In this chapter, we discuss the developments and discoveries which will prove key to the experimental results presented in later chapters. We begin with a discussion of semiconductor and superconductor properties, in their constituent parts and then the rich physics which emerges when they are brought together. We then look at the basic properties of Josephson junctions, how they behave under a current bias, their interference effects in magnetic fields and their response to irradiation with an electromagnetic field. To conclude the chapter, we examine different effects which emerge in hybrid Josephson junctions when subject to large in-plane magnetic fields.

2.1. Semiconductors and Superconductors

In this section, we review the basic properties of semiconductor and superconductor materials, in the context of the hybrid InAs/Al heterostructures used throughout this thesis. We therefore focus our discussion of semiconductors on the specific topic of two-dimensional electron gases (2DEGs) which form close to the surface of III-V materials. We then give a basic introduction to superconductivity, before concluding the chapter with a summary of the theory behind tunnelling spectroscopy techniques.

2.1.1. Two-Dimensional Electron Gases

A two-dimensional electron gas (2DEG) is an accumulation of electrons in a crystal lattice which are free to move in two dimensions, but are confined in the third by an electrostatic potential [130, 131]. A semiconductor heterostructure provides this spatially-varying electrostatic potential using layers of different material composition, such that the conduction band energy changes between the layers [132]. A potential well is formed, either at the surface of the material or at an interface within the heterostructure. For hybrid materials, where a superconductor is deposited on top of the semiconductor surface, the 2DEG must be sufficiently close to the superconductor at the surface to exhibit proximitised superconductivity (see Section 2.2). Therefore, the first hybrid 2DEG platforms were realised in p-doped InAs [133, 134], where the 2DEG forms at the semiconductor surface [see Fig. 2.1(a)]. Broken crystal periodicity at the surface leaves atomic bonds to reconstruct or adsorb other atoms or molecules, which modifies the electron structure at the surface. This is described by charged surface states within the band gap of the semiconductor, which cause the valence and conduction bands to

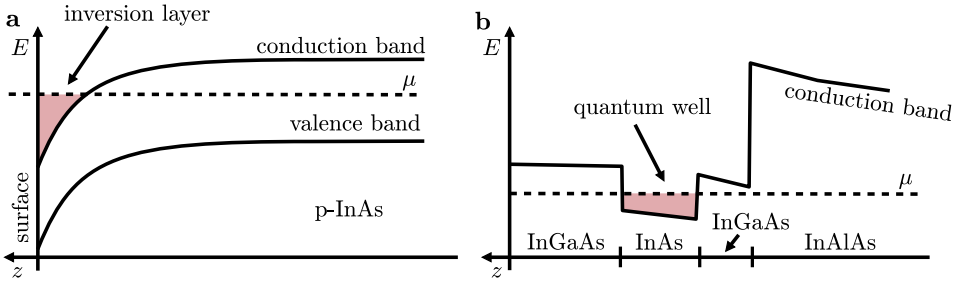

Figure 2.1. Schematics of band-bending in semiconductor heterostructures. a Sketch of the conduction and valence band bending in p-doped InAs, forming an inversion layer at the surface. **b** Sketch of the conduction band profile in an InGaAs/Al heterostructure, such that a quantum well forms in the InAs. Figure inspired by [130] and [50].

bend leading to a inversion layer of accumulated electrons at the surface [135]. The electron mobility, which quantifies how the electron velocity depends on an applied electric field, is limited by ionised impurity scattering and material roughness at the surface. To achieve high mobility transport, where electrons might travel considerable distances between scattering events, it is beneficial to form the 2DEG below the surface termination to separate the electrons from scattering sites. This can be done by engineering a heterostructure consisting of materials with different band gaps, such that a quantum well forms in a low band gap material (e.g. InAs) when confined between two high band gap materials (e.g. InGaAs) [see Fig. 2.1(b)]. This quantum well heterostructure allows for higher mobility than the surface inversion layer. The semiconductor heterostructure is designed such that the 2DEG is close to the surface for a strong proximity effect, but separated from the surface for a high carrier mobility [50, 130, 136].

The dispersion relation of electrons in a 2DEG is typically approximated with a parabolic relation, with an effective mass m^* and g-factor g^* which depend on the periodic lattice potential [137]. The electrons move in an electric field $\mathcal{E}$ with a drift velocity $v_\mathrm{D} = \mu\mathcal{E}$, where the mobility $\mu = e\tau_\mathrm{e}/m^*$ is characterised by the time τ_e between scattering events. The corresponding length scale is the mean free path $l_\mathrm{e} = v_\mathrm{F}\tau_\mathrm{e}$, where the Fermi velocity relates to the Fermi wavevector by $v_\mathrm{F} = \hbar k_\mathrm{F}/m^*$. For a 2DEG with two-fold spin degeneracy and no valley degeneracy, characteristic of III-V materials, the Fermi wavevector depends on the electron sheet density as $k_\mathrm{F} = \sqrt{2\pi n}$. Transport over length scales $L \ll l_\mathrm{e}$ is considered to be ballistic, free of scattering, whereas for $L \gg l_\mathrm{e}$ transport is diffusive. The phase coherence length l_φ, which characterises the length scale over which phase information is lost in the semiconductor, is typically much longer than l_e in 2DEGs with high mobility measured at low temperature [131].

In crystal lattices without inversion symmetry, spin-orbit interaction couples the momentum and spin of charge carriers [138]. In two-dimensional heterostructures, this asymmetry can be present in both the bulk crystal [139–141] and the electrostatic confinement potential [142, 143], giving two spin-orbit contributions. In the case of electrons in InAs in 2DEGs, as will be discussed in this thesis, the term arising from structural inversion asymmetry in the confinement potential is dominant [50, 131, 138]. This Rashba

spin-orbit coupling has the form [138]

$$H_{\mathrm{SO}} = \alpha(k_y\sigma_x - k_x\sigma_y), \tag{2.1}$$

where the wavevector $\mathbf{k}$ is coupled to the spin σ in the transverse in-plane direction. The strength of this interaction is parametrised by α, which is proportional to the electric field in the confinement direction. A gate voltage applied to a device will therefore tune α, due to both the external electric field and the density-dependent internal field.

2.1.2. Superconductivity

Superconductivity describes a state of matter which occurs in some materials at low temperature, in which the electronic resistance of the material goes to zero [144]. Cooper described this state in terms of pairs of electrons with opposite momenta, which are coupled via an attractive interaction mediated by the lattice [145]. The preferential formation of these Cooper pairs leads to their condensation into a many-body ground state, until the binding energy for a pair goes to zero [146]. The ground state is therefore separated from single-particle excitations by an energy gap, which suppresses the scattering processes responsible for electrical resistance. The essential universal characteristic of the superconducting ground state is a many-particle condensate wavefunction with an amplitude and phase which maintain phase coherence over macroscopic distances [147].

A microscopic understanding comes from Bardeen-Cooper-Schrieffer (BCS) theory [146], where the ground state is described by a many-particle, spin-singlet wavefunction of electron pairs at $(\mathbf{k}\uparrow, -\mathbf{k}\downarrow)$ near the Fermi surface, occupied with probability amplitude $v_{\mathbf{k}}$ (and the corresponding value $u_{\mathbf{k}}$ for unoccupied $\mathbf{k}$). Solutions for the probability amplitudes can be found using the Bogoliubov-de Gennes equation [148]

$$\begin{pmatrix} H_0 & \Delta \\ \Delta^* & H_0 \end{pmatrix} \begin{pmatrix} u_{\mathbf{k}} \\ v_{\mathbf{k}} \end{pmatrix} = E_{\mathbf{k}} \begin{pmatrix} u_{\mathbf{k}} \\ v_{\mathbf{k}} \end{pmatrix}, \tag{2.2}$$

where H_0 is the single-electron Hamiltonian and the off-diagonal energy term Δ pairs $u_{\mathbf{k}}$ and $v_{\mathbf{k}}$ via the attractive scattering potential[1]. The superconductor is assumed to be homogeneous, such that plane wave solutions can be taken for the position dependence. In this case, $u_{\mathbf{k}}$ and $v_{\mathbf{k}}$ are given by

$$\begin{aligned} |v_{\mathbf{k}}|^2 &= \frac{1}{2}\left(1 - \frac{\epsilon_{\mathbf{k}}}{E_{\mathbf{k}}}\right) \\ |u_{\mathbf{k}}|^2 &= 1 - |v_{\mathbf{k}}|^2 \end{aligned} \tag{2.3}$$

with energy eigenvalues

$$E_{\mathbf{k}} = (\epsilon_{\mathbf{k}}^2 + \Delta^*\Delta)^{1/2} \tag{2.4}$$

as a function of the energy measured from the Fermi energy, $\epsilon_{\mathbf{k}}$.

The values of $|v_{\mathbf{k}}|^2$ and $|u_{\mathbf{k}}|^2$ are plotted as a function of $\epsilon_{\mathbf{k}}$ in Fig. 2.2(a), and the corresponding energy dispersion $E_{\mathbf{k}}$ in Fig. 2.2(b). The energy dispersion in a normal

[1] Note that here Δ^* corresponds to the complex conjugate of Δ.

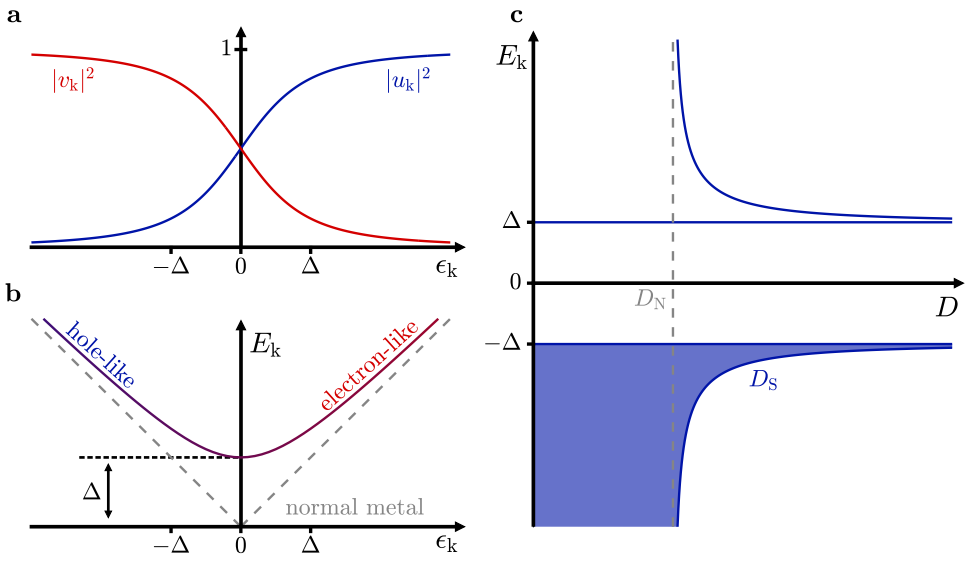

Figure 2.2. Fundamental characteristics of superconductors. **a** The probability $|v_k|^2$ ($|u_k|^2$) for an electron-like (hole-like) excitation of state k at energy $\epsilon_{\mathbf{k}}$. **b** Excitation spectrum E_k of quasiparticles in a superconductor (blue-red line), alongside that of charges in a normal metal (grey dashed line). No excitation states exist for $E_k < \Delta$. **c** Density of states of a superconductor (solid blue line) compared to the normal state (dashed grey line). Plotted in semiconductor representation, such that quasiparticle states at $E_k < 0$ are occupied (shading). Figure inspired by [147].

metal close to the Fermi energy is plotted as the grey dashed lines in Fig. 2.2(b), with electrons (holes) corresponding to the line with positive (negative) gradient. First, we see that the wavefunction described by $(u_{\mathbf{k}}, v_{\mathbf{k}})$ is predominantly hole-like for $\epsilon_{\mathbf{k}} < 0$ and predominantly electron-like for $\epsilon_{\mathbf{k}} > 0$: we therefore describe these wavefunctions as Bogoliubov quasiparticles [148]. Second, the pair potential Δ represents the energy gap from the Cooper pair condensate to quasiparticle excitations, and corresponds to the binding energy of a Cooper pair. Finally, at finite temperature quasiparticles will be excited to energies $E_{\mathbf{k}}$, suppressing the energy gap such that

$$\frac{\Delta(T)}{\Delta(0)} \approx 1.74 \left(1 - \frac{T}{T_C}\right)^{1/2}, \tag{2.5}$$

until $\Delta(T) \to 0$ at the critical temperature $T = T_C$. This result gives

$$\Delta(0) = 1.764 k_B T_C. \tag{2.6}$$

The characteristic length scale over which the pairing potential acts is characterised by $\xi_0 \sim \hbar v_F/\Delta \sim \hbar v_F/k_B T_C$, consistent with the Ginzburg-Landau coherence length which describes the characteristic length for variations in the superconducting order parameter [149].

The density of states (DOS) D_S in the superconducting state is readily calculated from $D_S dE = D_N d\epsilon$, since quasiparticle excitations are in one-to-one correspondence with electronic excitations in the normal metal. This gives

$$\frac{D_S}{D_N} = \frac{d\epsilon}{dE} = \frac{E}{(E^2 - \Delta^2)^{1/2}} \tag{2.7}$$

for $E > \Delta$, and 0 for $E < \Delta$ ($E > 0$, from Eq. 2.4). Equation 2.7 is plotted in Fig. 2.2(c) using the semiconductor representation, where energies are shown as two bands: the lower completely full at $T = 0$ and the upper completely empty, separated by a gap 2Δ.

2.1.3. Tunnelling Spectroscopy

The DOS in a material can be measured directly with a point contact geometry, where a probe is isolated from the device of study by a narrow conducting region [150]. The tunnel current between the two is described by [147]

$$I = A|T|^2 \int_{-\infty}^{\infty} D_1(E - eV_{SD}) D_2(E) [f(E - eV_{SD}) - f(E)] dE, \tag{2.8}$$

where V_{SD} is the source-drain voltage applied to the probe, D_1 (D_2) is the DOS in the probe (device) and $f(E)$ is the probability distribution describing occupation of the state at energy E. In the case where both probe and device are two-dimensional electronic reservoirs, both D_1 and D_2 are independent of energy as $T \to 0$. Therefore, Eq. 2.8 gives $I_{NN} = G_0 V$, where $G_0 \equiv (2e^2/h) \sum T_n$ is the multichannel Landauer equation for many conducting modes, each with transmission probability T_n [151, 152].

The semiconductor representation for the superconducting DOS is convenient to describe tunnelling processes between materials, since a potential difference simply adds an energy shift. This means that transitions are horizontal in energy, assuming only elastic processes, and multiple parallel conduction channels can be easily visualised. The case of normal-superconductor tunnelling is depicted in Fig. 2.3(a). The differential conductance is given by

$$G_{NS} \equiv \frac{dI_{NS}}{dV_{SD}} \propto D_1 \int_{-\infty}^{\infty} D_2(E) \frac{\partial f(E - eV_{SD})}{\partial V_{SD}} dE, \tag{2.9}$$

which tends to

$$G_{NS} \propto D_2(eV_{SD}) \tag{2.10}$$

at low temperature since $\partial f(E - eV_{SD})/\partial V_{SD} \to \delta(E - eV_{SD})$. The tunnel conductance is therefore directly proportional to the superconducting DOS D_2 in the device.

For a tunnelling probe with a superconducting DOS [Fig. 2.3(b)], D_1 cannot be taken

out of the integral so [153]

$$G_{\mathrm{SS}} \propto \int_{-\infty}^{\infty} D_2(E)\Big\{\frac{\partial D_1(E-eV)}{\partial V}[f(E)-f(E-eV_{\mathrm{SD}})] - D_1(E-eV_{\mathrm{SD}})\frac{\partial f(E-eV_{\mathrm{SD}})}{\partial V_{\mathrm{SD}}}\Big\}dE \tag{2.11}$$

$$\propto D_2 * g. \tag{2.12}$$

The conductance is therefore a convolution of the device DOS D_2 with a known function g, which is given by the DOS in the probe D_1. In the case of a superconducting probe at zero magnetic field (as in Chapters 6 and 7), D_1 is assumed to be a superconducting DOS with the same gap Δ as that of the device. This amounts to conductance features shifted in eV_{SD} by $\pm e\Delta$.

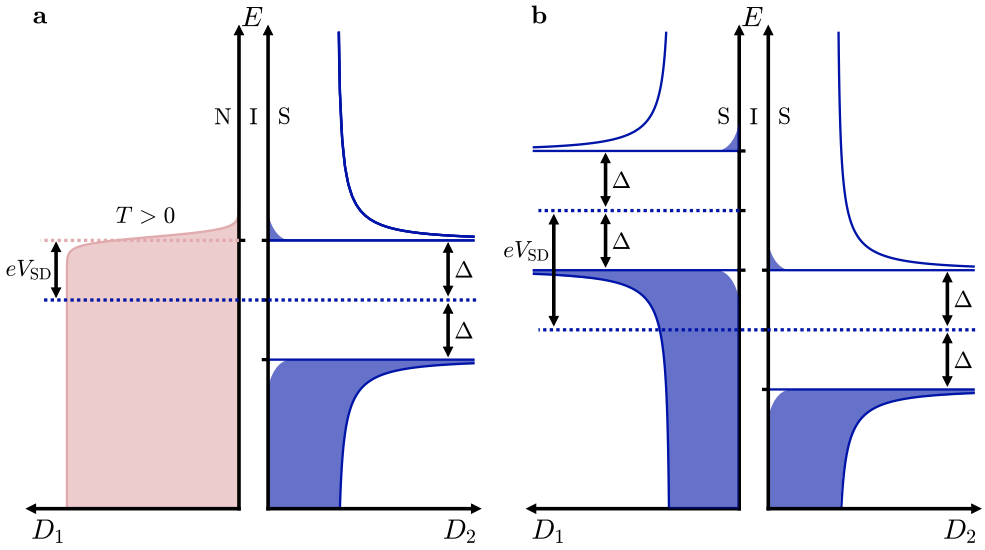

Figure 2.3. Sketch of tunnelling spectroscopy in the cases of a normal (N) or superconducting (S) probe. a Density of states in the probe (D_1) and the superconducting device (D_2), separated by a narrow insulating (I) barrier. A current can flow when a bias voltage $V_{\mathrm{SD}} = \Delta/e$ is applied across the NIS junction. **b** Same as (a) for the case of an S probe. In this case, a current can flow when $V_{\mathrm{SD}} = 2\Delta/e$. Figure inspired by [147].

2.2. Superconductor-Semiconductor Interface

We turn our attention to an interface between a superconductor (S) and normal semiconductor (N).

2.2.1. Andreev Reflection

Figure 2.4(a) depicts an electron in the N region at an energy E close to the Fermi energy E_F, incident on an NS interface. For energies below the superconducting gap, $|E| < \Delta$, there are no available states in the superconductor so the electron cannot propagate into the S region. However, the electron can be transmitted as a Cooper pair in the superconductor by taking an additional electron from the Fermi sea. In the normal region, this corresponds to a hole with the same wavevector as the incident electron. Since the trajectory of a hole is opposite to its wavevector [130], it retraces the path of the incident electron. This retroreflection process is shown in Fig. 2.4(b). For an s-wave superconductor, the Cooper pair must be spin singlet: the electron taken from the Fermi sea must have opposite spin to the incident electron. This leaves a net spin polarisation in the Fermi sea which is the same as that of the incident electron, so the reflected hole has the same spin as that of the incident electron. Disorder, impurities or a Fermi velocity mismatch lead to imperfect interfaces in real systems, such that spectral reflections of the incident electron are also possible [see dashed arrow in Fig. 2.4(b)].

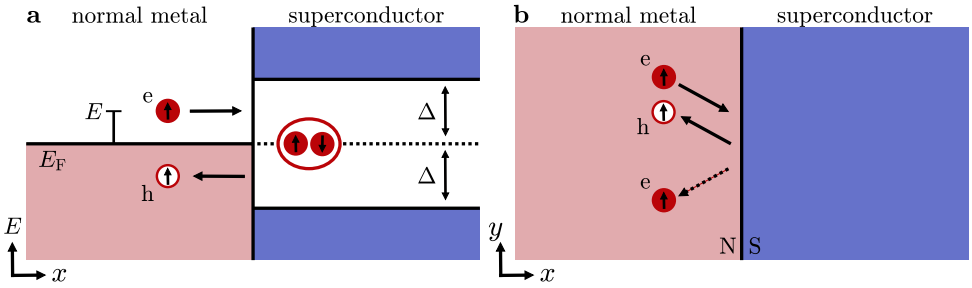

Figure 2.4. Schematic of Andreev reflection. **a** Interface between a normal metal (N) and superconductor (S), in an energy-position representation. An incident electron in N, at an energy E above the Fermi energy E_F, is transferred to a Cooper pair in S by taking a second electron from the Fermi sea, amounting to a reflected hole in N. **b** Andreev reflection in position space. The reflected hole retraces the trajectory of the incident electron. An imperfect interface can lead to spectral reflection of the incident electron (dashed arrow).

The electron-hole reflection process is referred to as Andreev reflection, after its formulation by Andreev in 1964 in the context of the thermal conductivity close to NS interfaces [67]. A model of the effect was first provided by Blonder, Tinkham and Klapwijk (BTK) [154], with a rigorous microscopic theory later given by Zaitsev [155] and Arnold [156]. Figure 2.5(a) shows the model set-up, which considers plane-wave solutions to Eq. 2.2. An electron (i) with wavevector $+k_e$ is incident on an imperfect NS interface,

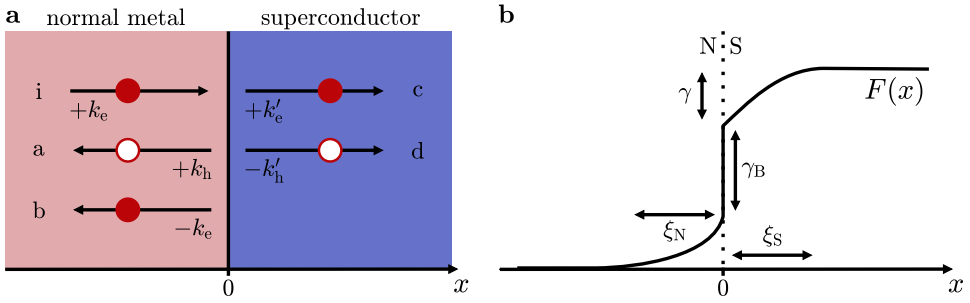

Figure 2.5. Blonder-Tinkham-Klapwijk formalism at a normal-superconductor (NS) interface. a Schematic representation of an incident electron (i) and the possible final states after interaction with the interface: Andreev reflected hole (a), specularly reflected electron (b), transmitted electron (c) and transmitted hole (d). **b** Sketch of the Cooper pair density $F(x)$ across the NS boundary. Superconductivity is weakened in S by γ over a distance ξ_S from the interface. Superconductivity is transferred to the N region over a distance ξ_N from the boundary, after a reduction γ_B depending on the interface quality. Figure inspired by [130].

with the following outcomes: (a) Andreev reflection, giving a hole with wavevector $+k_h$; (b) specular reflection to an electron with $-k_e$; (c) transmission of the electron, with wavevector $+k'_e$; (d) transmission of a hole with wavevector $-k'_h$. The incident, reflected and transmitted waves are described as

$$\begin{aligned}
\psi_i(x) &= \begin{pmatrix} 1 \\ 0 \end{pmatrix} e^{ik_e x} \\
\psi_{\text{refl.}}(x) &= a \begin{pmatrix} 0 \\ 1 \end{pmatrix} e^{ik_h x} + b \begin{pmatrix} 1 \\ 0 \end{pmatrix} e^{-ik_e x} \\
\psi_{\text{transm.}}(x) &= c \begin{pmatrix} u \\ v \end{pmatrix} e^{ik'_e x} + d \begin{pmatrix} v \\ u \end{pmatrix} E^{-ik'_h x}
\end{aligned} \tag{2.13}$$

with

$$\hbar k_{e,h} = \sqrt{2m^*}[E_F \pm E]^{1/2} \tag{2.14}$$

and

$$\hbar k'_{e,h} = \sqrt{2m^*}\left[E_F \pm (E^2 - \Delta^2)^{1/2}\right]^{1/2}. \tag{2.15}$$

The boundary conditions at the NS interface dictate that the wavefunction must be continuous and the gradient of the wavefunctions must match, up to the momentum absorbed by a scattering potential $\hbar v_{F,S} Z \delta(x)$, where $v_{F,S}$ is the Fermi velocity in the superconductor and Z is a dimensionless parameter characterising the barrier height.

Matching Eq. 2.13 to the boundary conditions gives the coefficients

$$a = \frac{uv}{\beta} \tag{2.16}$$

$$b = \frac{(v^2 - u^2)(Z_{\text{eff}}^2 + iZ_{\text{eff}})}{\beta} \tag{2.17}$$

$$c = \frac{u - iZ_{\text{eff}}}{\beta} \tag{2.18}$$

$$d = \frac{ivZ_{\text{eff}}}{\beta}, \tag{2.19}$$

where $\beta = u^2 + (u^2 - v^2)Z_{\text{eff}}^2$ and $Z_{\text{eff}} \equiv [Z^2 + (1-r)^2/4r]^{1/2}$ accounts for a Fermi velocity mismatch $r \equiv v_{\text{F,N}}/v_{\text{F,S}}$ between the semiconductor and superconductor [130, 157]. Scattering at the interface reduces the amplitude of Andreev reflection a, and results in non-zero values for b and d. From Eq. 2.3, we see that the amplitude of Andreev reflection depends on the quasipaticle energy. This is a crucial consideration for understanding the proximity effect in the context of Andreev reflections [158].

2.2.2. Proximity Effect

Up to this stage, we have considered a pair potential which is a step function: it is zero in N and Δ in S. However, from Ginzburg-Landau theory we know that the order parameter cannot abruptly fall to zero [149, 159]. In general, while the pair potential can be discontinuous at the NS interface, the fraction of paired electrons must be continuous [158]. Additionally, from Eq. 2.14 the wavevector of the incident electron and reflected hole is identical only at $E = E_{\text{F}}$, otherwise there is an energy-dependent shift in the wavevector given by $k_{\text{F,N}}(E/E_{\text{F}})$. This wavevector shift, in addition to disorder in N, leads to dephasing of the electron-hole pair over a length scale ξ_{N} into the N region [160, 161]. These correlated electrons and holes correspond to a finite Cooper pair density $F(x)$ in the normal region, which can be thought of as a leakage of Cooper pairs into N [130, 162]. This effective superconducting pairing opens up a proximitised superconducting gap Δ^* in the N region.

A theoretical treatment of the proximity effect was given by Kupriyanov [163] using the quasi-classical Eilenberger equations [164]. The effect on the Cooper pair density $F(x)$ is shown schematically in Fig. 2.5(b) [130]. The Cooper pair density is non-zero in the normal region over a distance ξ_{N}, and suppressed in the superconductor within ξ_{S} of the interface by an amount $\gamma = \rho_{\text{S}}\xi_{\text{S}}/\rho_{\text{N}}\xi_{\text{N}}$, which depends on the specific normal state resistances ρ in the superconductor and normal conductor. The barrier strength is parametrised by

$$\gamma_{\text{B}} = \frac{2}{3}\frac{l_e}{\xi_{\text{N}}}\left\langle Z_{\text{eff}}^2 \right\rangle, \tag{2.20}$$

where the scattering is averaged over incident angles. The connection to the BTK analysis is clear: the proximity effect is strong when the potential barrier at the NS interface is small, since the diffusion of Cooper pairs into the normal region is mediated by Andreev reflections.

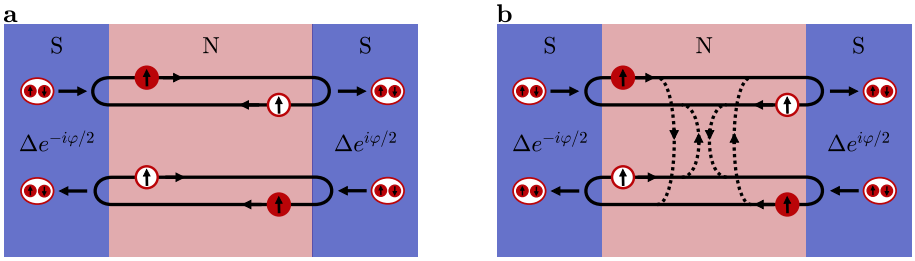

Figure 2.6. Schematic representation of Andreev bound states (ABSs) in a superconductor-normal-superconductor (SNS) junction, with a phase difference φ across the S contacts. a Trajectories of electron-hole reflections in an SNS junction with perfect transmission, forming two independent ABSs corresponding to right- and left-moving Cooper pairs. **b** Scattering in the N region allows the two trajectories to interact (dashed lines), leading to hybridisation between the two states. Figure inspired by [79].

2.2.3. Andreev Bound States

We extend the treatment of Andreev reflections to consider a superconductor-normal semiconductor-superconductor (SNS) junction, which is schematically shown in Fig. 2.6(a). It was shown by de Gennes that a supercurrent could flow across an SNS junction [165], and described in terms of Andreev reflections at the NS interfaces defining the junction [166–169]. Repeated Andreev reflection gives electron and hole wavefunctions which overlap on a common trajectory, since holes are retroreflected at the interfaces. Confinement between the two NS interfaces leads to discrete energy states below the superconducting gap, defined by the trajectories for which the quasiparticle phase is 2π-periodic for a round trip. The wavefunctions constructively interfere for these trajectories, and destructively interfere for all others. The discrete energy states are called Andreev bound states (ABSs).

An energy-dependent phase $\arccos(E/\Delta)$ is accumulated on reflection at an NS interface, since the Andreev reflection coefficient $a = v/u$ (Eq. 2.16 for $Z_{\text{eff}} \to 0$) depends on energy via Eq. 2.3 [147]. For junctions of finite length, carriers also accumulate a phase proportional to their wavevector while traversing the normal region [76, 78, 130, 170]. For a ballistic junction, in which scattering in the normal region can be ignored, the phase matching condition is given by

$$\frac{E}{\Delta}\frac{L}{\xi_{\text{N}}} = 2\arccos\left(\frac{E}{\Delta}\right) \mp \varphi - 2\pi n, \tag{2.21}$$

where φ is the phase difference between the superconducting contacts. In the limit of a short junction ($L \ll \xi_{\text{N}}$), the left side of the equation goes to zero and we obtain solutions

$$E_{\pm}(\varphi) = \pm\Delta\cos(\varphi/2), \tag{2.22}$$

with the two independent branches corresponding to right- and left-moving Cooper pair transport mediated by the ABSs [see Fig. 2.6(a)]. In the presence of scattering, there is

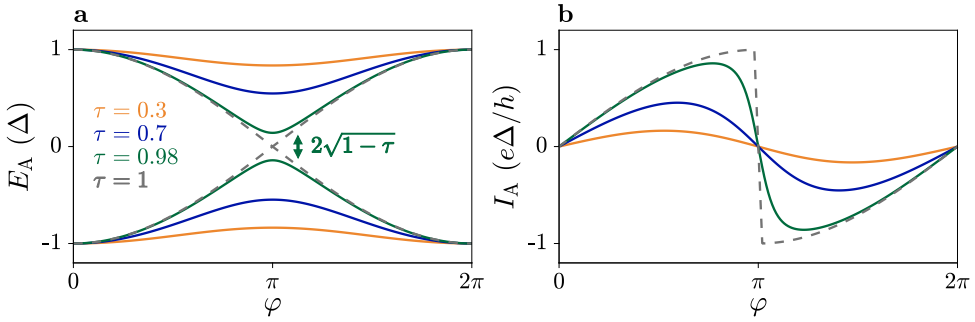

Figure 2.7. Energy and current-phase relation (CPR) of Andreev bound states (ABSs). **a** Energy E_A of ABSs with different transmissions τ (colours), as a function of phase difference φ across the junction. **b** The CPR corresponding to the ABS energies in (a), which has large amplitude and a pronounced forward skewness for $\tau \to 1$.

mixing between the two branches [171, 172], as depicted in Fig. 2.6(b). This gives the energy solutions

$$E_A = \pm\Delta\sqrt{1 - \tau\sin^2(\varphi/2)}, \tag{2.23}$$

where the transmission $\tau \equiv 1/(1 + 4Z_{\text{eff}}^2)$ parametrises the transparency of the NS interfaces. Examples of Eq. 2.23 are plotted in Fig. 2.7(a) for different transmission values τ. For larger τ the bound state energy moves closer to zero for $\varphi \sim \pi$ (coloured lines), until the limit of $\tau = 1$ where Eq. 2.22 is recovered (dashed grey line). From this picture, it is clear how scattering for $\tau < 1$ lifts the degeneracy at $\varphi = \pi$ and gives an avoided crossing of $2\Delta\sqrt{1-\tau}$. Note that, while time-reversal symmetry is broken for a phase difference $\varphi \neq (0, \pi)$, ABSs in a short two-terminal junction are spin-degenerate since their energies are in exact correspondence with transmission eigenvalues, which are Kramer's degenerate [173]. The energies E_A therefore correspond to two-fold degenerate levels, one spin up and one spin down.

At $T = 0$, only ABSs below the chemical potential contribute to the net supercurrent, giving the relation

$$\begin{aligned} I_A(\varphi) &\equiv -\frac{2e}{\hbar}\frac{\partial E_A}{\partial \varphi} \\ &= \frac{e\Delta}{2\hbar}\frac{\tau\sin\varphi}{E_A(\varphi)/\Delta}. \end{aligned} \tag{2.24}$$

The supercurrent $I_A(\varphi)$ carried by each ABS in Fig. 2.7(a) is plotted in Fig. 2.7(b). For small transmission τ the current-phase relation (CPR) is sinusoidal, but for large τ there is a pronounced forward skewness due to the higher-order φ terms in Eq. 2.24. The oscillation amplitude also increases for larger τ. This is understood from the net charge flow in an Andreev reflection process, which is doubled due to the retroreflected hole with positive charge. This leads to an excess current relative to the expectation for ohmic transport [154, 174–176].

Equations 2.23 and 2.24 were obtained for a single conducting channel forming in the normal region. In the case of many conducting channels, their contributions are summed to give the total supercurrent I_S. At finite temperature, ABSs are occupied according to a Fermi distribution function $f(E)$ such that

$$I_S = \sum_n I_A(\tau_n)[1 - 2f(E_{A,n})], \tag{2.25}$$

where ABSs corresponding to each channel have an energy $E_{A,n}$ given by Eq. 2.23 with a transmission τ_n. The critical current I_C is defined as the maximum value of $I_S(\varphi)$. For a tunnel junction, where $\tau_n \ll 1$, the critical current is given by $I_C = (\pi\Delta/2e)G_N$, where $G_N \equiv (2e^2/h)\sum\tau_n$ is the junction conductance in the normal state [151, 152, 177].

The concepts outlined in this section give the ingredients for understanding ABSs in planar Josephson junctions. Regions of 2DEG covered by the superconductor are proximitised via the proximity effect. The strength of the proximitised superconducting gap depends on the quality of the material interface. An SNS junction is formed by selectively removing a stripe of superconductor, to give a normal conducting region between two superconducting contacts. Both the normal and superconducting regions of the junction are formed in the 2DEG layer, meaning that the NS interfaces defining the junction are clean and free of defects. This enables ABSs with high transmission, which carry a supercurrent across the junction with a non-sinusoidal current-phase relation. In general, these junctions contain many conducting channels so the total measured current is a sum over contributions from all modes, which have a distribution of transmissions [178, 179]. The ABSs couple the phases of the two superconducting leads, giving an overlap of their wavefunctions. This coupling is described by the Josephson effect.

2.3. Macroscopic Phase in Josephson Junctions

In the previous section, we started from a microscopic model of Andreev reflection at NS interfaces and arrived at equations for the total current carried by Andreev bound states in an SNS junction. These equations describe a supercurrent flowing across the device due to a difference in the superconducting phases of the islands, in the absence of a voltage. This is called the Josephson effect [1]. While the exact formulation of the supercurrent in Eq. 2.24 is specific to the microscopic model of an SNS junction, the Josephson effect is general to a pair of superconducting electrodes coupled by a weak link [177, 180]. In this section, we will discuss the Josephson effect in ideal Josephson junctions and how it extends to a model of a physical device.

2.3.1. Josephson Effect

The Josephson effect was originally based on a microscopic theoretical analysis of paired electron transport between two superconducting electrodes through a thin insulating barrier [1]. The result was that a current

$$I_S = I_C \sin(\varphi) \tag{2.26}$$

flows across the junction due to a difference in the superconducting phases of the two electrodes, φ. Equation 2.26 is referred to as the first Josephson equation. The critical current, I_C, quantifies the maximum supercurrent that can be sustained by the junction. Notice that Eq. 2.26 is the same as Eq. 2.24 in the limit of small transmission coefficient τ. Models describing the Josephson effect, and the dynamical properties of Josephson junctions under a current bias, were derived in this low-transmission limit. Therefore, in the absence of a complete model describing Josephson junctions with a non-sinusoidal CPR, we use a Josephson junction with a sinusoidal CPR for the remainder of the chapter and consider the results to have only a small numerical deviation compared to a non-sinusoidal CPR (see Appendix B for an extended discussion).

The second Josephson equation is

$$\frac{\mathrm{d}\varphi}{\mathrm{d}t} = \frac{2eV}{\hbar}, \tag{2.27}$$

which describes a Josephson junction under a constant voltage bias V. The coupling free energy stored in the junction is $F = \int I_S V dt$, which gives [147]

$$F(\varphi) \propto -E_J \cos(\varphi) \tag{2.28}$$

by combination of Eqs. 2.26 and 2.27, where $E_J \equiv \hbar I_C/2e$. The Josephson energy E_J describes the strength with which the two superconducting contacts are coupled through the weak link [181].

2.3.2. The RCSJ Model

Equation 2.26 describes a perfect Josephson junction: a non-linear inductor carrying a dissipationless supercurrent. However, real devices typically have some dissipative and charging elements which must be included [182]. To do so, we consider an ideal Josephson junction shunted by a resistor and a capacitor [see Fig. 2.8(a)]; this representation is referred to as the resistively and capacitively shunted junction (RCSJ) model. The resistance R constitutes a dissipative current channel V/R which is dominant in the finite voltage regime, for bias currents above I_C. The shunt capacitance between the two electrodes, C, gives a displacement current $C\mathrm{d}V/\mathrm{d}t$. In the presence of an external bias current I, the total current is distributed over these three channels:

$$I = I_C \sin(\varphi) + \frac{V}{R} + C\frac{\mathrm{d}V}{\mathrm{d}t}. \tag{2.29}$$

Written in terms of the superconducting phase difference, Eq. 2.29 becomes

$$\frac{\mathrm{d}^2\varphi}{\mathrm{d}\tau^2} + Q^{-1}\frac{\mathrm{d}\varphi}{\mathrm{d}\tau} + \sin(\varphi) - \frac{I}{I_C} = 0, \tag{2.30}$$

where $\tau = \omega_{P0}t$ is a dimensionless time parametrised by the plasma frequency

$$\omega_{P0} = \left(\frac{2eI_C}{\hbar C}\right)^{1/2}, \tag{2.31}$$

and the quality factor Q is defined by

$$Q = \omega_{\mathrm{P0}} RC. \tag{2.32}$$

Equation 2.30 governs the dynamics of the superconducting phase difference in a Josephson junction under a current bias. It is often described with analogy to the equation of motion of a "phase particle" of mass $(\hbar/2e)^2 C$ in an effective potential

$$U(\varphi) = -E_{\mathrm{J}} \cos(\varphi) - (\hbar I/2e)\varphi, \tag{2.33}$$

and subjected to a drag force $(\hbar/2e)^2(1/R)\mathrm{d}\varphi/\mathrm{d}t$ [see Fig. 2.8(b)]. In the superconducting state, the phase particle sits in a local minimum of the so-called washboard potential ($\mathrm{d}\varphi/\mathrm{d}t = 0$), oscillating with a natural frequency ω_{P0}. The damping factor, proportional to Q^{-1}, relates the oscillation energy ($\propto \omega_{\mathrm{P0}}$) to the energy dissipated ($\propto R^{-1}$) [183, 184]. In the following, we consider underdamped junctions, that is when $Q \gtrsim 1$.

On application of a bias current I, the potential tilts and the position of the local minimum shifts [see Fig. 2.8(b)]. When the bias current reaches the critical current, the tilt of the potential is sufficiently large that there is no potential barrier to confine the phase particle, which subsequently "rolls" down the potential landscape. This corresponds to the finite voltage state, since $\mathrm{d}\varphi/\mathrm{d}t \neq 0$. After a transition to the resistive state, reducing the bias current below I_{C} is not sufficient to transition back to the superconducting state for $Q \gtrsim 1$. In the phase particle analogy, light damping is insufficient to "retrap" the phase in a local minimum because of the particle's inertia. Complete retrapping occurs when the bias current is lowered below $I_{\mathrm{R}} \approx 4I_{\mathrm{C}}/\pi Q$, where the dissipation over one 2π cycle reduces the phase particle energy to below that of the potential barrier.

2.3.3. Phase Escape by Fluctuations

The analysis above does not consider any fluctuations in the environment, neither from coupling to a thermal bath nor quantum mechanical fluctuations due to a zero-point energy. The inclusion of these fluctuations allows a transition from the superconducting to resistive state to occur for bias currents below the critical current. This is schematically depicted in Fig. 2.8(b), showing escape of the phase particle by macroscopic quantum tunnelling (MQT) and thermal activation (TA). When dissipation is large it is possible for the junction to transition from the resistive to the superconducting state, referred to as retrapping. In this regime, many escape events are required to turn the junction resistive. This is referred to as phase diffusion (PD) [see Fig. 2.8(b)]. Since fluctuations are stochastic in nature, switching events are probabilistic and occur according to a switching probability distribution (SPD): the probability for a switch to occur at a given bias current I_{SW}, per unit current.

The SPD is dependent on the rate at which the DC current is increased, ν. To obtain an experimentally-independent description for the mechanisms of phase dynamics, we must convert to an escape rate, Γ. This is done via a Kurkiärvi–Fulton–Dunkleberger

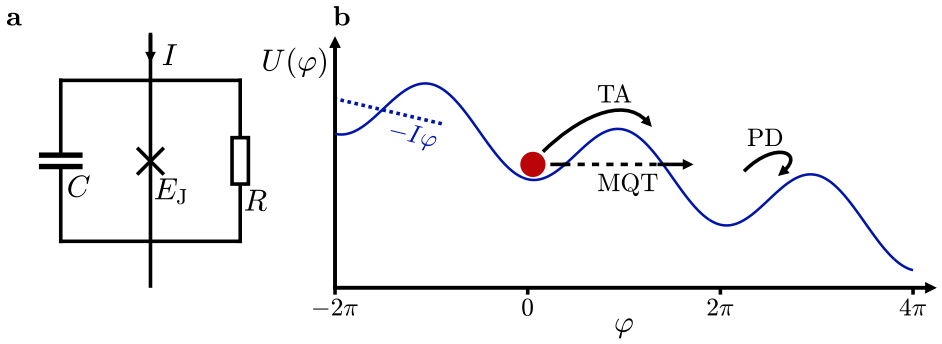

Figure 2.8. Resistively and Capacitively Shunted Josephson junction. **a** Schematic representation of the capacitive, Josephson and resistive elements, under a bias current I. **b** The washboard potential $U(\varphi)$, in which the phase variable (red circle) moves. A current bias I results in a tilt of the potential. Mechanisms which allow the phase particle to escape its local minimum are indicated for macroscopic quantum tunnelling (MQT) and thermal activation (TA). Retrapping events in subsequent local minima result in phase diffusion (PD).

(KFD) transformation using the equation [185, 186]

$$\Gamma(I_{\mathrm{SW}}) = \mathrm{SPD}(I_{\mathrm{SW}})\nu \left[1 - \int_0^{I_{\mathrm{SW}}} \mathrm{SPD}(I)dI\right]^{-1}. \tag{2.34}$$

The escape rate of a Josephson junction to the resistive state at a given DC bias $I_{\mathrm{DC}} = I_{\mathrm{SW}}$ follows the general dependence [187–189]

$$\Gamma(I_{\mathrm{SW}}, T) = \Omega(I_{\mathrm{SW}}, T)e^{-\Delta U(I_{\mathrm{SW}},T)/k_B T}, \tag{2.35}$$

where Ω is the attempt frequency and ΔU is the potential barrier height. Under a reduced DC bias of $\gamma = I_{\mathrm{DC}}/I_{\mathrm{C}}$, the approximate barrier height is $\Delta U = 2E_{\mathrm{J}}\left(\sqrt{1-\gamma^2} - \gamma\cos^{-1}\gamma\right)$.

In the case of MQT, Eq. 2.35 is adjusted to the analytical formula [189]

$$\Gamma_{\mathrm{Q}} = \frac{\omega_{\mathrm{P}}}{2\pi}\sqrt{\frac{864\pi\Delta U}{\hbar\omega_{\mathrm{P}}}}\exp\left(-7.2\left(1 + \frac{0.87}{Q}\right)\frac{\Delta U}{\hbar\omega_{\mathrm{P}}}\right), \tag{2.36}$$

where $\omega_{\mathrm{P}} = \omega_{\mathrm{P0}}\left(1-\gamma^2\right)^{1/4}$ is the plasma frequency at γ. The junction capacitance C enters in the bare plasma frequency ω_{P0} (Eq. 2.31) and quantifies the size of phase particle oscillations in the metastable state [190, 191].

For $Q \gg 1$, we can use an analytical formula for the retrapping rate [189]

$$\Gamma_{\mathrm{R}} = \frac{I_{\mathrm{SW}} - I_{\mathrm{R}}}{I_{\mathrm{C}}}\omega_{P0}\sqrt{\frac{E_{\mathrm{J}}}{2\pi k_B T}}\exp\left(-\left(\frac{I_{\mathrm{SW}} - I_{\mathrm{R}}}{I_{\mathrm{C}}}\right)^2\frac{E_{\mathrm{J}}Q^2}{2k_B T}\right), \tag{2.37}$$

where I_R is the retrapping current. We measure intermediately damped junctions with $Q \gtrsim 1$, so this relation can only be considered as an approximation.

Equations 2.35–2.37 describe the phase escape mechanisms for underdamped Josephson junctions, and will be used extensively in Chapters 4 and 5 to describe switching current measurements of planar Josephson junctions.

2.4. Interference Effects in Josephson Junctions

We have seen that the macroscopic phase is a defining characteristic of superconductors, and directly leads to the Josephson effect outlined in the previous section. The macroscopic phase variable also has implications for interference effects in a magnetic field. Since the superconducting wavefunction must be single valued, a closed path through a superconductor must return the same value modulo 2π. London considered the most simple case of a superconducting loop [192], finding that a quantity called the fluxoid satisfies

$$\Phi' = n\,\Phi_0, \tag{2.38}$$

where n is an integer and $\Phi_0 = h/2e$ is the magnetic flux quantum in a superconductor [193]. The fluxoid is defined as

$$\Phi' \equiv \Phi + \frac{m^*}{2e}\oint \mathbf{v}_s \cdot d\mathbf{s}, \tag{2.39}$$

where the first term accounts for a flux threading the superconducting loop $\Phi \equiv \oint \mathbf{A}\cdot\mathrm{d}\mathbf{s}$, and the second considers the supercurrent velocity $\mathbf{v}_s$ flowing in the loop. For a path deeper in the superconductor than the penetration depth, where the supercurrent density is zero, we have $\Phi' = \Phi$. We apply this principle to circuits containing Josephson junctions.

2.4.1. Fraunhofer Interference

Thus far, the Josephson junction phase φ has been understood as the difference between the macroscopic phases of the two superconducting contacts, i.e. $\varphi = \Delta\phi$. This is true for a hypothetical point-like junction, but is not gauge-invariant in a finite-sized junction due to a vector potential $\mathbf{A}$ threading the area between the contacts. We therefore define the gauge-invariant phase difference as $\varphi \equiv \Delta\phi - (2\pi/\Phi_0)\int \mathbf{A}\cdot\mathrm{d}\mathbf{s}$ [147].

Consider a JJ of finite size in a perpendicular magnetic field $B_\perp$, such that a flux Φ threads the area A of the junction [Fig. 2.9(a)]. The phase φ varies linearly with distance along each contact, due to the flux threading the junction. For a uniform current density, the total current across the junction is

$$\frac{I(\Phi)}{I_0} = \left|\frac{\sin(\pi\,\Phi/\Phi_0)}{\pi\,\Phi/\Phi_0}\right|, \tag{2.40}$$

as shown in Fig. 2.9(b). This Fraunhofer pattern is analogous to light passing through a narrow rectangular slit. In the case of a non-uniform current density, or a non-rectangular

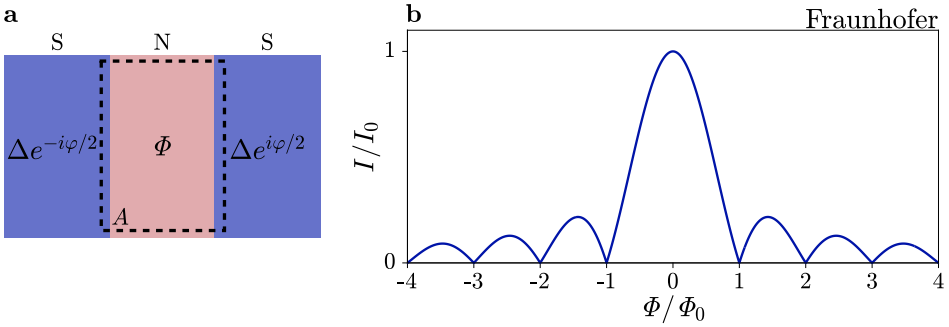

Figure 2.9. Fraunhofer interference in a Josephson junction of finite size. **a** Sketch of a junction with area A, into which a flux Φ penetrates. **b** Modulation of the supercurrent I flowing in the junction, relative to the maximum I_0, as a function of flux Φ through the junction area.

area, there is a distortion to the interference pattern and the result is a Fourier transform of a more complex shape. Measurements of the interference pattern in a single JJ can be used to infer properties of the junction shape or the supercurrent distribution [194, 195]. In planar JJs, screening by the superconducting leads has been shown to affect the Fraunhofer pattern, since the external field is repelled from the leads and instead threads the junction area. This flux focusing effect has been shown to increase the effective cross-section of the junction, and affect the behaviour of JJs in an in-plane magnetic field [196].

2.4.2. Orbital Effects

A similar interference effect results from a magnetic field below the superconducting leads of a planar Josephson junction [120]. An in-plane magnetic field $B_\parallel$ applied to a planar junction threads a flux $\Phi_\parallel$ in the area $A_\parallel$ underneath the superconducting leads [Fig. 2.10(a)], which leads to a position-dependent phase for Andreev reflection processes between the 2DEG and the superconductor. The induced order parameter in the 2DEG therefore varies along the length of the contact as $\Delta^*(y) = \Delta e^{iqy}$, where $q \equiv (2\pi/\Phi_0)B_\parallel d$. The length d is the distance between the 2DEG and superconductor, including penetration of the magnetic field into the superconducting layers. The effective induced superconducting gap in the 2DEG is given by the integral

$$\Delta^* = \frac{1}{L_{\mathrm{SC}}}\int_0^{L_{\mathrm{SC}}} \mathrm{d}y \Delta e^{iqy} = \Delta e^{iqL_{\mathrm{SC}}/2}\mathrm{sinc}(qL_{\mathrm{SC}}/2), \tag{2.41}$$

where L_{SC} is the length of the superconducting contact.

This modulation in the superconducting gap is plotted in Fig. 2.10(b), and shows that there is a complete suppression of the induced gap for $B_\parallel = \Phi_0/(dL_{\mathrm{SC}})$. This effect has been observed in planar Josephson junctions as a non-monotonic modulation of the supercurrent in an in-plane magnetic field [122, 197].

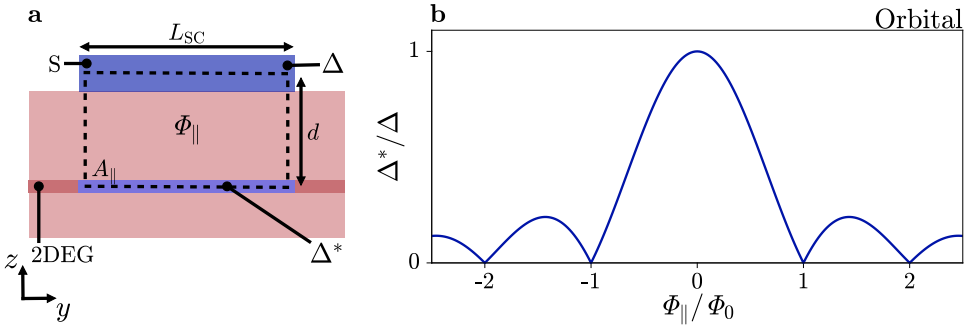

Figure 2.10. Orbital effects in planar Josephson junctions. a Sketched cross-section of the contact of a planar junction, with length L_{SC}. A flux $\Phi_\parallel$ threads the area $A_\parallel$ bounded by the superconductor (S) and the proximitised two-dimensional electron gas (2DEG). **b** Modulations of the induced superconducting gap Δ^* in the 2DEG, relative to Δ in S, as a function of $\Phi_\parallel$.

2.4.3. Superconducting Quantum Interference Device

The combination of flux quantisation and the Josephson effect is used to generate devices which are extremely sensitive to magnetic fields: superconducting quantum interference devices (SQUIDs). They consist of two Josephson elements connected with a superconducting loop, as shown in Fig. 2.11(a) for the case of two SNS junctions (labelled JJ1 and JJ2). Taking a closed path around the loop (dashed line), we obtain a relationship between the junction phases and the flux Φ threading the loop

$$\varphi_2 - \varphi_1 = 2\pi \frac{\Phi}{\Phi_0}. \tag{2.42}$$

In general, the flux Φ threading the loop not only originates from the externally applied flux Φ_x, but also has contributions from screening currents in the loop and fluxes coupled to the loop via a bias current [147]. For a lead inductance which is symmetric with respect to the device, there is no contribution from the bias current. However, fluxes from screening currents of $\Phi_s = I_s L$, where L is the loop inductance, can be significant in the case of superconducting films with large kinetic inductance [198] and large circulating currents I_s [153].

The total critical current through the SQUID is given by the sum of contributions through JJ1 and JJ2, namely

$$I = I_1 \sin\varphi_1 + I_2 \sin\varphi_2, \tag{2.43}$$

where I_i denotes the critical current of each Josephson junction. Combining Eqs. 2.42 and 2.43, we obtain a critical current for the SQUID of

$$I(\Phi) = \max_{\varphi_1} \left[I_1 \sin(\varphi_1) + I_2 \sin(\varphi_1 + 2\pi\Phi/\Phi_0) \right]. \tag{2.44}$$

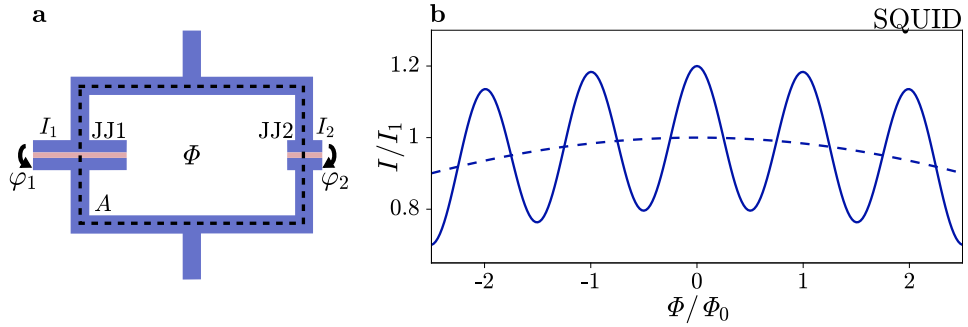

Figure 2.11. Interference effects in a superconducting quantum interference device (SQUID). a Sketch of a SQUID containing two Josephson junctions, JJ1 and JJ2, each with a phase difference φ_i and critical current I_i ($i \in \{1, 2\}$). A flux Φ threads the area A enclosed by the superconducting loop. **b** Oscillations in the current I through the SQUID when $I_1 \gg I_2$. Oscillations are due to a changing current through JJ2 as a function of $\varphi_2 \propto \Phi$, on a background corresponding to JJ1.

The maximum condition of Eq. 2.44 is reached at $\varphi_1 \equiv \varphi^*(\Phi)$. This maximising phase difference is calculated from the condition [199]

$$\frac{\partial I_1(\varphi_1)}{\partial \varphi_1} + \frac{\partial I_2(\varphi_1 + 2\pi\Phi/\Phi_0)}{\partial \varphi_1} = 0. \tag{2.45}$$

The maximising phase φ^* therefore depends not only on the relative size of the critical currents in the junctions, but also their relative gradients [199].

In the case of a strongly asymmetric SQUID, where $I_1 \gg I_2$, the maximising phase is close to the critical phase of the reference junction, JJ1. If $\varphi^*(\Phi)$ is well localised to this critical phase, then the phase across JJ2 is $\varphi_2 \approx 2\pi\Phi/\Phi_0$. The SQUID supercurrent of Eq. 2.44 then simplifies to

$$I(\Phi) \approx I_1 + I_2 \cos\left(2\pi\frac{\Phi}{\Phi_0}\right), \tag{2.46}$$

where I_1 and I_2 are the flux-dependent supercurrents given by Eq. 2.40, for JJ1 and JJ2 respectively. Equation 2.46 reveals that the current through an asymmetric SQUID has a background contribution from JJ1 and is modulated by the flux-dependent current through JJ2. This is plotted in Fig. 2.11(b) as the solid line, where the dashed line corresponds to the modulation of JJ1 due to its finite size (see Fig. 2.9). In this instance, the flux Φ directly corresponds to the phase difference φ_2 across JJ2.

By designing a SQUID with a large critical current asymmetry, and by limiting the effect of screening currents, a direct correspondence can be made between the externally applied magnetic field perpendicular to the device and the superconducting phase difference across the Josephson junction with small critical current: $\varphi_2 \approx 2\pi(\Phi/\Phi_0)$. After subtracting the background current of the large junction, the result is the current-phase relation of the small junction. This technique is used extensively in Chapters 5, 6 and 7.

2.5. Josephson Junctions and Microwave Fields

In the previous sections, we have studied the response of Josephson junctions to a DC source. In the following section, we consider how the behaviour of a Josephson junction changes when subjected to an AC driving source. The supercurrent response is to form constant-voltage Shapiro steps [200], while the coupling of quasiparticles to the driving field generates replication of conductance features by photon assisted tunnelling [201]. We also investigate the possibility of light-matter coupling between irradiated photons and the electronic wavefunctions, and the implications this might have for engineering energy bands in condensed matter systems [111, 113].

2.5.1. Shapiro Steps

Consider a Josephson junction biased with a voltage signal V, which has a time-varying component V_1 of angular frequency ω_1 [147]

$$V = V_0 + V_1 \cos \omega_1 t. \tag{2.47}$$

From Eq. 2.27, we obtain a time-varying phase difference across the junction

$$\varphi(t) = \varphi_0 + \omega_0 t + \frac{2eV_1}{\hbar\omega_1} \sin \omega_1 t \tag{2.48}$$

where $\omega_0 \equiv 2eV_0/\hbar$. Inserting this time-dependent phase into Eq. 2.26 we have

$$I_\mathrm{S} = I_\mathrm{C} \sum_n (-1)^n J_n \left[\frac{2eV_1}{\hbar\omega_1} \sin(\varphi_0 + \omega_0 t - n\omega_1 t) \right], \tag{2.49}$$

where $J_n(x)$ is an n^{th}-order Bessel function of the first kind [see Fig. 2.12(a)]. Due to the oscillatory term, there is only a time-averaged component to the supercurrent when $\omega_0 = n\omega_1$, or equivalently for DC bias values

$$V_n = n\frac{\hbar\omega_1}{2e}. \tag{2.50}$$

A DC current only flows when the condition of Eq. 2.50 is met, and has an average value

$$|\langle I_\mathrm{S} \rangle_n| = I_\mathrm{C} \left| J_n \left(\frac{2eV_1}{\hbar\omega_1} \right) \right|. \tag{2.51}$$

For increasing drive amplitude V_1, there is a greater contribution from higher order terms due to the shape of the Bessel function [see Fig. 2.12(a)].

In practice, the AC drive is never from an ideal voltage source, and in most cases is closer to that of a current source due to a large source impedance compared with the junction impedance [147]. Solutions are no longer analytical in this case and so the system must be solved numerically. We gain a phenomenological understanding by considering that an AC current in Eq. 2.33 is analogous to a time-varying tilt in the washboard potential, such that at some times the phase particle is confined in a

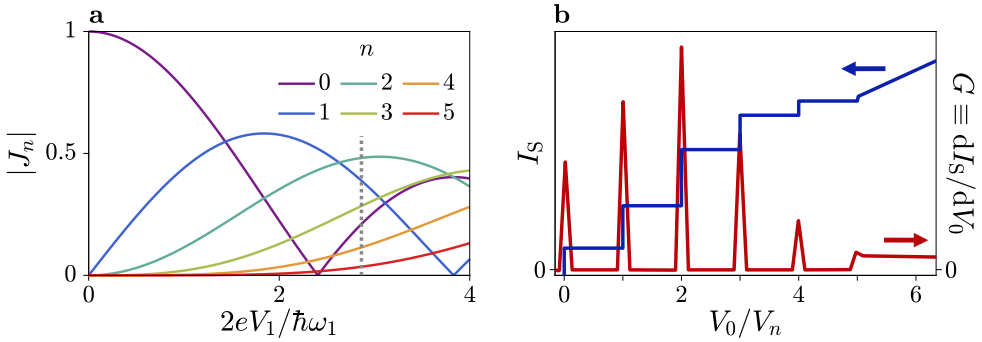

Figure 2.12. Schematic representation of Shapiro steps. **a** Absolute amplitude of Bessel functions $|J_n(x)|$ from $n = 0$ to 5 (colours), as a function of AC drive amplitude V_1. **b** Sketch of Shapiro steps, at a drive power indicated by the grey dashed line in (a). Steps in the current-voltage trace are shown in blue, with the corresponding peaks in differential conductance $G \equiv \mathrm{d}I_\mathrm{S}/\mathrm{d}V_0$ drawn in red.

local minimum and at some times the confining barrier goes to zero [202]. For situations satisfying Eq. 2.50, the oscillation period of the potential is synchronised with the motion of the phase particle such that the phase moves through an integer number of local minima, n, before being retrapped. Averaged over time, this corresponds to a voltage drop across the junction which takes the form of steps. Figure 2.12(b) schematically shows these Shapiro steps at a fixed V_1 [grey dashed line in Fig. 2.12(a)], alongside the differential conductance $G \equiv \mathrm{d}I_\mathrm{S}/\mathrm{d}V_0$ which has a peak at the transition of one step to another.

In Josephson junctions where the insulating barrier is very large, the superconducting wavefunctions of the two contacts are only very weakly coupled. In this case, a small current can flow by stochastic tunnelling events, where the time between tunnelling events is long compared with other timescales in the system. We therefore do not expect time-correlated effects, meaning that a time-varying voltage signal cannot be directly attributed to a time-varying phase difference across the junction [203–207]. Nevertheless, interaction with the oscillating electromagnetic field can promote transport across the junction by absorption or emission of photons, leading to a DC supercurrent [203]

$$I_\mathrm{S} = \sum_{n=-\infty}^{\infty} J_n^2\left(\frac{2eV_1}{\hbar\omega_1}\right) I_{\mathrm{S},0}\left(V_0 + \frac{n\hbar\omega_1}{2e}\right) \tag{2.52}$$

where $I_{\mathrm{S},0}$ is the DC supercurrent in absence of an AC drive. This is readily related to a differential conductance

$$\begin{aligned} G &\equiv \frac{\mathrm{d}I_\mathrm{S}}{\mathrm{d}V_0} \\ &= \sum_{n=-\infty}^{\infty} J_n^2\left(\frac{2eV_1}{\hbar\omega_1}\right) G_0\left(V_0 + \frac{n\hbar\omega_1}{2e}\right). \end{aligned} \tag{2.53}$$

This process is schematically shown in Fig. 2.13(a), for a source-drain bias

$V_{SD} = -\hbar\omega_1/(2e)$. This result has a similar form to that of quasiparticle transport, obtained in the general case by Tien and Gordon [201] and described in the next section.

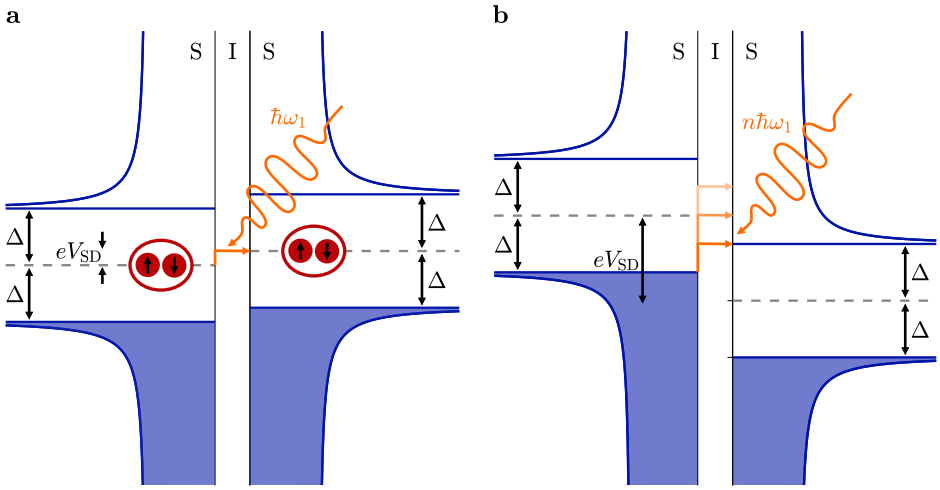

Figure 2.13. Photon assisted tunnelling across a superconductor-insulator-superconductor (SIS) junction. a Microwave-induced tunnelling of Cooper pairs across an SIS junction, by absorption of a photon of energy $\hbar\omega_1$. A current can flow at a bias $2eV_{SD} = \pm n\hbar\omega_1$. **b** Microwave-induced tunnelling of quasiparticles across an SIS junction at a bias $eV_{SD} = 2\Delta \pm n\hbar\omega_1$. Single photon (bright orange) and multi-photon (pale orange) processes are indicated in parallel.

2.5.2. Photon Assisted Tunnelling

Transport of quasiparticles across a Josephson junction is highly non-linear with voltage, due to the sharp peak in the DOS at the superconducting gap edge. The contribution of quasiparticle transport to the total current must take this into account, in addition to the interaction of the quasiparticle DOS with an AC voltage across the junction electrodes. The effect of this AC drive is to introduce a time-dependent shift in the relative energies of the superconducting electrodes [201]. It is assumed that there is no effect of the internal energy levels. This time-dependent shift enters the quantum mechanical phase factor $\phi(t)$ as

$$e^{-i\phi(t)} = e^{-iE_k t/\hbar} e^{-i(eV_1/\hbar/\omega_1)\sin\omega_1 t}, \tag{2.54}$$

where the second term can be written in terms of a sum over Bessel functions. The total quasiparticle current is then given by [208]

$$I_{qp}(V_0) = \sum_{n=-\infty}^{\infty} J_n^2\left(\frac{eV_1}{\hbar\omega_1}\right) I_{qp,0}\left(V_0 + n\frac{\hbar\omega_1}{e}\right), \tag{2.55}$$

where $I_{\mathrm{qp},0}$ is the non-linear quasiparticle current in the absence of irradiation. The corresponding differential conductance is

$$G(V_0) = \sum_{n=-\infty}^{\infty} J_n^2\left(\frac{eV_1}{\hbar\omega_1}\right) G_0\left(V_0 + n\frac{\hbar\omega_1}{e}\right). \tag{2.56}$$

The effect of Eq 2.55 is to distribute the current flow corresponding to the alignment of occupied and unoccupied states across a number of channels, with a weighting given by the squared Bessel function [147]. These parallel current paths are schematically shown in Fig. 2.13(b), where multiple quasiparticle current channels are possible by absorbing n photons of energy $\hbar\omega_1$. This can be interpreted as the quasiparticle level at energy E effectively splitting into many levels at $E \pm n\hbar\omega_1$, however this does not constitute a modulation in the DOS, rather an effective expression of the parallel current paths. Since the sum over squared Bessel functions is identically one, the quasiparticle current is conserved independent of the AC drive strength V_1. These quasiparticle tunnelling events are referred to as photon assisted tunnelling and give rise to conductance peaks offset by $\pm n\hbar\omega_1$. They are inelastic, stochastic processes which are not phase coherent for charge transport across the junction.

2.5.3. Floquet States

The treatments for both Shapiro steps and photon assisted tunnelling do not consider any change to the eigenstates of the system. However, an eigenstate change might arise from coherent coupling to the electromagnetic field, giving rise to complex structures in the energy spectrum [110, 209–215].

In general, solutions to the Schrödinger equation with a time-periodic potential can be written in terms of time-periodic wavefunctions with associated quasi-energies ϵ_i, analogously to Bloch wavefunctions for spatial periodicity [216–219]. These states, called Floquet states, form a complete basis, with quasi-energies ϵ_i that are evenly separated

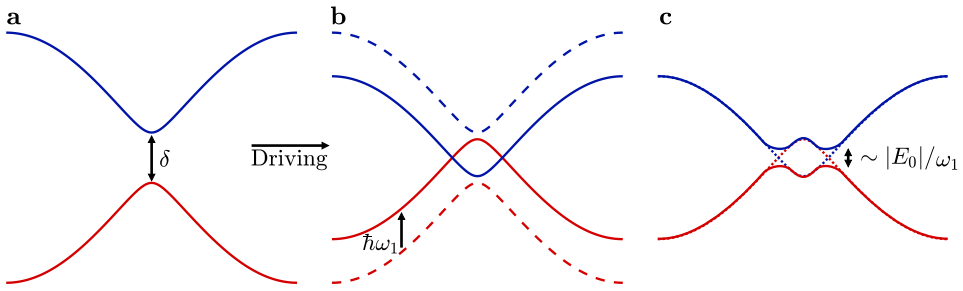

Figure 2.14. Schematic of bandgap engineering via light-matter coupling. a Discrete electronic states separated by an energy gap δ. **b** Upon driving with an electromagnetic field with frequency ω_1, coupling to the electronic states causes a shift in energy $\hbar\omega_1$. **c** Interaction between the branches leads to the opening of a new bandgap, which is proportional to the amplitude of the electromagnetic field $|E_0|$. Figure inspired by [113].

by the drive photon energy $\hbar\omega_1$. Consider discrete electronic states [see Fig. 2.14(a)] subject to a time-varying potential. The driving field generates replicas in the energy bands separated by the photon energy [see Fig. 2.14(b)], resulting in coherent avoided crossings when the photon energy exceeds the energy separation between discrete states [see Fig. 2.14(c)]. This could be used to manipulate bandstructures into complex non-equilibrium phases [220].

The energy gap is proportional to the ratio of the driving field strength and the frequency, meaning that large powers are needed to drive in the optical domain [111, 113, 221]. Relaxation and thermalisation of this out-of-equilibrium process puts a limit on the timescales available, since many-body interactions ultimately lead to heating and decoherence in the system [111, 112, 221–225]. Notably, a recent work explored the tunnelling conductance of a planar Josephson junction under microwave irradiation, and interpreted replicas of conductance features as evidence of Floquet-Andreev states stable over long timescales [114].

2.6. Andreev Bound States in In-Plane Magnetic Fields

In contrast to superconducting tunnel junctions, the planar geometry of hybrid superconductor-semiconductor junctions enables operation at large in-plane magnetic fields. The introduction of a Zeeman energy term lifts the spin degeneracy of ABSs, enabling each spin state to be individually addressed. For a semiconductor with strong spin-orbit interaction, charge carriers in the normal region exhibit coupling between the spin and momentum degrees of freedom, which can facilitate spin-dependent transport. This section will examine the basic properties of ABSs in magnetic fields, and how coupling to a Zeeman field can result in phase transitions and anomalous phase shifts in the ground state.

2.6.1. $0-\pi$ Phase Transitions

We investigate the behaviour of ABSs in a magnetic field, first in the absence of spin-orbit interaction. Consider the ABS energy in a short Josephson junction ($L \ll \xi$) at zero magnetic field, given by Eq. 2.23. For N conducting channels, there are $4N$ ABSs: $2N$ at positive energy and $2N$ at negative energy, with the factor of 2 from spin degeneracy. From the symmetry of the Bogoliubov-de Gennes equation in the absence of a magnetic field (Eq. 2.2), the time reversal operator acting on the Hamiltonian changes the sign of the phase. Therefore, time-reversal symmetry gives $E_n(\varphi) = E_n(-\varphi)$. This is also the case in the presence of a Zeeman field, in the absence of spin-orbit interaction [87, 226]. The ABS energies $E_n(\varphi)$ are given by the transmission eigenvalues, which are two-fold degenerate in a two-terminal junction by Kramer's degeneracy [see Fig. 2.6(a)].

In the presence of a magnetic field B, the Zeeman interaction couples the field to the spin magnetic moment of electrons and holes traversing the junction [87, 177, 226, 227]. This introduces an additional energy term $E_\mathrm{Z} = |g^*\mu_\mathrm{B}B|/2$, where g^* is the effective g-factor and μ_B is the Bohr magneton, resulting in a spin-dependent shift to

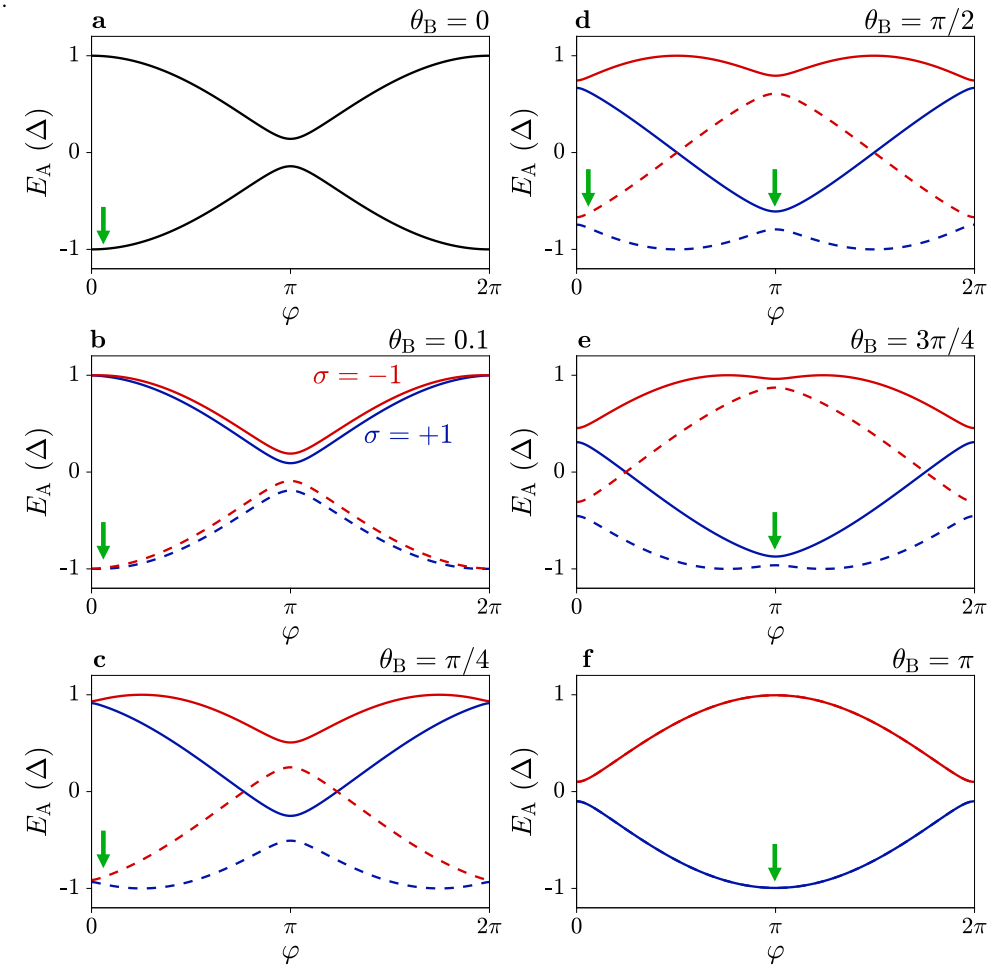

Figure 2.15. Andreev bound states (ABSs) for increasing Zeeman field θ_B, in the absence of spin-orbit interaction. a Spin-degenerate ABSs at zero magnetic field. States at positive (negative) energy are indicated by solid (dashed) lines. **b, c** A magnetic field of $\theta_B = 0.1$ and $\pi/4$, respectively, lifts the spin degeneracy into positive (blue) and negative (red) spin states. **d-f** For $\theta_B > \pi/2$, the state at lowest energy (green arrow) shifts from being at $\varphi = 0$ to $\varphi = \pi$. In (f), states at negative energy have the same spin character. Figure inspired by [87].

the wavevector. This gives different phase-matching conditions for the different spin states, lifting the spin degeneracy. The analytical result for the ABS energies obtained by [226] for a single channel is

$$\begin{aligned} E_{\uparrow,\pm}(\varphi) &= \pm\Delta\cos\left[\frac{\theta_B}{2} + \arccos\left(\pm\sqrt{1-\tau\sin^2(\varphi/2)}\right)\right] \\ E_{\downarrow,\pm}(\varphi) &= \pm\Delta\cos\left[-\frac{\theta_B}{2} + \arccos\left(\pm\sqrt{1-\tau\sin^2(\varphi/2)}\right)\right], \end{aligned} \tag{2.57}$$

where the magnetic field strength is parametrised by an effective phase shift

$$\theta_{\mathrm{B}} = \frac{|g^*|\mu_{\mathrm{B}} BL}{\hbar v_{\mathrm{F}}} = \frac{\pi}{2}\frac{E_{\mathrm{Z}}}{E_{\mathrm{Th}}}. \tag{2.58}$$

Since $E_{\mathrm{Th}} = \pi\hbar v_{\mathrm{F}}/(2L)$ is the Thouless energy for a ballistic system, the relative size of the Zeeman and Thouless energies determine the size of the energy splitting. Further details on the Zeeman splitting of ABSs are given in Appendix C.

Figures 2.15(a) and (b) show spin splitting of ABSs at moderate in-plane magnetic fields. For large fields, the splitting of ABSs is sufficient for them to cross zero energy [Fig. 2.15(c)], until the position of lowest energy (indicated by the green arrow) shifts from $\varphi = 0$ to $\varphi = \pi$ [Fig. 2.15(d)]. This constitutes a phase transition which occurs at $\theta_{\mathrm{B}} = \pi/2$, or equivalently at $E_{\mathrm{Z}} = E_{\mathrm{Th}}$. For $\theta_{\mathrm{B}} = \pi$, ABSs have completely moved through each other and the ground state is a spin doublet rather than a spin singlet for all values of φ.

The supercurrent is proportional to the derivative of the energy with respect to phase, meaning that it is proportional $\cos\theta_{\mathrm{B}}/2$. A signature of the phase transition is therefore the supercurrent going to a minimum at a certain magnetic field, and then increasing for larger magnetic fields. The field at which this transition occurs is

$$B = \frac{\pi}{2}\frac{\hbar v_{\mathrm{F}}}{|g^*|\mu_{\mathrm{B}} L}, \tag{2.59}$$

which gives $B \gtrsim 9$ T in the case of an InAs/Al heterostructure[2] [124].

2.6.2. Anomalous φ_0-Shifts

We can understand the Zeeman effect at small magnetic fields in terms of the dispersion relation of electrons in the normal region [87, 226, 228]. To do this, we make an analogy between a short Josephson junction and a nanowire: both are quasi-one-dimensional, with strong confinement in one direction (which we define to be along y). This confinement leads to subbands, which are schematically depicted in Fig. 2.16(a). In the presence of a magnetic field, the spin-degeneracy of the bands is lifted. This is depicted in Fig. 2.16(b), which is a zoom-in of the region close to the Fermi energy. The wavevectors for the two spin states $\sigma = \pm 1$ (blue and red, respectively) are shifted in opposite directions, which gives rise to the phase shift θ_{B} described in the previous section. Note that the size of the wavevector shift is equal and opposite for $k > 0$ and $k < 0$, since the Fermi velocity (given by the gradient of the dispersion relation at the Fermi energy) is symmetric.

We now consider the case with Rashba spin-orbit coupling, by introducing an additional contribution to the Hamiltonian given by Eq. 2.1. The two terms of Eq. 2.1 give rise to different effects: the $k_x\sigma_y$ term causes the subbands to split, so that they are shifted in k [see dashed lines in Fig. 2.16(c)]; the $k_y\sigma_x$ term couples the spin terms in neighbouring subbands, such that they are mixed [solid lines in Fig. 2.16(c)] [228]. Due

[2] Assuming $|g^*| \sim 10$, $v_{\mathrm{F}} \sim 1 \cdot 10^6$ ms^{-1} and $L \lesssim 200$ nm.

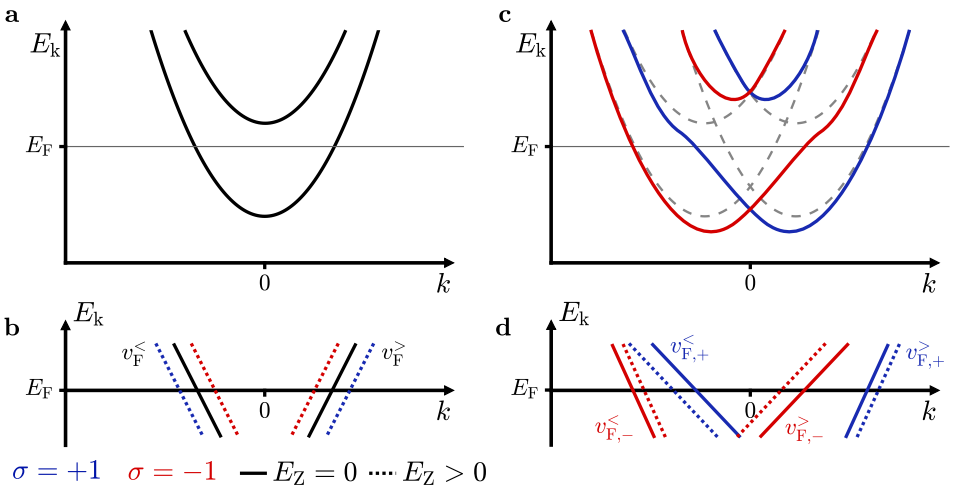

Figure 2.16. Influence of spin-orbit interaction on anomalous phase shifts. **a** Schematic representation of the dispersion relation in the absence of spin-orbit interaction. The Fermi energy E_F is indicated as the horizontal line. **b** Zoom-in of the region around E_F. Application of a magnetic field causes spin up (down) bands to move down (up) in energy, represented by the blue (red) dotted lines moving away from the zero-field case (black solid line). The Fermi velocity is independent of spin, and symmetric around $k = 0$. **c** Schematic representation of the dispersion relation in the presence of spin-orbit interaction, after spin splitting (dashed lines) and band mixing (solid lines). **d** Application of a magnetic field causes an energy shift (dotted lines) with respect to the zero field case (solid lines), as in (c). However, the spin-dependent Fermi velocity $v_{F,\pm}$ gives different spin-dependent changes in wavevector. Figure inspired by [87].

to the band mixing, the Fermi velocity in a given momentum direction depends on the spin texture (or equivalently, the Fermi velocity for a given spin texture is different for $k > 0$ and $k < 0$) [226]. This is evident in Fig. 2.16(d), which shows a zoom-in of Fig. 2.16(c) close to the Fermi energy. In a magnetic field, the spin-dependent shift in the wavevector is no longer symmetric with respect to k [dotted lines in Fig. 2.16(d)]. This gives an additional contribution to the wavevector shift, $\pm k_\alpha$, and results in a phase shift $\varphi \to \varphi - \varphi_0$, where

$$\begin{aligned} \varphi_0 &= -\frac{L}{2}(k_{F,+}^{>} + k_{F,+}^{<} + k_{F,-}^{>} + k_{F,-}^{<}) \\ &= E_Z L \left(\frac{1}{\hbar v_{F,-}} - \frac{1}{\hbar v_{F,+}} \right). \end{aligned} \tag{2.60}$$

Note that the φ_0-shift is not present in a single mode system, since it is the mixing of modes via the spin-orbit interaction which allows the phase shift.

The energy spectrum no longer satisfies $E_n(\varphi) \neq E_n(-\varphi)$ due to the interaction of spin-orbit coupling and the external magnetic field. The energy minimum occurs at φ_0,

and so the system is referred to as a φ_0-junction. The size of this phase shift is governed by the strength of the spin-orbit interaction α, and gives the result [229]

$$\varphi_0 = \frac{4\alpha L E_\mathrm{Z}}{(\hbar v_\mathrm{F})^2} \tag{2.61}$$

for a short ballistic junction. Anomalous phase shifts have been observed in hybrid Josephson junctions [106, 108, 230], however measured values of the phase shift in planar junctions [230] were much larger than predicted by Eq. 2.61.

3 Material and Methods

3.1. Material

Hybrid superconductor-semiconductor materials are an excellent platform for studying fundamental physics, and have applications in quantum computing [53, 61, 127], superconducting electronics [97, 99] and beyond. However, high quality material is crucial for realising these promises [48]. For the semiconducting component, low scattering is important to realise ballistic systems and large spin-orbit interaction is needed to resolve spin-split phenomena [50, 136, 231, 232]. The superconductor must be thin to enable superconductivity up to large in-plane magnetic fields [233], while hosting a clean superconducting gap free of unintentional sub-gap states [230, 234, 235]. An important factor is the semiconductor-superconductor interface, which must be free of contamination and defects to give a large, clean proximitised superconducting gap in the semiconductor and a high transmission probability across a Josephson junction [49, 236–239]. The following sections describe how these conditions are achieved in an InAs/Al heterostructure [50, 240].

3.1.1. Growth and Material Composition

Heterostructures were grown by molecular beam epitaxy (MBE), whereby crystalline semiconductor layers are grown on a substrate in an ultra-high vacuum chamber, with atomic-layer precision [130, 131]. Figure 3.1(a) shows a transmission electron microscopy (TEM) image of the full heterostructure, alongside a schematic representation of the composition of each layer. The heterostructure consisted of a step-graded InAlAs buffer on a semi-insulating InP (001) substrate, onto which an $In_{0.75}Ga_{0.25}As$/InAs/$In_{0.75}Ga_{0.25}As$ quantum well was grown with a termination of two GaAs monolayers. The 8 nm InAs layer hosted a two-dimensional electron gas (2DEG), buried 13.4 nm below the semiconductor surface, as measured by TEM [see Fig. 3.1(b)]. A 15 nm layer of Al was deposited onto the semiconductor surface, *in situ* without breaking vacuum in the growth chamber. See Ref. [240] for full details on the material growth.

The 2DEG wavefunction is schematically drawn in Fig. 3.1(b), to show a finite overlap into the superconductor. This overlap, facilitated by the small separation of the 2DEG from the surface and the moderate confinement of the $In_{0.75}Ga_{0.25}As$, enables a strong proximity effect [136, 230]. The *in situ* superconductor deposition also allowed for a high quality semiconductor-superconductor interface, which was atomically sharp and free of defects and impurities [see Fig. 3.1(c)]. Highly transparent interfaces are expected to result in a proximitised gap which is free of sub-gap states [48, 49, 236, 237, 239].

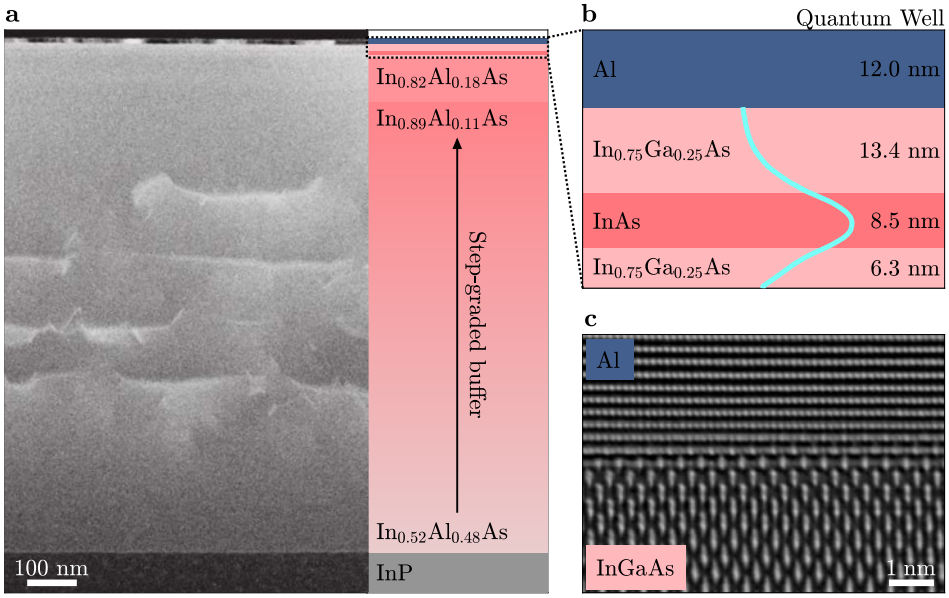

Figure 3.1. Superconductor-semiconductor material. **a** Transmission electron microscopy (TEM) image of a characteristic wafer over the full layer stack, alongside a schematic representation of the layer compositions. **b** Schematic zoom-in of the region closest to the material surface, containing the quantum well and the superconductor. Materials and measured thicknesses are labelled. A sketch of the expected semiconductor wavefunction is drawn in light blue. **c** TEM image at the interface between the $In_{0.75}Ga_{0.25}As$ and Al layers. TEM images were taken by Filip Krizek. Figure adapted from Ref. [240].

The step-graded metamorphic buffer compensated the lattice mismatch between the InP and InAs, and was designed such that dislocations due to strain relaxations occurred deep in the heterostructure, far from the 2DEG [see Fig. 3.1(a)]. This enabled an InAs layer mostly free from dislocations, reducing the density of scattering sites for charge carriers in the 2DEG and thereby facilitating a high electron mobility. In InAs quantum wells, spin-orbit coupling of Rashba-type is dominant due to the strong structural inversion asymmetry of the confining potential [138]. Measurements of the spin-orbit coupling strength in similar heterostructures [50, 136, 232] have found values of $\alpha = 50--300$ meVÅ, depending on the electron sheet density.

The GaAs capping layers provided a barrier for In diffusion into the superconducting layer, while also being an etch stop for the Al etch. The impact of these interlayers on the crystal structure of the deposited Al, and on the semiconducting and induced-superconducting properties of the material, is discussed in detail in Ref. [240]. The Al layer was made sufficiently thin to be resilient to large in-plane magnetic fields, while being thick enough for the film to remain continuous and superconducting after device fabrication.

3.1.2. Material Characterisation

The material quality was evaluated by measuring its semiconducting and superconducting properties. Measurements of a gated Hall bar [Fig. 3.2(a)], performed at a base temperature of $T = 20$ mK, give the resistivity $\rho_{XX} \equiv (V_{XX}/I)(W/L)$ and $\rho_{XY} \equiv V_{XY}/I$ as a function of perpendicular magnetic field $B_\perp$ [Fig. 3.2(b)], for different gate voltages V_G applied to a gate covering the semiconducting region. The electron sheet density n and mobility μ are given by [131]

$$n = \frac{1}{|e|\mathrm{d}\rho_{XY}/\mathrm{d}B_\perp|_{B_\perp=0}} \qquad \mu = \frac{\mathrm{d}\rho_{XY}/\mathrm{d}B_\perp|_{B_\perp=0}}{\rho_{XX}(B_\perp = 0)}, \tag{3.1}$$

with the result shown in Fig. 3.2(c) as a function of V_G.

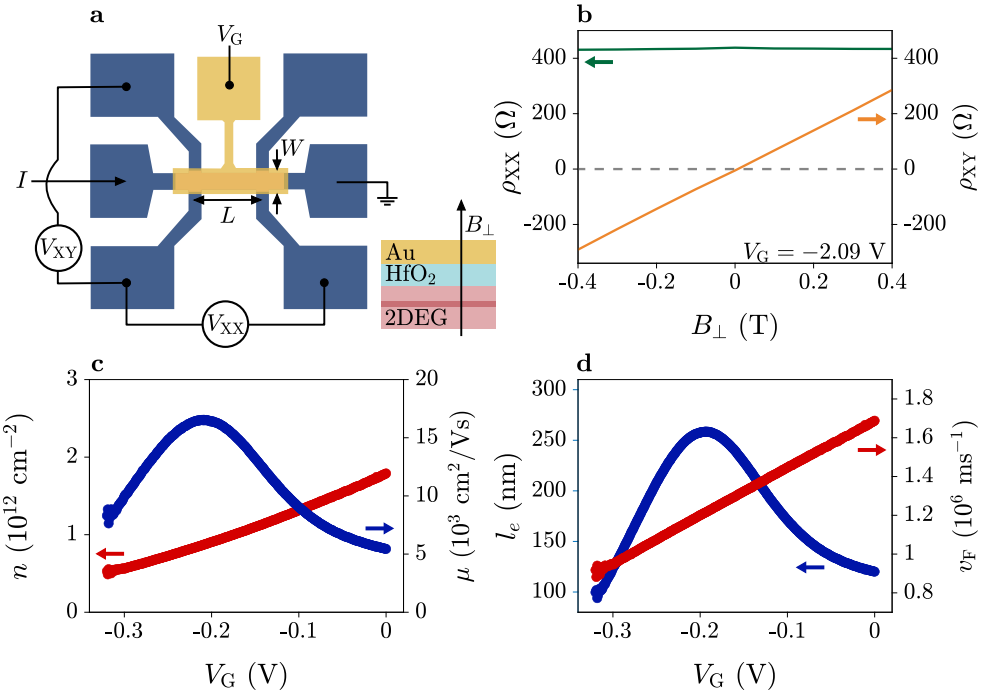

Figure 3.2. Characterisation of semiconducting properties. **a** Schematic of a gated Hall bar device, where the Al (blue) was removed to expose the InAs (pink) to an electrostatic Au gate (yellow). A current I is sourced to one contact, and the voltages V_{XX} and V_{XY} are measured as a function of the magnetic field perpendicular to the device, $B_\perp$ (see inset schematic). **b** Resistivities $\rho_{XX} \equiv (W/L)(V_{XX}/I)$ (green) and $\rho_{XY} \equiv V_{XY}/I$ (yellow), respectively parallel and perpendicular to the current flow, as a function of $B_\perp$ for $V_G = -2.09$ V. **c** Electron sheet density n and mobility μ as a function of gate voltage V_G, calculated from (b) using Eqs. 3.1. **d** Electron mean free path l_e and Fermi velocity v_F as a function of gate voltage V_G, calculated from values in (c). Measurements were performed at $T = 20$ mK.

A peak mobility of 18000 $\mathrm{cm}^2/\mathrm{Vs}$ at an electron sheet density of $8 \cdot 10^{11}$ cm^{-2} gives an electron mean free path of $l_\mathrm{e} \gtrsim 260$ nm. The reduced mobility for higher V_G is attributed to increased surface scattering, since the electron distribution is shifted closer to the material surface [231, 241, 242]. Occupation of the second subband is expected for larger electron sheet densities $n \gtrsim 1.2$ cm^{-2}, where the mobility begins to saturate [136, 231]. Since $l_\mathrm{e} > 100$ nm across the full range of sheet density n [Fig. 3.2(d)], Josephson junctions with length L shorter than this were in the quasi-ballistic limit [130]. The Fermi velocity v_F was calculated to be $\sim 1 \cdot 10^6$ ms^{-1} [Fig. 3.2(d)]. Measurements in similar material have shown a phase coherence length exceeding $l_\varphi \sim 1$ μm at low temperatures [50, 243].

Measurements of the superconducting film in a Hall bar geometry gave a critical temperature of $T_\mathrm{C} \approx 1.3$ K and a critical in-plane magnetic field of $B_{\parallel,\mathrm{C}} \approx 1.1$ T, consistent with a superconducting gap of $\Delta \approx 180$ μeV. The measured normal state resistance per unit square was $R_\square \approx 1.5$ Ω. Since the Al film was thin, it had a considerable kinetic inductance L_K which generates a flux $\Phi_\mathrm{K} = L_\mathrm{K} I$ for a current I through the superconducting film. The kinetic inductance per unit square is estimated to be [198]

$$L_{\mathrm{K},\square} = \frac{h}{2\pi^2} \frac{R_\square}{\Delta} \approx 1.7 \text{ pH}. \tag{3.2}$$

Beyond independent characterisation of the semiconducting and superconducting components, a planar Josephson junction [Fig. 3.3(a)] was used to evaluate the quality of the semiconductor-superconductor interface. The differential resistance $R \equiv V_\mathrm{AC}/I_\mathrm{AC}$ was measured as a function of a DC current bias I_DC, for different temperatures T. Figure 3.3(b) shows R for $T = 20$ mK (blue line), with a clear transition from the superconducting to the resistive state at the switching current I_SW. For $I_\mathrm{DC} > I_\mathrm{SW}$, there were peaks in the differential resistance corresponding to multiple Andreev reflections (MAR) [244–246]. The voltage drop across the junction V_DC is calculated by numerical integration of $R(I_\mathrm{DC})$, and is plotted as the red line. For large I_DC, $V_\mathrm{DC} = I_\mathrm{DC} R_\mathrm{N}$ where R_N is the normal state resistance. The extrapolation of V_DC at high current bias (grey dashed line) intersects the horizontal axis at a finite current $I_\mathrm{exc.}$: the excess current due to Andreev reflections at the superconductor-semiconductor interfaces [154].

The product of the switching current with the normal state resistance gives a value of $I_\mathrm{SW} R_\mathrm{N} = 305$ μV at base temperature $T = 20$ mK, which decreases to zero as $T \to T_\mathrm{C}$ [see Fig. 3.3(c)]. Figure 3.3(d) shows the product $I_\mathrm{exc.} R_\mathrm{N}$, which has a low-temperature value of 550 μV. Traces of the differential resistance are shown in Fig. 3.3(e), where the MAR peaks identified in Fig. 3.3(b) change with temperature (grey dashed lines).

The voltage at which MAR peaks occur is indicative of the induced superconducting gap, by the relation $V_\mathrm{SD} = 2\Delta^*/ne$ [244–246]. We identify peaks at 383, 183 and 118 μV for $n = 1,\ 2,\ 3$ respectively, corresponding to an induced gap of $\Delta^* \approx 180$ μeV [240]. This is close to the gap in the Al film, implying a strong proximity effect. The $I_\mathrm{C} R_\mathrm{N}$ product is proportional to the proximitised superconducting gap, since it describes the energy of the overlaping superconducting wavefunctions ($\propto I_\mathrm{C}$) across multiple conducting channels ($\propto R_\mathrm{N}^{-1}$) [181]. In the ballistic limit, $I_\mathrm{C} R_\mathrm{N} = \pi\Delta^*/e \approx 565$ μV for a clean

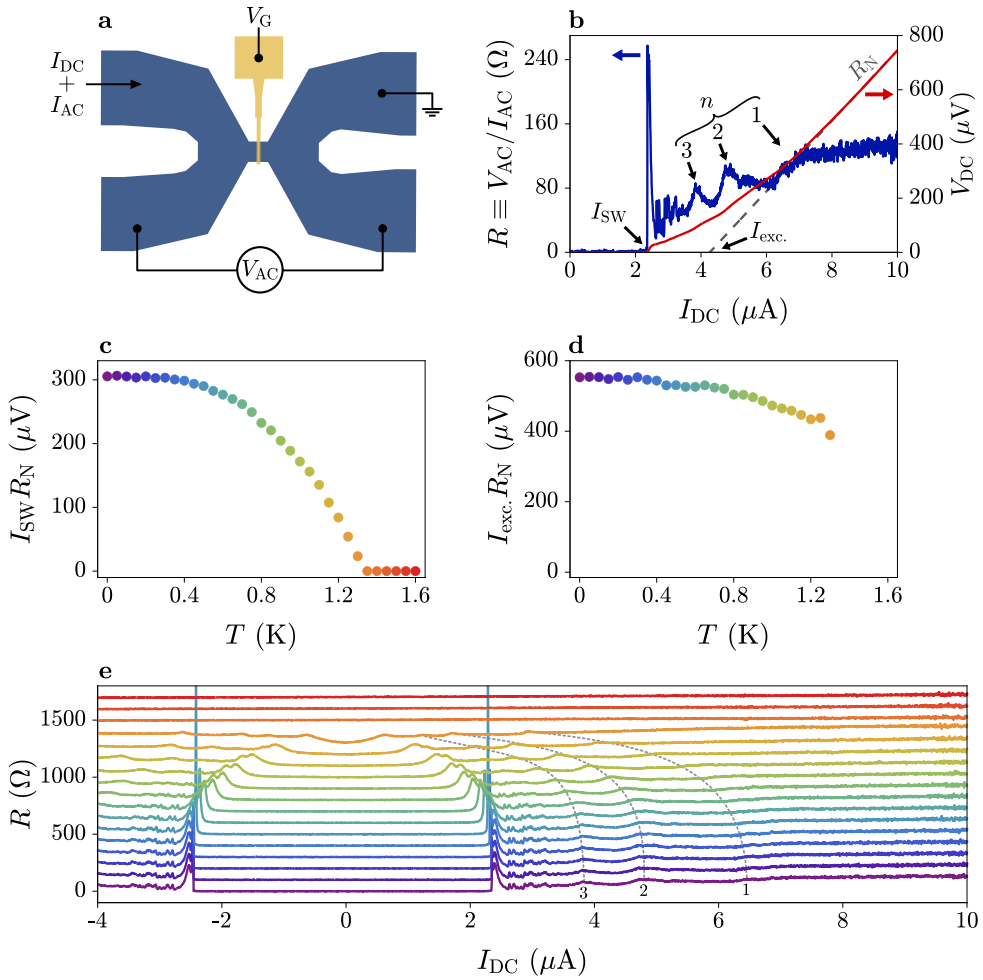

Figure 3.3. Characterisation using a planar Josephson junction a Schematic of the planar junction, where the Al (blue) was removed in a narrow stripe to expose the InAs (pink) to an electrostatic Au gate (yellow). A current $I_{DC} + I_{AC}$ is sourced to one contact, and the differential voltage V_{AC} is measured. **b** Differential resistance $R \equiv V_{AC}/I_{AC}$ at $T = 20$ mK as a function of I_{DC} (blue, left axis). The voltage drop V_{DC} (red, right axis) is calculated by integrating the $R(I_{DC})$ curve. The switching current I_{SW}, excess current $I_{exc.}$ and multiple Andreev reflection peaks are indicated. **c** The switching current-normal state resistance product $I_{SW}R_N$ as a function of temperature. **d** The excess current-normal state resistance product $I_{exc.}R_N$ as a function of temperature. Due to distortions in the high bias data at large temperatures, data points for $T > 1.25$ K are removed. **e** Differential resistance R as a function of I_{DC} for different temperatures [colours, defined in (c)]. Each curve is offset by 50 Ω for visibility. Peaks corresponding to multiple Andreev reflections are indicated by the grey dashed lines. Figure is adapted from [240], using data measured by D.Z.H.

superconductor ($l_e \gg \xi$) [247] and $I_C R_N = \pi\Delta^*/2e \approx 280$ μV for a dirty superconductor ($l_e \lesssim \xi$) [248]. The switching current is indicative of I_C (although smaller, due to stochastic phase fluctuations), and gives a value $I_{SW} R_N = 305$ μV which is between the dirty and clean limits. The excess current is sensitive to the transparency of the superconducting interfaces, since it involves many Andreev reflection processes [154, 174–176]. Therefore, the large measured excess current relative to Δ^* implies a highly transparent interface.

While these techniques are only approximate in their evaluation of the superconductor-semiconductor interface, all point towards a large induced superconducting gap in the InAs with highly transparent interfaces for quasi-ballistic transport between the superconducting contacts. This is a strong indication of excellent quality material, and gives results which are comparable to those found in literature [230, 249].

3.2. Fabrication Process

The heterostructure was grown uniformly across a 2 inch wafer, which was diced into 5x5 mm chips such that each chip was fabricated independently. Design patterns were transferred to the chip by electron-beam lithography. The chip was covered with an electron-sensitive polymer resist, which becomes soluble in a developing solvent on exposure to a focused electron beam, thereby exposing the material underneath. The exposed material can then be selectively etched, or contacted via metal deposition. Device fabrication consisted of four lithography steps: defining a mesa structure; defining the superconductor etch; and two lithography steps to pattern metallic gate electrodes. These fabrication steps are depicted in Fig. 3.4 and are described in the following sections. A detailed process flow is described in Appendix A.

Mesa Etch

The first fabrication step was to isolate large mesa structures, onto which each device was patterned [see Fig. 3.4(b)]. Each device was therefore isolated from its neighbours, since the InP substrate was insulating at cryogenic temperatures < 4 K. This etch step was done by selectively removing the top Al layer with Transene Al etchant – Type D ("Transene D"), before etching $\gtrsim 350$ nm into the III-V heterostructure using a chemical wet etch ($220 : 55 : 3 : 3$ solution of $H_2O : C_6H_8O_7 : H_3PO_4 : H_2O_2$). It was important to etch deep into the heterostructure, since parallel conduction was observed between neighbouring devices if the etch depth was not sufficiently large. This was only observed after deposition of a dielectric layer; while the source of this parallel conduction is unknown, it is presumed to originate from a conducting layer of charges trapped at the interface of the dielectric and the top-most layer of the etched heterostructure. Etch depths were measured with a profilometer on every chip, to account for fluctuations in the etch rate. The III-V etch was isotropic, meaning that etching was lateral as well as vertical. This left portions of Al overhanging the mesa edge, which were removed with an additional Al etch.

Aluminium Etch

The second step was to pattern the superconducting structures on top of the mesa [see Fig. 3.4(c)]. This was done by selective etching of the Al with chemical etchant Transene D at 50°C for 4 s. Etching was performed at high temperature to accelerate the etch rate, and was seen to result in smoother feature edges and leave fewer residues. Feature sizes expanded relative to the design dimensions due to the isotropic wet etch, but this was limited to the thickness of the Al film by careful optimisation of the exposure, development and etching processes. As a result, Josephson junctions were $\sim$ 20 nm longer than the designed length. Lengths reported throughout this thesis correspond to the designed length.

Dielectric Deposition

A dielectric layer of Al_2O_3 (3 nm) and HfO_2 (15 nm) was deposited across the chip by atomic layer deposition [see Fig. 3.4(d)], to isolate the device structure from metallic gates (deposited in a later step). These depositions were performed at $\lesssim$ 120°C, since higher temperatures were shown to degrade the material. In addition, exposure of the Al surface to a plasma-induced deposition resulted in thickening of the native Al oxide, sometimes leading to portions of the Al film being resistive at low temperature. A thermally-induced Al_2O_3 deposition was introduced to alleviate this issue.

Metallic Gates

Gate electrodes were defined on top of the dielectric layer by evaporation and lift-off [see Fig. 3.4(e)]. Fine gate features were defined in a first step consisting of 5 nm Ti and 20 nm Au. A comparatively large resist thickness of 250 nm and an aggressive resist stripping process in heated dimethyl sulfoxide (DMSO) was used so that gate features could be defined with $\gtrsim$ 50 nm separation.

A second deposition of Ti (10 nm) and Al (420 nm) connected the gates on top of the mesa structures to bonding pads, which were defined in the same step [see Fig. 3.4(f)]. The exact composition and thickness of the second layer varied between experiments presented here (in some cases both Al and Au were used), but no impact on device performance was observed provided that the metal was sufficiently thick to overcome the step height to the top of the mesa.

Wire Bonding

After fabrication, 5x5 mm chips were glued to a QDevil daughter board using baked resist. Wire bonds of Al were used between Au pads on the daughter board and bonding pads on the chip using wedge bonding. The daughter board was screwed to a Al block, with electrical contact to all 50 pins such that they were shorted together. The Al block was connected to the ground of the wire-bonding machine throughout bonding to limit electrostatic discharge; this procedure improved the device yield.

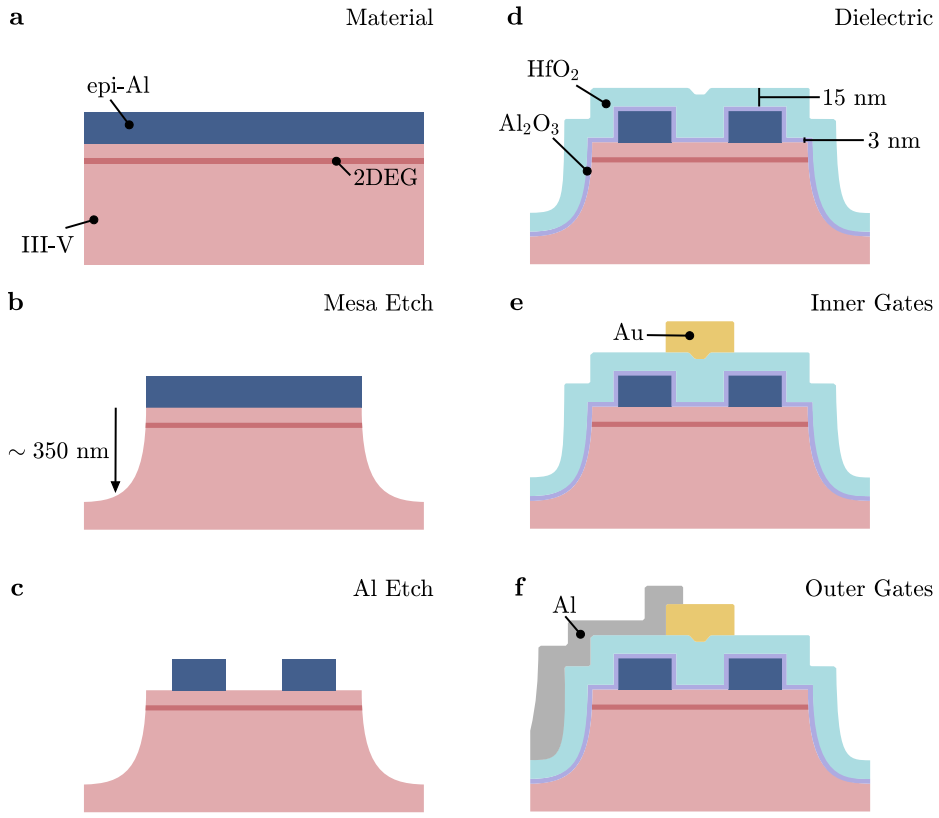

Figure 3.4. Fabrication process, from heterostructure to devices. **a** Schematic representation of the material after growth, before fabrication (not to scale). The III-V semiconductor (pink) contains the two-dimensional electron gas (2DEG), with epitaxial Al (blue) on the surface. **b** The first lithographic step defines areas to etch into the layer stack. An etch depth of ~ 350 nm defines mesa structures, onto which devices will be fabricated. **c** Aluminium etch of features on top of mesa structure. **d** Deposition of dielectric layers by atomic layer deposition: 3 nm of Al_2O_3 (purple) and 15 nm of HfO_2 (light blue). **e** Inner gate structures of Au (yellow) are defined on top of the mesa in the third lithography step, above the patterned Al. **f** The final lithography step defines the outer gates: a thick Al layer (grey) which connects the inner gates to bonding pads far from the device.

3.3. Measurement Setup

Measurements performed in this thesis were carried out in the same cryogenic setup. This section provides details on the dilution refrigerator and setup for electronic measurements which are relevant for results presented in later chapters.

3.3.1. Dilution Refrigerator

Measurements were performed in a dilution refrigerator with a base temperature below 10 mK. Samples were positioned in a bottom-loading mechanism, for fast sample exchange with a cycle time of < 24 hours. In experiments where microwave (MW) irradiation was applied to a sample, a room temperature MW source provided a continuous-wave signal to the sample space via a coaxial line with 47 dB attenuation, terminated in an antenna positioned approximately 1 cm from the chip surface. Samples were unshielded in the loading environment, due to the requirement of applying large global magnetic fields.

Magnetic fields were applied using a three-axis vector magnet, with field directions nominally oriented perpendicular to the device ($B_\perp$) and in the plane of the device ($B_\parallel$, B_t). Global magnetic fields were generated by currents sourced to a three-axis vector magnet. For large magnetic fields (> 30 mT), currents were sourced by an AMI 430 Power Supply. For small magnetic fields, where careful tuning was required, currents were sourced using the current output of either a Yokogawa GS200 or a Keysight Precision Source-Measure Unit.

3.3.2. Electronic Measurements

Measurements were performed at low frequency (< 1 kHz) using room-temperature electronics. Low-impedance contacts in the epitaxial Al connected the device to resistive phosphor-bronze twisted-pair looms in the dilution refrigerator. Low-pass filters were installed on the mixing chamber plate, consisting of RC- and $\pi-$filters for low (cutoff frequency $f_\mathrm{co} = 65$ kHz) and high ($f_\mathrm{co} = 225$ MHz) frequency noise, respectively. Additional RC-filters ($f_\mathrm{co} = 130$ kHz) were installed on a QDevil mother board, onto which the daughter board holding the sample was loaded. The measured resistance of each line was found to be 2.9 kΩ, consistent with the filter resistances. In all measurements, static voltages were applied to gates from a QDevil Digital to Analogue Converter (DAC) via low-pass RC filters with $R = 10$ kΩ and $C = 1$ μF ($f_\mathrm{co} = 16$ Hz).

3.4. Measurement Methods

Measurements presented in this thesis can be divided into two categories: current-biased and voltage-biased measurements. In the first, currents were sourced to the sample and a voltage difference across two terminals was measured. The primary purpose of this technique was to measure a switch between voltage states of the device: low voltage in the superconducting state and high voltage in the resistive state. The bias current at

which this transition occurred is called the switching current, and was used to infer the phase escape dynamics (Chapters 4 and 5) and current-phase relation (Chapters 6 and 7) of planar Josephson junctions. The second measurement approach involved applying a voltage bias across two contacts and measuring the resulting current flow. This technique was used to measure the tunnelling conductance through a quantum point contact close to a planar junction, to infer the density of states in the region close to the probe.

3.4.1. Current-Biased Measurements

First characterisation measurements were performed using lock-in amplifier techniques. A current $I = I_{\mathrm{AC}} + I_{\mathrm{DC}}$ was sourced to the device, using a Stanford Research SR860 lock-in amplifier and a QDevil DAC for the AC and DC components respectively. An AC voltage, with a typical frequency between 100 and 400 Hz, was applied from the lock-in amplifier via a large resistor in series with the device ($\gtrsim 100$ MΩ), such that $I_{\mathrm{AC}} \lesssim 10$ nA. A DC voltage was applied from the DAC to the same contact, via a series resistor with a much larger resistance than that of the device. The value of this bias resistance was chosen based on the desired current flowing through the device (e.g. 1 V outputted from the DAC through a 1 MΩ bias resistor gave a 1 μA current). The differential voltage V_{AC} across the device was measured in a four-terminal configuration via a home-made differential voltage amplifier with gain 1000, detected by the same lock-in amplifier as the AC current source. The differential resistance was given by $R \equiv V_{\mathrm{AC}}/I_{\mathrm{AC}}$.

While lock-in amplifier techniques were effective at measuring the switching current and properties in the resistive state of the device, they were inefficient for collecting switching current statistics and were not appropriate for measuring small modulations in large switching currents. Therefore, an alternative approach was used for most of the switching current results presented in this thesis.

The switching current was measured efficiently by using current ramps with fast repetition rates and voltage triggers to detect a transition to the resistive state. Currents were sourced by symmetrically biasing the device, such that the device potential was not significantly raised with respect to the ground of the electrostatic gates. This prevented effective gating due to a large current bias. A sawtooth voltage bias was applied to the device from two synchronised channels of a Keysight 33600 Waveform Generator, with opposite sign for the two channels. The repetition rate of the sawtooth signal was between 133 Hz and 798 Hz for measurements of the switching statistics (Chapters 4 and 5), such that the ramp rate was constant for varying voltage amplitude. The repetition rate for measurements of the current-phase relation (Chapters 6 and 7) was 133 Hz, and reported switching current values were averaged between 16 and 32 times to account for broad switching current distributions. Waveforms were applied to the device via bias resistors at the source and drain contacts. For devices containing an Al constriction, bias currents of ~ 40 μA were obtained using bias resistors of 163 kΩ. The voltage drop across the device was measured in a four-terminal configuration, via a differential voltage amplifier with gain 1000 and a further amplification stage provided by the internal gain of a Stanford Research SR860 lock-in amplifier, and ultimately detected at a Keysight DSOX2024A oscilloscope. The oscilloscope measured the time needed for the voltage

across the device to exceed a threshold $< 15\%$ of the maximum voltage in the resistive state. This threshold was chosen to be sufficiently low that it was representative of the switch to the resistive state, but sufficiently high to be insensitive to fluctuations in the measured voltage in the superconducting state. The time was readily converted to a current, since the oscilloscope was synchronised to the output of the waveform generator. The switching currents obtained via this method were reliable when the transition from the superconducting to resistive state was sharp. However, for large temperatures or in-plane magnetic fields, where superconductivity was suppressed in the device, a finite resistance was measured below the transition to the fully resistive state. Thus, the voltage exceeded the measurement threshold for bias currents different to the switching current. For this reason, switching current measurements at temperatures $T \gtrsim 1$ K or in-plane magnetic fields $B_{\parallel} \gtrsim 1$ T are excluded from reported results.

In devices containing a tunnelling probe, both contacts at the probe were floated such that no current flowed there during current-biased measurements. Global gates were set to negative values, such that regions of InAs surrounding the superconducting loop were depleted and that transport was confined to regions below the Al, where the effect of the gates was screened.

3.4.2. Voltage-Biased Measurements

Measurements of the differential conductance were performed with standard lock-in amplifier techniques. An AC voltage $V_{\mathrm{AC}} = 3$ μV was applied to the contact of the superconducting probe with frequency 311 Hz from a Stanford Research SR860 lock-in amplifier, in addition to a variable DC source-drain voltage V_{SD} from a DAC. The AC current I_1 and DC current I_{SD} flowing through the probe to ground was measured via a current-to-voltage (I-V) converter with gain $1 \cdot 10^8$ and bandwidth 10 kHz. The differential voltage across the tunnel barrier V_1 was measured at a lock-in amplifier, via a differential amplifier with 1000 gain, to give the differential conductance $G \equiv I_1/V_1$. Measurements were performed in the tunnelling regime, where $G \ll G_0 = 2\mathrm{e}^2/h$. A constant bias offset of < 50 μV was subtracted from all datasets, due to a DC offset at the I-V converter.

4 Phase Dynamics in Planar Josephson Junctions Part I: Single Junctions

Planar Josephson junctions (JJs) carry a gate-tunable supercurrent due to a phase difference across the superconducting contacts. Voltage control of dissipationless supercurrents means that they are less susceptible to heating and crosstalk [57], presenting significant advantages for tunable superconducting qubits [53–55, 250] and low temperature electronics [91, 99]. An important property of a Josephson junction is its critical current: the maximum supercurrent that can flow through the junction before it transitions to the resistive state. The critical current relates to the macroscopic properties of a JJ as a circuit element, and gives insights into the behaviour of microscopic current-carrying states. To utilise planar JJs effectively in superconducting circuits, and to understand the physics which govern their behaviour, it is crucial to have reliable measurements of the critical current. In this chapter, we investigate the transition from the superconducting to resistive state of planar Josephson junctions under a current bias, and the mechanisms which influence this transition. The text and figures of this chapter were adapted from Ref. [251].

This chapter is adapted from the following publication:

Measurements of Phase Dynamics in Planar Josephson Junctions and SQUIDs
D. Z. Haxell, E. Cheah, F. Krizek, R. Schott, M. F. Ritter, M. Hinderling, C. Bruder, W. Wegscheider, H. Riel, and F. Nichele
Physical Review Letters **130**, 087002 (2023).

Author contributions: F.N. conceived the experiment. E.C., F.K., R.S., and W.W. performed the material synthesis and characterisation. D.Z.H. designed the samples, F.N. gave support. D.Z.H. fabricated the samples, M.F.R. provided advice and support. F.N. and D.Z.H. performed the measurements. D.Z.H. analysed the data, C.B. provided theoretical support on the appropriate formulae and F.N. contributed to the Monte Carlo script. D.Z.H. and F.N. analysed and interpreted the data, with contributions from all authors. F.N. and D.Z.H. wrote the manuscript, with contributions from all authors.

4.1. Device and Initial Characterisation

Figure 4.1(a) shows a micrograph of the device under study. It consists of a superconducting quantum interference device (SQUID), two gate-tunable planar JJs (JJ1 and JJ2) embedded in a superconducting loop, all defined in an InAs quantum well (pink) covered by a thin layer of in-situ-deposited Al (blue) [50]. Gate voltages V_{G1} and V_{G2} allowed tuning of JJ1 and JJ2, respectively. The gate voltage V_{Global} was kept constant at -600 mV to prevent parallel conduction in the semiconductor. The design was optimised to reach a critical current in JJ1 ($I_{C,1}$) that was much larger than the critical current in JJ2 ($I_{C,2}$) [122, 153]. This was achieved by changing the lateral extent of the Al electrodes (5 μm in JJ1 vs. 1.6 μm in JJ2) and their separation (50 nm in JJ1 vs. 100 nm in JJ2).

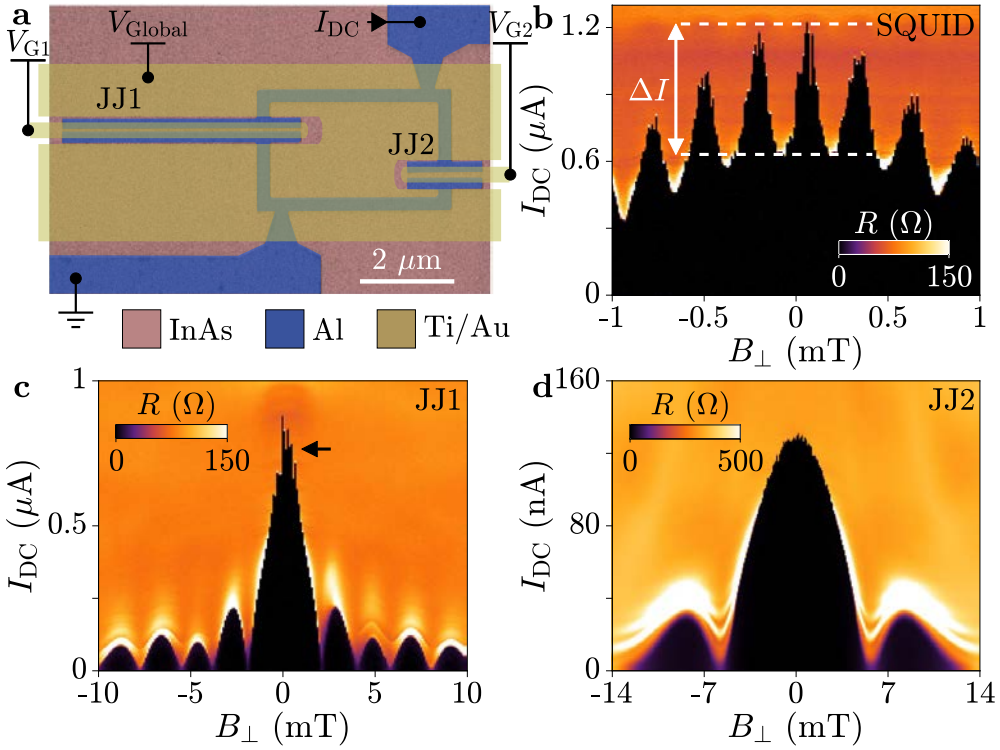

Figure 4.1. Characterisation measurements of device under study. **a** False-coloured electron micrograph of the device under study and measurement configuration. The InAs is highlighted in pink and the Al in blue. Gates are drawn on the image and highlighted in yellow. **b** Differential resistance R as a function of $B_\perp$ and I_{DC} obtained with $V_{G1} = -180$ mV and $V_{G2} = -140$ mV. The amplitude of the switching current oscillations, ΔI, is marked. **c** Differential resistance of JJ1 in isolation, with $V_{G1} = -180$ mV and $V_{G2} = -450$ mV. Large fluctuations close to $B_\perp = 0$ are marked with an arrow. **d** Differential resistance of JJ2 in isolation, with $V_{G1} = -550$ mV and $V_{G2} = -140$ mV. The peak at $B_\perp = 0$ is less than half $\Delta I/2$ in (b).

We first present switching currents obtained with low-frequency lock-in techniques, similar to previous work [109, 122, 153]. A source-drain current I_{DC} was swept over timescales of seconds, while the SQUID differential resistance R was recorded. Figure 4.1(b) shows R as a function of out-of-plane magnetic field $B_\perp$ with $V_{\mathrm{G1}} = -180$ mV and $V_{\mathrm{G2}} = -140$ mV, where $I_{\mathrm{C},1}$ and $I_{\mathrm{C},2}$ were independently maximised. The SQUID switching current I had a periodicity of 350 μT, corresponding to a flux $h/2e$ threading the loop. The amplitude of the SQUID oscillations, ΔI, reveals the switching current of JJ2 as $I_2 = \Delta I/2 = 350$ nA, while the mean value gives the switching current of JJ1, $I_1 = 850$ nA. Figure 4.1(c) shows R when JJ2 is closed and with JJ1 in the gate configuration of Fig. 4.1(b). The Fraunhofer interference pattern emerges [234], with a maximum of I_1 matching the mean switching current of Fig. 4.1(b). Furthermore, large switching current fluctuations were present at $B_\perp = 0$ (black arrow). Figure 4.1(d) shows similar measurements performed with I_{DC} flowing in JJ2 only. Surprisingly, the maximum of I_2 is 120 nA; a significant difference with the 350 nA deduced from Fig. 4.1(b).

Both the fluctuations in Fig. 4.1(c) and the switching current enhancement in Fig. 4.1(b) with respect to Fig. 4.1(d) are manifestations of the phase dynamics in our devices. Therefore, we evaluate the phase escape mechanisms in JJ1 and JJ2 separately (this Chapter), and in the SQUID loop formed by their combination (Chapter 5). To capture the stochastic characteristics of phase escape, we modulate the input current with a sawtooth function using a ramp rate $\nu = 240$ $\mu\mathrm{As}^{-1}$ and monitor the voltage across the SQUID with an oscilloscope. This technique allows us to record the switching current I_{SW} for 10,000 switching events in approximately ten minutes, and produce the switching probability distribution (SPD), that is the probability for a switch to occur per unit of input current. Similar techniques were used for detailed studies of conventional [182, 185, 190, 252] and hybrid JJs [253–257], metallic nanowires [258–260] and SQUIDs [261–265].

4.2. Phase Dynamics of JJ1

We first investigate the phase dynamics of JJ1. The top-gate voltage was set to $V_{\mathrm{G1}} = -180$ mV, and $V_{\mathrm{G2}} = -450$ mV such that JJ2 was fully depleted [identical configuration to Fig. 4.1(c)].

4.2.1. Temperature Dependence

Figure 4.2(a) shows the SPDs of JJ1, measured at various mixing chamber temperatures T. The corresponding escape rates Γ, computed using a KFD transformation (Eq. 2.34) [185, 186], are shown in Fig. 4.2(b).

Figures 4.2(c) and (d) show the mean value of the SPDs in JJ1 ($I_{\mathrm{M},1}$) and the standard deviation (σ_1), respectively, both as a function of T. For $T < 400$ mK, σ_1 is constant and large, and Γ increases exponentially with I_{SW}, indicating that macroscopic quantum tunnelling (MQT) dominates the phase dynamics. For higher T, σ_1 decreases as T increases, signalling the crossover to phase diffusion (PD), where escape and retrapping

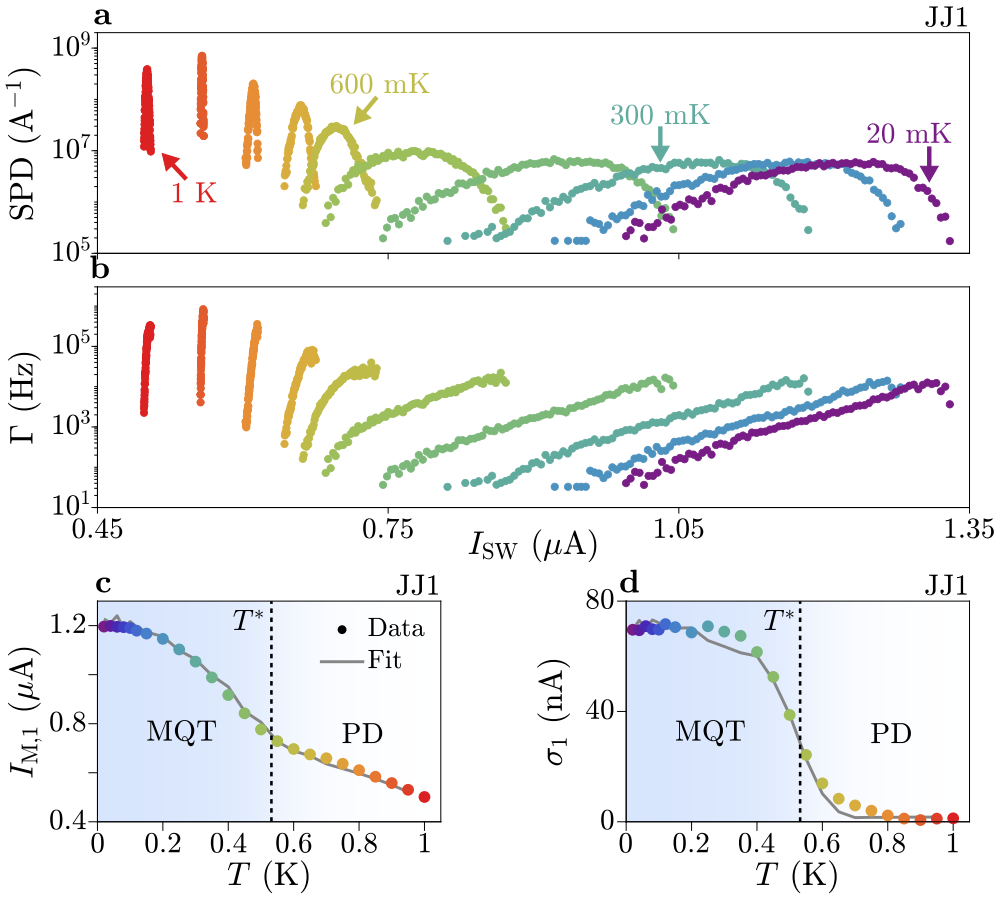

Figure 4.2. Temperature dependence of stochastic phase escape mechanisms in JJ1. a Switching probability distributions (SPDs) for JJ1 for various temperatures. Colors are defined in (c) and are consistent throughout the chapter. **b** Escape rate Γ of JJ1, obtained from the data in (a) using Eq. (2.34). **c** Mean switching current I_{SW} of SPDs as a function of temperature (circles) together with a fit to a Monte Carlo simulation (line). Transition temperature T^* is indicated by a vertical line, dividing a regime of macroscopic quantum tunnelling (blue shading) and phase diffusion. **d** Standard deviation σ_1 of SPDs, as a function of temperature.

events have similar probabilities to occur, so that many escape events are required to transition to the resistive state. The temperature $T^* \sim 0.55$ K marks the crossover between a regime dominated by MQT and one dominated by PD. Regimes with σ_1 increasing with T, which indicate thermal activation (TA), were not observed. The width of the low-temperature SPD, expressed as $\sigma/I_1 = 0.058$, is particularly large and results in pronounced switching current fluctuations, as seen in the measurements of Fig. 4.1(c) (black arrow). Broad SPDs at low T, together with the absence of an intermediate TA regime, which is unusual in conventional JJs [266], indicate a large critical current $I_{C,1}$ and a small capacitance C for JJ1. Finally, the relevance of PD,

together with measuring a finite resistance at $I_{DC} = 0$ for $T > 1$ K, which is well below the critical temperature T_C of the Al, indicates moderate damping.

4.2.2. Monte Carlo Simulation

The temperature dependence of $I_{M,1}$ and σ_1 is well captured by a Monte Carlo simulation of the phase dynamics [grey line in Figs. 4.2(c, d)] [267], an approach previously adopted for the study of moderately damped JJs [268, 269]. While this model was developed for tunnelling JJs with sinusoidal current-phase relation and large quality factor Q, in the absence of a more complete theory, we tentatively apply it to our devices and consider the results to be of qualitative nature.

The Monte Carlo simulation consists of a simulated junction with critical current I_C, capacitance C and zero-temperature quality factor Q_0 as input parameters. These are used to calculate the rates for escape Γ_Q and retrapping Γ_R, using Eqs. 2.36 and 2.37 respectively. As the DC bias current is increased, the simulated junction stochastically switches between the superconducting (0) and resistive (1) states according to the relative escape and retrapping rates. The junction is said to be resistive when the state, averaged over a window of current, exceeds 0.1. This process is performed 20,000 times and the generated I_{SW} values are combined into an SPD.

The capacitance C and the zero-temperature critical current $I_{C,1}$ of JJ1 are first obtained by comparing the low-temperature data to a model of MQT (Eq. 2.36), obtaining $I_C = 3$ μA and $C = 1$ fF . The impact of a thermal bath at low temperature is neglected, since $\Gamma_Q \gg \Gamma_T$ for low temperatures at the mixing chamber. We use the Bardeen formula for the temperature dependence of $I_C(T) = I_C(1 - T^2/T_C^2)^{3/2}$, with $T_C = 1.18$ K from experimental results. Since $Q \propto I_C^{1/2}$, we use $Q(T) = Q_0(1 - T^2/T_C^2)^{3/4}$. We use the low-temperature fit result and the assumed temperature dependence to simulate the full dataset. The quality factor Q_0 is determined by comparing the full temperature dependence to the Monte Carlo simulation, obtaining $Q_0 = 7$.

In a simple model as used here, the quality factor of the junction is described by $Q = RC\omega_P$. For $I_C = 3$ μA and $C = 1$ fF we get a resistance of $R = 2.33$ kΩ, much larger than the normal state resistance at low frequency of $R_{N,1} = 150$ Ω. We therefore conclude that damping at high frequency is relevant in the case of these junctions, giving a complex frequency-dependent relationship between the quality factor Q and the shunt impedance. For $Q \gg 1$, we can relate the quality factor to the ratio of critical and retrapping currents: $Q = 4I_C/\pi I_R$. For JJ1, $I_R = 600$ nA giving $Q = 6.4$, close to the fit value.

We show in Figs. 4.3(a-c) the relevant rates in the system for the fit parameters for JJ1: $I_C = 3$ μA, $C = 1$ fF and $Q_0 = 7$. Each panel corresponds to a different temperature: $T = 20$ mK, $T = 500$ mK and $T = 800$ mK, respectively. The interplay between Γ_Q and Γ_R determines the phase escape regime: $\Gamma_Q \gg \Gamma_R$ in the MQT regime, whereas the reverse is true for phase diffusion. These highlight the change in the dominant regime from MQT to PD on increasing T. Figures 4.3(d) and (e) show the SPDs and escape rates for JJ1, respectively. The experimental data (circles) are fitted well by the simulated

curve (lines). Deviation at high temperatures between the fit and the data is explained by the simple model used for the temperature dependence. Despite this, we capture the characteristic trend in the data.

As expected, JJ1 is moderately damped and has a small intrinsic capacitance, leading to a large plasma frequency. The estimated $I_{C,1}$ is 2.5 times higher than $I_{M,1}$, indicating that moderate input currents already result in a high switching probability.

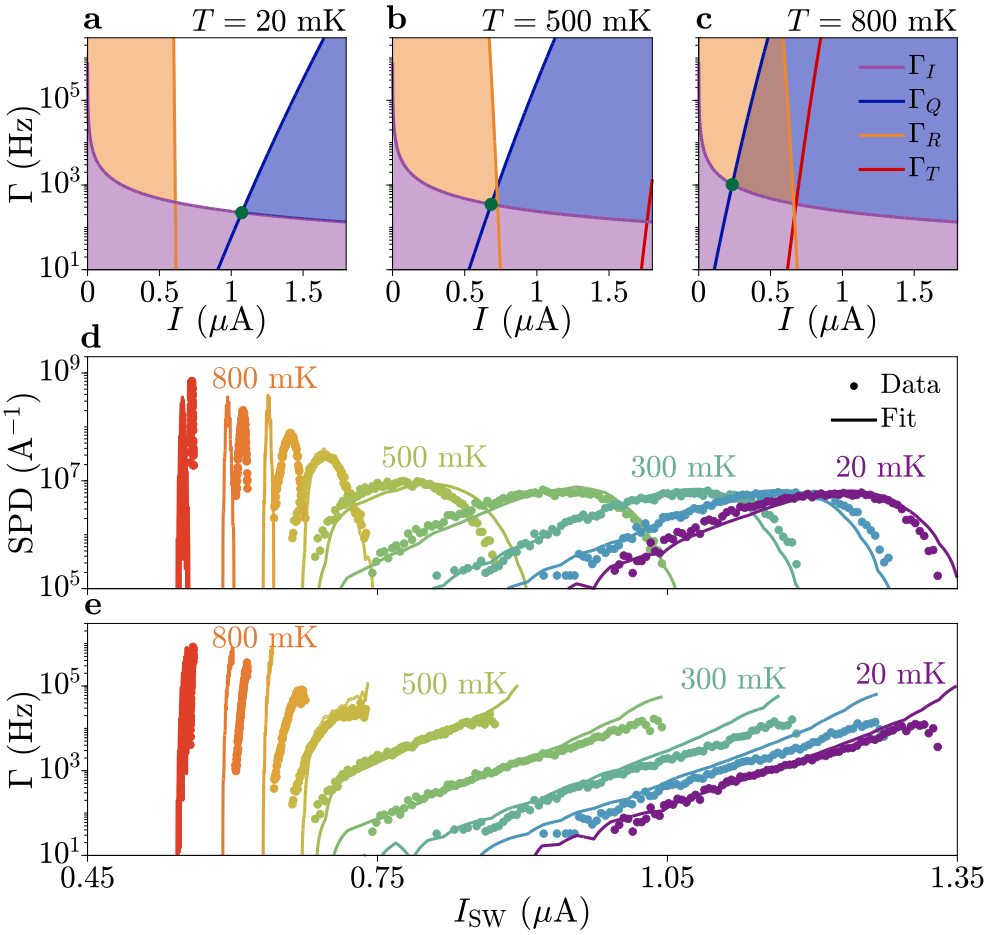

Figure 4.3. Monte Carlo simulation of JJ1. a-c Simulated escape rates for $T = 20$ mK, 500 mK and 800 mK respectively, for the fit parameters of JJ1. Bias-current ramp-rate Γ_I, MQT escape rate Γ_Q, retrapping rate Γ_R and thermal escape rate Γ_T are compared across the bias range I. The green dot indicates $\Gamma_I = \Gamma_Q$, at which point escape events are measurable. **d** SPDs of JJ1: Experimental data (points) compared with Monte Carlo simulation (lines) for temperatures 20 mK to 1 K. The temperature is indicated by the colour. **e** Escape rates corresponding to the SPDs in (d).

4.2.3. Understanding the Phase Escape Regimes

To understand the phase escape regimes in more detail, we can look again at Figs. 4.3(a–c). The ramp rate $\Gamma_{\mathrm{I}}(I) = \nu/I$ defines the lowest frequencies at which an escape event can be measured, for a given bias current I. The point at which this intersects the escape rate gives the lowest bias current I_{IE} at which an escape event is measurable. Since quantum tunnelling is the dominant escape mechanism, we define I_{IE} as the current at which $\Gamma_{\mathrm{I}} = \Gamma_{\mathrm{Q}}$, marked in Figs. 4.3(a–c) with the green dot. The retrapping rate Γ_{R} is large for low bias currents but quickly decreases with an increase in I.

At the lowest temperature, escape by quantum tunnelling dominates. This is clear since $\Gamma_{\mathrm{Q}} \gg \Gamma_{\mathrm{R}}$ for $I > I_{\mathrm{IE}}$. No retrapping of the phase occurs: a single escape event is sufficient to transition to the resistive state. At $T = 500$ mK, $\Gamma_{\mathrm{Q}} \lesssim \Gamma_{\mathrm{R}}$ close to I_{IE}. For these low bias currents, the retrapping probability is high so the probability of escape in the junction is reduced relative to quantum tunnelling alone. However, $\Gamma_{\mathrm{Q}} \gg \Gamma_{\mathrm{R}}$ at larger bias so escape occurs unhindered by phase diffusion. The standard deviation is approximately constant in the MQT regime for small increases in temperature, since the size of fluctuations is given by the plasma frequency ω_{P} (Eq. 2.36) which has a weak temperature dependence. As the temperature increases, the effect of retrapping becomes more significant. At the high temperature of 800 mK, phase diffusion is dominant since $\Gamma_{\mathrm{Q}} \ll \Gamma_{\mathrm{R}}$ across the range of escape currents. The standard deviation decreases with temperature in the PD regime since retrapping has a high probability for low I, truncating the SPD [see Fig. 4.3(c)].

The transition temperature T^* between MQT and PD regimes is experimentally defined as the inflection point of the standard deviation as a function of temperature. This is the point at which the retrapping rate Γ_{R} becomes dominant above MQT escape Γ_{Q}. We can specify this further as the temperature at which the escape, retrapping and ramp rates are equal, T^*_{IER}. This is similar to the definition in Ref. [267]. The trend of $I_{\mathrm{M,1}}$ with temperature changes at T^*, which suggests that our definition of T^* is appropriate as a measure of the transition between MQT and PD regimes.

4.2.4. Absence of Thermal Activation

With the fit parameters, we estimate $E_{\mathrm{J}}/E_{\mathrm{C}} = 73$ at $T = 20$ mK. This situation is very different from conventional metallic Josephson junction, where strong suppression of I_{SW} from I_{C} requires $E_{\mathrm{J}}/E_{\mathrm{C}} \leq 1$ [270–272]. Due to the small C and large I_{C}, we estimate that the transition from MQT to TA would occur for $T \gtrsim T_{\mathrm{C}}$ so that, in the entire PD regime, phase escape takes place via MQT. We can see this by comparing Eqs. 2.35 and 2.36, to obtain an effective temperature of quantum tunnelling escape,

$$k_{\mathrm{B}} T_{\mathrm{Q}} = \frac{\hbar \omega_{\mathrm{P}}}{7.2(1 + 0.87/Q)}. \tag{4.1}$$

At low temperature, $T_{\mathrm{Q}} \approx 3$ K for JJ1. This exemplifies the large scale of quantum fluctuations relative to thermal excitations. The temperature at which $T_{\mathrm{Q}} < T$ for the parameters of JJ1 is approximately 1 K: thermal activation is not significant up to the critical temperature.

4.2.5. Small Intrinsic Capacitance

The capacitance $C = 1$ fF obtained in the Monte Carlo simulation is consistent with the geometrical capacitance of JJ1, calculated as the coplanar capacitance between epitaxial Al electrodes and given by the formula [273]:

$$C = \frac{\epsilon_0 \epsilon_\mathrm{r} W}{\pi} \ln\left[-2\left(\frac{\beta+1}{\beta-1}\right)\right], \tag{4.2}$$

where $\beta = \sqrt[4]{1 - \frac{L^2}{(L+2L_\mathrm{SC})^2}}$. We use the dielectric constant $\epsilon_\mathrm{r} = 12.3$ of InAs at high frequency. The geometrical parameters of the junction are: lateral extent of JJ electrodes, $W = 5$ μm; separation of JJ electrodes, $L = 40$ nm; and length of superconducting leads, $L_\mathrm{SC} = 250$ nm. This gives $C = 1.4$ fF. The calculation does not consider the effect of the top gate electrode, which is grounded via a low-impedance terminal. It therefore acts as a screening layer for the electric field between the two junction electrodes. This reduces the capacitance, up to a factor of two for complete screening of half of the field between the Al electrodes. The presence of JJ2 in the SQUID loop contributes an additional shunt capacitance of $C_2 = 0.2$ fF, for junction parameters $W_2 = 1.6$ μm, $L_2 = 100$ nm and $L_{\mathrm{SC},2} = 250$ nm. Screening of the field by the electrostatic gates may reduce this by up to a factor of two. The contribution of JJ2 to the capacitance of JJ1 is therefore small, and does not modify the main conclusions.

The large leads of the device might also contribute to the shunt capacitance. Their geometrical capacitance, calculated with Eq. 4.2, is approximately 3 fF. This value is likely decreased by the presence of the large gate electrodes between them. This analysis does not consider shunt capacitances present in the bonding pads and in the wiring of the dilution refrigerator. The extent to which shunt capacitances contribute to the plasma frequency is an open question, investigated in [274–276]. The interpretation of a planar Josephson junction with a small capacitance C is supported by the result of an analytical fit to Eq. 2.36, a Monte Carlo simulation of the temperature dependence, a consideration of the geometrical capacitance of the junction and a comparison to values previously reported in literature [109, 254].

4.3. Gate and Magnetic Field Dependence of Phase Dynamics

The phase escape dynamics in JJ1 are investigated as a function of top-gate voltage V_G1 and an in-plane magnetic field $B_\parallel$.

4.3.1. Dependence on Top Gate Voltage

We tune the phase dynamics of JJ1 with a gate voltage V_G1. We measure SPDs for JJ1 as a function of temperature at gate voltages spanning the range of critical currents. In Figs. 4.4(a, b) we plot the mean and standard deviation of SPDs, respectively. As V_G1 is tuned to more negative values, the transition temperature T^* decreases until $V_\mathrm{G1} = -400$ mV, where JJ1 is fully phase diffusive at the lowest temperature in the

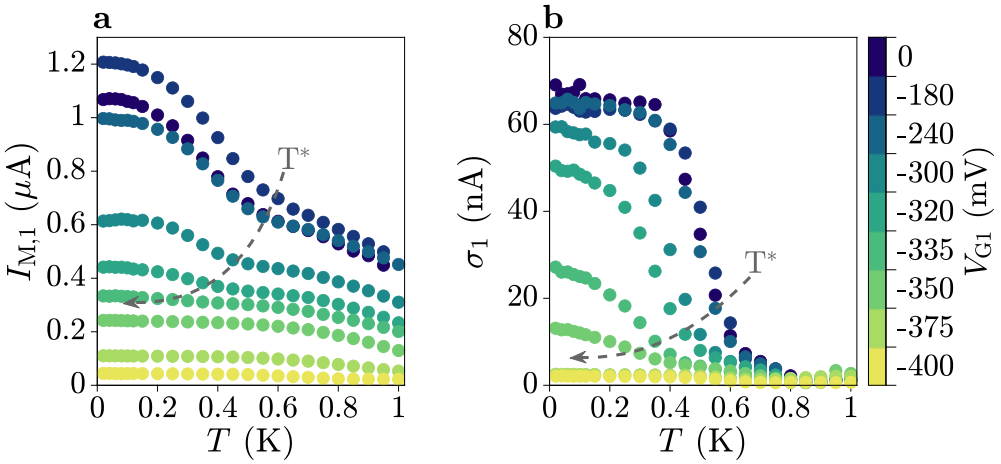

Figure 4.4. Gate voltage dependence of phase escape processes. **a** Mean switching current $I_{M,1}$ of switching probability distributions (SPDs) of JJ1 as a function of temperature. Measured for different gate voltages V_{G1}, as indicated by the color. The decrease in transition temperature T^* with V_{G1} is indicated by the arrow. **b** Standard deviation σ_1 of SPDs of JJ1 as a function of temperature, for different gate voltages V_{G1}. The decrease in T^* with V_{G1} is indicated by the arrow.

measurement. This transition is clear from both the mean switching current $I_{M,1}$ and standard deviation σ_1. At $V_{G1} = -320$ mV, σ_1 at $T = 20$ mK is 50 nA, reduced relative to 65 nA at $V_{G1} = -180$ mV. Additionally, σ_1 is not constant with temperature even down to the lowest measured value of T. Finally, the kink in $I_{M,1}$ and the inflection point in σ_1 occur at $T^* \approx 0.4$ K. These features all indicate a stronger relevance of PD, such that it is present at 20 mK and becomes dominant at a lower temperature: T^* is decreased.

The resistance in the normal state increased for more negative V_{G1}. The action of V_{G1} therefore changes both the critical current and the normal state resistance, which changes the quality factor Q. The change in both quantities determines the transition to the PD regime. We assume that the capacitance stays constant as a function of gate voltage, since it appears to be dominated by the geometry of the superconducting leads.

4.3.2. Dependence on In-Plane Magnetic Field

We additionally tune the phase dynamics of JJ1 using an in-plane magnetic field $B_\parallel$, applied perpendicular to the direction of current flow. We measure SPDs for JJ1 as a function of temperature at different magnetic fields, until the switching current is fully suppressed. In Figs. 4.5(a, b) we plot the mean and standard deviation of SPDs, respectively. For larger $B_\parallel$, the mean switching current $I_{M,1}$ is reduced for all values of temperature, and the standard deviation σ_1 at $T = 20$ mK decreases and is not constant with temperature. Additionally, both the kink in $I_{M,1}$ and the inflection point of σ_1 move to lower temperatures. These all indicate that the transition temperature T^* decreases

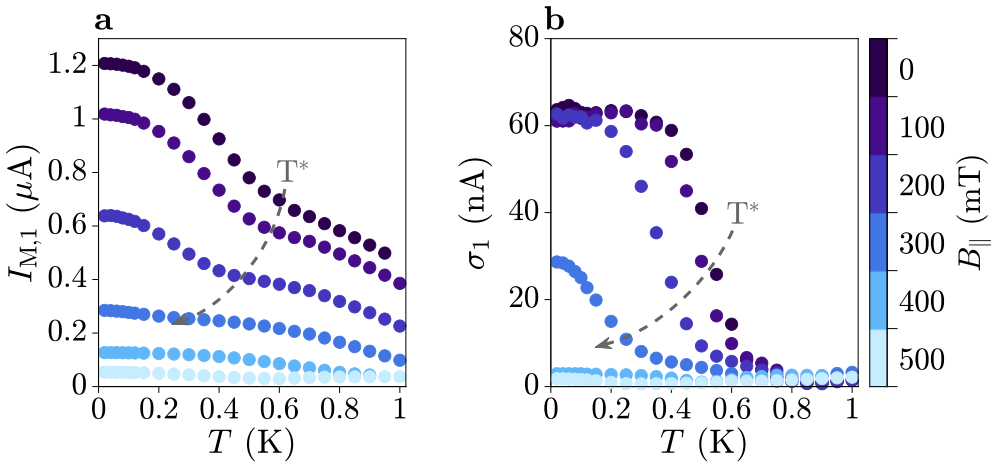

Figure 4.5. Magnetic field dependence of phase escape processes. a Mean switching current $I_{M,1}$ of switching probability distributions (SPDs) of JJ1 as a function of temperature. Measured for different in-plane magnetic fields $B_\parallel$, as indicated by the colour. The decrease in transition temperature T^* with $B_\parallel$ is indicated by the arrow. **b** Standard deviation σ_1 of SPDs of JJ1 as a function of temperature, for different in-plane magnetic fields $B_\parallel$. The decrease in T^* with $B_\parallel$ is indicated by the arrow.

as $B_\parallel$ increases, until JJ1 is fully diffusive for $B_\parallel \gtrsim 300$ mT.

An in-plane magnetic field applied to the junction suppresses the supercurrent flowing across it, by suppression of the superconducting gap in the thin Al [147] and by orbital effects underneath the superconducting leads [120, 122, 197]. It does not change the normal state resistance of the junction, unlike a gate voltage. We therefore interpret the decrease in transition temperature T^* to a change in the critical current, for constant normal state resistance and capacitance. The suppression of switching current for $B_\parallel \gtrsim 500$ mT, far below the critical in-plane field of approximately 1 T, suggests that orbital effects were the dominant cause of critical current suppression in JJ1.

4.4. Dependence on Device Geometry

The phase escape dynamics are investigated in three additional JJs, with a different geometry to JJ1: one with a smaller junction width and length (JJ2), and two where the geometry of the superconducting leads is altered (JJ3 and JJ4).

4.4.1. Phase Dynamics of JJ2

Measurements of the switching statistics were also performed in JJ2. Figure 4.6(a) shows the SPDs for JJ2 at different mixing chamber temperatures T, with the corresponding escape rates Γ in Fig. 4.6(b). The SPDs were almost fully symmetric with respect to bias current, and the escape rates deviated from an exponential. The mean $I_{M,2}$ and standard deviation σ_2 of the SPDs are shown in Figs. 4.6(c, d), respectively, and are

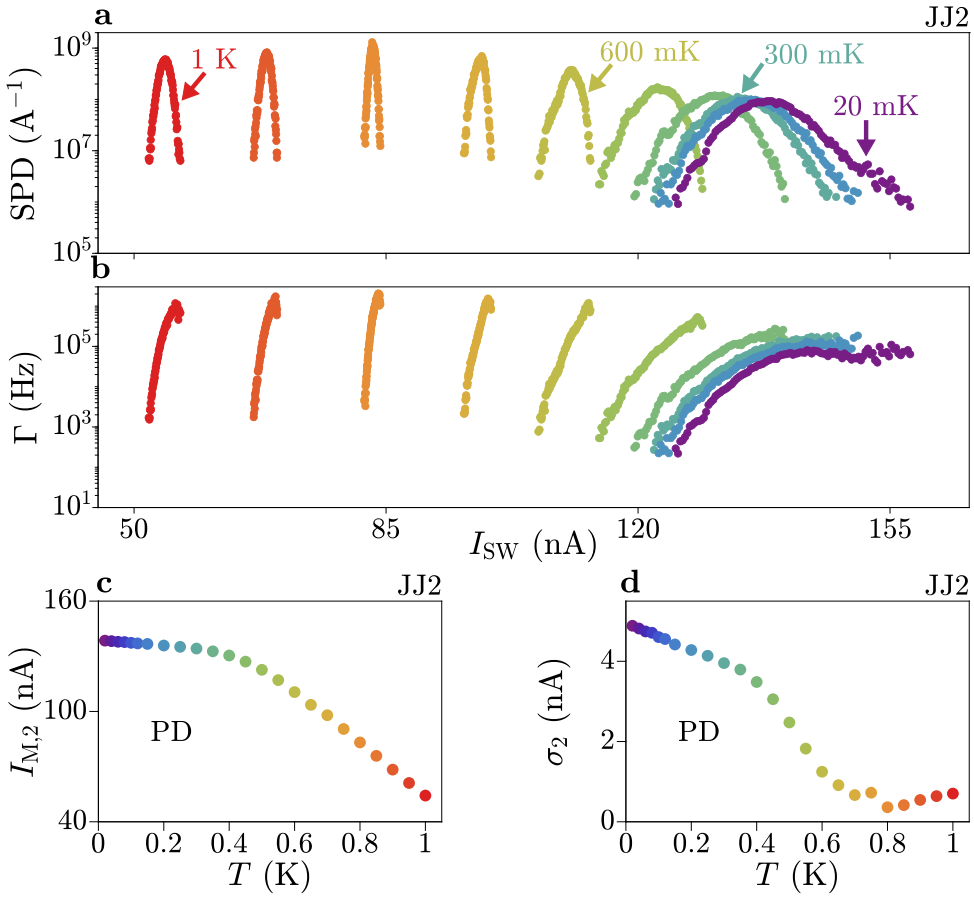

Figure 4.6. Temperature dependence of stochastic phase escape processes in JJ2. **a** Switching probability distributions (SPDs) for JJ2 for various temperatures. Colours are defined in (c). **b** Escape rate Γ of JJ2, obtained from the data in (a) using Eq. (2.34). **c** Mean switching current I_{SW} of SPDs for JJ2 as a function of temperature. **d** Standard deviation σ_2 of SPDs for JJ2, as a function of temperature.

notably different to those of JJ1. The mean switching currents are much smaller, and decrease gradually with increasing temperature without a kink [see Fig. 4.2(c)]. The standard deviation σ_2 is smaller by a factor of more than 10 compared with σ_1, and does not saturate for $T \to 0$. These results indicate that, while MQT is the dominant phase escape mechanism in JJ2, large dissipation results in a significant retrapping probability and places JJ2 in the PD regime down to base temperature. The small $I_{C,2}$ likely sets $Q_0 \sim 1$, which is outside the range of validity of our Monte Carlo simulations.

The critical current of JJ2 is expected to have a much smaller critical current than JJ1, from the designed junction dimensions. The reduction of the critical current increases the susceptibility of JJ2 to phase diffusion relative to JJ1: the barrier height is reduced, meaning that escape events can occur for bias currents a small fraction of the critical current, and damping is increased so the probability for retrapping is high.

By changing the geometry of JJ2 compared with JJ1, the phase escape dynamics changed dramatically. The modifications to the geometry altered the critical current of the junction, in a similar way to a gate voltage (Fig. 4.4) or in-plane magnetic field (Fig. 4.5). They are also expected to impact the capacitance: based on Eq. 4.2, the geometrical capacitance of JJ2 is estimated to be approximately 0.2 fF. This would act to increase the plasma frequency, and therefore increase quantum fluctuations in the macroscopic phase. The phase dynamics of JJ2 will be revisited in Chapter 5, where JJ2 is measured in parallel with JJ1 in a SQUID configuration.

4.4.2. Changing the Superconducting Leads

We further investigate the influence of device geometry on phase escape dynamics using JJ3 and JJ4, which are schematically shown in Figs. 4.7(a) and (b) respectively. The former, JJ3, consisted of two large superconducting leads separated by a stripe of exposed semiconductor of length $L = 50$ nm and width $W = 3.5$ μm. In contrast to JJ1 and JJ2, where the superconducting leads extended 250 nm away from the junction region, the leads of JJ3 were semi-infinite. The junction region of JJ4 was similar to that of JJ1: the junction had length $L = 50$ nm and width $W = 5$ μm, and the superconducting leads were 250 nm long. However, a metallic island was deposited on top of the insulating dielectric layer such that it had a large overlap with the Al contacts on either side of the junction. This was designed to give a large parallel-plate capacitance C_{pp} between each Al contact and the Au island, such that there would be a total shunt capacitance

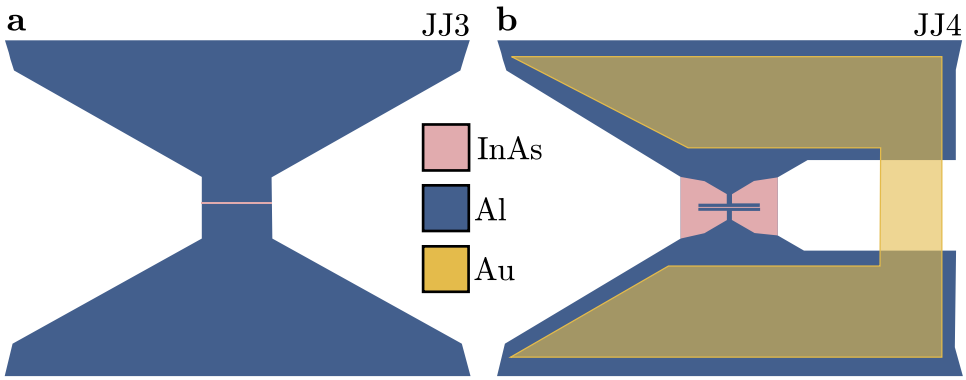

Figure 4.7. Schematic representation of Josephson junctions with different designs of the superconducting leads. **a** Schematic of JJ3, similar to JJ1 except with large superconducting leads. The Al (blue) is removed to expose the InAs (pink) only in a small rectangular section, which defines the junction region. The gate over the junction region is not drawn, to more clearly show the junction shape. **b** Schematic of JJ4, similar to JJ1 with the addition of a large Au island (yellow) overlapping the left and right contacts. Since the Au is isolated from the Al leads, it acts as a shunt capacitance for the junction. Gates in the junction region are not drawn, to more clearly show the junction shape.

$C_s = C_{pp}/2 \approx 1$ pF. The exposed semiconducting regions in JJ3 and JJ4 were controlled with electrostatic gates, to control the switching current and, in the case of JJ4, deplete the semiconductor around the junction. These gates are not drawn in Fig. 4.7, so that the junction shape is clearly visible for each device.

Switching current measurements were performed on JJ3, at a top-gate voltage $V_G = 150$ mV where the switching current was maximum. Figures 4.8(a) and (b) respectively show the SPDs and escape rates, as a function of mixing chamber temperature T. For low temperatures, the standard deviation [Fig. 4.8(d)] had an approximately constant value of $\sigma = 4.2$ nA. For $T > 250$ mK, σ decreased with temperature until a minimum of 2 nA at $T = 600$ mK, after which σ increased with increasing temperature.

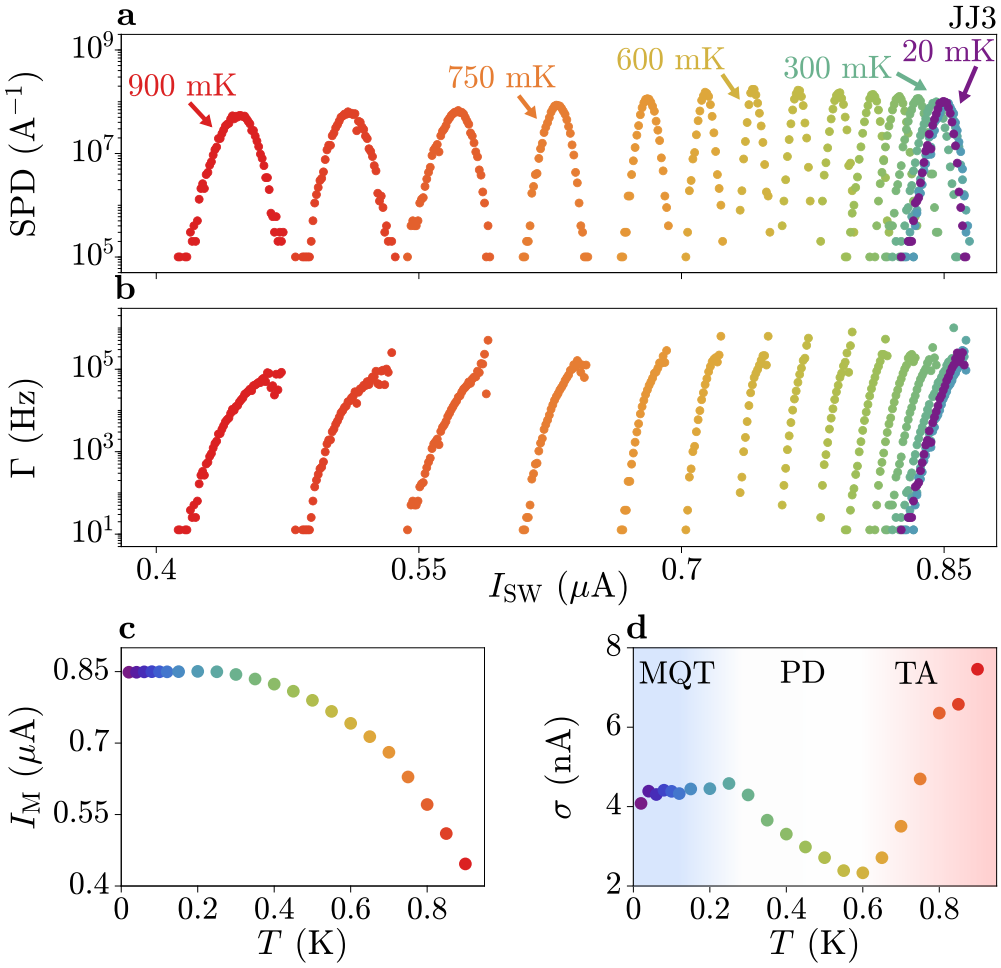

Figure 4.8. Temperature dependence of stochastic phase escape processes in JJ3. **a** Switching probability distributions (SPDs) for JJ3, similar to JJ1 with thick Al leads, for various temperatures. Colours are defined in (c). **b** Escape rate Γ of JJ3, obtained from the data in (a) using Eq. (2.34). **c** Mean switching current I_{SW} of SPDs for JJ3 as a function of temperature. **d** Standard deviation σ_2 of SPDs for JJ3, as a function of temperature.

The temperature dependence of σ suggests that JJ3 was in the MQT regime for $T < 200$ mK and was phase diffusive for $T > 200$ mK up to approximately 600 mK. For $T > 600$ mK, the increasing σ with T implies the onset of TA processes. The small σ in the MQT regime, relative to JJ1, is indicative of small quantum fluctuations, i.e. smaller plasma frequency, due to a larger capacitance and smaller critical current. This is supported by the onset of TA, which was not observed in JJ1 or JJ2, since the crossover temperature given by Eq. 4.1 is reduced [277]. A fit to Γ at $T = 20$ mK in the MQT regime (Eq. 2.36) returns a critical current of $I_C = 0.84$ μA and a capacitance of $C = 43$ fF, consistent with this interpretation. We estimate that the quality factor at low temperature is $Q_0 \sim 1.5$, which is outside the range of validity of our Monte Carlo

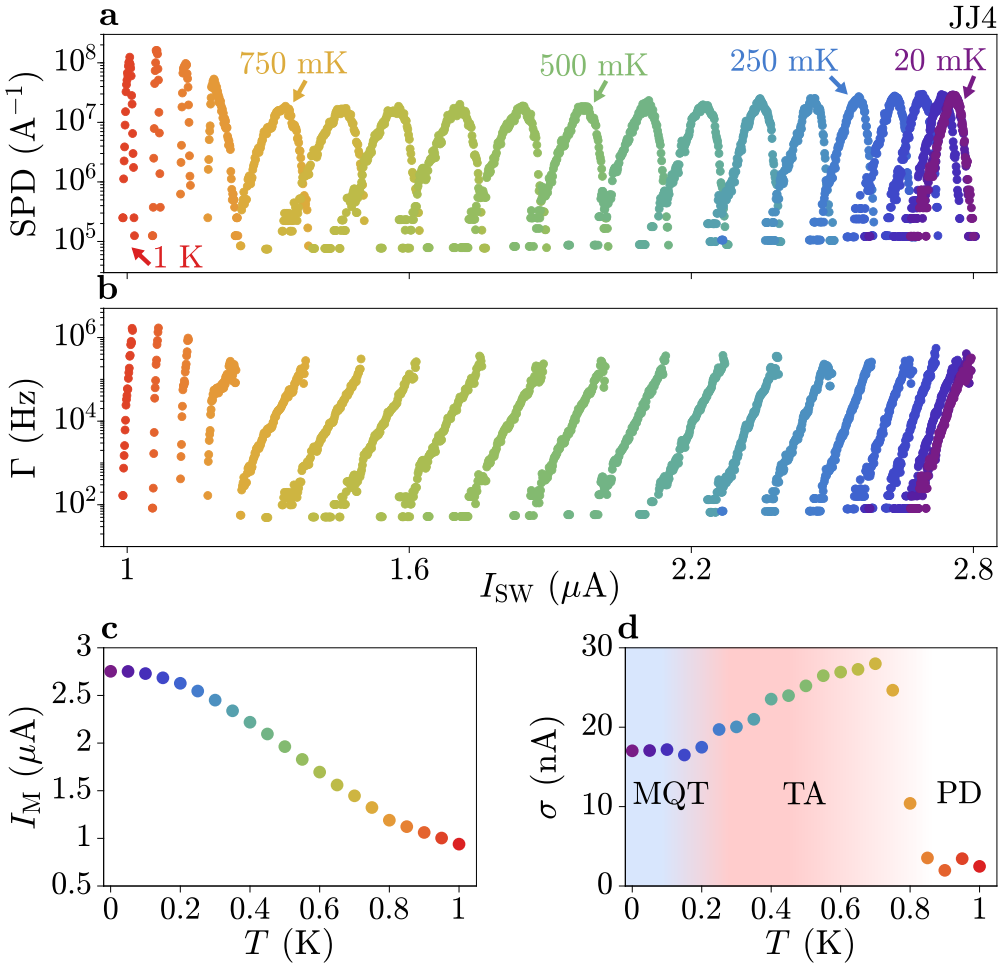

Figure 4.9. Temperature dependence of stochastic phase escape processes in JJ4. **a** Switching probability distributions (SPDs) for JJ4 for various temperatures. Colours are defined in (c). **b** Escape rate Γ obtained from the data in (a) using Eq. (2.34). **c** Mean switching current I_{SW} of SPDs as a function of temperature. **d** Standard deviation σ_2 of SPDs as a function of temperature.

simulations.

Switching current measurements performed on JJ4 are summarised in Fig. 4.9, for zero top-gate voltage. For temperatures $T \lesssim 0.7$ K, the SPDs had a regular shape with negative skewness [Fig. 4.9(a)] and the escape rates had a pure exponential form [Fig. 4.9(b)]. For large temperatures $T \gtrsim 0.7$ K, the SPDs and escape rates were distorted. The dependence of I_{M} on temperature was similar to that of JJ3 [see Fig. 4.9(c)], although gave much larger values. This could be explained by the larger width W of JJ4 relative to JJ3, and fabrication differences between the devices. In contrast, σ for JJ4 is qualitatively different from that of JJ3 [see Fig. 4.9(d)]. At low temperature, $\sigma \approx 17$ nA up to $T \sim 0.15$ K, after which it increased with temperature up to a maximum of $\sigma = 28$ nA at $T = 0.7$ K. For $T > 0.7$ K, σ decreased sharply with temperature.

The temperature dependence of σ implies that JJ4 was in the MQT regime for low temperature, and experienced TA processes for $T \gtrsim 0.15$ K. Phase diffusion did not become significant until $T \gtrsim 0.7$ K. This shows that JJ4 was in a qualitatively different regime to the other measured JJs, since a transition from MQT to TA escape was observed at much lower temperatures than the PD regime. The inclusion of a large metallic island connecting the two superconducting leads resulted in a dramatic change in the phase escape dynamics.

This is consistent with an increase in the effective capacitance of the junction, which suppresses quantum fluctuations such that the cross-over temperature to thermal activation is much lower. However, the standard deviation at low temperature was much larger in JJ4 than JJ3, and a fit to $\Gamma(T = 0.02\ \mathrm{K})$ in the MQT regime (Eq. 2.36) returned a critical current of $I_{\mathrm{C}} \sim 2.9\ \mu$A and a capacitance of $C \sim 10$ fF. The fitted capacitance is much smaller than the estimated shunt capacitance $C_{\mathrm{s}} \sim 1$ pF, based on the overlap area of 200 $(\mu\mathrm{m})^2$ on each side of the junction. Since the metallic island overlaps with the leads more than 1 μm from the junction, a more sophisticated model might be needed to account for shunt impedances in the circuit far from the junction [275]. This analysis is beyond the scope of this work.

4.5. Conclusions

In conclusion, we have shown that macroscopic quantum tunnelling (MQT) and phase diffusion (PD) are the most relevant phase escape regimes in planar Josephson junctions (JJs) in InAs/Al heterostructures; contrary to conventional metallic JJs, no indication of thermal activation (TA) is observed. Characteristic experimental features are reproduced with a Monte Carlo simulation of the phase dynamics, revealing that the low-temperature mean switching current I_{M} is a small fraction of the critical current I_{C}, even though the Josephson energy E_{J} is significantly larger than the charging energy E_{C}. In JJs with small I_{C}, the suppression of I_{M} is strong enough that PD dominates at low temperature. The transition temperature T^* between MQT and PD regimes could be tuned using a gate voltage and an in-plane magnetic field, via tuning of the critical current and the normal state resistance. The phase escape dynamics are significantly altered by changing the junction environment. Increasing the superconducting lead dimensions

results in a reduction in switching current fluctuations in the MQT regime, due to a larger capacitance. Further, the inclusion of a shunt capacitor promotes TA phase escape, such that the TA regime occurs at lower temperatures than the onset of PD.

With both *in situ* tuning of device parameters, and alterations to the device design, we have investigated how the phase escape mechanisms in planar JJs depend on three macroscopic junction properties: critical current, normal state resistance and capacitance. Our results indicate that phase dynamics significantly affect the switching current of hybrid devices, and guide towards the realisation of improved quantum architectures.

Future studies could extend the analytical escape rate equations used here to account for a non-sinusoidal current-phase relation, relevant for hybrid JJs containing highly transmissive Andreev bound states. The influence of shunt capacitances on phase escape dynamics could also be investigated further, to understand the impact of large capacitances on suppressing quantum fluctuations and promoting TA processes.

5 Phase Dynamics in Planar Josephson Junctions Part II: SQUIDs

Superconducting quantum interference devices (SQUIDs) are realised by embedding a Josephson junction (JJ) in a superconducting loop, such that the phase difference between the superconducting contacts of the JJ is related to the total flux through the loop. Their sensitivity to magnetic fields enables SQUIDs to be used for delicate magnetometry and sensing [17], and they allow phase biasing to probe novel material properties such as topological transitions [120, 122, 123]. When using a SQUID to probe an individual JJ, it is particularly important to understand effects arising from the coupled system. This chapter investigates the stochastic behaviour of a SQUID composed of JJ1 and JJ2 (introduced in Chapter 4), connected via a superconducting loop, and how the phase escape dynamics in the SQUID relate to those of the individual JJs outlined in the previous chapter. The text and figures of this chapter are adapted from Ref. [251].

This chapter is adapted from the following publication:

Measurements of Phase Dynamics in Planar Josephson Junctions and SQUIDs
D. Z. Haxell, E. Cheah, F. Krizek, R. Schott, M. F. Ritter, M. Hinderling, C. Bruder, W. Wegscheider, H. Riel, and F. Nichele
Physical Review Letters **130**, 087002 (2023).

Author contributions: F.N. conceived the experiment. E.C., F.K., R.S., and W.W. performed the material synthesis and characterisation. D.Z.H. designed the samples, F.N. gave support. D.Z.H. fabricated the samples, M.F.R. provided advice and support. F.N. and D.Z.H. performed the measurements. D.Z.H. analysed the data, C.B. provided theoretical support on the appropriate formulae and F.N. contributed to the Monte Carlo script. D.Z.H. and F.N. analysed and interpreted the data, with contributions from all authors. F.N. and D.Z.H. wrote the manuscript, with contributions from all authors.

5.1. Measuring JJ1 and JJ2 in a SQUID

We present the phase dynamics when both JJ1 and JJ2 are activated.

5.1.1. Temperature Dependence

Figures 5.1(a) and (b) show the mean, $I_{\mathrm{M,S}}$, and standard deviation, σ_{S}, of each SPD obtained in the gate configuration $V_{\mathrm{G1}} = -180$ mV and $V_{\mathrm{G2}} = -140$ mV [the same as Fig. 4.1(b)] as a function of $B_\perp$ and T. Each SPD was obtained by recording 5,000 switching events. In Fig. 5.1(a), SQUID oscillations are clearly captured by $I_{\mathrm{M,S}}$. In Fig. 5.1(b), the curves at low T have a large σ_{S}, independent of $B_\perp$. As T increases further, σ_{S} is modulated by $B_\perp$ and ultimately becomes small and independent of $B_\perp$. In Fig. 5.2(a) we compare $I_{\mathrm{M,2}}$ [squares, as in Fig. 4.6(c)] to the half-amplitude of the oscillations in $I_{\mathrm{M,S}}$ (circles). In the absence of phase fluctuations, the two quantities would coincide. Instead, we find a significant discrepancy, highlighted by green shading, which is large at low T and vanishes above T^* of JJ1. By tuning T^* via V_{G1}, we confirm that the enhancement of $\Delta I_{\mathrm{M,S}}/2$ with respect to $I_{\mathrm{M,2}}$ was always correlated to T^* in JJ1 [see the full dataset in Appendix E]. The mean value of $I_{\mathrm{M,S}}$ matched $I_{\mathrm{M,1}}$ [see Fig. 5.3(a)] and the mean of σ_{S}, $\langle\sigma_{\mathrm{S}}\rangle$, was similar to σ_1 [Fig. 5.2(b)].

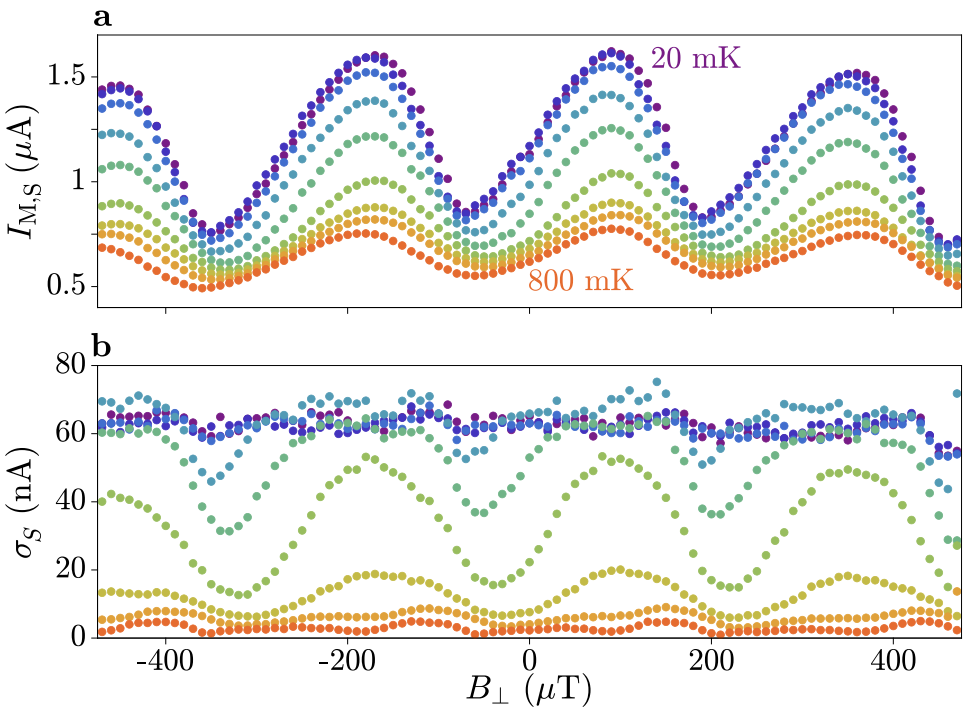

Figure 5.1. Phase escape in a superconducting quantum interference device (SQUID). Mean $I_{\mathrm{M,S}}$ **a** and standard deviation σ_{S} **b** of the SPDs in the SQUID configuration as a function of $B_\perp$, for temperatures between 20 and 800 mK.

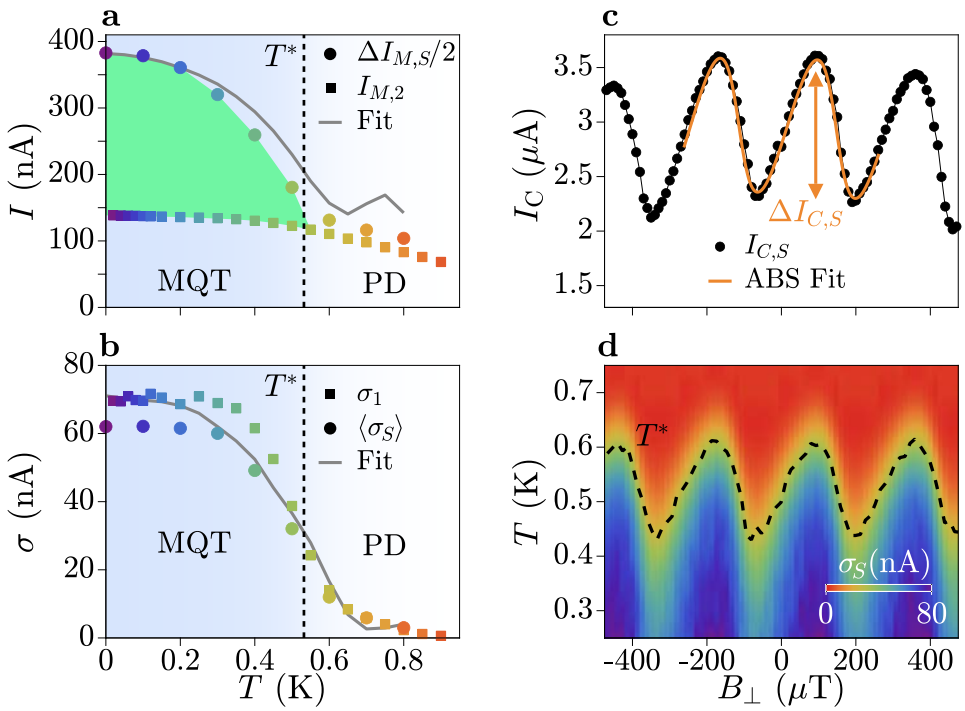

Figure 5.2. Comparison between phase escape of single JJs and a SQUID. a Mean switching current of JJ2 as a function of T, derived from the SQUID oscillations (circles) and measured with JJ2 in isolation (squares). The solid line is $\Delta I_{\mathrm{M,S}}/2$ obtained from a Monte Carlo simulation fitted to the experimental results. **b** Standard deviation of the SPD in JJ1 measured in isolation (squares) together with the mean of σ_{S} from Fig. 5.1(b) (circles) as a function of temperature. The solid line is the result of the Monte Carlo simulation presented in (a). **c** SQUID critical current obtained by fitting the SPDs for $T = 20$ mK to an MQT escape rate. **d** Colour map of fitted standard deviation σ_{S}, with transition temperature T^* marked by a dashed line.

The results presented in Figs. 5.1 and 5.2 are intuitively understood by considering phase-locking by the loop inductance. For JJ2 alone, phase escape is more likely at moderate currents compared to JJ1. Coupling JJ2 to JJ1 effectively realises a new JJ with higher Josephson energy and similar phase dynamics to JJ1, so that the dominant switching mechanism is MQT and, consequently, the suppression of I_{M} is reduced. However, protection of $I_{\mathrm{M,2}}$ is maintained while JJ1 stays in the MQT regime ($T < T^*$), where phase uncertainty is less than in the PD regime.

Consistent with this interpretation, phase dynamics in the asymmetric SQUID configuration are well described by a Monte Carlo simulation of a fictitious JJ with a field-dependent critical current $I_{\mathrm{C,S}}(B_\perp)$, and with C and Q as derived for JJ1. The sole fit parameter was $I_{\mathrm{C,S}}$ for $T = 20$ mK, which is shown in Fig. 5.2(c) as a function of $B_\perp$ (circles). The curve is consistent with the presence of highly-transmissive Andreev bound states (ABSs), resulting in a forward-skewed current-phase relation [153, 171]. Also for

the SQUID, the critical current $I_{\mathrm{C,S}}$ and mean switching current $I_{\mathrm{M,S}}$ [Fig. 5.1(a)] differ by a factor of approximately 2.5. After obtaining $I_{\mathrm{C,S}}(B_\perp)$ for $T = 20$ mK, the entire dataset of Figs. 5.1(a) and (b) was simulated without free parameters. We show the simulated half-amplitude $\Delta I_{\mathrm{M,S}}/2$ and the mean of σ_{S} as grey lines in Figs. 5.2(a) and (b) respectively. Despite the simplicity of our model, experimental results are reproduced to a large extent. Figure 5.2(d) shows a colour map of the simulated standard deviation, $\sigma_{\mathrm{S}}(B_\perp, T)$, with T^* indicated by a dashed line and marking the crossover between MQT and PD. The phase dynamics are completely described by MQT and PD for low and high T, respectively. For intermediate T, the phase escape mechanism periodically varies between MQT and PD as a function of $B_\perp$.

5.1.2. Monte Carlo Model

Figure 5.1 shows the switching probability in the SQUID configuration, as a function of $B_\perp$ and T. From $I_{\mathrm{M,S}}$ and σ_{S} as a function of $B_\perp$ we extract $\Delta I_{\mathrm{M,S}}/2$ and $\langle \sigma_{\mathrm{S}} \rangle$. In Fig. 5.3, we plot the remaining extracted parameters $\langle I_{\mathrm{M,S}} \rangle$ and $\Delta\sigma_{\mathrm{S}}$ (circles) with the corresponding results for the Monte Carlo simulation (lines). Figure 5.3(a) shows the field-averaged value of the oscillations in $I_{\mathrm{M,S}}$ (circles) compared with $I_{\mathrm{M,1}}$, the mean switching current for JJ1 (squares). The two align across all temperatures, confirming that JJ1 dominates the average SQUID behaviour.

The SQUID results are compared with the Monte Carlo simulation (grey lines in Figs. 5.2 and 5.3). The fit parameter $I_{\mathrm{C,S}}$ is obtained from the low-temperature data. Since the SQUID is in the MQT regime, we fit the escape rate at each value of $B_\perp$ with Eq. 2.36 using a fixed $C = 1$ fF and $Q_0 = 7$ from JJ1. The skewness of $I_{\mathrm{C,S}}$ indicates that highly transmissive modes are present in the junction. To capture this skewness, we consider a JJ with many modes N of equal transmission $\bar{\tau}$:

$$I_{\mathrm{C,S}} = I_{\mathrm{C,1}} + I_{\mathrm{N}} \frac{\sin(\varphi)}{\sqrt{1 - \bar{\tau}\sin^2(\varphi/2)}}, \tag{5.1}$$

with $I_{\mathrm{C,1}} = 3$ μA, $I_{\mathrm{N}} = 480$ nA and effective transmission $\bar{\tau} = 0.77$ [orange line in Fig. 5.2(c)]. This gives $\Delta I_{\mathrm{C,S}}/2 = 650$ nA. The mean value of $I_{\mathrm{C,S}}$ at $T = 20$ mK is given by the solid line in Fig. 5.3(a). We use the low-temperature result to simulate the full dataset by varying $I_{\mathrm{C,1}}$ and I_0 with a Bardeen dependence, as in Chapter 4.

The Monte Carlo simulation (grey line) follows the data at low temperatures, but some deviations emerge above $T = 600$ mK when the junction is almost completely phase diffusive [see Figs. 5.2(a) and 5.3(a)]. The escape rates are particularly sensitive to the damping Q in this regime, so deviations between simulations and experiment at high temperature might be accounted for with a more complex temperature dependence.

We observe a strong magnetic-field-dependence of the standard deviation in the SQUID, which is characterised by $\Delta\sigma_S$ in Fig. 5.3(b). Close to the transition temperature $T^* \approx 0.55$ K, $\Delta\sigma_{\mathrm{S}}$ is more than 35 nA. Both at low and high temperature, σ_{S} is almost constant across magnetic field. However, oscillations in the simulated σ_{S} were observed at low temperature, hence the larger simulated $\Delta\sigma_{\mathrm{S}}$.

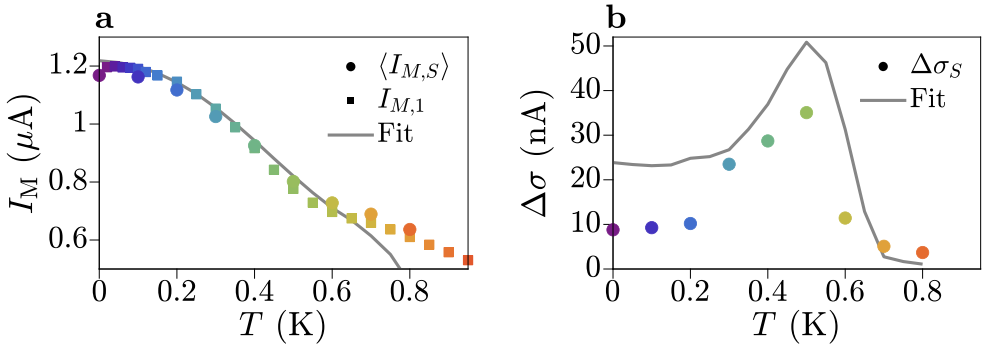

Figure 5.3. Monte Carlo simulation of the SQUID. a Average value of $I_{\mathrm{M,S}}$ across $B_\perp$ (circles), as a function of temperature (as indicated by the colour), compared with the mean switching current of JJ1 in isolation $I_{\mathrm{M},1}$ (squares) and a fit obtained by Monte Carlo simulation (grey curve). **b** Difference between the maximal and minimal σ_{S} across $B_\perp$, $\Delta\sigma_{\mathrm{S}}$ (circles), which indicates the size of the field-dependence in σ_{S} at a given temperature. This is compared with a Monte Carlo simulation (grey line), which reproduces the trend.

The above analysis gave the results $I_{\mathrm{C},1} = 3\ \mu$A and $I_{\mathrm{C},2} = 650$ nA. We can further quantify the properties of JJ1 and JJ2 by considering their $I_{\mathrm{C}}R_{\mathrm{N}}$ product [181]. This gives $I_{\mathrm{C},1} \cdot R_{\mathrm{N},1} = 3\ \mu\mathrm{A} \cdot 150\ \Omega = 450\ \mu$V and $I_{\mathrm{C},2} \cdot R_{\mathrm{N},2} = 650$ nA $\cdot 540\ \Omega = 350\ \mu$V, for JJ1 and JJ2 respectively. The expected $I_{\mathrm{C}}R_{\mathrm{N}}$ product is $\pi\Delta/e$ in the clean limit, or $\pi\Delta/2e$ in the dirty limit ($l_e < \xi$). For a superconducting gap of $\Delta = 180\ \mu$eV, this gives $I_{\mathrm{C}}R_{\mathrm{N}} = 565\ \mu$V or 283 μV, respectively. Hence, both JJ1 and JJ2 are in an intermediate regime between the clean and dirty limits, with JJ2 closer to the dirty limit than JJ1.

5.2. Gate and Flux Control of Phase Dynamics

In the following, we discuss how the phase escape dynamics vary as $I_{\mathrm{C},1}$ and $I_{\mathrm{C},2}$ are tuned with gate voltages.

5.2.1. Top-Gate Dependence of JJ2

In an asymmetric SQUID ($I_{\mathrm{C},1} \gg I_{\mathrm{C},2}$), the amplitude of oscillations as a function of $B_\perp$ is an indication of the current flowing through the small junction. We use Eq. 2.46 to extract the critical current of JJ2 in the asymmetric SQUID, as a function of gate voltage V_{G2}. We measure SQUID oscillations at $T = 20$ mK and fixed $V_{\mathrm{G1}} = -180$ mV, with different V_{G2} [see Fig. 5.4(a)]. The SQUID is always in the MQT regime, independent of V_{G2}, and the asymmetry is large. For each V_{G2}, we extract $\Delta I_{\mathrm{M,S}}/2$. We extract the critical current $I_{\mathrm{C,S}}$ by fitting each SPD with Eq. 2.36 in the MQT regime, with fixed capacitance C and quality factor Q_0 defined by JJ1. The result is shown in Fig. 5.4(b), from which we extract $I_{\mathrm{C},2} = \Delta I_{\mathrm{C,S}}/2$.

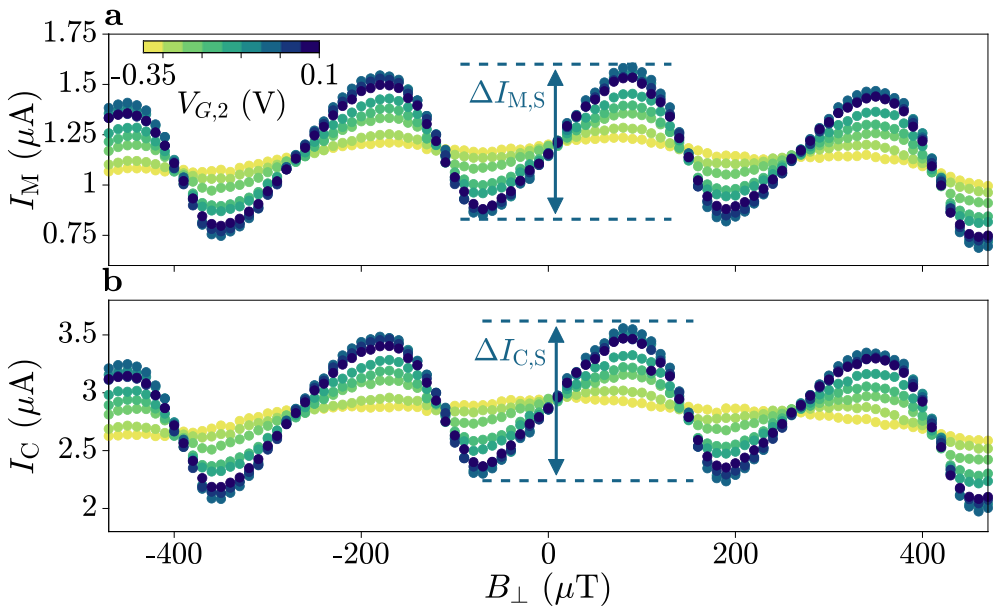

Figure 5.4. Dependence on the gate voltage of JJ2. a Mean switching current $I_{\mathrm{M,S}}$ as a function of $B_\perp$, taken at $T = 20$ mK for different values of the JJ2 gate voltage, V_{G2}. The oscillation amplitude $\Delta I_{\mathrm{M,S}}/2$ gives the switching current of JJ2 in the SQUID, as indicated by the arrow for $V_{\mathrm{G2}} = -100$ mV. **b** Critical current $I_{\mathrm{C,S}}$, obtained from the curves in (a) by fitting SPDs in the MQT regime. The oscillation amplitude $I_{\mathrm{C,2}} = \Delta I_{\mathrm{C,S}}/2$ gives the critical current of JJ2 as a function of V_{G2}, as indicated by the arrow for $V_{\mathrm{G2}} = -100$ mV.

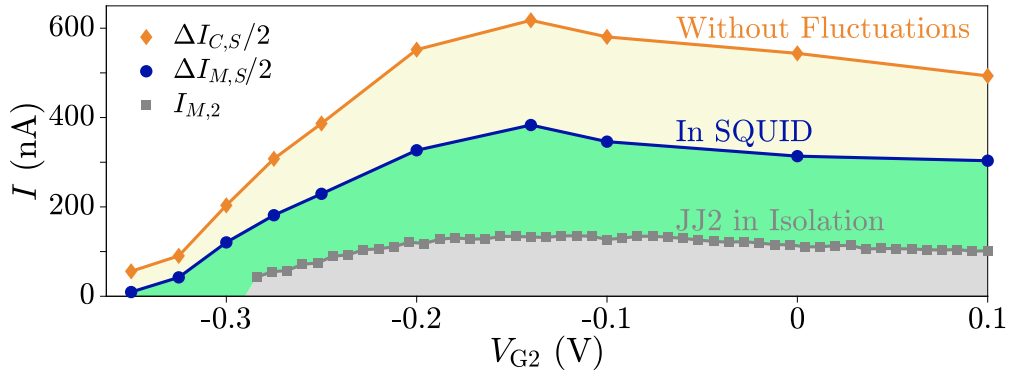

Figure 5.5. Summary of switching current suppression. Switching currents of JJ2 as a function of V_{G2} when measured in isolation (squares) and in the SQUID configuration (circles), together with the critical current derived from Monte Carlo simulations (diamonds).

Figure 5.5(a) summarises results for JJ2 as V_{G2} was varied. When JJ2 was measured in isolation, switching currents $I_{M,2}$ were small and PD was the dominant regime throughout the accessible range of V_{G2}. We highlight this condition with grey shading. When the SQUID was formed, the switching current of JJ2 deduced from the SQUID oscillations ($\Delta I_{C,S}/2$) was significantly higher than when JJ2 was measured in isolation. We highlight this situation with green shading. For $V_{G2} < 300$ mV JJ2 was resistive, if measured in isolation, presumably due to $E_J/E_C \approx 1$ [270–272], but SQUID oscillations were still observed. Finally, the $I_{C,2}$ obtained by fitting the SPDs in the SQUID with the Monte Carlo simulation [as in Fig. 5.2(e)] is highlighted in yellow.

5.2.2. Top-Gate Dependence of JJ1

The regime of the SQUID is dominated by JJ1, the large I_C component, so we can change the SQUID behaviour by varying V_{G1}. Decreasing $I_{C,1}$ via V_{G1} made the SQUID more symmetric and shifted JJ1 towards a regime of PD (see Fig. 4.4). Figure 5.6 shows σ_S for decreasing values of V_{G1}. For $V_{G1} = -300$ mV and -350 mV [Figs. 5.6(a) and (b), respectively] escape dynamics varied between MQT (blue shading) and PD already at base temperature, with σ_S oscillating between 10 and 60 nA within one SQUID oscillation. For $V_{G1} = -375$ mV [Fig. 5.6(c)] PD dominated at low T, although modulations in σ_S persisted. The full dataset is shown in Appendix E.

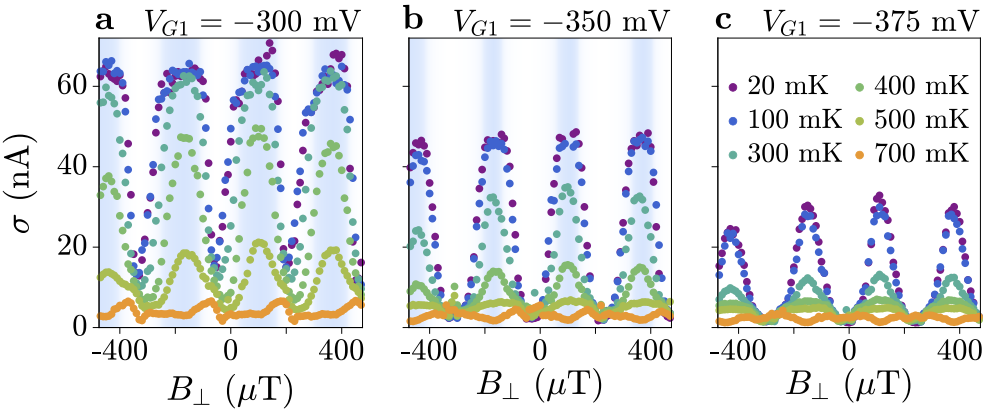

Figure 5.6. Flux-dependent phase escape regimes. Standard deviation of switching probability distributions measured in the SQUID configuration for three values of V_{G1}. Blue shading highlights macroscopic quantum tunnelling regimes.

5.3. Conclusions

In conclusion, we have shown that embedding a Josephson junction (JJ) in an asymmetric SQUID modifies the phase escape dynamics. Thus, the mean switching current I_{M} may significantly vary when a junction is measured in isolation or in a SQUID, by a factor of approximately 2.5 in the present case. This result resolves the discrepancy in switching current measurements introduced at the beginning of Chapter 4. The dominant phase escape mechanism is further tuned via temperature, gate voltages and fluxes threading the SQUID. This intricate physics is relevant for realising gate-tunable quantum devices and investigating topological phenomena, where hybrid JJs with phase control are widespread.

In this chapter, we have assumed that the phase particle moves in an effective one-dimensional potential, which is a good approximation for strongly asymmetric SQUIDs. However, future work might consider escape mechanisms in two-dimensional phase space, where the phase can follow a complex trajectory through the potential landscape. A full quantum treatment of phase escape in a two-dimensional potential might facilitate accurate modelling of the data shown in Fig. 5.6.

6 Spectroscopy of Andreev Bound States Part I: Photon Assisted Tunnelling

The supercurrent is a macroscopic property of a Josephson junction. It is composed of the sum over individual contributions from all transverse modes, each corresponding to a sub-gap state with properties depending on the mode transmission. To understand these microscopic states, and to relate their properties to potential applications, it is necessary to use spectroscopic methods which probe the states more directly. One approach is tunnelling spectroscopy, where a probe is weakly coupled to a Josephson junction via a potential barrier, and the tunnel current through the barrier is used to infer the density of states in the junction [278, 279]. This chapter explores the tunnelling spectroscopy method in the context of a device under microwave irradiation, and outlines an approach to distinguish interactions of the microwave field with the tunnel probe from signatures of novel Floquet-Andreev states in the Josephson junction. The text and figures of this chapter are adapted from Ref. [280].

This chapter is adapted from the following publication:

Microwave-Induced Conductance Replicas in Hybrid Josephson Junctions without Floquet–Andreev States
D. Z. Haxell, M. Coraiola, D. Sabonis, M. Hinderling, S. C. ten Kate, E. Cheah, F. Krizek, R. Schott, W. Wegscheider, W. Belzig, J. C. Cuevas, F. Nichele
Nature Communications **14**, 6798 (2023).

Author contributions: F.N. conceived the experiment. E.C., F.K., R.S., and W.W. performed the material synthesis and characterisation. D.Z.H. designed the samples, F.N. gave input. D.Z.H. fabricated the samples, M.C. provided fabrication assistance. D.Z.H. performed the experiments, M.C. and F.N. provided support. D.Z.H. analysed the data, W.B. and J.C.C. provided theoretical support. J.C.C. analysed the non-thermal distribution in the current-phase relation. D.Z.H., D.S., W.B., J.C.C. and F.N. interpreted the data, with contributions from all authors. D.Z.H. wrote the manuscript with input from D.S. and F.N., and with contributions from all authors.

6.1. Device and Measurement Concept

6.1.1. Photon Assisted Tunnelling and Floquet-Andreev States

An attempt to realise light-matter coupling was recently pursued using an aluminium/graphene SNS junction under microwave (MW) irradiation [114]. Andreev bound states (ABSs) with energy E_A were measured with tunnelling spectroscopy via a superconducting lead, as shown by the density of states (DOS) schematic in the top panel of Fig. 6.1(a). A current (yellow) flowed between a superconducting probe and an SNS junction, when occupied (red) and unoccupied (grey) states were aligned in energy by a source-drain bias V_{SD}. Without microwave irradiation, this gave a differential conductance qualitatively similar to the blue curve in Fig. 6.1(b), with peaks corresponding to ABSs at $V_{SD} = \pm(\Delta + E_A)/e$.

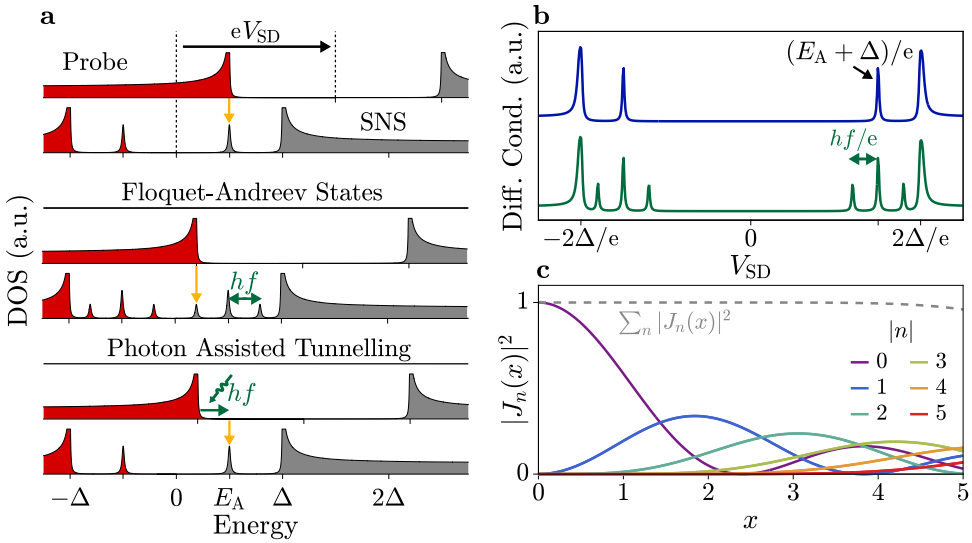

Figure 6.1. Conductance signatures of Floquet-Andreev states and photon assisted tunnelling. **a** Schematic representation of density of states (DOS) and tunnelling spectroscopy into a superconducting-semiconducting-superconducting (SNS) junction using a superconducting probe (top). Andreev bound states (ABSs) are present in the DOS of the SNS junction at energies $\pm E_A$. A current (yellow) flows when the source-drain voltage V_{SD} aligns occupied (red) to unoccupied (grey) states. In a Floquet-Andreev scenario (middle), replicas of Andreev peaks shifted by the photon energy hf emerge in the DOS of the SNS junctions, giving rise to additional tunnelling resonances. Floquet-Andreev states are represented as replicas of Andreev peaks shifted by hf. In a photon assisted tunnelling scenario (bottom), absorption of a photon (green) induces tunnelling into an ABSs for $eV_{SD} = E_A - hf$. **b** Schematic representation of tunnelling conductance measured in the absence (blue) and presence (green) of microwave irradiation. **c** Squared Bessel function $|J_n(x)|^2$ for $n \in [-5, 5]$ (colours). The sum $\sum_n |J_n(x)|^2$ (grey dashed line) is constant for the range of x where $J_{n>5}(x)$ is small.

Under microwave irradiation with frequency f, replicas of ABSs and the superconducting gap edge, separated in voltage bias by hf/e, were observed in the conductance spectrum, with h being the Planck constant. These were interpreted in Ref. [114] as signatures of steady Floquet-Andreev states (FASs) in the junction at energies $E_\mathrm{A} \pm nhf$, as schematically shown in the middle panel of Fig. 6.1(a). Alternatively, photon assisted tunnelling (PAT) [201, 204, 206, 207, 219, 281–283] can promote tunnelling across the barrier by absorption or emission of photons (green) with energy hf. The bottom panel of Fig. 6.1(a) depicts an example of electron tunnelling into an ABS assisted by absorption of a photon. Both FASs and PAT give, at least qualitatively, conductance curves as shown in the bottom panel of Fig. 6.1(b), with peaks at $V_\mathrm{SD} = (\Delta + E_\mathrm{A} \pm nhf)/\mathrm{e}$, where n is an integer. Conductance replicas arising from both PAT and FASs follow a squared-Bessel-function dependence on power, schematically depicted in Fig. 6.1(c). The sum over squared Bessel functions is identically constant [see grey dashed line in Fig. 6.1(c), which is constant for the range of x where $J_{n>5}(x)$ is small]. Therefore, the sum of conductance replicas is expected to be constant for both PAT and FASs. Distinguishing the generation of FASs from PAT, which was not considered in Ref. [114], is crucial for the realisation of light-matter band engineering in nanoscale hybrid devices.

6.1.2. Device with Gate-Tunable Tunnelling Barrier

Figure 6.2(a) shows a false-coloured micrograph of the device, which consisted of a planar SQUID containing a planar Al/InAs/Al junction and an Al constriction, all defined in the epitaxial Al (blue). The Al constriction was designed to limit the switching current of the metal arm, while being significantly larger than that of the SNS junction. This configuration allowed for a stable phase drop across the SNS of $\varphi = 2\pi(\Phi/\Phi_0)$, where Φ is the flux threading the SQUID and $\Phi_0 = h/2\mathrm{e}$ is the superconducting flux quantum. The Al loop was connected to two low-impedance superconducting leads, which allowed switching current measurements. A superconducting tunnelling probe with gate-tunable transparency was integrated close to the SNS junction, allowing for spectroscopy into the normal region. Two gates controlled the transparency of the tunnelling probe by the gate voltage V_T. A zoom-in close to the tunnelling probe, obtained prior to gate deposition, is shown in Fig. 6.2(b), where tunnelling gates are shown schematically. The SNS junction was controlled by a top gate, which was set to $V_\mathrm{TG} = -0.8$ V unless otherwise stated. An additional gate was kept to $V_\mathrm{Probe} = 0$ for the whole experiment. Microwave signals were applied via an attenuated coaxial line terminated in an antenna configuration and placed approximately 1 cm away from the chip surface.

Figure 6.2(c) shows the differential conductance $G \equiv I_1/V_1$ of the tunnelling probe as a function of V_T and V_SD, as the gate-tunable probe transitioned from the open to the tunnelling regime [top and bottom part of Fig. 6.2(c), respectively]. The open regime was characterised by a zero-bias conductance peak, which represents a supercurrent flowing through the tunnelling probe (green dashed line), and several finite bias features, which indicate multiple Andreev reflections (blue dashed line). The tunnelling regime displayed pronounced features at a voltage $2\Delta/\mathrm{e} = 380$ μV (white arrow), consistent with the superconducting gap $\Delta = 190$ μeV of Al [249]. Figure 6.2(d) shows G at low

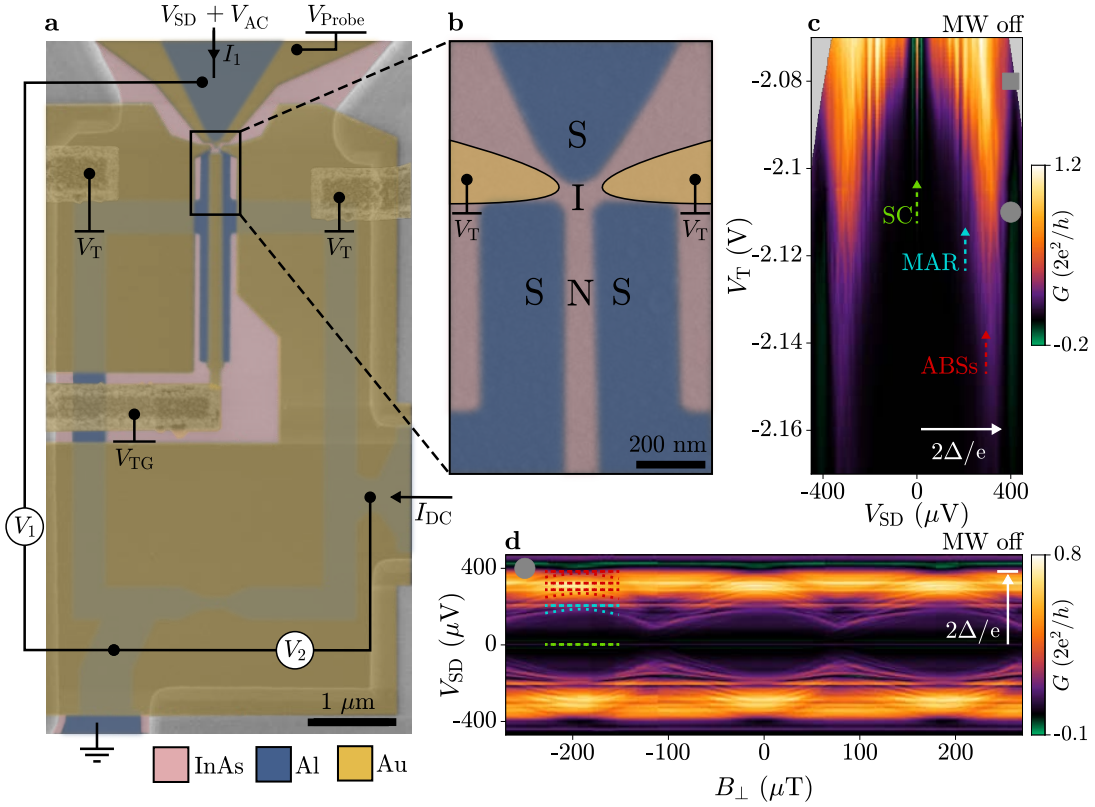

Figure 6.2. Device under study and tunnelling spectroscopy of sub-gap states. **a** False-coloured electron micrograph of a device identical to that under study, composed of InAs (pink) and Al (blue) and controlled via electrostatic gates (yellow). **b** Zoom-in of the tunnelling junction before gate deposition. The gates controlling the tunnelling barrier transparency are drawn in yellow. **c** Differential conductance G of the tunnelling probe as a function of bias V_{SD} and gate voltage V_T. Conductance features associated with the supercurrent (SC, green), multiple Andreev reflections (MAR, light blue) and Andreev bound states (ABSs, red) are indicated by dashed arrows. The transport gap is indicated as $2\Delta/e$ (white arrow). **d** Tunnelling spectroscopy of sub-gap states at $V_T = -2.11$ V, as a function of perpendicular magnetic field $B_\perp$. Conductance features as defined in (c) are indicated by coloured lines.

barrier transparency ($V_T = -2.11$ V), as a function of perpendicular magnetic field $B_\perp$ and voltage bias V_{SD}. Several finite bias conductance peaks are evident in Fig. 6.2(d) (red dashed lines). In addition to some highly transmissive ABSs present within the superconducting gap of the SNS junction, additional features may result from multiple Andreev reflections, disorder in the tunnelling barrier and sub-gap states in the DOS of the superconducting probe [284].

6.2. Conductance Replicas Under Microwave Irradiation

6.2.1. Emergence of Conductance Replicas

The effect of microwave irradiation on the tunnelling conductance G for $B_\perp = 0$ is summarised in Figs. 6.3 and 6.4. The top rows show G measured with the probe in the tunnelling regime ($V_\mathrm{T} = -2.11$ V), where conductance features at finite bias are associated with the DOS in the SNS junction. A remnant of the supercurrent is visible in these plots by saturating the colourscale and zooming in close to zero bias, as we show in the bottom row of Figs. 6.3(a-c) and 6.4(a–c). Figure 6.3(a) shows G without microwave irradiation, while Figs. 6.3(b, c) and 6.4(b, c) show G as a function of microwave source power P at frequencies $f_i = \{4.65,\ 7.40,\ 9.20,\ 12.65\}$ GHz. Similar plots, obtained in a more open regime ($V_\mathrm{T} = -2.08$ V), are plotted in Figs. 6.3(d–f) and 6.4(d-f). In these plots, the supercurrent flowing through the tunnelling probe is clearly visible. For each frequency, conductance features at both zero and finite bias split into replicas as P increased. Crucially, all conductance features split at the same power (see blue arrows) and evolved in an identical fashion as a function of P as $V_\mathrm{SD} = (hf/\mathrm{e})\alpha$, where $\alpha = \alpha_0 \cdot 10^{P/20}$. This was true for each frequency investigated. An exemplary fit to the data of Fig. 6.3(c), which yields $\alpha_0 = 3.0$, is plotted as the dotted blue line. Spacing between conductance replicas is indicated by green dashed lines, and is measured as hf_i/e and $hf_i/2\mathrm{e}$ for finite and zero bias features, respectively. While performing this analysis, it is important to distinguish conductance peaks that exclusively appear under microwave irradiation, to those already present without irradiation and that are caused by sample-specific features such as multiple Andreev reflections or sub-gap states in the superconducting probe [see red arrows in Figs. 6.3(a) and (d)]. Selected linecuts of Figs. 6.3(b, c) and 6.4(b, c) are presented in Fig. 6.5(a), after subtraction of a slowly varying background, together with a periodic grid with spacing hf_i/e. Figure 6.5(b) summarises the spacing between conductance replicas as a function of microwave frequency, which also includes additional frequencies, another V_TG value and a second device (see Appendix F). Conductance replicas at finite bias are indicated by circles and depend on frequency as $\Delta V_\mathrm{SD} = hf/\mathrm{e}$ (dashed line). Supercurrent replicas are indicated as squares and follow the dependence $\Delta V_\mathrm{SD} = hf/2\mathrm{e}$ (dashed-dotted line).

6.2.2. Dependence on Top-Gate Voltage

An example of conductance replicas at $V_\mathrm{TG} = -1.4$ V is shown in Fig. 6.5(c). Blue lines indicate a coupling strength $\alpha_0 = 3.0$, identical to that in Figs. 6.3(c, f). Decreasing the top-gate voltage from $V_\mathrm{TG} = -0.8$ V to $V_\mathrm{TG} = -1.4$ V is expected to reduce the Fermi velocity by $\sim 25\%$ (see Section 6.6 for more details). In a model of FASs, α is proportional to the Fermi velocity [114], and therefore, assuming that all other parameters in the system stay the same, α is predicted to decrease by the same factor in Fig. 6.5(c) relative to Figs. 6.3(c, f) (yellow lines). However, there is no observed change in α as a function of V_TG, consistent with conductance replicas induced by PAT in the tunnel barrier and incompatible with FASs generated in the SNS junction.

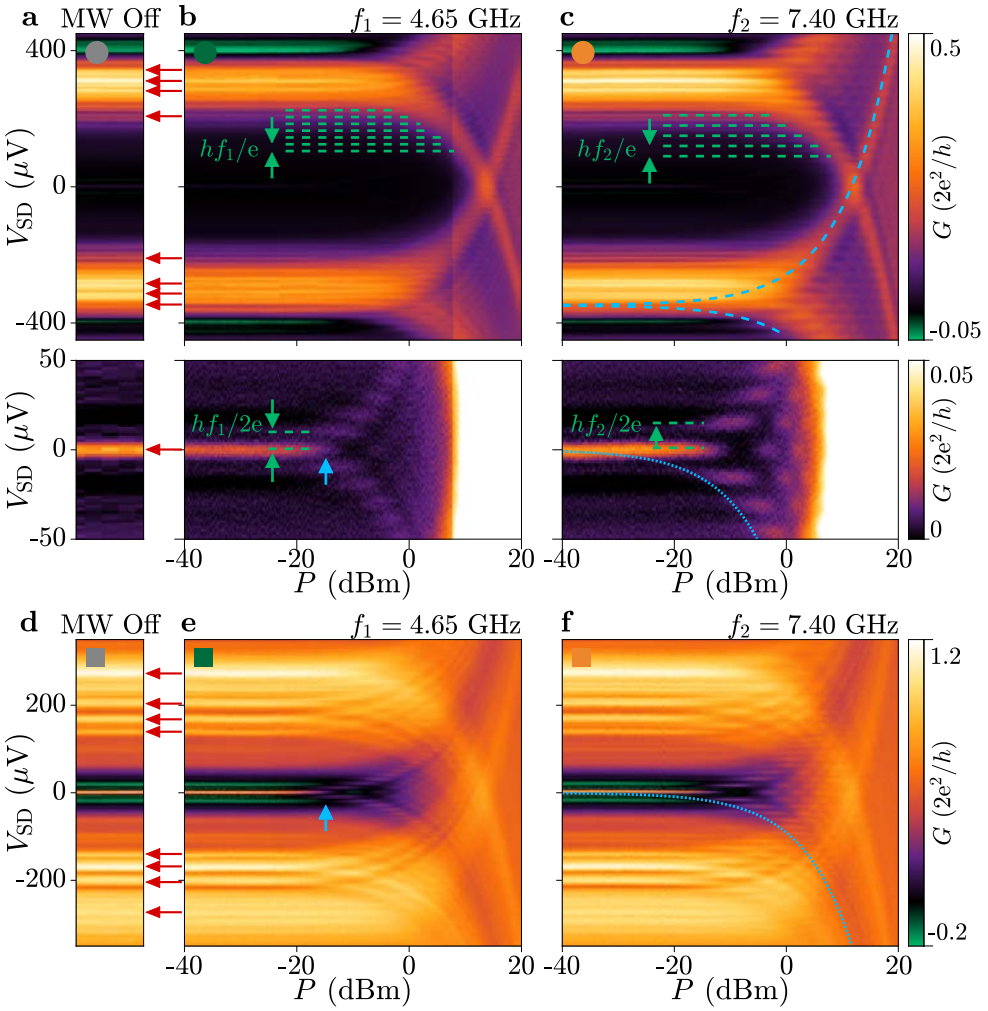

Figure 6.3. Tunnelling conductance under microwave irradiation of frequency $f_1 = 4.65$ GHz and $f_2 = 7.40$ GHz. **a** Conductance at $V_T = -2.11$ V with no microwave signal applied (top). Red arrows indicate sample-specific features present without irradiation. Zoom-in close to zero bias highlights remnant superuccrent (bottom). **b, c** Conductance at $V_T = -2.11$ V for irradiation frequencies f_3 and f_4 as a function of microwave source power P and V_{SD} (top), with corresponding zoom-ins close to zero bias to highlight remnant supercurrent (bottom). The onset of splitting in conductance features is indicated by blue arrows. Blue dotted lines indicate the power dependence of split-conductance features at low bias, and dashed lines indicate the same power dependence shifted to high bias. Periodic replication of conductance features is indicated by green dashed lines. **d** As (a) but for $V_T = -2.08$ V. **e, f** As (b, c) but for $V_T = -2.08$ V. Blue dotted lines indicate the power dependence of split-conductance features at low bias.

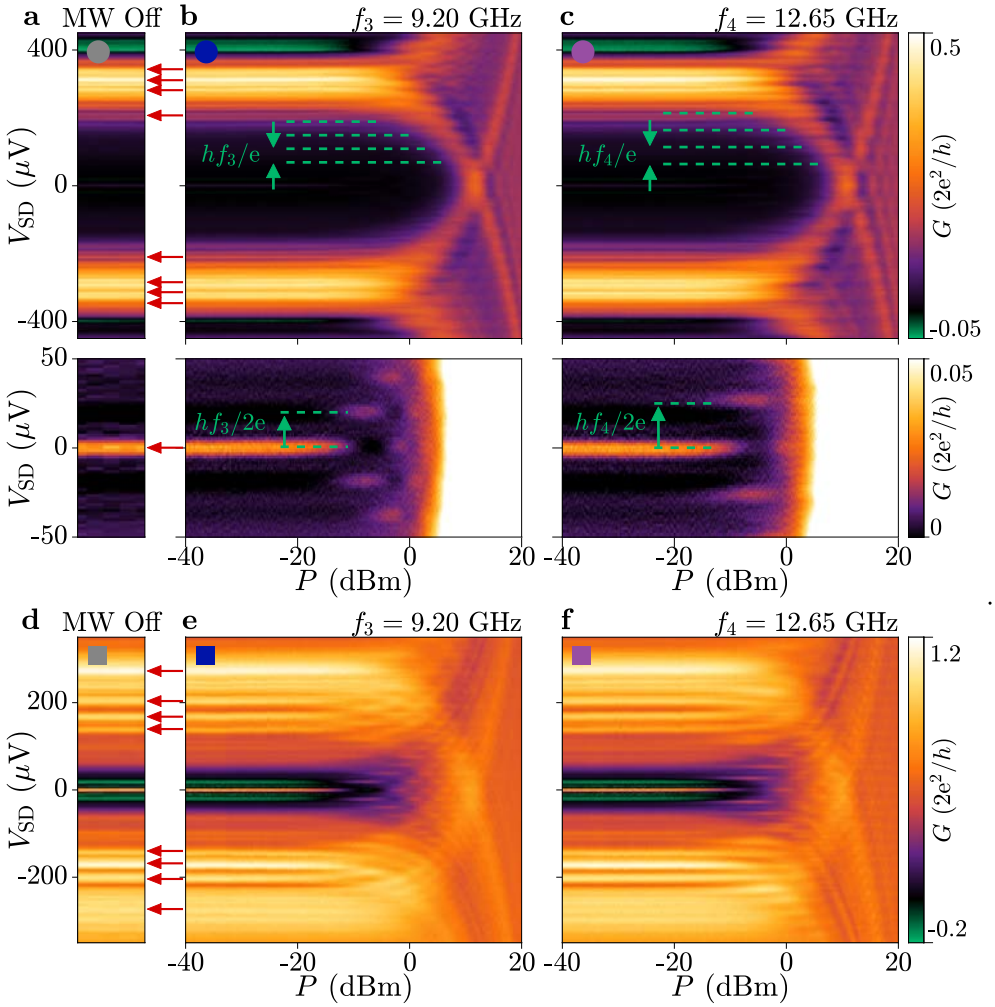

Figure 6.4. Tunnelling conductance under microwave irradiation of frequency $f_3 = 9.20$ GHz and $f_4 = 12.65$ GHz. **a** Conductance at $V_T = -2.11$ V with no microwave signal applied (top). Red arrows indicate sample-specific features present without irradiation. Zoom-in close to zero bias highlights remnant superuccrent (bottom). **b, c** Conductance at $V_T = -2.11$ V for irradiation frequencies f_3 and f_4 as a function of microwave source power P and V_{SD} (top), with corresponding zoom-ins close to zero bias to highlight remnant supercurrent (bottom). The onset of splitting in conductance features is indicated by blue arrows. Blue dotted lines indicate the power dependence of split-conductance features at low bias, and dashed lines indicate the same power dependence shifted to high bias. Periodic replication of conductance features is indicated by green dashed lines. **d** As (a) but for $V_T = -2.08$ V. **e, f** As (b, c) but for $V_T = -2.08$ V. Blue dotted lines indicate the power dependence of split-conductance features at low bias.

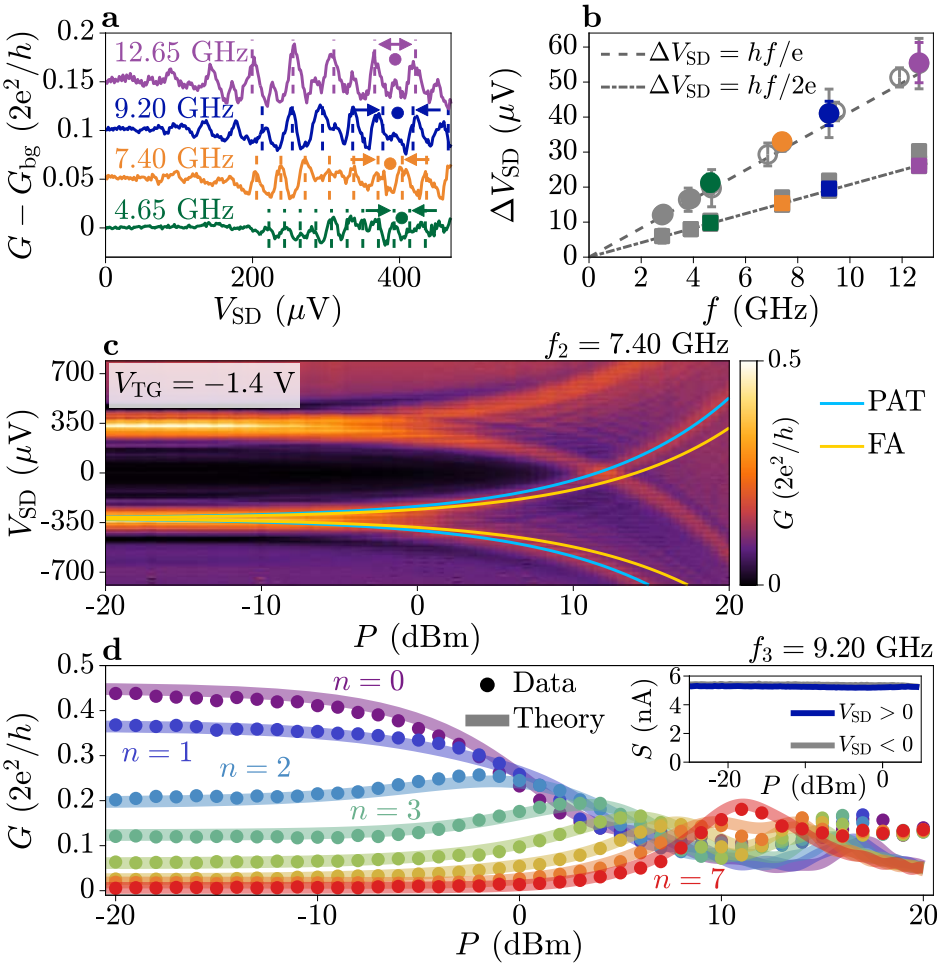

Figure 6.5. Frequency and power dependence of conductance replicas. **a** Linecuts of conductance from Figs. 6.3 and 6.4, after subtraction of a slowly varying background, successively offset by $0.05\ G_0$. Dashed lines mark the expected peak positions. Linecuts are taken at $P = 1.5, 4.5, 4, \text{and } 4.5$ dBm, respectively. **b** Spacing of conductance replicas measured at finite (circles) and close to zero (squares) bias. Dashed and dotted lines respectively represent the equations $\Delta V_{SD} = hf/e$ and $\Delta V_{SD} = hf/2e$. Filled and empty grey markers refer to additional data collected on the same device and on a second device, respectively (see Appendix F). **c** Conductance at a top-gate voltage $V_{TG} = -1.4$ V, as a function of microwave source power for irradiation frequency $f_2 = 7.20$ GHz. Blue lines indicate a microwave coupling strength of $\alpha_0 = 3.0$, identical to Figs. 6.3(c, f). Yellow lines indicate a coupling strength $\alpha_0 = 2.25$, reduced by 25% with respect to Figs. 6.3(c, f). Blue (yellow) lines show the expectation for photon assisted tunnelling (Floquet-Andreev states). **d** Conductance of the first seven replicas in Fig. 6.4(b), taken at constant bias V_{SD} (circles), alongside the simulated conductance from a photon assisted tunnelling model (lines, see Figs. 6.7–6.10). Inset shows the sum S of conductance features in Fig. 6.4(b) over positive (blue) and negative (grey) bias. Data is shown for the range of powers where all conductance replicas are within the measured bias range.

6.2.3. Power Dependence of Conductance Replicas

Finally, we present the power dependence of conductance replicas shown in Figs. 6.3 and 6.4. Linecuts of Fig. 6.4(b) are shown in Fig. 6.5(d), for $n = 7$ replicas (coloured circles). Their power dependence is modelled by a theory for PAT (lines) [201, 219], in which the conductance scales as a squared Bessel function $G \propto |J_n(\alpha)|^2$. This is similar to the theory used in Ref. [114], which follows the same dependence. The PAT model takes two input parameters: the low-power conductance [Fig. 6.3(d)] and α_0, which is calculated from the low-bias conductance replicas (see Figs. 6.7–6.9). With no free parameters, a good agreement with the data is obtained up to $P \approx 10$ dBm, corresponding to $\alpha \approx 8$. This demonstrates that high bias conductance features are explained by PAT, with an identical coupling strength to the microwave field as those at low bias (see Section 6.5 for more details). The sum over conductance features S is constant for the range of powers where conductance replicas remain within the measured range of bias V_{SD} [see inset of Fig. 6.5(d)]. This is consistent with conservation of the tunnel current, and stems from the result that squared Bessel functions sum to unity. Hence, the sum rule argument cannot be used to distinguish between PAT and FA interpretations.

6.2.4. Phase Dependence and Avoided Crossings

Similar to Ref. [114], we observed phase modulation of replicas originating from ABSs with energy $E_{\mathrm{A}} = \Delta\sqrt{1 - \bar{\tau}\sin^2(\varphi/2)}$, where $\bar{\tau}$ is the effective junction transmission [171]. Figures 6.6(a–c) show the tunnelling conductance as a function of perpendicular magnetic field $B_\perp$ measured under microwave irradiation of frequency $f = 9.20$ GHz and applied power $P = -5$, 0 and 5 dBm, respectively. Replicas of phase-dependent ABS features are indicated by green dashed lines, which describe ABSs with transmission $\bar{\tau} = 0.84$. When P was increased, more replicas appeared in the spectrum [Fig. 6.6(b)] until replicas originating from positive and negative bias overlapped [Fig. 6.6(c)]. No avoided crossing was observed for overlapping conductance features, in disagreement with predictions for FASs [110, 113, 285].

6.2.5. Discussion on the Origins of Conductance Replicas

Measurements presented in Figs. 6.3, 6.4 and 6.5 demonstrate that conductance replicas originating from the supercurrent and from finite bias features (superconducting gap edge and ABSs) have identical coupling strength to the applied microwave field. Conductance replicas in the supercurrent are readily interpreted as Shapiro steps [147], which only occur by photon absorption or emission in the tunnel barrier. Furthermore, all conductance replicas can be described by a PAT model up to large irradiation powers and the coupling strength was shown to be independent of top-gate voltage V_{TG}, incompatible with FASs. Finally, overlapping conductance features at large microwave powers showed no avoided crossings, contrary to predictions for FASs. We therefore conclude that finite bias replicas originate from PAT of electrons through the tunnelling barrier, and are not a manifestation of replicas in the DOS of the SNS junction.

6.3. Microwave-Induced Distortions to the Current-Phase Relation

After demonstrating that spectral replicas at high bias are caused by PAT in the tunnelling junction used to perform spectroscopy, we investigate how ABSs in the SNS junction couple to the applied electromagnetic field. These experiments probe the macroscopic superconducting state and do not rely on the microscopic processes taking place within the tunnelling probe, which was left floating. In particular, each occupied ABS in the SNS carries a supercurrent $I = -(2\mathrm{e}/\hbar)[\partial E_{\mathrm{A}}(\varphi)/\partial\varphi]$. The total supercurrent flowing in the SNS is obtained by summing the contributions of each ABS [153]. Figure 6.6(d) shows the CPR of the SNS junction as a function of microwave power. For $P < -20$ dBm, we observed a forward-skewed CPR, which indicates the presence of highly-transmissive ABSs [107, 153, 171], consistent with the spectrum in Fig. 6.2(d).

Increasing the applied microwave power, both the amplitude and skewness of the CPR decreased. This behaviour is described by an adiabatic theory of ABSs with a time-varying phase $\phi(t) = \varphi + 2\alpha\cos(2\pi ft)$, where the electromagnetic field strength is $\alpha = \mathrm{e}V_{\mathrm{MW}}/hf$ [286, 287]. In this framework, the adiabatic current is given by $I_{\mathrm{ad.}} = \sum_n J_0(2n\alpha)I_n(\varphi)$, where J_0 is a Bessel function of the first kind and $I_n(\varphi)$ are the experimentally-determined harmonics of the CPR at equilibrium [286]. A fit with α as the sole free parameter describes the data well (solid lines), with fitted values of α shown in Fig. 6.6(e). At $P = 0$ dBm we extract $\alpha_0 = 0.6$, significantly smaller than $\alpha_0 = 2.5$ obtained for $f_3 = 9.20$ GHz from Fig. 6.4(c) (see Section 6.5). This indicates that the coupling strength of the microwave field to the ABSs in the SNS junction, which is the parameter controlling the formation of FASs, is much smaller than that extracted from spectral replicas. This discrepancy is fully consistent with a PAT origin of spectral replicas, not linked to processes taking place in the SNS junction.

The adiabatic theory describes the data well up to an applied power of $P \sim 5$ dBm, corresponding to $\alpha \sim 0.6$. For larger P, the adiabatic model still captures the CPR envelope, but does not account for dips in the CPR appearing at specific values of $B_\perp$ [arrows in Fig. 6.6(d)]. Supercurrent dips are explained by non-equilibrium ABS occupation due to absorption or emission of microwave photons [286, 288, 289]. Transitions occur when an integer multiple of the photon energy hf matches the separation between two ABSs or between an ABS and the continuum. Once a transition occurs across the gap, the newly occupied ABS contributes to the total supercurrent with opposite sign with respect to the ground state, resulting in a dip in the CPR. Dips are resolved in the CPR for $\alpha > 0.6$, consistent with a model of non-equilibrium ABS distribution in a JJ containing highly-transmissive modes (see Section 6.7). Therefore, the dominant effects on the CPR in our devices are an adiabatic modulation of the phase and a non-equilibrium distribution function of ABS occupation, up to $\alpha \gtrsim 1$. It is possible that supercurrent signatures of FASs would emerge for larger microwave powers, but conductance features would be masked by the much stronger PAT effects.

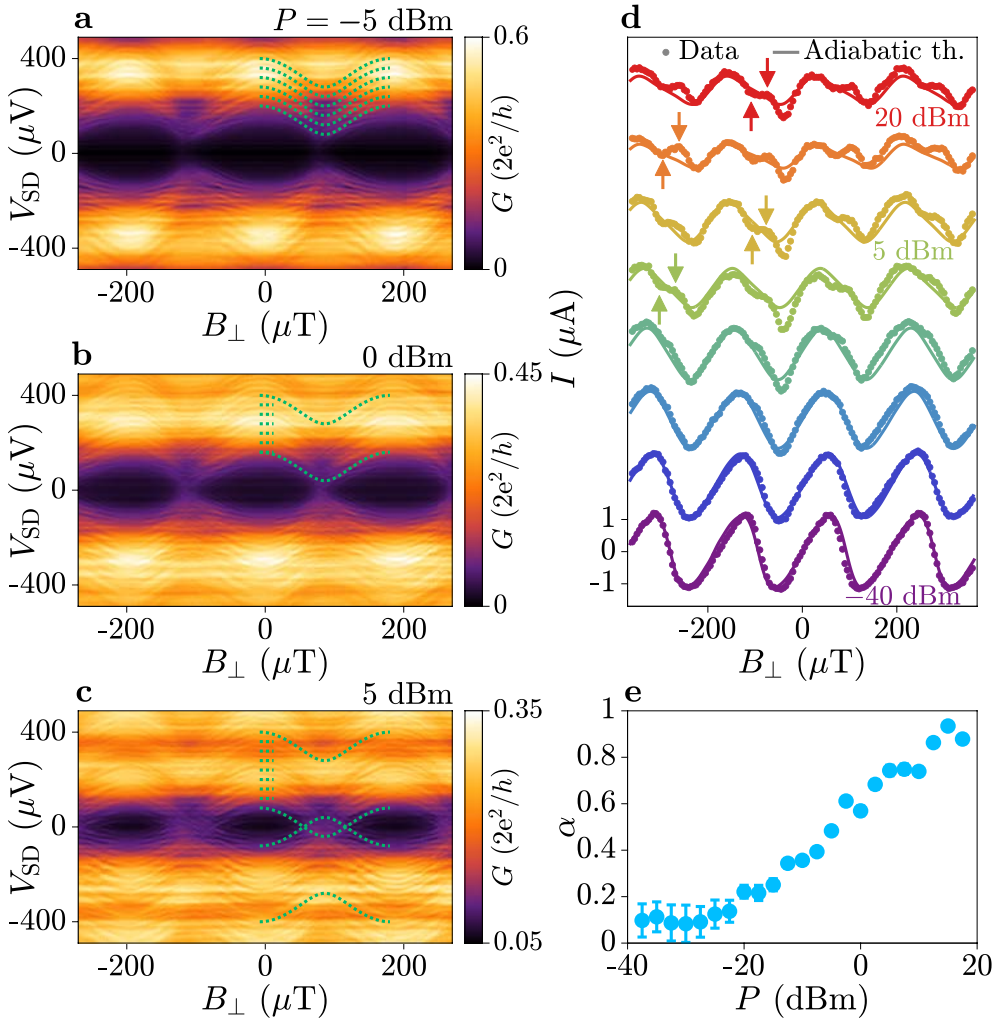

Figure 6.6. Phase-dependent measurements under microwave irradiation. **a** Tunnelling conductance as a function of perpendicular magnetic field $B_\perp$ for microwave irradiation with frequency $f = 9.20$ GHz and power $P = -5$ dBm. Green dashed lines mark bound state replicas with effective transmission $\bar{\tau} = 0.84$. **b, c** Same as (a) for $P = 0$ dBm and $P = 5$ dBm, respectively. **d** Current-phase relation as a function of microwave power (circles) fitted with an adiabatic theory (lines). Traces are successively offset by 2.05 μA. Deviations of the data from the adiabatic theory at high power are marked with arrows. **e** Microwave field strength α obtained from the adiabatic theory fit presented in (d).

6.4. Conclusions

In summary, conductance replicas were realised in a hybrid Josephson junction with highly transmissive ABSs under microwave irradiation. Conductance replicas also obeyed a sum rule, consistent with both FAS and PAT interpretations. By performing additional tests, conductance replicas in our devices were shown to be inconsistent with FASs and instead caused by PAT, an effect not considered in Ref. [114]. First, the power dependence of conductance replicas was identical to that of Shapiro steps in the tunnelling junction, whereas a difference is expected for FASs. Second, the coupling strength α associated with conductance replicas was significantly larger than that associated with ABSs in the SNS junction and measured via switching currents, but should be equal in the case of FASs. Third, the coupling strength was independent on the Fermi velocity, inconsistent with the linear dependence predicted for FASs. Fourth, conductance replicas brought to zero energy crossed each other, while anti-crossing is expected for FASs.

Complementary measurements of the current-phase relation of the Josephson junction are consistent with an interaction between ABSs and the microwave field mediated by the superconducting phase difference, without the need to invoke FASs. The weak coupling of the microwave field to ABSs is presumably due to the use of an off-chip microwave antenna, which predominantly interacts with the device via the large leads. Future work can engineer more efficient coupling schemes, for example by applying local microwave signals via gate electrodes [76], enabling stronger interaction with ABSs while limiting heating in the setup.

Our results show that caution should be used to attribute replicas in the tunnelling conductance to the presence of Floquet states in hybrid Josephson junctions. However, the techniques outlined here constitute a baseline to evaluate the effect of light-matter interaction in nanoscale devices, as they give distinct signatures for FASs and PAT, and can be applied in generic cases.

6.5. Supporting Information: Modelling of Conductance Replicas by Photon Assisted Tunnelling

6.5.1. Microwave Field Strength from Shapiro Steps

The conductance of replicas appearing under microwave irradiation depends on the applied power P. We first consider the power dependence of Shapiro steps close to $V_{\mathrm{SD}} = 0$ [see blue dotted lines in Figs. 6.3(c, f)]. Conductance peaks occurred when the source-drain bias V_{SD} was equal to the Josephson voltage $V_{\mathrm{J}} = nhf/2\mathrm{e}$, where n is an integer denoting the order of the Shapiro step. The conductance of the n^{th} Shapiro step is proportional to the n^{th}-order Bessel function of the first kind, $J_n(2\mathrm{e}V_{\mathrm{MW}}/hf)$, where V_{MW} is the amplitude of the oscillating voltage due to the applied microwave signal. This corresponds to the most likely number of photons absorbed in the system. This scales linearly with n, such that there is an almost exact correspondence between V_{MW} and the V_{SD} at which the highest conductance peak occurs. The applied microwave signal is given as a power P in units of dBm. We therefore express the oscillating voltage at the sample as $V_{\mathrm{MW}} = V_0 \cdot 10^{P/20}$, where V_0 contains the output voltage, device-antenna coupling and coaxial line attenuation of 47 dB. In dimensionless units, the coupling strength to the microwave field is therefore defined as $\alpha \equiv \mathrm{e}V_{\mathrm{MW}}/hf = (\mathrm{e}/hf)V_0 \cdot 10^{P/20}$.

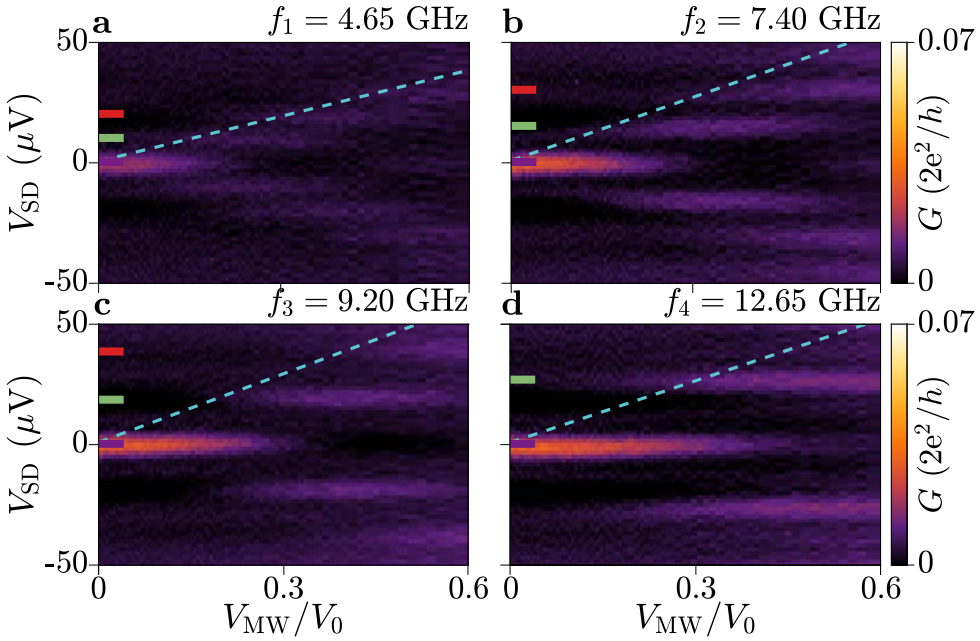

Figure 6.7. Microwave field strength from Shapiro steps. Conductance of Figs. 6.3(b, c) and 6.4(b, c), plotted as a function of microwave field strength $V_{\mathrm{MW}}/V_0 = 10^{P/20}$. Shapiro steps at $V_{\mathrm{SD}} = nhf/2\mathrm{e}$ are indicated by the coloured bars. Blue dashed lines indicate V_0, as calculated from a fit.

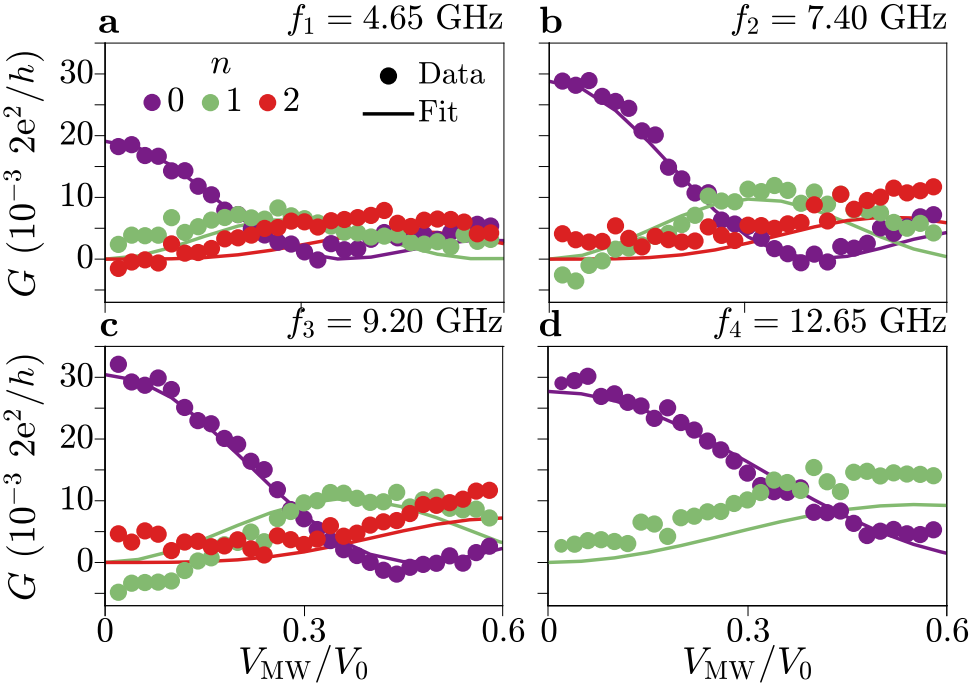

Figure 6.8. Extracting the microwave coupling strength from the Shapiro steps. Linecuts of conductance in Fig. 6.7 at bias values corresponding to the $n = 0,\ 1,\ 2$ order Shapiro steps (circles). Fit to the conductance (lines) to obtain the parameter V_0.

The Shapiro steps in the closed regime [Figs. 6.3(b, c) and 6.4(b, c)] are plotted in Fig. 6.7 as a function of microwave field strength V_{MW}/V_0. The emergence of the n^{th} Shapiro step scales linearly with V_{MW} as indicated by the blue dashed lines, the gradient of which is given by V_0. Linecuts of the $n = 0$, 1, and 2 Shapiro steps are plotted in Fig. 6.8 as the purple, green and red circles, respectively. The plotted data is sampled from the raw data at intervals $\Delta V_{\mathrm{MW}}/V_0 = 0.02$, to have a regular separation of datapoints. Due to the weak coupling between the probe and device, the conductance of the n^{th} Shapiro step, $G_n(V_{\mathrm{MW}}) \equiv G(V_{\mathrm{SD}} = nhf/2\mathrm{e},\ V_{\mathrm{MW}})$, is fitted with a squared Bessel function of the form [147, 201, 206, 207, 219]

$$G_n(V_{\mathrm{MW}}) = G_n(V_{\mathrm{MW}} = 0)\left[J_n\left(\frac{2\mathrm{e}}{hf}V_{\mathrm{MW}}\right)\right]^2 = G_n(V_{\mathrm{MW}} = 0)\left[J_n\left(\frac{2\mathrm{e}}{hf}V_0 \cdot 10^{P/20}\right)\right]^2, \tag{6.1}$$

with $G_n(V_{\mathrm{MW}} = 0)$ the conductance at bias $V_{\mathrm{SD}} = nhf/2\mathrm{e}$ with no microwaves applied. The fit with the free parameter V_0 returns $V_0 = \{64,\ 91,\ 96,\ 87\}$ μV and is plotted as the lines in Fig. 6.8 for frequencies f_1 to f_4, respectively. The corresponding dimensionless microwave field strengths are $\alpha_0 = \{3.3,\ 3.0,\ 2.5,\ 1.7\}$.

6.5.2. Modelling of Photon Assisted Tunnelling Data

Figures 6.9(a–d) show the conductance maps of Figs. 6.3(b, c) and 6.4(b, c) plotted as a function of microwave field strength V_{MW}/V_0. Conductance replicas emerge linearly with increasing microwave field strength. The experimental data is simulated using a model for photon assisted tunnelling, based on the coupling parameters V_0 obtained from the Shapiro steps (see Fig. 6.8). The n^{th}-order conductance replicas are expected to scale as a squared Bessel function [147, 201, 206, 207, 219]

$$G_n\left(V_{\mathrm{MW}},\ V_{\mathrm{SD}}+n\frac{hf}{\mathrm{e}}\right)=G\left(V_{\mathrm{MW}}=0,\ V_{\mathrm{SD}}+n\frac{hf}{\mathrm{e}}\right)\left[J_n\left(\frac{\mathrm{e}V_{\mathrm{MW}}}{hf}\right)\right]^2. \tag{6.2}$$

Using the experimentally measured conductance with no applied microwaves, $G(V_{\mathrm{MW}}=0,\ V_{\mathrm{SD}})$, the conductance at each V_{MW} was calculated by summing the contributions from N replicas

$$G(V_{\mathrm{MW}},\ V_{\mathrm{SD}})=\sum_{n=-N}^{N}G_n\left(V_{\mathrm{MW}},\ V_{\mathrm{SD}}\right), \tag{6.3}$$

where $N=(1\ \mathrm{mV})\cdot \mathrm{e}/hf$ was chosen to consider conductance replicas emerging across the full range of measured source-drain bias. The simulated conductance is plotted in Figs. 6.9(e–h) as a function of microwave field strength V_{MW}/V_0, using the values of V_0 obtained from the Shapiro steps at each frequency. The replication of conductance features is well described by the simulation, up to the highest measured microwave field, in terms of the number of replicas, their dependence on microwave field strength and the absolute value of their conductance. Some discrepancy at large V_{MW}/V_0 can be attributed to a background conductance in the measurement data, potentially due to device heating which is not accounted for in the simulation.

Figure 6.10 shows the conductance of replica peaks at fixed bias V_{SD} as a function of applied power P, up to the seventh replica (circles, replica number indicated by the colour). Data is plotted for frequencies $f_1=4.65$ GHz, $f_2=7.40$ GHz and $f_4=12.65$ GHz, since the equivalent data for $f_3=9.20$ GHz is plotted in Fig. 6.5(c). The simulated conductance at the same bias is plotted as the shaded lines, and matches the data for low and intermediate powers $P\lesssim 10$ dBm. Data is plotted for $P\gtrsim -20$ dBm to better highlight the power dependence, since only small changes in conductance were observed in the range $-40\ \mathrm{dBm}<P\lesssim -20$ dBm.

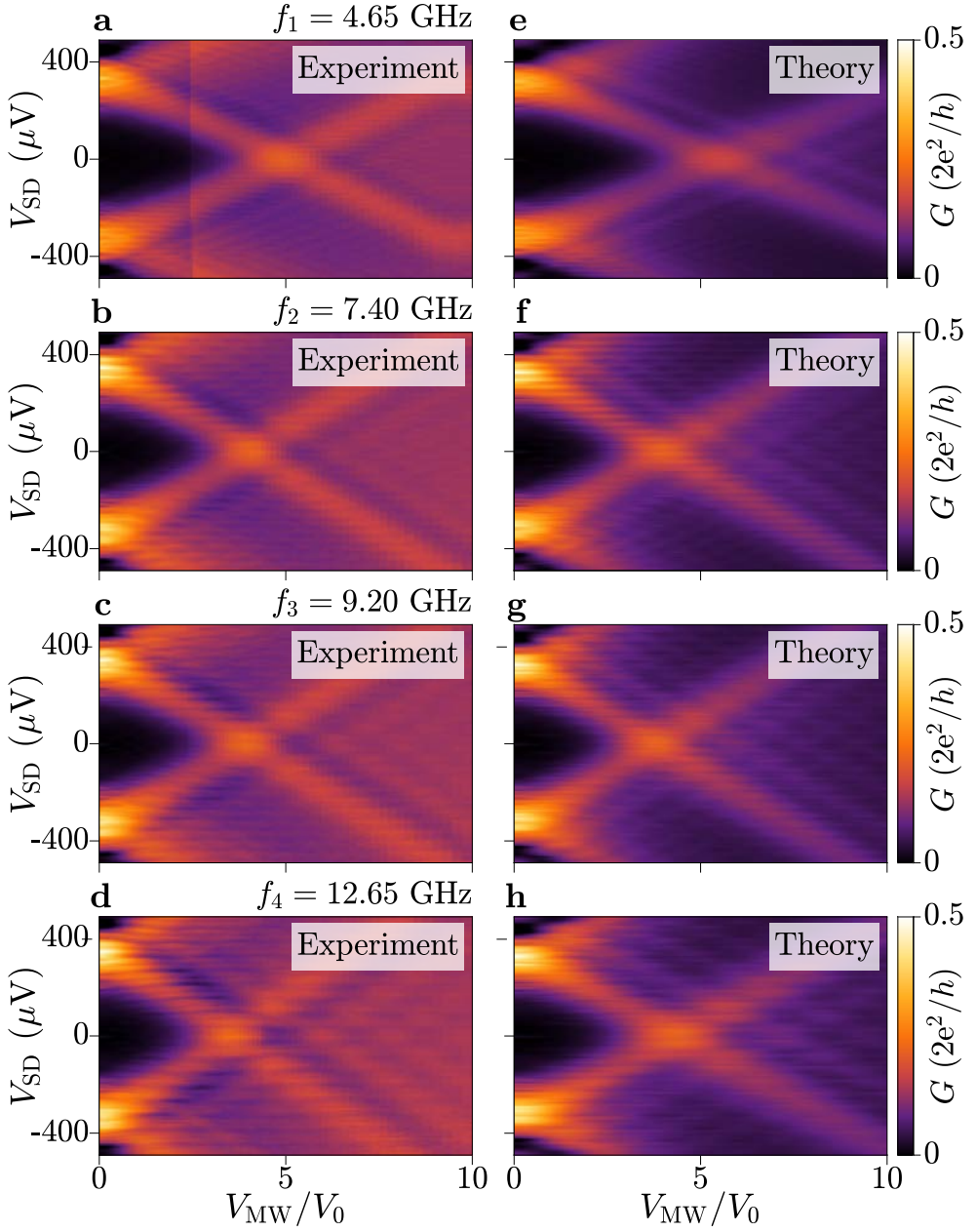

Figure 6.9. Experimental and simulated conductance replicas as a function of microwave field strength. **a–d** Differential conductance of Figs. 6.3(b, c) and 6.4(b, c), plotted as a function of microwave field strength $V_{MW}/V_0 = 10^{P/20}$. **e–h** Simulated conductance features as a function of microwave field strength, using the coupling parameters V_0 obtained in Fig. 6.8 and the measured conductance in the absence of microwave irradiation.

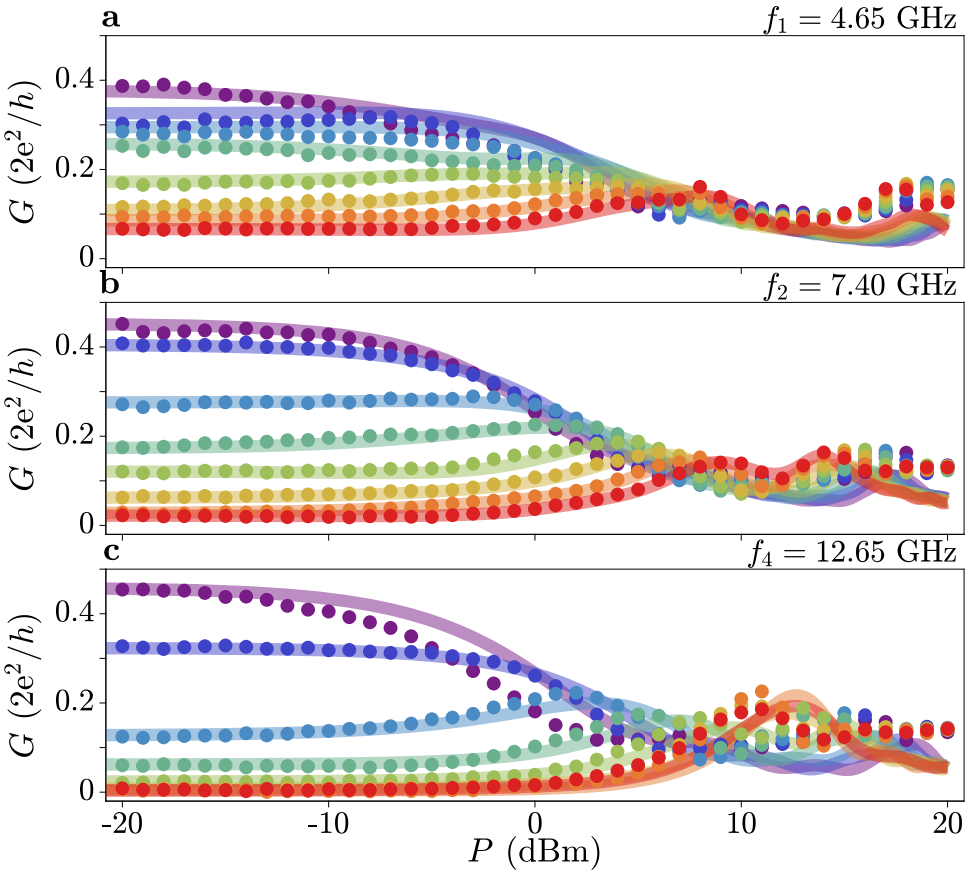

Figure 6.10. Power dependence of conductance replicas. Conductance of the first seven replica peaks in Figs. 6.3(b, c) and 6.4(c) (circles), respectively. Colours denote the order n of the replica. Plotted alongside simulated conductance from Fig. 6.9 (lines), as a function of applied microwave power P.

6.5.3. Removal of Background Conductance

The conductance maps in Figs. 6.3 and 6.4 show the complete response of the system to a microwave drive of increasing power. Figure 6.11 shows a slowly-varying background conductance G_{bg}, obtained by averaging the conductance trace at each power P over a bias window of 70 μV. Dashed lines show the dependence of high conductance features on power P, with the relation $V_{\mathrm{MW}} = V_0 \cdot 10^{P/20}$ for values of V_0 calculated from the Shapiro steps (see Fig. 6.8).

Conductance replicas were isolated by subtracting the slowly-varying background, $G - G_{\mathrm{bg}}$ (see Fig. 6.12). The linecuts in Fig. 6.5(a) were taken at powers $P = 1.5$, 4.5, 4 and 4.5 dBm from Fig. 6.12 respectively, such that multiple conductance replicas were visible. The separation between conductance features ΔV_{SD} shown in Fig. 6.5(b) was calculated by taking the average conductance peak separation across the full power range displayed in Fig. 6.12.

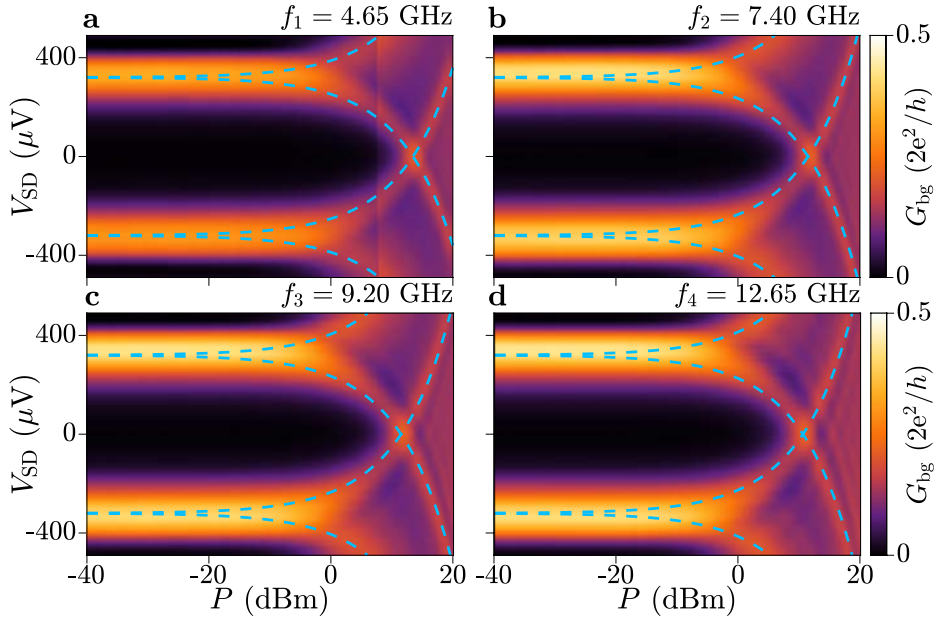

Figure 6.11. Slowly-varying background of conductance data. Power dependence of Figs. 6.3 and 6.4, averaged at each power across a bias voltage window $V_{\text{window}} = 70\ \mu\text{V}$. Dashed lines indicate the power dependence of high conductance features.

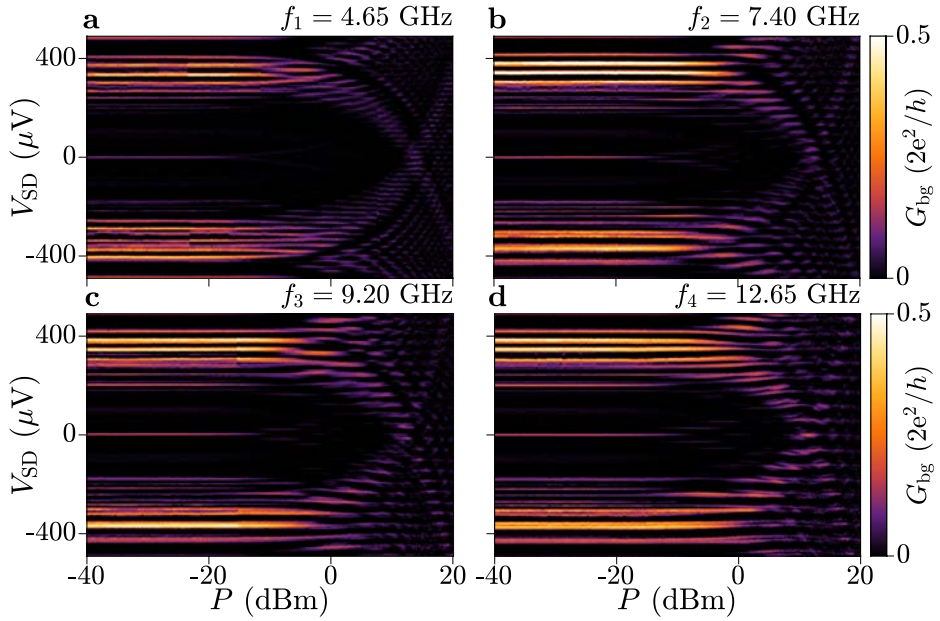

Figure 6.12. Bias spectroscopy after the removal of a slowly-varying background. Power dependence of Figs. 6.3 and 6.4, with the averaged background removed $G - G_{\text{bg}}$.

The background conductance contained features from the complex ABS spectrum at low power. Multiple high-conductance lines were visible, in both the background conductance and the difference, due to replication of different features in the low-power conductance map. Such conductance features could include sub-gap ABSs at $V_{SD} = \pm(\Delta + E_A)/e$ and the superconducting gap at $V_{SD} = 2\Delta/e$.

6.5.4. Sum Rule for Conductance Replicas

Reference [114] described the importance of a sum rule for conductance replicas to support their interpretation of Floquet-Andreev states emerging under microwave irradiation. The sum rule brought forward in Ref. [114] states that the sum of conductance over source-drain bias should be constant as a function of power, independent of the emergence of conductance replicas. This is expressed by the equation $S = \int_0^{\pm\infty}(\mathrm{d}I/\mathrm{d}V)\mathrm{d}V$, which is equivalent to a numerical integral of the experimental data. We applied the same technique to the results shown in Figs. 6.3(b, c) and 6.4(b, c) [see Fig. 6.13, data of Fig. 6.13(c) also plotted in inset of Fig. 6.5(c)]. The sum S was calculated for each value of applied power P by numerical integration of the differential conductance $G \equiv \mathrm{d}I/\mathrm{d}V$ over positive (negative) bias values, indicated by the coloured (grey) circles (left axis).

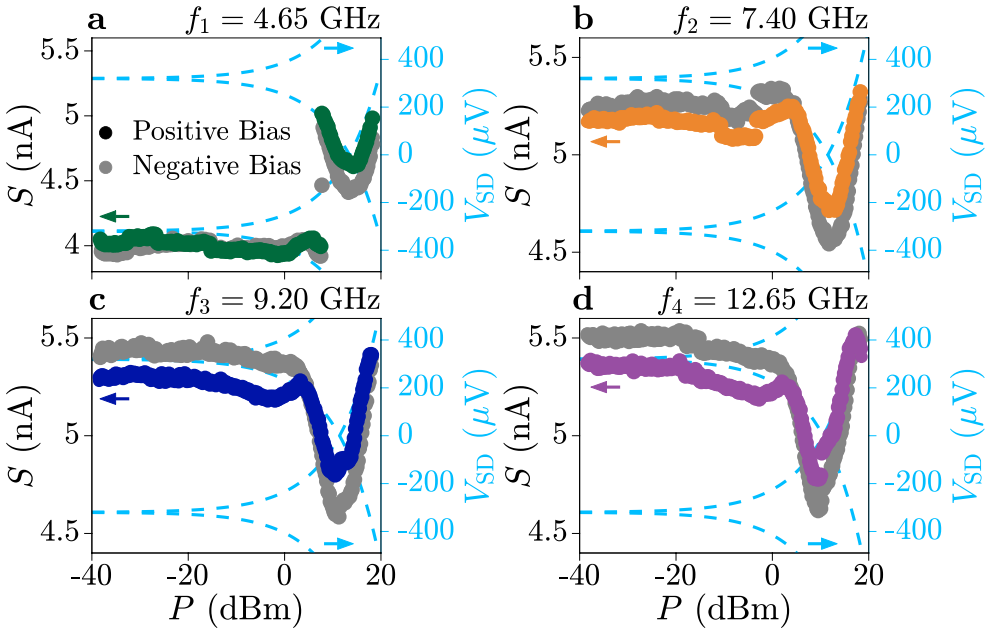

Figure 6.13. Sum of conductance replicas under microwave irradiation of different frequencies. (Left axis) Sum of conductance over bias, S, as a function of power P for the data in Figs. 6.3(b, c) and 6.4(b, c), respectively. Frequencies f_i correspond to those of Figs. 6.3 and 6.4, where colours are defined. Coloured (grey) circles correspond to a sum over positive (negative) bias, $V_{SD} > 0$ ($V_{SD} < 0$). (Right axis) Dashed lines indicate the power dependence of conductance replicas, identical to Fig. 6.11.

Dashed lines in Fig. 6.13 indicate the power dependence of high conductance features, as a function of bias V_{SD} (right axis). The power dependence is identical to those shown in Fig. 6.11. The sum S was approximately constant as a function of power up to $P \approx 5$ dBm. For $P \gtrapprox 5$ dBm, high conductance features were outside of the measurement range $-490\ \mu\mathrm{V} < V_{\mathrm{SD}} < 490\ \mu\mathrm{V}$. The change in S was therefore consistent with conductance replicas exiting the measurement range, such that they were not included in S. The constant S at low power is consistent with our conclusion that PAT was the dominant mechanism for conductance replicas, since it represents conservation of the number of states in the tunnel barrier and the junction. Equivalently, using Eq. 6.2 we see that $S \propto \sum_n |J_n(x)|^2$ which is constant for a sum over all n. Hence, the total tunnel current through the barrier is constant as a function of power.

6.5.5. Microwave Coupling Strength from High-Bias Conductance

The coupling strength to the microwave field was calculated from the Shapiro steps in Figs. 6.7 and 6.8. We complement these values with calculations of the coupling strength directly from conductance features at high source-drain bias V_{SD}. First, the background conductance (see Fig. 6.11) was fitted with a Gaussian function for each value of power P, or equivalently each value of microwave field amplitude V_{MW}. Thus, values for the conductance peak position $V_{\mathrm{p}}(V_{\mathrm{MW}})$ and standard deviation $\sigma(V_{\mathrm{MW}})$ were obtained as a function of V_{MW}. Then, the conductance peak position was fitted with a linear curve to obtain V_0. The values $V_{\mathrm{p}}(V_{\mathrm{MW}})$ included in the fit were weighted by the standard deviations $\sigma(V_{\mathrm{MW}})$. This method produced a value of V_0 for each microwave frequency f, along with an error δV_0 describing the uncertainty of the coupling strength to describe the data given the standard deviation σ. The obtained values are displayed in Table 6.1. The standard deviation of the conductance peak was $60 < \sigma < 75\ \mu$V for all datasets.

f (GHz)	4.65	7.20	9.40	12.65
V_0 (μV)	83.7 ± 0.4	97.6 ± 1.5	99.5 ± 1.7	100.6 ± 2.9
α_0	4.35 ± 0.02	3.19 ± 0.05	2.62 ± 0.04	1.92 ± 0.06

Table 6.1. Microwave coupling strength obtained from high-bias conductance replicas at $V_{\mathrm{TG}} = -0.8$ V.

6.6. Supporting Information: Gate Dependence of Microwave Coupling Strength

Replicas in the conductance spectrum shown in Figs. 6.3 and 6.4 were obtained at $V_{\mathrm{TG}} = -0.8$ V. Here we show measurements on the same device at $V_{\mathrm{TG}} = -1.4$ V. Figure 6.14 shows bias spectroscopy as a function of applied microwave power, for tunnel-gate voltages $V_{\mathrm{T}} = -2.1$ V. On increasing applied microwave power, conductance replicas emerged at high bias with separation $\Delta V_{\mathrm{SD}} = hf/\mathrm{e}$. Measurements were

performed for different values of V_T (see Appendix E), and conductance replicas at high and low bias were seen in all cases. The mean separation of low and high bias replicas are displayed as filled grey squares and circles in Fig. 6.5(b), respectively. The bias separation of conductance replicas was consistent with $\Delta V_{SD} = hf/q$, where q is the charge tunnelling across the barrier. Concurrent replicas in low and high bias features indicated PAT as the dominant mechanism.

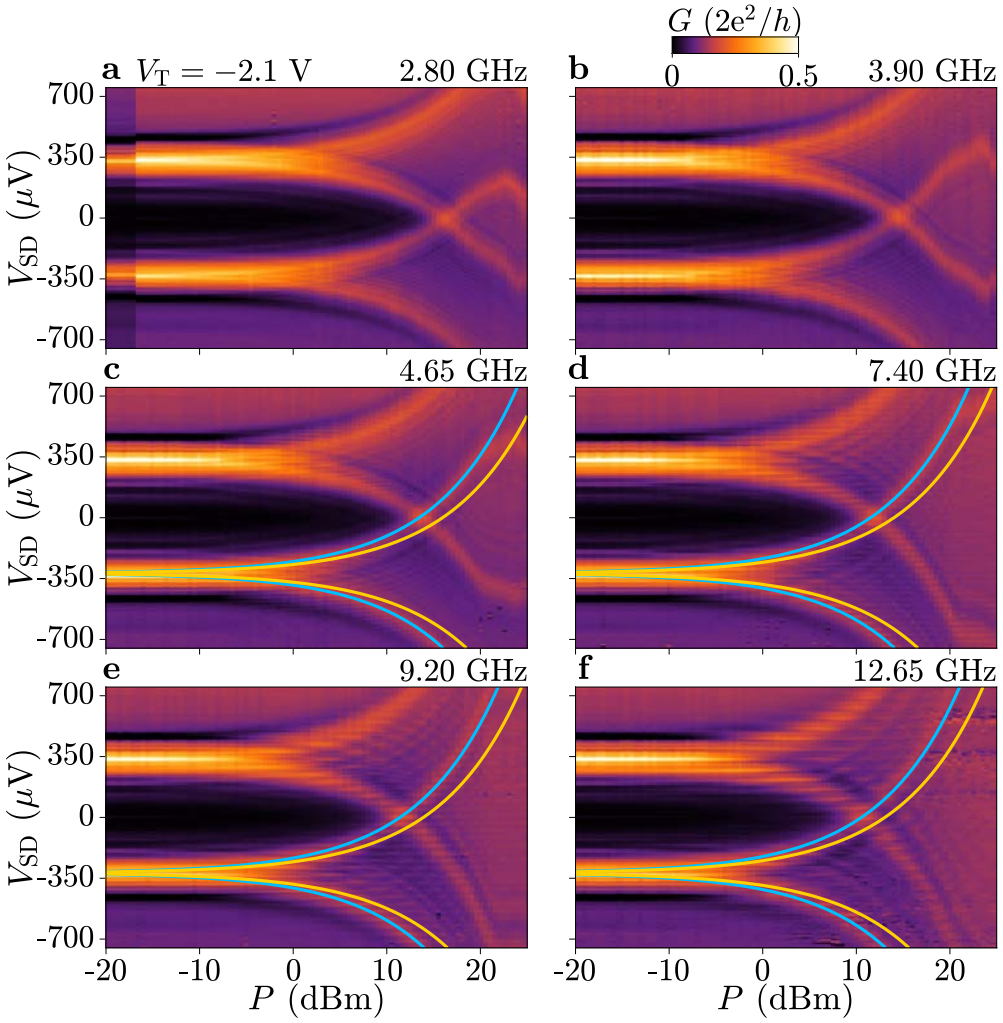

Figure 6.14. Power dependence at $V_{TG} = -1.4$ V and $V_T = -2.1$ V. Conductance G as a function of source-drain bias V_{SD} and power P, for frequencies $f = \{2.80,\ 3.90,\ 4.65,\ 7.40,\ 9.20,\ 12.65\}$ GHz. Mean separation of replicated conductance features is shown in the Fig. 6.5(b) (full grey circles). Power dependence of conductance replicas obtained for $V_{TG} = -0.8$ V (blue lines, identical to Fig. 6.11) is plotted in (c–f), alongside the expectation for a 25% decrease in coupling strength due to smaller Fermi velocity (yellow lines).

The coupling strength to the microwave field is calculated for this V_{TG} value from conductance features at high source-drain bias in Fig. 6.14, using the same procedure as outlined in the previous section. The obtained values are displayed in Table 6.2. As for the data taken at $V_{\mathrm{TG}} = -0.8$ V, the standard deviation of the conductance peak was $60 < \sigma < 75$ μV for all datasets.

f (GHz)	4.65	7.20	9.40	12.65
V_0 (μV)	80.6 ± 2.3	100.2 ± 2.6	99.1 ± 2.7	96.0 ± 2.3
α_0	4.19 ± 0.12	3.27 ± 0.08	2.60 ± 0.07	1.84 ± 0.04
$\Delta\alpha_0$	-0.16 ± 0.12	0.08 ± 0.09	-0.02 ± 0.08	0.08 ± 0.07

Table 6.2. Microwave coupling strength obtained from high-bias conductance replicas at $V_{\mathrm{TG}} = -1.4$ V.

The values for α_0 at $V_{\mathrm{TG}} = -1.4$ V show remarkable agreement with those at -0.8 V [see blue lines in Figs. 6.14(c–f)]. The change in coupling strength as a result of the more negative V_{TG} is quantified by $\Delta\alpha_0 \equiv \alpha_0(V_{\mathrm{TG}} = -0.8) - \alpha_0(V_{\mathrm{TG}} = -1.4)$, displayed as the final row in Table 6.2. Uncertainties are calculated from the sum over variances of each α_0 value. These results show that the change in coupling strength as a result of the more negative gate voltage was at most 4%.

The carrier density in the SNS junction is expected to change as a function of V_{TG}. The maximum switching current I_0 of Device 1 is plotted in Fig. 6.15(a) as a function of V_{TG}. Data points corresponding to $V_{\mathrm{TG}} = -0.8$ V and -1.4 V are indicated by dashed lines, and show that I_0 at $V_{\mathrm{TG}} = -1.4$ V was $\sim 25\%$ the value at $V_{\mathrm{TG}} = -0.8$ V. The change in maximum switching current was $\Delta I_0 \approx 0.8$ μA. At $V_{\mathrm{TG}} = -0.8$ V, I_0 reached a peak after a linear increase from the most negative V_{TG} values. We associate this linear regime to the trend in electron mobility μ for increasing occupation of the first subband in the semiconductor. Gated Hall bar measurements in the same material are shown in Fig. 6.15(b). The density n and mobility μ are plotted as a function of the gate voltage V_{G}. The gate lever arm was different in the Hall bar and SNS junction due to different fabrication processes for each chip. Therefore, we estimate the change in density from the range of single subband occupation, where the mobility μ increased linearly with n. The carrier density at peak μ was compared to that where the mobility was 25% above its lowest measured value. This was chosen to approximately correspond to the I_0 value at $V_{\mathrm{TG}} = -1.4$ V relative to $V_{\mathrm{TG}} = -0.8$ V. This gave an approximate change in carrier density of $\Delta n \approx 0.5 \cdot 10^{12}$ cm^{-2}, or $\Delta n/n \approx 0.5$. We therefore estimate a 25% decrease in the Fermi velocity for $V_{\mathrm{TG}} = -1.4$ V relative to $V_{\mathrm{TG}} = -0.8$ V. While this value is an approximation, the large change in I_0 is indicative of an appreciable change in the carrier density.

From the theory of Floquet-Andreev states [114], a 25% decrease in the Fermi velocity would correspond to a 25% decrease in the microwave coupling strength α_0. This is plotted as the yellow lines in Figs. 6.14(c–f), and does not match the experimental result. To be consistent with a Floquet-Andreev interpretation, calculated values of $\Delta\alpha_0$ imply

a change in the Fermi velocity of less that 4%, incompatible with switching current and Hall bar measurements, or an alternative mechanism which almost exactly compensates for the change in carrier density. In contrast, no gate dependence is expected in the PAT interpretation. This further supports PAT as the dominant mechanism for conductance replicas.

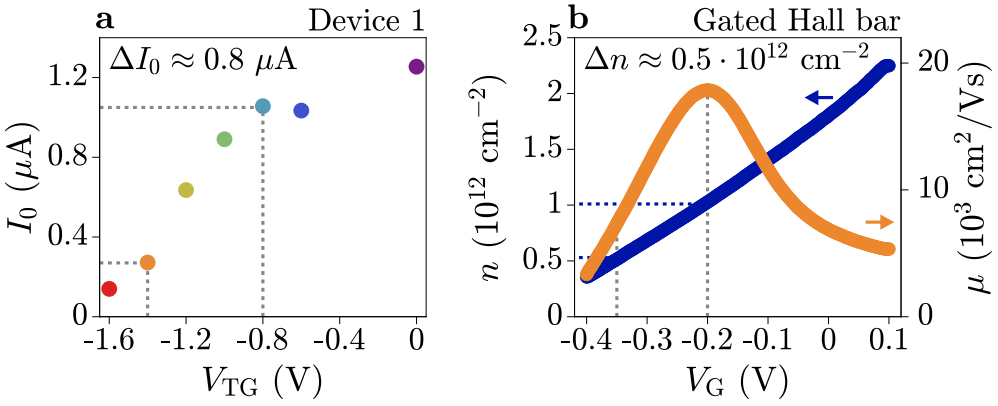

Figure 6.15. Estimating the change in carrier density as a function of V_{TG}. a Maximum switching current I_0 in Device 1 as a function of top-gate voltage V_{TG}. Data points at $V_{TG} = -0.8$ V and -1.4 V are indicated by dashed lines, corresponding to a difference $\Delta I_0 \approx 0.8\ \mu$A. **b** Measurements of a gated Hall bar in the same material. Carrier density n (blue, left axis) and mobility μ (orange, right axis) are plotted as a function of the global gate voltage V_G. Dashed lines indicate the estimated change in carrier density as $\Delta n \approx 0.5 \cdot 10^{12}$ cm^{-2}.

6.7. Supporting Information: Modelling Distortions to the Current-Phase Relation

6.7.1. Switching Current of the Planar SQUID

The switching current of the planar SQUID is shown in Fig. 6.16(a), for increasing microwave power P. At low power (purple circles), oscillations with a period of $B_{\text{Period}} \approx 200\ \mu$T and peak-to-peak amplitude of 2 μA were observed, on top of a constant background of 36 μA. For increasing applied power, the amplitude of the oscillations decreased and their shape was distorted, while the background switching current decreased and developed a pronounced minimum close to $B_\perp = 0$. The decrease in the switching current of the constriction under microwave irradiation is assigned to pair-breaking in the Al by photon absorption, which may also account for the enhanced switching current suppression close to $B_\perp = 0$ by quasiparticle generation in the constriction and the superconducting leads [290].

The CPR of the SNS junction was obtained by subtracting the switching current of the constriction, as shown in Fig. 6.16(b) for $P = -40$ dBm (purple circles). The switching

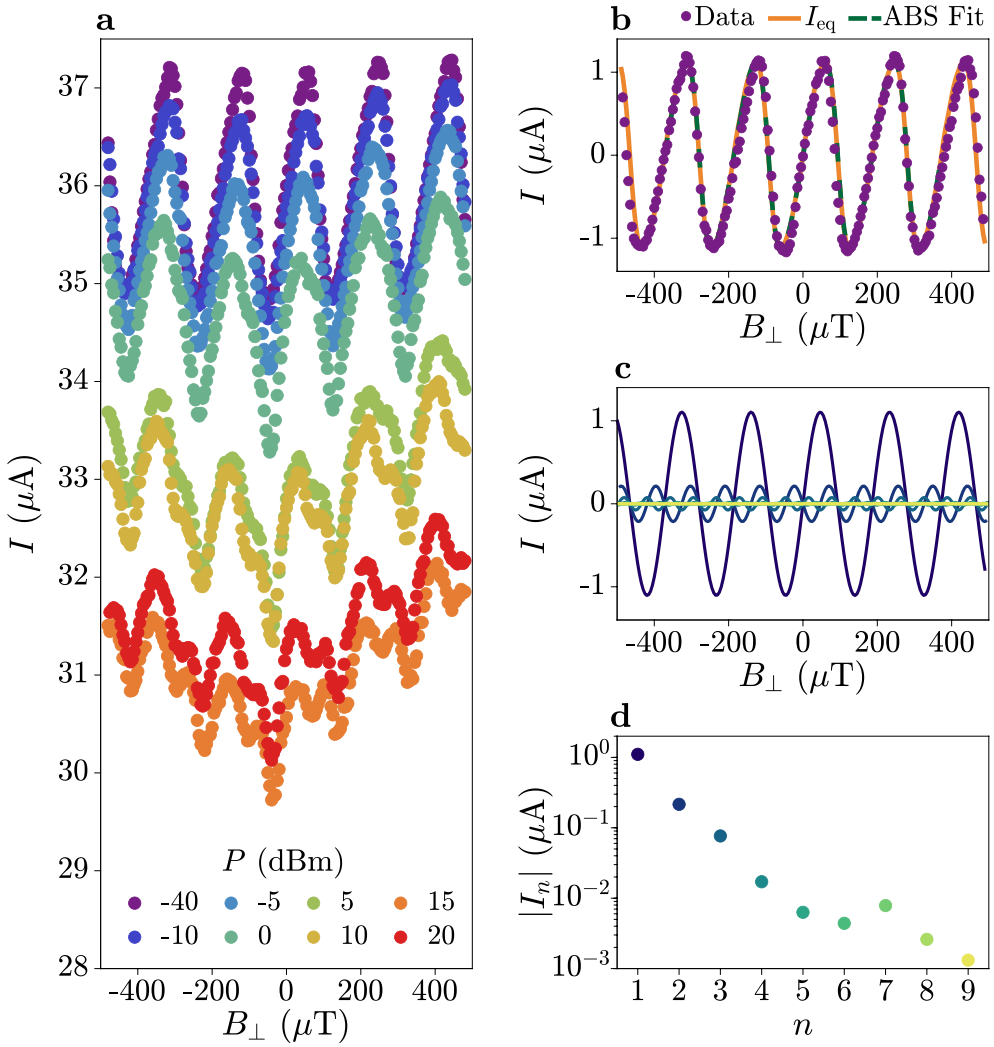

Figure 6.16. Current-phase relation under microwave irradiation at $f = 9.20$ GHz. **a** Switching current I of the planar SQUID as a function of $B_\perp$, as a function of power P. **b** CPR data at $P = -40$ dBm, after subtraction of background current corresponding to Al constriction (circles). Equilibrium current I_{eq} determined from harmonics I_n up to tenth order (orange line). Fit to CPR using Eq. 6.5 (green dashed line), giving an effective transmission of $\bar{\tau} = 0.84$. **c** Harmonics $I_n \sin(n\varphi)$ extracted from the CPR up to the tenth order. Colours are defined in (d). **d** Absolute amplitude $|I_n|$ of the harmonics plotted in (c).

current of the constriction was found by a polynomial fit to the data across six full periods, such that the resulting CPR amplitude was over all periods and the integral of the CPR was zero over a full period. The microwave field did not affect the switching current at this low power, so the CPR is considered to be at equilibrium. We described the data by extracting the harmonics up to the 10^{th} order, using the equation

$$I_{\mathrm{eq}} = \sum_n I_n \sin(n\varphi), \tag{6.4}$$

where $I_n = (1/\pi)\int_0^{2\pi} I_{\mathrm{eq}} \sin(n\varphi)\mathrm{d}\varphi$.

The equilibrium supercurrent is plotted as the orange line in Fig. 6.16(b), composed of the harmonics in Fig. 6.16(c) with amplitudes $|I_n|$ plotted in Fig. 6.16(d). The presence of $n > 1$ terms, which gives the forward skewness of the CPR, is indicative of the presence of highly transmissive ABSs in the junction [107, 153, 171]. Since these ABSs carry the supercurrent, the CPR is described in terms of the ABS properties. However, the junction contained many modes, each with a distinct transmission τ, which all contribute to the supercurrent. It was not feasible to assign a transparency to each individual mode, so we instead considered a junction where all modes have an equal effective transmission $\bar{\tau}$. This describes the macroscopic properties of the junction, but does not capture details of the individual microscopic states. The CPR was then described by

$$I_{\mathrm{ABS}} = I_{\mathrm{N}} \frac{\bar{\tau}\sin(\varphi)}{E_{\mathrm{A}}(\varphi)/\Delta}, \tag{6.5}$$

where $E_{\mathrm{A}} = \Delta\sqrt{1 - \bar{\tau}\sin^2(\varphi/2)}$ is the ABS energy and $I_{\mathrm{N}} = (\mathrm{e}/2\hbar)\bar{N}\Delta$, where $\bar{N}$ is the effective number of modes in the junction. A fit to the low power data gave $\bar{\tau} = 0.84$ [green dashed line in Fig. 6.16(b)], consistent with the presence of highly transmissive modes observed in tunnelling spectroscopy [see Fig. 6.2(d)].

6.7.2. Adiabatic Theory of the Current-Phase Relation under Microwave Irradiation

We use an adiabatic theory of an SNS junction under microwave irradiation to describe the CPR under increasing applied power [286, 287, 291]. A monochromatic drive at frequency f generates a time-varying voltage $V(t) = V_{\mathrm{MW}}\sin(2\pi f t)$, resulting in a time-varying phase across the SNS junction of $\varphi(t) = \varphi_0 + 2\alpha\cos(2\pi f t)$. The electromagnetic field strength is described by the parameter $\alpha = \mathrm{e}V_{\mathrm{MW}}/hf$. In the adiabatic approximation, the stationary phase at equilibrium (Eq. 6.4) is replaced by the time-varying phase $\varphi(t)$. No excitation of ABSs is considered in this model. The resulting CPR is

$$I_{\mathrm{ad.}} = \sum_n I_n J_0(2n\alpha)\sin(n\varphi), \tag{6.6}$$

where J_0 is a zero-order Bessel function of the first kind and I_n are the harmonic coefficients obtained for the equilibrium CPR. The CPR traces under microwave irradiation were therefore fitted with α as a single free parameter, using the I_n shown in Fig. 6.16(d). The results of the fit are shown in Fig. 6.6(e).

6.7.3. Non-Thermal ABS Occupation

Analysis in the following subsection, Section 6.7.3, was performed by Juan Carlos Cuevas with input from D.Z.H.

At large applied microwave power, the measured CPR deviated from the fitted curve obtained from the adiabatic model. At some values of the perpendicular magnetic field $B_\perp$, corresponding to certain phase values φ, the measured switching current was closer to zero than expected from the adiabatic model. This is interpreted as a non-thermal occupation of ABSs in the SNS junction, due to excitations driven by the microwave field. A microwave photon can induce a transition when the excitation energy $2E_\mathrm{A}$ is an integer multiple of the photon energy hf. Since E_A depends on the phase difference φ, absorption is expected only at specific φ for a given frequency f. This is schematically shown in Fig. 6.17(a), for the case of $\tau = 0.84$. The current carried by an excited ABS is equal and opposite to that in the ground state, resulting in a suppression in the average measured current. For large drive powers, multi-photon processes are possible, and transitions can occur into or out of ABSs from the quasiparticle continuum. Excitation is most likely to occur close to $\varphi = \pi$, since this is where $2E_\mathrm{A}$ is smallest. This is particularly true for highly transmissive ABSs, where the separation of the ABS from the superconducting gap edge can be large. To describe the impact of these different microwave-induced transitions on the CPR, we employed the theory of Refs. [286, 288]. This theory, which is based on non-equilibrium Green's functions techniques, describes the CPR of a single channel superconducting point contact for arbitrary junction transparency (τ) and strength of the coupling between the microwave field and the Josephson current ($\alpha = \mathrm{e}V_\mathrm{MW}/hf$). Figure 6.17(b) shows the simulated CPR for microwave irradiation of $hf = 0.19\Delta$, corresponding to a frequency of 9.20 GHz, for increasing α up to 1. The full model (solid lines) deviates from the adiabatic theory (dashed lines) for $\alpha \gtrsim 0.6$, consistent with the experimental observation.

The simulated CPR considers transitions in a single mode of transmission $\tau = 0.84$, equal to the effective transmission of the junction. However, this does not consider the many modes present in the junction. Figure 6.17(c) shows a distribution of transmissions in an SNS junction with a disordered interface, following the relation $\rho(\tau) = 1/(\pi\tau^{3/2}\sqrt{1-\tau})$ [179]. The transmission distribution was chosen to give a CPR at equilibrium which matched the experimental result. The evolution of the CPR under microwave irradiation is shown in Fig. 6.17(d). The suppression in switching current is less pronounced than in the single mode case, but occurs across a wider range of φ. The experimental data shows strong suppression across a wide range of φ, suggesting that the SNS junction is between the two extremes outlined in Fig. 6.17. This is consistent with a junction containing many modes, some of which have a high transmission.

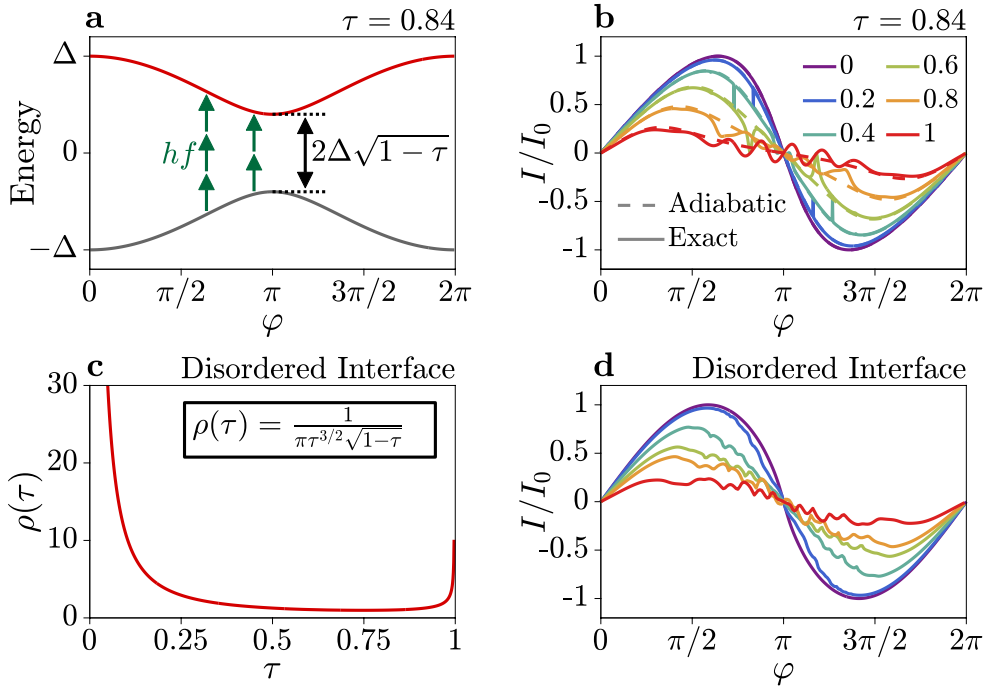

Figure 6.17. Non-thermal occupation of Andreev bound states (ABSs). **a** ABS spectrum for transmission $\tau = 0.84$. Transitions (green) from occupied (grey) to unoccupied (red) states can occur close to $\varphi = \pi$ by absorption of microwave photons with energy hf. **b** Normalised current-phase relation for transmission $\tau = 0.84$ under increasing microwave field amplitude α. Deviations of exact model (solid line) from adiabatic theory (dashed lines) occur at some values of φ due to non-thermal occupation. **c** Distribution of channel transmissions for a planar Josephson junction with a disordered interface. The transmission distribution follows the equation in inset [179]. **d** Normalised current-phase relation for a junction modelled with a disordered interface, under increasing microwave field amplitude α [colour defined in (b)]. Simulations presented in panels (b) and (d) were performed by Juan Carlos Cuevas.

7 Spectroscopy of Andreev Bound States Part II: Anomalous Phase Shifts

Josephson junctions (JJs) defined in hybrid superconductor-semiconductor materials gain additional functionalities due to the interplay between spin-orbit interaction and external magnetic fields. Tunnelling spectroscopy experiments of planar InAs/Al JJs have revealed the onset of zero-energy states at large in-plane magnetic fields [122, 123], and more refined devices [292] have since shown zero-energy states accompanied by closure and reopening of the superconducting gap, consistent with a topological transition. Supercurrent measurements in superconducting quantum interference devices (SQUIDs) demonstrated gate-tunable phase shifts in small magnetic fields [109], as well as large phase jumps at larger fields [124] accompanied by a minimum in the supercurrent amplitude, also consistent with a topological transition [120]. However, several questions remain on the behaviour of planar JJs subject to in-plane magnetic fields. For instance, Ref. [109] reported anomalous phase shifts at small magnetic fields which were considerably larger than theoretical expectations [229]. Additionally, orbital effects can resemble the behaviour expected from a topological transition [120, 293]: a magnetic flux threading the cross-section underneath the superconducting leads can produce non-monotonic switching currents [122, 197] together with closure and reopening of the induced superconducting gap.

In this chapter, we address these questions by presenting a comprehensive investigation of planar SQUIDs subject to in-plane magnetic fields, using a device which allowed simultaneous measurements of the Andreev bound state (ABS) spectrum of a planar JJ and its current-phase relation (CPR), including anomalous phase shifts relative to an absolute phase reference. The text and figures from this chapter have been adapted from Ref. [294].

This chapter is adapted from the following publication:

Zeeman- and Orbital-Driven Phase Shifts in Planar Josephson Junctions
D. Z. Haxell, M. Coraiola, D. Sabonis, M. Hinderling, S. C. ten Kate, E. Cheah, F. Krizek, R. Schott, W. Wegscheider, F. Nichele
ACS Nano **17**, 18139 (2023).

Author contributions: F.N. conceived the experiment. E.C., F.K., R.S., and W.W. performed the material synthesis and characterisation. D.Z.H. designed the devices, and F.N. gave contributions. D.Z.H. fabricated the devices, M.C. provided fabrication support. D.Z.H. performed the measurements, M.C. and F.N. provided measurement support. D.Z.H. analysed the data. M.C. extracted the Type A phase shifts from tunnelling spectroscopy (shown in Fig. 7.12). D.Z.H. interpreted the data, with support from M.C., D.S. and F.N., and with contributions from all authors. D.Z.H. wrote the manuscript with input from D.S. and F.N., and with contributions from all authors.

7.1. Device and Measurement Setup

7.1.1. Devices

Experiments were performed on six devices. Figure 7.1(a) shows a false-coloured scanning electron micrograph of Device 1, the principal device under study, which consisted of a planar SQUID, defined in the epitaxial Al (blue), containing a superconductor-normal semiconductor-superconductor (SNS) JJ and a narrow Al constriction. The SNS junction had length $L = 80$ nm, width $W = 2.5$ μm and Al leads of length $L_{\mathrm{SC}} = 250$ nm[1]. The constriction had a width $W_{\mathrm{cons.}} = 130$ nm, chosen to limit the switching current of the planar SQUID, while still being much larger than that of the SNS junction. The constriction was 500 nm long, to clearly define the narrow region of the Al, for both improved control in fabrication and consistency in average switching currents. The CPR of the Al constriction is expected to be a sawtooth shape, with a maximum supercurrent at a well defined phase [199]. This asymmetric configuration, and sharp constriction CPR, resulted in a phase drop across the SNS junction of $\varphi \approx 2\pi(\Phi/\Phi_0)$, where a flux $\Phi = AB_{\perp}$ threaded the area $A = 10.2$ $(\mu\mathrm{m})^2$ enclosed by the SQUID loop ($\Phi_0 = h/2\mathrm{e}$ is the superconducting flux quantum). Data was periodic with a perpendicular field $B_{\mathrm{Period}} = 200$ μT. Differently from previous work [109, 122, 124, 153], where two InAs JJs were used, the Al constriction cannot introduce anomalous phase shifts in an in-plane magnetic field due to the absence of spin-orbit and orbital effects. A superconducting probe was integrated close to one end of the SNS junction, comprising a contact of epitaxial Al separated from the SNS junction by a tunnel barrier defined in the InAs. The transparency of the tunnel barrier was controlled by the gate voltages $V_{\mathrm{T,L}}$ and $V_{\mathrm{T,R}}$, applied to the left and right tunnel gates respectively. The carrier density in the SNS junction was controlled via a top-gate voltage V_{TG}. An additional gate was kept at $V_{\mathrm{Probe}} = 0$ throughout. Devices 2 to 5 were similar to Device 1 except for L_{SC}[2], resulting in different orbital coupling to in-plane magnetic fields [see Fig. 7.1(b)]. Each measurement presented here was acquired in parallel with measurements of a Reference Device fabricated on the same chip, which consisted of an asymmetric SQUID with two Al constrictions of different widths [see Fig. 7.1(c)].The oscillation periods of Devices 1 to 5 and the reference device were similar (all within 9 μT, corresponding to 5% of B_{Period}). Parallel conduction in the InAs surrounding Reference Devices was prevented by setting a global gate to $V_{\mathrm{Global}} = -3$ V, such that the switching current in the Reference Device was independent of V_{Global}. Further, no V_{Global}-dependent phase shifts were observed in the Reference Device at elevated in-plane magnetic fields, showing the absence of spin–orbit effects.

[1] Device 1 was identical to the device presented in Chapter 6.

[2] Devices 2, 3 and 4 did not have a tunnel probe, so only supercurrent measurements were possible. See Section 7.8 for more details.

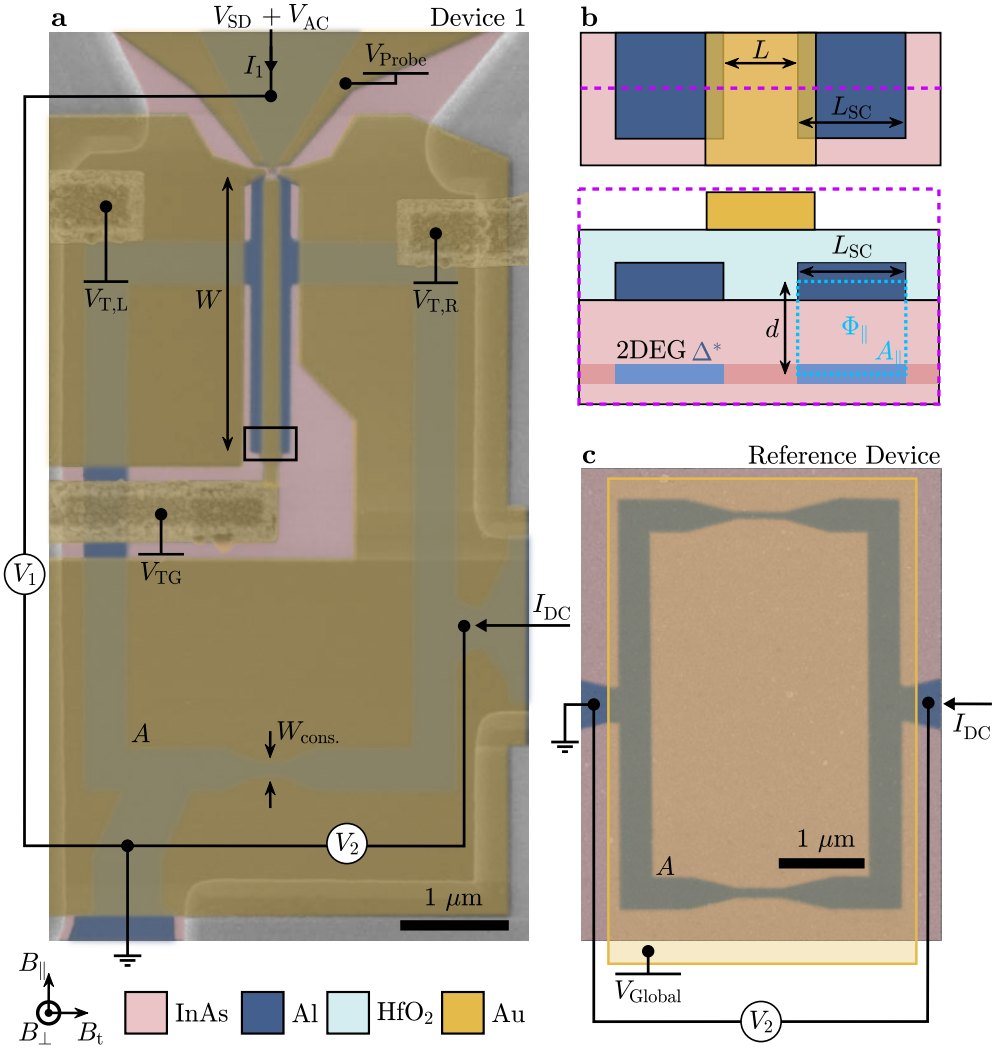

Figure 7.1. Device under study and Reference Device. a False-coloured scanning electron micrograph (SEM) of Device 1, the planar superconducting quantum interference device (SQUID), consisting of InAs (pink) and Al (blue). Exposed InAs regions were controlled via electrostatic gates (yellow). **b** Schematic zoom-in of the Josephson junction region (top), with junction length $L = 80$ nm and superconducting lead length $L_{SC} = 250$ nm indicated. The purple dashed line indicates the position of a schematic cross-section (bottom). An in-plane magnetic field $B_\parallel$ generates a flux $\Phi_\parallel$ between the superconducting leads and the proximitised two-dimensional electron gas (2DEG), with area $A_\parallel = L_{SC}d$. **c** False-coloured SEM of the Reference Device, prior to gate deposition, consisting of two Al constrictions embedded in a superconducting loop. A global gate V_{Global} is indicated schematically (yellow).

7.1.2. Measurement Techniques

Switching currents I were measured using fast current ramps and voltage triggers. A ramped current I_{DC} was injected into the SQUID loop while monitoring the voltage V_2 across the device with an oscilloscope. The switching current was defined as the value of I_{DC} at which V_2 exceeded a threshold. Particular care was taken to inject the current I_{DC} by symmetrically biasing the measurement circuit, to prevent significant voltage build-up between SQUID and gates. Each CPR data point shown here was obtained by averaging over 32 data points measured with $I_{\mathrm{DC}} > 0$ and 32 with $I_{\mathrm{DC}} < 0$. This procedure allowed us to improve the experimental accuracy, limit the effect of the broad switching current distributions typical of planar devices (see Chapters 4 and 5), and to cancel trivial phase shifts originating from the kinetic inductance of the loop [235]. The CPR of the SNS junction was obtained by subtracting the switching current of the Al constriction I_{Al} from that of the SQUID loop, which had a value between 30 and 45 μA for all devices. Tunnelling conductance measurements were performed by low-frequency lock-in techniques. A voltage bias $V_{\mathrm{SD}} + V_{\mathrm{AC}}$ was sourced at the tunnelling probe and the resulting AC current I_1 and voltage V_1 gave the differential conductance $G \equiv I_1/V_1$. Global magnetic fields were applied via a three-axis vector magnet, nominally along the directions $B_\perp$, $B_\parallel$ and B_{t} as indicated in Fig. 7.1(a). Further details on the procedures used to accurately align the chip to the external magnetic field are presented in the Supporting Information (Section 7.8).

7.1.3. Reference Device

A Reference Device was used to calibrate the position of zero perpendicular magnetic field. An example of the switching current of the Reference Device, $I_{\mathrm{ref.}}$, is shown in Fig. 7.2(a) as a function of perpendicular magnetic field $B_\perp$. The asymmetry in width of the Al constrictions gave an asymmetric SQUID behaviour, with a large average switching current $\langle I_{\mathrm{ref.}} \rangle = 40$ μA (green dashed line) for the wide constriction ($W_{\mathrm{cons.}} = 130$ nm) and a small modulation $I_{\mathrm{ref.}} - \langle I_{\mathrm{ref.}} \rangle$ corresponding to the narrow constriction ($W_{\mathrm{cons.}} = 100$ nm). The position where $I_{\mathrm{ref.}} - \langle I_{\mathrm{ref.}} \rangle = 0$ was taken to be the perpendicular field at which no magnetic flux threaded the loop, B_0 (marked by the triangle). The flux dependence of the switching current deviates from the expected sawtooth pattern, which is attributed to an appreciable kinetic inductance in the loop relative to the inductance of the narrow constriction, and the comparable gradients of the CPR for the narrow and wide constrictions (see Eq. 2.45). While this affects the flux dependence of $I_{\mathrm{ref.}}$, the trend in B_0 is unaffected and so is a reliable indicator for zero perpendicular magnetic field.

Figure 7.2(b) shows the maximum switching current of the wide and narrow constriction as a function of in-plane magnetic field $B_\parallel$ (green and blue circles, respectively). At $B_\parallel = 0$, the switching current was suppressed relative to that at a small in-plane field. This suppression is attributed to a reduced superconducting gap at $B_\parallel = 0$, due to large quasiparticle populations which were unable to relax into the superconducting leads [290, 295]. At a small magnetic field the number of relaxation channels would

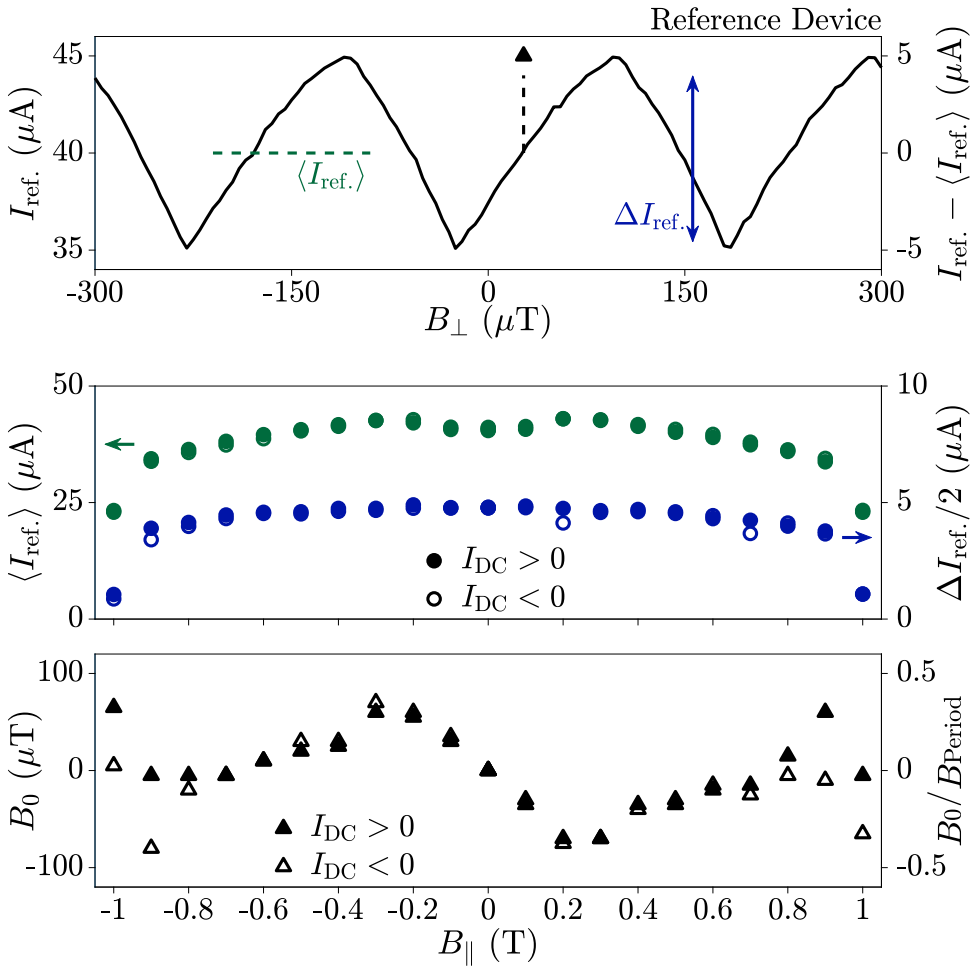

Figure 7.2. Characterisation of the Reference Device. a Current-phase relation of Reference Device $I_{\mathrm{ref.}}$ before (left) and after (right) subtraction of average $\langle I_{\mathrm{ref.}} \rangle$ (indicated by green dashed line). Amplitude of oscillations $\Delta I_{\mathrm{ref.}}$ is indicated by the blue arrow. Perpendicular field $B_\perp$ at which $I_{\mathrm{ref.}} - \langle I_{\mathrm{ref.}} \rangle = 0$, B_0, is indicated by the black triangle. **b** Average switching current of Reference Device $\langle I_{\mathrm{ref.}} \rangle$ (green, left axis) and half the oscillation amplitude $\Delta I_{\mathrm{ref.}}/2$ (blue, right axis) as a function of in-plane magnetic field $B_\parallel$. **c** Perpendicular field offset B_0 as a function of in-plane magnetic field $B_\parallel$ (left axis), and normalized to the oscillation period B_{Period} (right axis). Values in (b) and (c) are plotted for positive (negative) current bias I_{DC} as full (empty) markers.

increase, partially alleviating the gap suppression and giving an increased switching current. This effect was observed for both in-plane and perpendicular magnetic fields. For $B_\parallel > 0.9$ T, a large reduction was observed in the switching current of both constrictions, presumably caused by some portion of the superconducting loop becoming resistive. For this reason, no further studies were performed in this regime.

The perpendicular magnetic field offset B_0 of the Reference Device as a function of in-plane magnetic field $B_\parallel$ is shown in Fig. 7.2(c). A weak "S"-shaped dependence of B_0 persisted after accurate alignment of the external magnetic field. We speculate that the residual trend in B_0 originated from flux focusing [234] or a non-linearity of the vector magnet. Flux-focusing effects in the Reference Device for in-plane fields directed along the junction axis, $B_\parallel$, were consistent with those measured in all devices.

7.2. Phase Shifts in the Current-Phase Relation

Figure 7.3 shows the CPR of Device 1 at $V_{\mathrm{TG}} = 0$ (blue line, left axis) and Reference Device (grey line, right axis), both at $B_\parallel = 0.1$ T. We highlight the maximum switching current $\Delta I/2$ and a $B_\perp$-field shift B_0, which was measured where the CPR crossed zero with positive slope (circle and triangle for Device 1 and Reference Device, respectively).

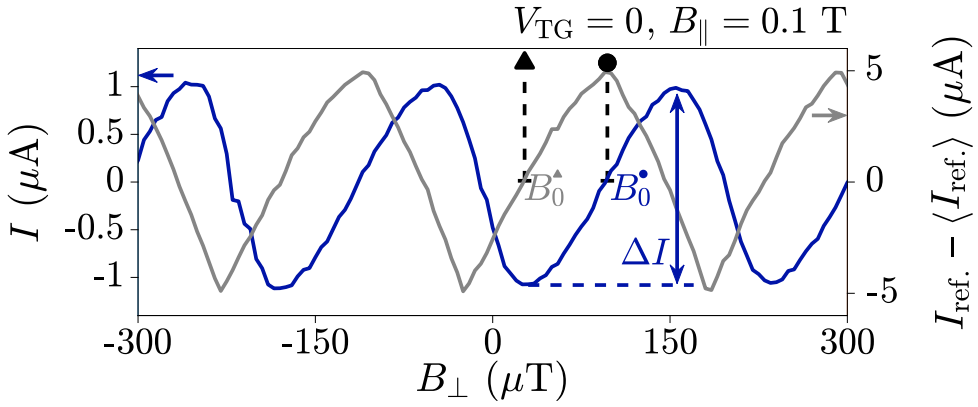

Figure 7.3. Current-phase relation of Device 1 and Reference Device. Switching current I of Device 1 as a function of perpendicular magnetic field $B_\perp$ (blue) at $V_{\mathrm{TG}} = 0$ and $B_\parallel = 0.1$ T, after removing a background of $I_{\mathrm{Al}} = 37$ μA. Switching current of the Reference Device $I_{\mathrm{ref.}}$ (grey) at the same $B_\parallel$, after subtracting the average $\langle I_{\mathrm{ref.}} \rangle$. The zero-current position for Device 1 (Reference Device) is indicated by the circle (triangle).

Figures 7.4(a) and (b) show $\Delta I/2$ and B_0, respectively, as a function of $B_\parallel$ and for various values of V_{TG}. Black triangles in Fig. 7.4(b) represent magnetic field shifts measured in the Reference Device. In Fig. 7.4(a) we plot $\langle \Delta I/2 \rangle$, that is the maximum supercurrent $\Delta I/2$ averaged over positive and negative I_{DC}. We observe a non-monotonous dependence of $\langle \Delta I/2 \rangle$ as a function of $B_\parallel$, with minima at $B_\parallel = \pm|B_\parallel^\Phi| = \pm 0.6$ T (see turquoise arrows). The magnetic field shift B_0 in Fig. 7.4(b) shows two distinctive trends. For $|B_\parallel| \lesssim 0.4$ T , B_0 shows a gate-dependent deviation with respect to the Reference Device (orange shaded area). For simplicity, we define this as a Type A shift. These phase shifts were larger for $V_{\mathrm{TG}} = 0$ (purple) than for $V_{\mathrm{TG}} = -1.6$ V (red). For $|B_\parallel| \gtrsim 0.4$ T we observe a more pronounced shift (green shading), without any measurable gate voltage dependence. We define this as a Type B shift.

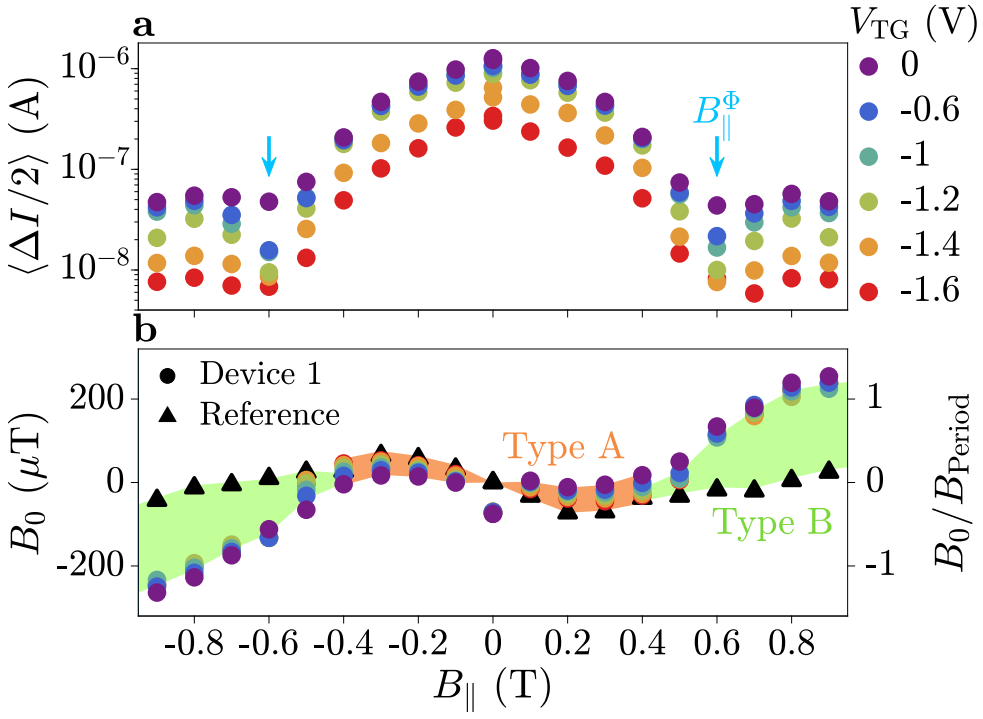

Figure 7.4. Current-biased measurements in an in-plane magnetic field $B_{\parallel}$. a Averaged half-amplitude of a SQUID oscillation $\langle \Delta I/2 \rangle$ as a function of in-plane magnetic field $B_{\parallel}$, for different top gate voltages V_{TG} (colours). A minimum in $\langle \Delta I/2 \rangle$ occurred at $B_{\parallel} = B_{\parallel}^{\Phi}$ (turquoise arrows). **b** Shift in perpendicular magnetic field B_0 of Device 1 (circles) and Reference Device (triangles), as a function of $B_{\parallel}$. Deviation of Device 1 from the Reference Device is highlighted in orange for $|B_{\parallel}| \lesssim 0.4$ T and green for $|B_{\parallel}| \gtrsim 0.4$ T.

7.2.1. Type A Shifts

We first examine Type A shifts in more detail. Figure 7.5(a) shows ΔB_0, that is B_0 as in Fig. 7.4(b) after subtraction of the data at $V_{\mathrm{TG}} = -1.6$ V, which is the most negative top-gate voltage and follows the trend of the Reference Device for $|B_{\parallel}| \leq 0.4$ T. At each gate voltage, the field shift (circles) was approximately linear in $B_{\parallel}$, as highlighted by the linear fits (solid lines). The slope β extracted from the linear fits increased for more positive V_{TG}. Remarkably, no significant Type A phase shift was observed for in-plane fields B_{t} applied along the transverse direction, as shown in Fig. 7.5(b). The lack of Type A shifts as a function of B_{t} implies a direction-dependent coupling to the external field, with a coupling strength indicated by β.

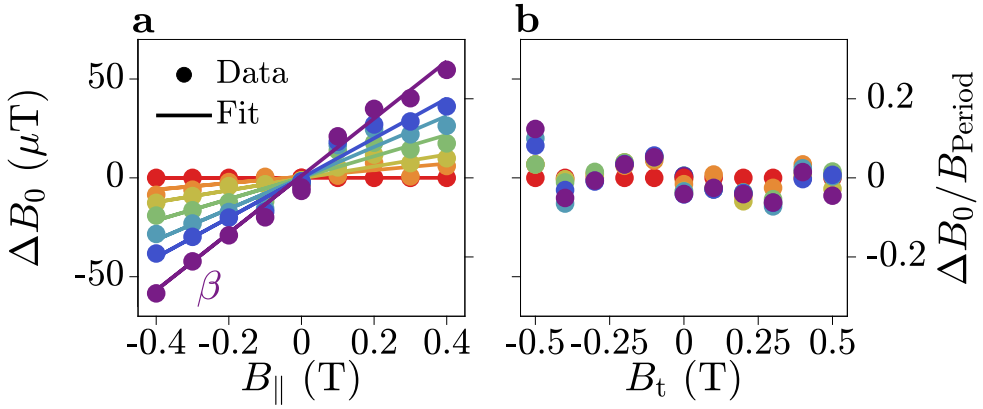

Figure 7.5. Current-biased measurements in an in-plane magnetic field. a Perpendicular field shift ΔB_0 for small $B_\parallel$ for each V_{TG} (circles), with a linear fit (lines) of gradient β. Data is plotted relative to $V_{\mathrm{TG}} = -1.6$ V. **b** Perpendicular field shift ΔB_0 for in-plane fields B_t applied along the transverse direction.

7.2.2. Magnetic Fields in the Transverse Direction

Figure 7.6 shows the complete dependence of switching currents in Devices 1 and 4 on magnetic fields B_t applied along the transverse direction. No minimum and increase in the switching current was observed [Figs. 7.6(a) and (d)], nor was there an associated phase jump [Figs. 7.6(b) and (e)], up to the largest value of B_t for which oscillations in the switching current were observed. This shows that Type B shifts were absent for in-plane fields applied in the transverse direction. The small difference between B_0 for Device 1 and the Reference Device, measured for the same applied B_t, is attributed to different flux focusing effects between the two devices. Figures 7.6(c) and (f) show ΔB_0, the field shift relative to the most negative top-gate voltage which followed the trend of the Reference Device ($V_{\mathrm{TG}} = -1.6$ V for Device 1, $V_{\mathrm{TG}} = 0.2$ V for Device 4). No gate-dependent shift was observed for Device 1 [see also Fig. 7.5(b)], however a linear gate-dependent trend was present for Device 4. The maximum shift was $\Delta B_0/B_{\mathrm{Period}} = 0.1$ for $B_t = 0.8$ T, a factor of 5 smaller than the equivalent shift in $B_\parallel$ [see Figs. 7.5(a) and 7.10(a) for comparison]. We therefore attribute this gate-dependent shift in Device 4 to stray in-plane fields, or to an additional direction-dependent coupling in devices with narrow superconducting leads ($L_{\mathrm{SC}} = 180$ nm).

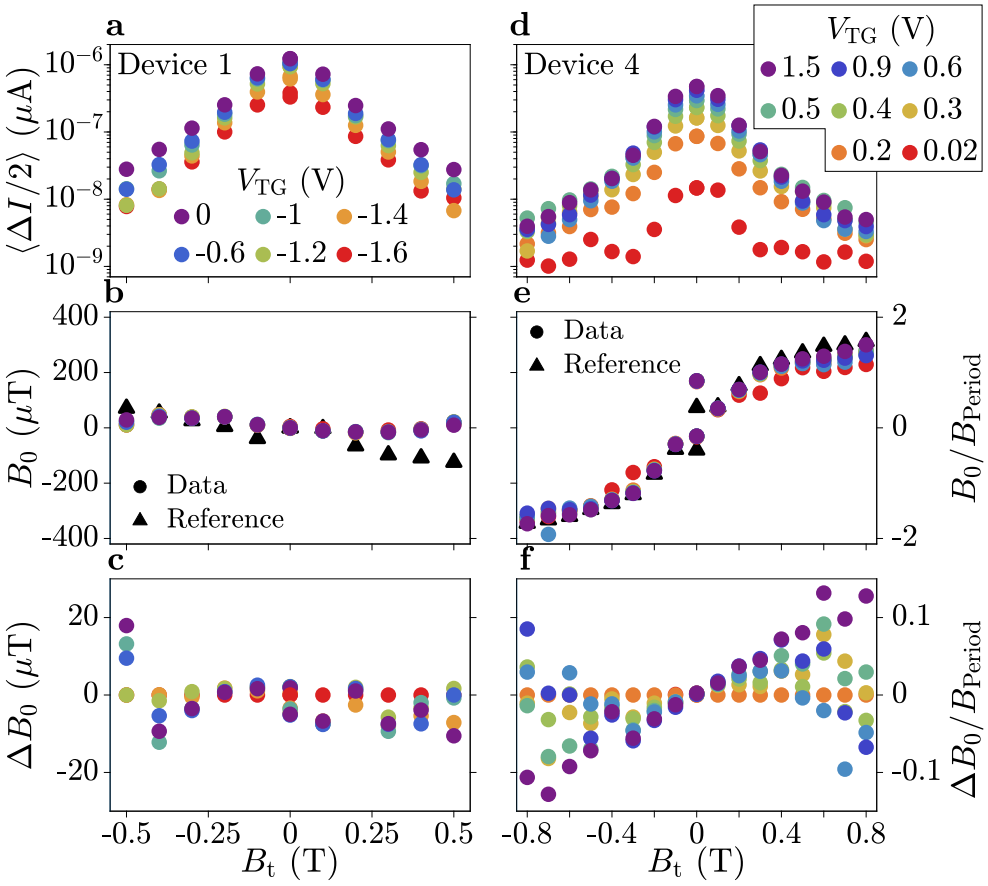

Figure 7.6. Switching current measurements in a transverse in-plane magnetic field B_t. **a, d** Half-amplitude of switching current oscillations, $\langle \Delta I/2 \rangle$, for different top-gate voltages V_{TG}, as a function of in-plane magnetic field B_t in Devices 1 and 4, respectively. No oscillations in switching current were observed for values of B_t outside of the presented range. **b, e** Perpendicular field offset B_0 of switching current oscillations as a function of B_t, for Devices 1 and 4. The field offset normalised to the oscillation period, B_0/B_{Period}, is plotted on the right axis. Data points for each Device (Reference Device) correspond to circles (triangles). The B_0 for Device 1 and the Reference Device do not align, due to the different level of flux focusing in the two devices. **c, f** Perpendicular field offset B_0 plotted with respect to that for the most negative top-gate voltage which followed the Reference Device, $V_{TG} = -1.6$ V ($V_{TG} = 0.2$ V) for Device 1 (Device 4).

7.2.3. Type B Shifts

We now turn our attention to Type B shifts, highlighted as the green shading in Fig. 7.4(b). To clarify the phase shift we plot the CPR at a single top-gate voltage, $V_{TG} = -1$ V, as a function of in-plane magnetic field $B_{\parallel}$ (see Fig. 7.7). Each CPR trace is normalised to its maximum switching current I_0, and the perpendicular field

$B_\perp$ is plotted with respect to the value of B_0 in the Reference Device at that in-plane field [see Figs. 7.2(c) and 7.4(b)]. This reference is indicated by the vertical dashed line at $B_\perp = 0$. For increasing $B_\parallel$, the position of $I = 0$ shifted to positive values of $B_\perp$. Notably, at $B_\parallel = \pm B_\parallel^\Phi$, where the supercurrent was at a minimum [see Fig. 7.4(a)], the shift was approximately half a SQUID period, corresponding to a phase shift of $\sim \pm\pi$. At $B_\parallel = 0.9$ T, the magnetic field shift accumulated in Device 1 moved towards zero, or equivalently towards $\Delta B_0/B_{\text{Period}} = 1$ as shown in Fig. 7.4(b).

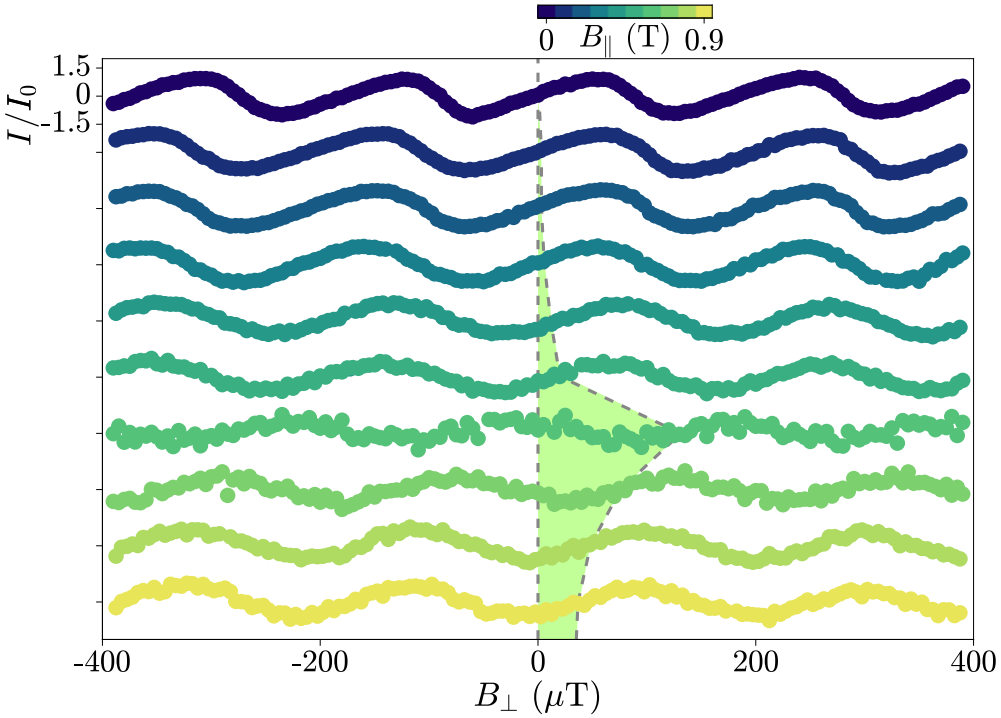

Figure 7.7. Current-phase relation (CPR) for increasing in-plane magnetic field $B_\parallel$. Currents I are normalized to the maximum switching current I_0 at each $B_\parallel$. CPR traces are offset by the perpendicular field offset B_0 of the Reference Device at the corresponding in-plane field $B_\parallel$. The shift in $B_\perp$ of the zero-current position is indicated by the green shading, between the two grey dashed lines. Data points where the switching current was significantly lower than its neighbours were removed, since they correspond to early switching events in the device by stochastic fluctuations. Each trace is offset by 3 μA to improve visibility.

7.3. Investigation of Orbital Effects

We now present CPR data obtained from Devices 2, 3 and 4, where L_{SC} was 400, 350 and 180 nm, respectively. Switching currents $\langle \Delta I/2 \rangle$ are shown in Figs. 7.8(a, c) for Devices 2 and 3 respectively, with field shifts B_0 in Figs. 7.8(b, d) for each device (coloured markers) alongside those of a Reference Device measured in parallel (black

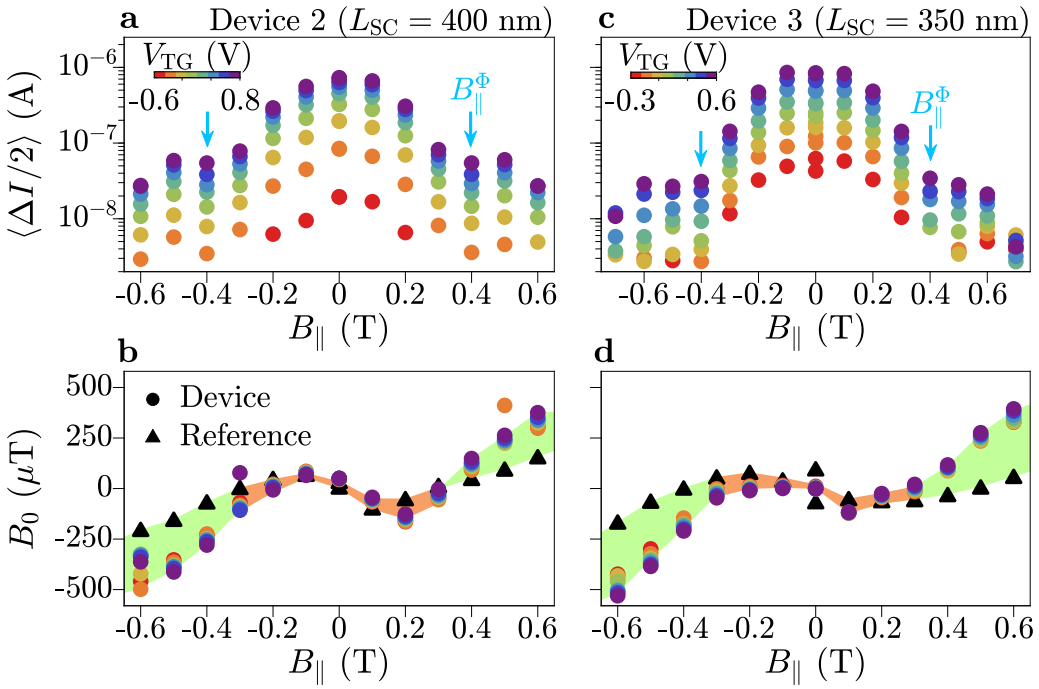

Figure 7.8. Switching current and perpendicular magnetic field shift for Device 2 and 3. **a** Average oscillation amplitude $\langle \Delta I/2 \rangle$ of Device 2: a planar superconducting quantum interference device (SQUID) with a superconducting lead length of $L_{SC} = 400$ nm, as a function of in-plane magnetic field $B_{\parallel}$ for different top-gate voltages V_{TG} (colours). Minima in the oscillation amplitude, $B_{\parallel}^{\Phi}$, are marked with the blue arrows. **b** Shift in perpendicular magnetic field, B_0, of Device 2 (circles) and the Reference Device (triangles), as a function of $B_{\parallel}$. Deviation of Device 2 from the Reference Device is highlighted in orange for small $B_{\parallel}$ and green for large $B_{\parallel}$. **c, d** The same as (a, b) for Device 3, which has $L_{SC} = 350$ nm.

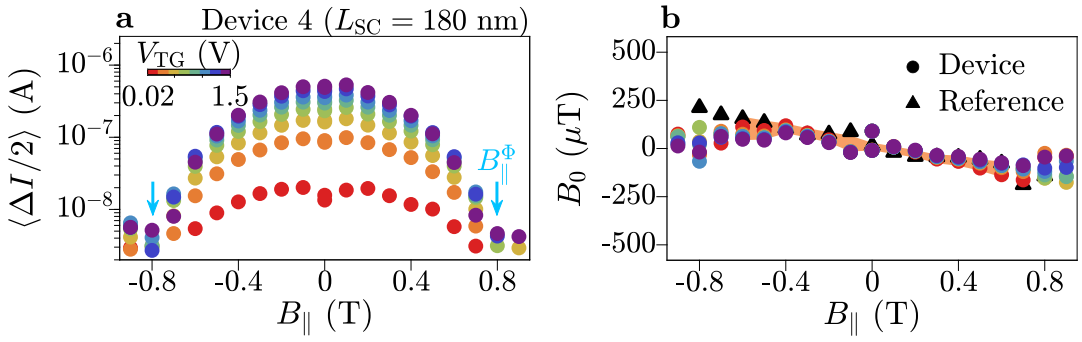

Figure 7.9. Switching current and perpendicular magnetic field shift for Device 4. The same as 7.8(a, b) for Device 4, which has $L_{SC} = 180$ nm.

triangles). Figure 7.9 shows $\langle \Delta I/2 \rangle$ and B_0 for Device 4. Devices 2, 3 and 4 showed a qualitatively similar behaviour to Device 1, despite having $B_{\parallel}^{\Phi} = 0.4$ T, $B_{\parallel}^{\Phi} = 0.4$ T and $B_{\parallel}^{\Phi} = 0.8$ T, respectively.

We repeated the analysis on Type A phase shifts presented in Fig. 7.5(a) on the data of Figs. 7.8(b, d) and Fig. 7.9(b), and show the extracted β in Fig. 7.10(a) (see Supporting Information, Section 7.12 for more details). As each device operated in a different range of V_{TG}, we compare them by plotting β as a function of ΔV_{TG}, the top-gate voltage relative to the most negative value at which oscillations were observed. Despite some scattering for small ΔV_{TG}, where data analysis was intricate due to the small switching current, we note that β follows a similar trend for all devices. In particular, β increases with ΔV_{TG} and does not depend on L_{SC}. Figure 7.10(b) shows $B_{\parallel}^{\Phi}$ as a function of the inverse superconducting lead length $1/L_{\mathrm{SC}}$. The data (blue circles) followed a linear trend, fitted by $B_{\parallel}^{\Phi} = (\Phi_0/d)/L_{\mathrm{SC}}$ (orange line) describing one flux quantum threading an area $L_{\mathrm{SC}}d$. The result of $d = 15$ nm agrees with the separation of Al and InAs layers, indicating a crucial role of orbital effects in inducing Type B phase shifts.

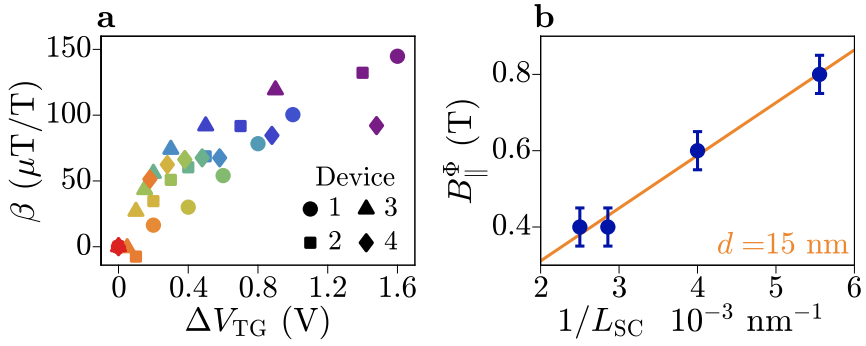

Figure 7.10. Summary of magnetic field shifts for devices with varying L_{SC}. **a** Gradient β of Type A phase shifts at small $B_{\parallel}$, for Devices 1–4 (circles, squares, triangles and diamonds respectively), plotted against the change in top-gate voltage ΔV_{TG} with respect to the minimum value. **b** In-plane magnetic field where the supercurrent is minimum, $B_{\parallel}^{\Phi}$, as a function of inverse superconducting lead length $1/L_{\mathrm{SC}}$ (blue circles), with a linear fit $B_{\parallel}^{\Phi} = (\Phi_0/d)/L_{\mathrm{SC}}$ (orange line) giving $d = 15$ nm.

7.4. Tunnelling Spectroscopy around Reentrant Field

We now complement CPR measurements with spectroscopic data obtained on Device 1. Figure 7.11 presents a series of differential conductance maps as a function of $B_{\perp}$ and V_{SD}, for increasing values of $B_{\parallel}$. All data were obtained at $V_{\mathrm{TG}} = -1$ V (data at more values of V_{TG}, and in a device with larger L_{SC}, are reported in the Supporting Information, Section 7.11).

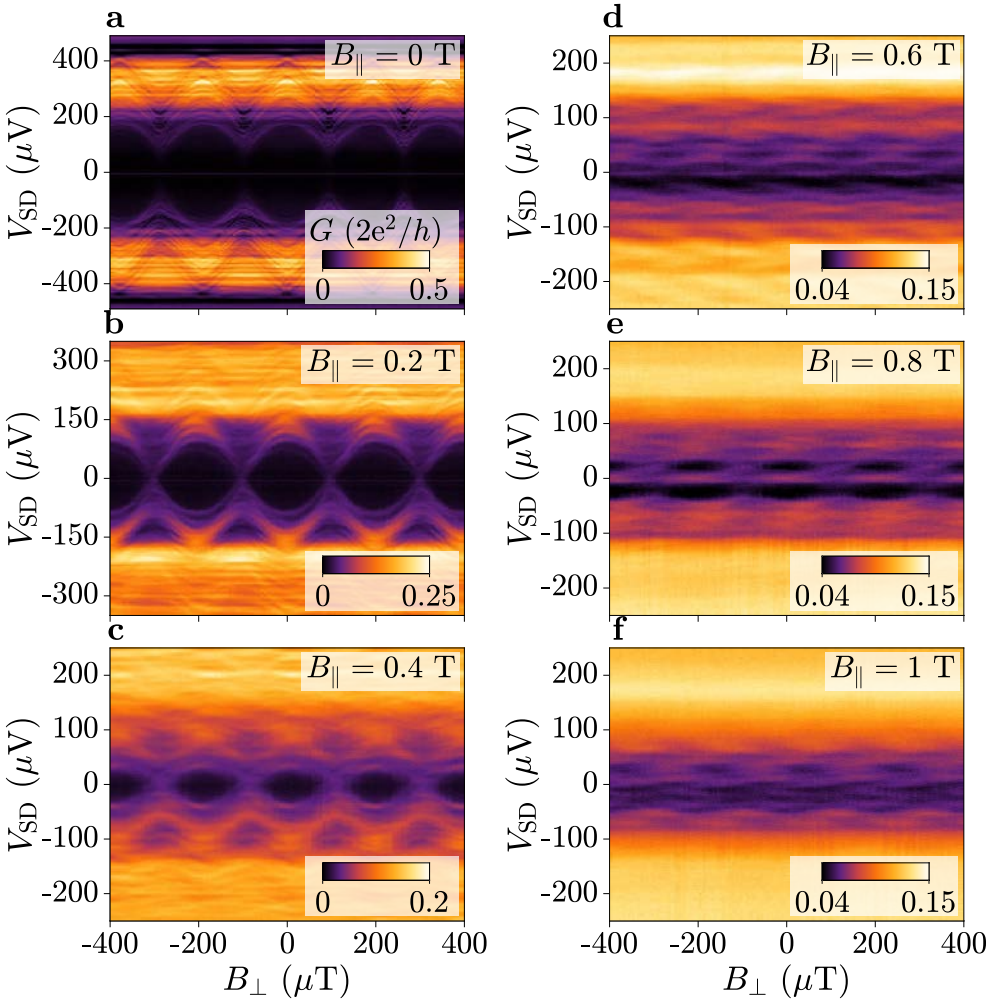

Figure 7.11. Tunnelling spectroscopy of Andreev bound states as a function of in-plane magnetic field $B_\parallel$. Differential conductance G through the tunnelling probe, as a function of source-drain bias voltage V_{SD} and perpendicular magnetic field $B_\perp$, for increasing values of $B_\parallel$. Measurements were taken at a top-gate voltage of $V_{TG} = -1$ V, with tunnel-barrier voltages $(V_{T,L}, V_{T,R}) = (-1.495, -1.65)$ V.

As the tunnelling probe used a superconducting lead, the differential conductance G at $B_\parallel = 0$ indicates the density of states in the junction up to a bias shift of $\pm e\Delta$. Further conductance peaks at zero and high bias are attributed to a residual supercurrent and multiple Andreev reflections through the tunnelling probe, respectively. For $B_\parallel \geq 0.2$ T, a finite density of states at the Fermi level was induced in the lead facing the tunnelling probe, resulting in a direct mapping of the density of states in the junction [234].

For $B_\parallel \leq 0.2$ T [Figs. 7.11(a) and (b)], the conductance demonstrates a conventional spectrum containing multiple ABSs, some of which have transmission approaching unity, and an induced superconducting gap of approximately 180 μeV. For $B_\parallel = 0.4$ T, phase-

dependent conductance features approached zero energy, resulting in a significant decrease of the superconducting gap [Fig. 7.11(c)]. For $B_{\parallel} = B_{\parallel}^{\Phi} = 0.6$ T [Fig. 7.11(d)], conductance features oscillated close to $V_{\mathrm{SD}} = 0$ with no clear separation between states at positive and negative bias. As $B_{\parallel}$ was further increased, a gap reopened in the ABS spectrum, with discrete states around zero energy. Finally, the gap closed for $B_{\parallel} \geq 1$ T. Conductance features close to $V_{\mathrm{SD}} = 0$ in Fig. 7.11(e) were reminiscent of zero-bias peaks reported for similar devices at high in-plane magnetic fields and understood in terms on topological states [122, 123]. However, zero-bias features of Fig. 7.11(e) were not robust to small changes in the top-gate voltage V_{TG} or tunnel-gate voltage V_{T} (see Supporting Information, Section 7.10).

7.5. Tunnelling Spectroscopy of Type A Shifts

The analysis described in this section, and plotted in Fig. 7.12(i), was performed by Marco Coraiola with input from D.Z.H. Measurements were performed by D.Z.H.

Figure 7.12 compares spectroscopic maps obtained at $B_{\parallel} = 0.2$ T (a–d) and 0.4 T (e–h), for multiple values of V_{TG}. The value of $B_{\perp}$ at which the ABS energy was closest to the gap was found for each value of V_{TG}, as indicated by the blue circles. This was determined as the $B_{\perp}$ value where the gradient $\partial G/\partial B_{\perp}$ was zero, at a fixed bias V_{SD} and averaged over multiple periods. Blue dashed lines indicate the minimum energy position at $V_{\mathrm{TG}} = -1.4$ V, which is defined as $B_{\perp} = 0$ in Fig. 7.12(d). For both $B_{\parallel} = 0.2$ T and 0.4 T, a clear deviation of the ABS spectrum took place as a function of V_{TG}. The shift in perpendicular field ΔB_0 measured from the ABS spectrum is summarised in Fig. 7.12(i) as a function of V_{TG} for $B_{\parallel} = 0.2$ T (blue) and $B_{\parallel} = 0.4$ T (orange). The Type A shift ΔB_0 obtained from the CPR is plotted on the same axis (squares, dashed lines) and shows remarkable agreement.

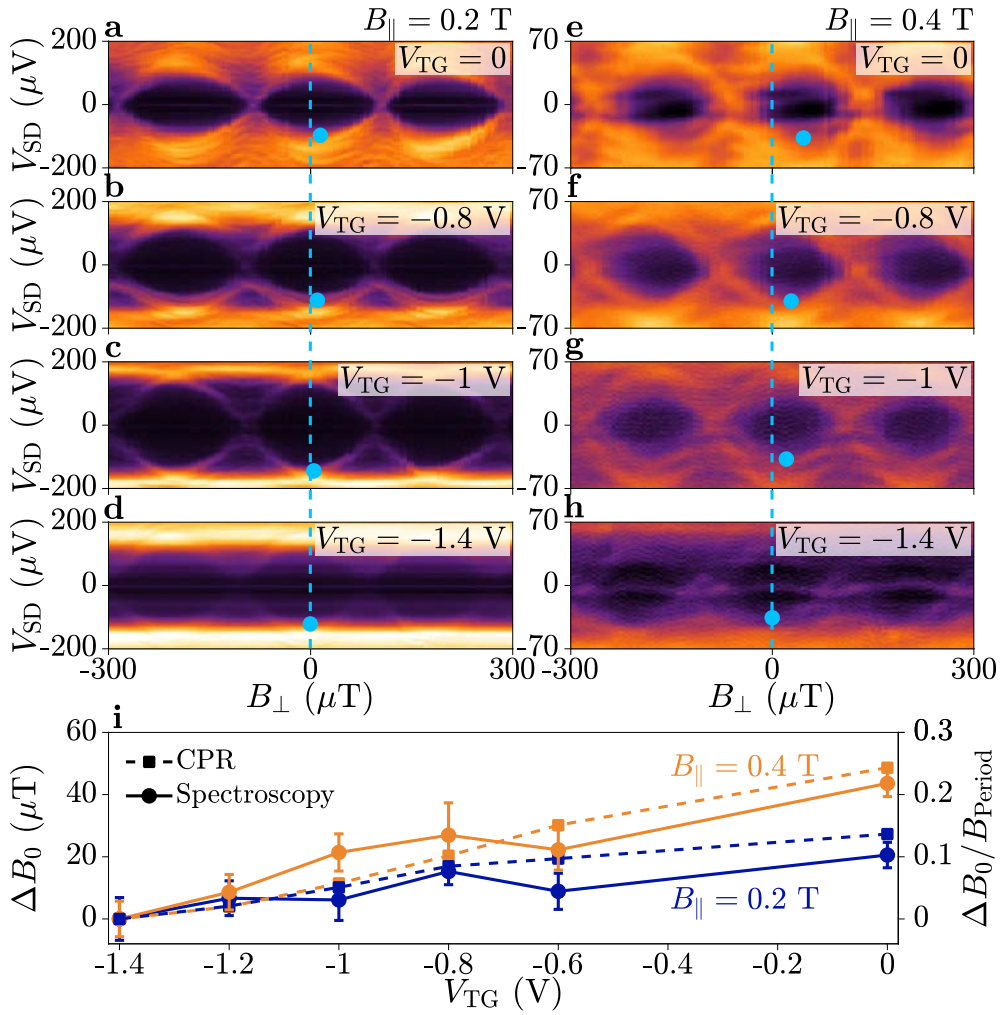

Figure 7.12. Top-gate dependence of the energy minimum at a finite in-plane magnetic field $B_\parallel$. a-d Differential conductance G as a function of bias V_{SD} and perpendicular magnetic field $B_\perp$, at an in-plane magnetic field of $B_\parallel = 0.2$ T. Spectroscopy was performed at a top-gate voltage of $V_{TG} = \{0, -0.8, -1, -1.4\}$ V, respectively. The blue dashed line indicates the energy minimum at $V_{TG} = -1.4$ V. Blue markers show the shift of the energy minimum as a function of V_{TG} relative to $V_{TG} = -1.4$ V. **e-h** Bias-dependent spectroscopy as in (a-d) at an in-plane magnetic field of $B_\parallel = 0.4$ T. **i** Shift in perpendicular magnetic field ΔB_0 relative to $V_{TG} = -1.4$ V, at an in-plane magnetic field of $B_\parallel = 0.2$ T (blue) and $B_\parallel = 0.4$ T (orange), obtained from tunnelling spectroscopy (circles, solid lines) and current-phase relation (CPR) measurements (squares, dashed lines). The phase shift $\varphi_0/2\pi \equiv \Delta B_0/B_{Period}$ is plotted on the right axis. Extraction of the phase shifts from tunnelling spectroscopy [plotted as the circles in (i)] was performed by Marco Coraiola.

7.6. Discussion

After demonstrating that two types of anomalous phase shifts occur in hybrid SQUIDs in in-plane magnetic fields, we now discuss their origin. Type A phase shifts, which were approximately linear in $B_\parallel$ and depended on V_{TG} [Fig. 7.5(a)], are associated with spin-orbit-induced anomalous phase shifts [87, 229, 296–298], as recently reported in similar devices [109]. Since phase shifts were much more pronounced for in-plane fields aligned perpendicular to the current flow direction ($B_\parallel$) than parallel to it (B_t) [Fig. 7.5(b)], and were stronger for higher electron density (more positive V_{TG} [136, 232]), we conclude that spin-orbit interaction in our samples is predominantly of Rashba type.

Type A phase shifts reported here, which are of similar size to those in Ref. [109], are considerably larger than theoretical predictions [229]. Reference [109] proposed that observed phase shifts could be explained by the contribution of several low-transmission modes. However, we show that Type A shifts in the CPR matched those from tunnelling spectroscopy, where conductance features at both high and low bias showed a phase shift. Since conductance features at low bias correspond to ABSs with high transmission, we conclude that highly transmissive modes participate in the overall phase shift despite their large Fermi velocity. While this result does not resolve the discrepancy between theoretical predictions and experiments [109], it rules out diffusive modes with small Fermi velocities as the dominant cause of Type A phase shifts.

Type B phase shifts were concomitant with a reentrant supercurrrent and a closure and reopening of the superconducting gap, independent of top-gate voltage V_{TG}. At $B_\parallel = \pm B_\parallel^\Phi$, where the supercurrent was at a minimum and the proximitised superconducting gap was suppressed, the phase shift was approximately $\pm\pi$. For $|B_\parallel| > B_\parallel^\Phi$, a gap reopened in the ABS spectrum and the phase shift increased to above 2π. A phase shift occurring with a supercurrent minimum and gap closure indicates a $0-\pi$ transition at $B_\parallel = B_\parallel^\Phi$, where the minimum ABS energy moves from $\varphi \approx 0$ to $\varphi \approx \pi$ due to coupling of the magnetic and superconducting orders by Zeeman interaction [87, 299, 300]. All experimental signatures of Type B shifts were shown to depend on the length L_{SC}, consistent with a flux quantum threading an area $L_{\mathrm{SC}}d$ underneath the superconducting leads. The experimentally obtained value of $d = 15$ nm agrees with the separation between the Al and InAs layers (13.4 nm), up to some flux penetration into each layer. We therefore conclude that orbital effects strongly contributed to inducing Type B phase shifts. Type B shifts were observed for in-plane fields $B_\parallel < 1$ T, much lower than the values $B_{0-\pi} \gtrsim 9$ T expected for InAs/Al heterostructures [124]. We explain this by orbital effects, which were responsible for the induced gap suppression, forcing ABSs to move closer in energy. This enabled ABSs to cross even with small Zeeman splitting. The phase shift extended over a range of in-plane fields since the junction contained many ABSs with different transmissions, which therefore require different Zeeman energies to cross. Previous work reported similar phase shifts [124], where a π jump in the junction phase was accompanied by a minimum in the switching current. However, phase shifts depended on the top-gate voltage, unlike the Type B shifts reported here. This result shows that orbital effects alone are not sufficient to explain the results of Ref. [124].

7.7. Conclusions

In conclusion, measurements of the current-phase relation (CPR) and Andreev bound state (ABS) spectrum in hybrid quantum interference devices showed phase shifts with two distinct characters, referred to as Types A and B.

Type A phase shifts are attributed to coupling of the external magnetic field with an internal Rashba spin-orbit field, resulting in a φ_0-junction. Highly transmissive ABSs were shown to make a significant contribution to the phase shift, which was much larger than expected for a single ballistic channel. The discrepancy might be due to the presence of many transverse modes, which future studies could investigate by varying the junction width or using electrostatic gating, either in a split-gate [301] or multi-gate [195] geometry. The influence of spin-orbit coupling on φ_0-shifts could be further investigated by measuring junctions with different lengths, and comparing results with theoretical expectations [229, 298].

Type B shifts were consistent with a $0 - \pi$ transition, where orbital effects in the superconducting leads played a critical role. This suggests that the geometry of the superconducting leads, and their impact on orbital effects, is a key ingredient for realising π-junctions for superconducting electronics [92, 93] or in interpreting signatures of topological superconductivity [120]. Future studies could implement spectroscopic probes on both ends of the junction to investigate the effect of magnetic vector potentials on ABS properties [302], and establish how the superconducting gap changes across the device using non-local spectroscopy techniques [292].

Non-reciprocal transport was not observed in this work. One challenge in resolving distortions to the CPR, or small changes in the direction-dependent supercurrent, was the removal of a large background switching current corresponding to the Al constriction, which had a weak dependence on perpendicular magnetic field. Future measurements could partially alleviate this issue by fabricating Al constrictions with smaller switching currents (~ 10 μA rather than ~ 40 μA), performing careful independent measurements of the Al constriction and using local flux control to mitigate field-dependent quasiparticle thermalisation effects in the Al constriction.

7.8. Supporting Information: Measurement Techniques

In this section, we describe in detail the measurement techniques used to extract the current-phase relation and to align the magnetic field to be in the plane of the device chip.

7.8.1. Extracting the Current-Phase Relation

An example of the switching current of Device 1 is shown in Fig. 7.13(a) (circles), as a function of perpendicular magnetic field $B_\perp$. A slowly-varying background is associated with the switching current of the Al constriction, which had a large switching current of $I \approx 37$ μA. A weak dependence of the background switching current on $B_\perp$ is consistent with a change in the number and distribution of quasiparticle relaxation channels, as described in Section 7.1.3 [290, 295]. To remove this background, the data was fitted with a polynomial function over four complete periods, each defined by $B_{\text{Period}} \equiv \Phi_0/A = 200$ μT where $\Phi_0 = h/2e$ is the superconducting magnetic flux quantum and $A = 10.2$ $(\mu\text{m})^2$ is the area enclosed by the superconducting loop. This background contribution is shown as the dashed line in Fig. 7.13(a). The SQUID switching current after removing the background is plotted as the circles in Fig. 7.13(b), at $B_\parallel = 0$ for different top-gate voltages V_{TG} [denoted by colour, defined in Fig. 7.13(c)]. The data showed a large forward skewness, consistent with the presence of highly transmissive ABSs in the junction [171].

The CPR of an SNS junction containing N modes is described by

$$I(\varphi) = -\frac{2e}{\hbar}\sum_{n=1}^{N}\frac{\partial E_{\text{A},n}(\varphi)}{\partial\varphi}, \tag{7.1}$$

where $E_{\text{A},n} = \Delta\sqrt{1-\tau_n\sin^2(\varphi/2)}$ is the energy of the n^{th} ABS with transmission τ_n, Δ is the superconducting gap and φ is the phase difference across the SNS junction. The total supercurrent is a sum over the contributions of each ABS in the junction. The junctions studied in this work all had a large width $W = 2.5$ μm, and therefore contained many transverse conducting modes. Since detailed knowledge about individual modes is missing, we instead consider an effective transmission $\bar{\tau}$ to describe the properties of the CPR: the transmission which would reproduce the CPR in a junction where all modes have identical transmission. With the application of an in-plane magnetic field, the CPR is expected to obtain a phase shift φ_0 [87]. Accounting for these considerations, we obtain the equation

$$I(\varphi) = I_{\text{N}}\frac{\bar{\tau}\sin(\varphi-\varphi_0)}{E_{\text{A}}(\varphi-\varphi_0)/\Delta}, \tag{7.2}$$

where $I_{\text{N}} = (e/2\hbar)\bar{N}\Delta$ and $\bar{N}$ is the effective number of modes in the junction. The phase difference across the junction is related to the perpendicular magnetic field by $\varphi = 2\pi(B_\perp \cdot A/\Phi_0)$. The switching current as a function of perpendicular magnetic field is therefore fitted using Eq. 7.2 obtaining three parameters: I_{N}, $\bar{\tau}$ and $\varphi_0 \equiv 2\pi(B_0 \cdot A/\Phi_0)$. The maximum switching current I_0 is obtained as the maximum of $I(\varphi)$ from the fit.

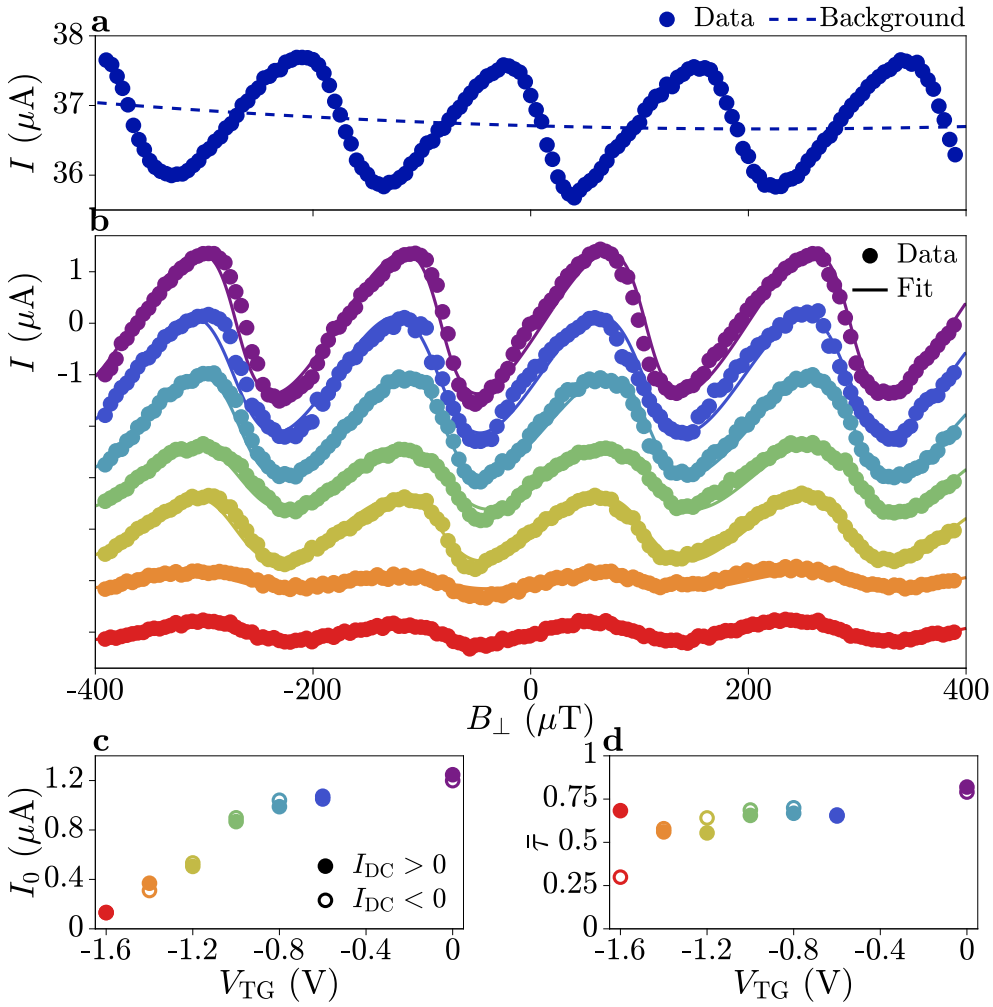

Figure 7.13. Method to extract the current-phase relation from switching current measurements. **a** Switching current I of Device 1 as a function of perpendicular magnetic field $B_\perp$. Data (circles) is fitted with a polynomial (dashed line) to extract the background switching current corresponding to the Al constriction. **b** Switching current after background extraction, as a function of perpendicular magnetic field $B_\perp$ for different top-gate voltages V_{TG} [colours, defined in (c)]. Data (circles) is fitted with a formula for the current-phase relation of Andreev bound states (line). Each trace is offset by 1 μA. **c, d** Results of the fits presented in (b): maximum switching current I_0 and transmission $\bar{\tau}$, for (c) and (d) respectively. Results for positive (negative) applied current I_{DC} plotted as full (empty) markers.

The fits to the data in Fig. 7.13(b) are shown as the solid lines, with the maximum switching current I_0 and effective transmission $\bar{\tau}$ plotted in Figs. 7.13(c) and (d), respectively. The maximum switching current decreased as a function of top-gate voltage V_{TG}, until no oscillations were visible at $V_{\mathrm{TG}} < -1.6$ V. The effective transmission did not change appreciably across this range, indicating the presence of highly transmissive ABSs across the full gate range. Results are plotted for positive ($I_{\mathrm{DC}} > 0$) and negative ($I_{\mathrm{DC}} < 0$) bias current directions, as the full and empty markers respectively. An apparent discrepancy between the effective transmissions at $V_{\mathrm{TG}} = -1.6$ V for $I_{\mathrm{DC}} > 0$ and $I_{\mathrm{DC}} < 0$ is attributed to slight differences in the CPR shape arising from the background current subtraction, which is particularly sensitive for small switching current modulations at very negative V_{TG}.

At a given in-plane magnetic field $B_{\parallel}$, the CPR of the SQUID was found by measuring the switching current as a function of perpendicular field $B_{\perp}$, which was swept multiple times across a small range such that it was stable. The switching current was measured for positive and negative currents, before changing the top-gate voltage V_{TG}. Once the switching current had been collected for all top-gate voltages, $B_{\parallel}$ was ramped to the next value. The in-plane field was always swept away from $B_{\parallel} = 0$, such that sweeps in the positive and negative $B_{\parallel}$ directions began at $B_{\parallel} = 0$. As such, all measurements are relative to the values obtained at zero in-plane field in that field sweep. Since fitting with Eq. 7.2 always returned values for φ_0 in the range $[-\pi,\ \pi]$, results at a given in-plane field were shifted by integer multiples of the oscillation period B_{Period} such that B_0 values followed a monotonic trend. The magnetic field $B_{\parallel}$ was swept multiple times, from -1 T to 1 T, before measurements were taken to minimise hysteresis effects. Nevertheless, some hysteresis was observed at $B_{\parallel} = 0$, where flux focusing effects were most prevalent. Hence, results for $B_{\parallel} > 0$ and $B_{\parallel} < 0$ were combined such that current-averaged B_0 features were symmetric for $|B_{\parallel}| \geq 0.1$ T. The results of Figs. 7.4, 7.8 and 7.9 were plotted following this procedure. An identical procedure was followed for in-plane magnetic fields applied transverse to the junction axis, B_{t}.

7.8.2. Devices with Varying Superconducting Lead Length

Measurements were performed on devices with varying superconducting lead length L_{SC} (see Figs. 7.8 and 7.9). Devices consisted of a superconducting loop identical to that of Device 1, other than the length of the superconducting leads which had values $L_{\mathrm{SC}} = 400$ nm, 350 nm and 180 nm for Devices 2–4 respectively. These devices did not have a tunnel probe proximal to the SNS junction, so only current-biased measurements were possible. Each device had two gates: a top-gate V_{TG} identical to that of Device 1 to tune the charge density in the SNS junction; and a global gate covering the exposed InAs regions around the junction and superconducting loop. The global gate was set to $V_{\mathrm{Global}} < -1.5$ V throughout the experiment, such that the exposed InAs was depleted everywhere other than in the junction region.

Switching current measurements were performed for increasing in-plane magnetic field $B_{\parallel}$. At each value of $B_{\parallel}$, the switching current was first measured across a wide range of $B_{\perp}$ at the most positive top-gate voltage. After subtracting a slowly varying background

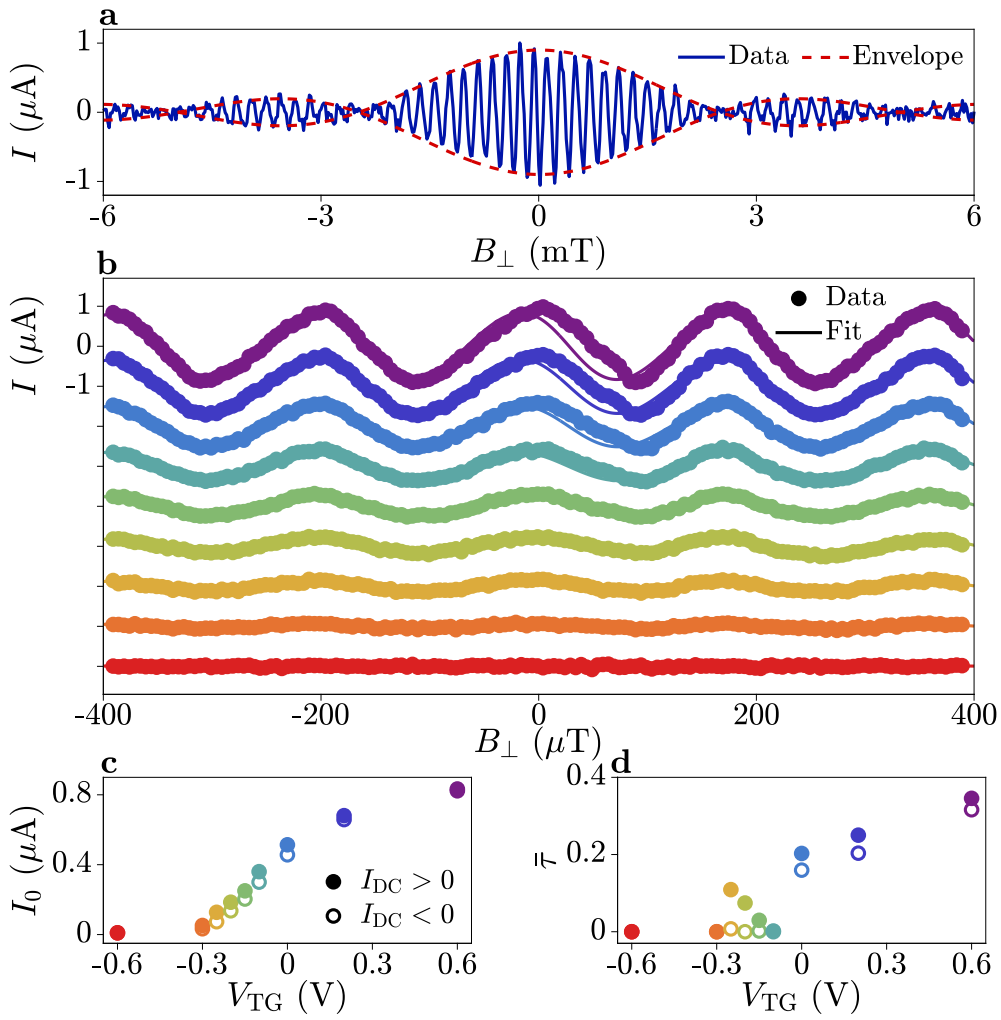

Figure 7.14. Method to extract the current-phase relation from Devices 2-4. a Switching current I of Device 2 as a function of perpendicular magnetic field $B_\perp$, across a wide range of ± 6 mT. Data (blue solid line) is fitted with an envelope function (red dashed line) of a Fraunhofer interference pattern. **b** Switching current as a function of perpendicular magnetic field $B_\perp$, after subtracting the background corresponding to the Al constriction. The background is determined from $V_{TG} = -0.6$ V (red circles), where the planar junction is considered to be completely closed since no oscillations in switching current were observed. Data at different top-gate voltages (circles) are fitted with a formula for the current-phase relation of Andreev bound states (line), at each top-gate voltage V_{TG} denoted by the colour [defined in (c)]. The fit incorporates the results obtained for the envelope in (a). Each trace is offset by 1 μA. **c, d** Results of the fit presented in (b): maximum switching current I_0 and transmission $\bar{\tau}$, for (c) and (d) respectively. Results for positive (negative) applied current I_{DC} plotted as full (empty) markers.

corresponding to the Al constriction, a recognisable Fraunhofer interference pattern was observed [Fig. 7.14(a), blue line]. In Devices 2 and 3, where the superconducting leads were large, flux focusing effects were strong. This caused a minimum in the Fraunhofer interference pattern at relatively small perpendicular fields $B_\perp$. It was therefore important to consider the envelope of switching current oscillations due to Fraunhofer interference. This was extracted from the data by filtering out the high frequency oscillatory component, and fitting the result with the following equation

$$I^{(\mathrm{env})}(B_\perp) = I_0^{(\mathrm{env})} \left| \mathrm{sinc}\left(\frac{B_\perp - B_0^{(\mathrm{env})}}{B_{\mathrm{min.}}} \right) \right|. \tag{7.3}$$

There were three free parameters: the maximum current $I_0^{(\mathrm{env})}$, the perpendicular field at which the current was maximum $B_0^{(\mathrm{env})}$ and the perpendicular field at which the first minimum occurred $B_{\mathrm{min.}}$. The result of this fit for the data in Fig. 7.14(a) is shown as the dashed red line. The in-plane field was aligned such that the maximum of the Fraunhofer pattern was close to $B_\perp = 0$ for each value of in-plane field. This was different in each device, due to flux-focusing effects, so a different alignment was needed for each device. As such, a Reference Device was measured with each field alignment, to make a direct comparison.

At a given in-plane magnetic field, the switching current was measured as a function of perpendicular magnetic field $B_\perp$ for different top-gate voltages V_{TG}. The most negative top-gate voltage was chosen such that no oscillations were visible, where the SNS junction was assumed to be completely closed. The bias current therefore only flowed through the Al constriction, giving a direct evaluation of the switching current of the constriction as a function of $B_\perp$. This background switching current was subtracted from the data at other V_{TG}, to obtain the current-phase relation at each top-gate voltage [see Fig. 7.14(b)]. The data (circles) for each V_{TG} [colours, defined in (c)] was fitted with Eq. 7.2, adjusted to account for the envelope given by Eq. 7.3, resulting in

$$I(B_\perp) = I_0^{(\mathrm{env})} \left| \mathrm{sinc}\left(\frac{B_\perp - B_0^{(\mathrm{env})}}{B_{\mathrm{min.}}} \right) \right| \cdot \frac{\bar{\tau} \sin\left[2\pi \frac{(B_\perp - B_0)A}{\Phi_0} \right]}{E_{\mathrm{A}}\left[2\pi \frac{(B_\perp - B_0)A}{\Phi_0} \right] / \Delta}. \tag{7.4}$$

Equation 7.4 takes the fixed parameters $B_0^{(\mathrm{env})}$ and $B_{\mathrm{min.}}$ obtained from an independent dataset fitted with Eq. 7.3. There are therefore only three free parameters, as in Eq. 7.2: $I_0^{(\mathrm{env})}$, $\bar{\tau}$ and B_0. As for Device 1, I_0 is calculated as the maximum $I(B_\perp)$. The fit to the data in Fig. 7.14(b) is shown as the coloured lines, with the results for I_0 and $\bar{\tau}$ in (c) and (d) respectively [positive (negative) bias currents are indicated by the full (empty) markers]. This procedure was applied to every switching current measurement for Devices 2–4, to obtain the values shown in Figs. 7.8 and 7.9. Measurements for positive and negative $B_\parallel$ were combined using the same method as for Device 1, as described above.

7.8.3. Tunnelling Spectroscopy as a Function of $B_{\parallel}$

Measurements presented in Fig. 7.11 show conductance maps as a function of $B_{\perp}$, for increasing in-plane magnetic field $B_{\parallel}$. Conductance features at high source-drain bias which change as a function of $B_{\perp}$ are attributed to ABSs. In addition to ABSs, we can attribute some features in the conductance spectrum to multiple Andreev reflections or to disorder in the tunnelling barrier and sub-gap states in the density of states of the tunnelling probe [284]. For tunnelling spectroscopy measurements at an in-plane magnetic field, a first calibration measurement was performed at each in-plane field by sweeping the perpendicular field $B_{\perp}$ across a range of more than ± 3 mT. The position of $B_{\perp} \approx 0$ was determined from spectroscopic features, including the size of the superconducting gap, the shape and peak conductance of high-bias features, and the sharpness of spectral lines. Then, each spectroscopic map was taken across more than 5 oscillation periods. In all measurements, spectral features were consistent over the full range.

7.9. Supporting Information: Transverse Magnetic Field

Current-biased measurements for in-plane magnetic fields aligned perpendicular to the junction axis (B_{t}) are supported by tunnelling spectroscopy (see Fig. 7.15). Measurements were taken with an identical gate voltage configuration to those in Fig. 7.11. For small values of B_{t}, superconductivity in the tunnel probe was quickly softened such that conductance features occurred at low bias V_{SD} [Figs. 7.15(a, b)]. Conductance features were periodic with perpendicular magnetic field $B_{\perp}$, but with a weak dependence consistent with the small switching currents observed in Fig. 7.6. Conductance features did not resemble those of ABSs described by $E_{\mathrm{A}} = \Delta\sqrt{1 - \tau \sin^2(\varphi/2)}$, instead forming a complex network and crossing $V_{\mathrm{SD}} = 0$ in many places [Figs. 7.15(c, d)]. This became more pronounced at larger B_{t} [Figs. 7.15(e, f)] until the superconducting gap was largely suppressed and conductance features changed very little with $B_{\perp}$ [Figs. 7.15(g, h)].

No reopening of the superconducting gap was observed in these spectroscopic maps, up to large in-plane fields well beyond the value at which no oscillations in the switching current were visible. Conductance features are not well described by a simple model of ballistic ABSs in a short junction, instead showing crossings and interactions at high and low bias. These results indicate the absence of a phase transition, since there was no reopening of the superconducting gap. This is consistent with the lack of orbital effects for in-plane fields applied perpendicular to the junction axis. More sophisticated modelling of ABSs would be required to understand the conductance features in detail, which is beyond the scope of this work.

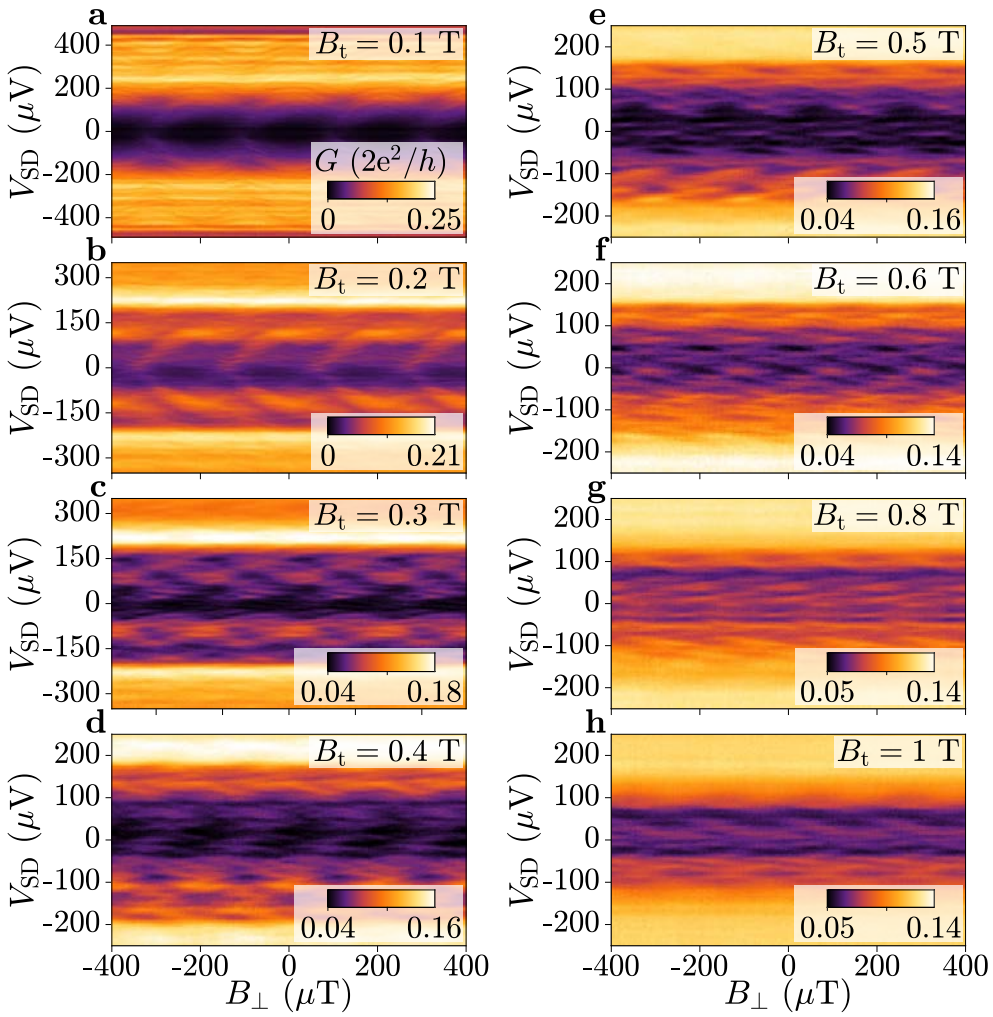

Figure 7.15. Tunnelling spectroscopy as a function of transverse in-plane magnetic field B_t. Differential conductance G as a function of source-drain bias voltage V_{SD} and perpendicular magnetic field $B_\perp$, for different values of in-plane magnetic field B_t. Measurements were taken at $V_{TG} = -1$ V, in an identical gate configuration as that of Fig. 7.11.

7.10. Supporting Information: Zero-Bias Peak in Tunnelling Spectroscopy

Tunnelling spectroscopy measurements at large in-plane fields $B_\parallel \approx 0.8$ T showed a peak in the differential conductance G close to zero source-drain bias V_{SD} [see Fig. 7.11(e)]. In measurements of similar devices, a zero-bias peak (ZBP) has been associated with the emergence of a topological phase [122, 123]. Here, we show additional data of the ZBP observed in Fig. 7.11(e) and comment on its origin.

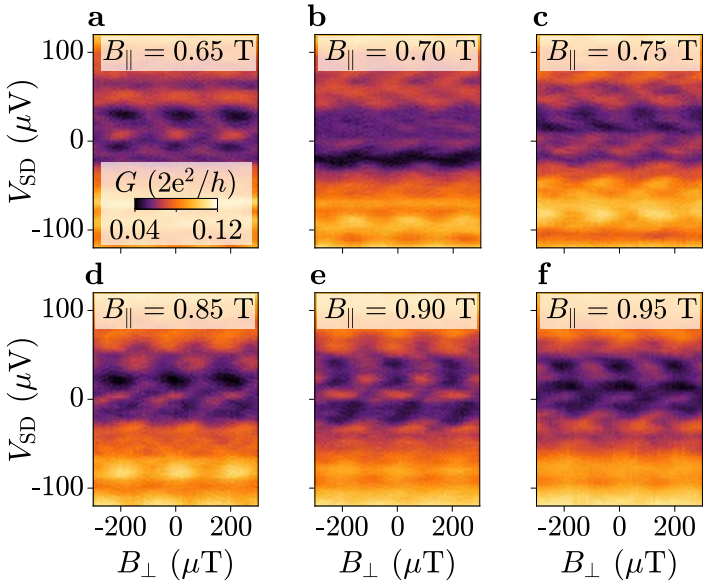

Figure 7.16. Dependence of zero-bias conductance peak of in-plane magnetic field. Differential conductance G as a function of source-drain bias V_{SD} and perpendicular magnetic field $B_\perp$, for different in-plane magnetic fields $B_\parallel$. The gate configuration was identical to that of Fig. 7.11, with $V_{TG} = -1$ V.

Figure 7.16 shows the conductance G as a function of perpendicular magnetic field $B_\perp$, for in-plane magnetic fields $B_\parallel > 0.6$ T (i.e. after the closure of the superconducting gap at $B_\parallel = 0.6$ T). Conductance maps show periodic lobe-like features: each map is plotted such that the centre of a lobe is aligned to $B_\perp = 0$. The top-gate voltage was set to $V_{TG} = -1$ V, identical to that in Fig. 7.11. A high-conductance feature is visible close to $V_{SD} = 0$ in many maps, but does not appear robustly for all in-plane fields and is rarely well separated from conductance features at higher source-drain bias.

To test the robustness of this ZBP, the magnetic field was fixed to $B_\parallel = 0.8$ T and $B_\perp = 0$, then the top-gate was varied from $V_{TG} = -0.92$ V to $V_{TG} = -1.05$ V [Fig. 7.17(a)]. Conductance features moved close to $V_{SD} = 0$ as a function of V_{TG}, but were not stable at $V_{SD} = 0$ for more than a few millivolts. Figures. 7.17(b-d) show the differential conductance as a function of perpendicular field $B_\perp$, at top-gate voltages offset from $V_{TG} = -1$ V by $-\delta V$, where $\delta V = 0$, 21 mV and 34 mV for (b-d) respectively. The conductance spectrum changed appreciably, and a high-conductance feature is evident in Fig. 7.17(b) but not in the others. Note also that the regime of Fig. 7.11(e) was not recovered in Fig. 7.17(b), despite the identical gate and field configuration.

Figure 7.18 shows the differential conductance G as a function of tunnel-barrier gate voltage, in the symmetric (V_T) and asymmetric ($V_{T,asymm.}$) configurations. The asymmetric configuration is defined such that $(V_{T,L}, V_{T,R}) \equiv (V_{T,asymm.}, V_{T,asymm.} - 16\ \mu V)$. High-conductance features were dependent on the tunnel gate voltage, and moved across the low-bias region.

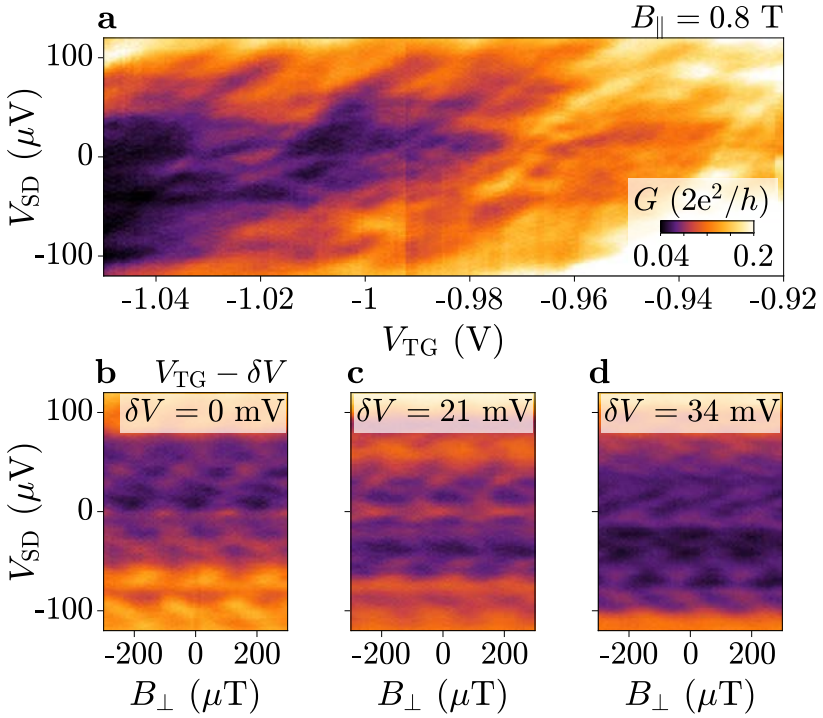

Figure 7.17. Dependence of zero-bias conductance peak on top-gate voltage. **a** Differential conductance as a function of top-gate voltage V_{TG}, at $B_{\parallel} = 0.8$ T and $B_{\perp} = 0$. **b-d** Conductance maps as a function of perpendicular field $B_{\perp}$, at $B_{\parallel} = 0.8$ T. The top-gate voltage was set to $V_{\mathrm{TG}} - \delta V$, where $V_{\mathrm{TG}} = -1$ V and $\delta V = 0$, 21 and 34 mV for (i–k) respectively.

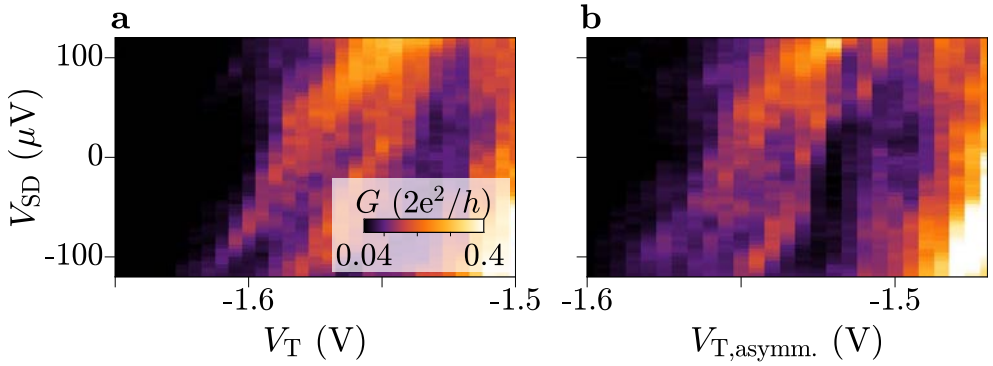

Figure 7.18. Dependence of zero-bias conductance peak on tunnel barrier voltages. **a** Differential conductance as a function of bias V_{SD} and tunnel-gate voltage V_{T}, at $B_{\parallel} = 0.8$ T and $B_{\perp} = 0$. The top-gate voltage was set to $V_{\mathrm{TG}} = -1$ V. High conductance features are tuned by V_{T} across the full bias range. **b** Same as (a), with the tunnel-gate voltage set to an asymmetric configuration $(V_{\mathrm{T,L}}, V_{\mathrm{T,R}}) \equiv (V_{\mathrm{T,asymm.}}, V_{\mathrm{T,asymm.}} - 16\ \mu\mathrm{V})$.

Zero-bias peaks were shown to be sensitive to in-plane magnetic fields $B_{\parallel}$ and the top-gate voltage V_{TG}, and tunnel-barrier-dependent conductance features were shown to move close to $V_{\mathrm{SD}} = 0$. These results suggest that ZBPs were most likely due to ABSs coalescing close to zero energy, rather than being topological in origin. This is despite the gap closure and opening, shown in Fig. 7.11 and associated with orbital effects in the superconducting leads. This result suggests that additional levels of caution are needed in interpreting ZBPs as indicative of a topological transition, even in the presence of gap closure and reopening. We note that the top-gate voltage $V_{\mathrm{TG}} = -1$ V was chosen to have good visibility of conductance features at low $B_{\parallel}$, to be in a regime of single-subband occupation (based on supercurrent measurements) and to match a value used in supercurrent measurements (see Figs. 7.4 and 7.5). It was not chosen based on the observation of a ZBP; the emergence of a ZBP after gap closure and reopening was by coincidence rather than by fine-tuning of V_{TG}.

7.11. Supporting Information: Type B Shifts

In this section we present additional tunnelling spectroscopy measurements performed as a function of in-plane magnetic field $B_{\parallel}$. First, we show measurements of Device 1 taken at different gate voltages to that presented in Section 7.4, namely $V_{\mathrm{TG}} = -0.6$ V and $V_{\mathrm{TG}} = -1.4$ V. The induced superconducting gap closed at the same in-plane magnetic field $B_{\parallel} = B_{\parallel}^{\Phi} = 0.6$ T, independent of gate voltage. Second, we present measurements of Device 5, which was identical to Device 1 other than the length of the superconducting leads $L_{\mathrm{SC}} = 400$ nm. Gap closure and reopening was observed at $B_{\parallel} = 0.4$ T, consistent with supercurrent measurements on a similar device shown in Section 7.3.

7.11.1. Tunnelling Spectroscopy for Different Top-Gate Voltages

Figures 7.19 and 7.20 show tunnelling spectroscopy maps for increasing in-plane magnetic field $B_{\parallel}$, at top-gate voltages of $V_{\mathrm{TG}} = -0.6$ V and $V_{\mathrm{TG}} = -1.4$ V respectively. The tunnel-barrier gates were adjusted to be in the tunnelling regime, so were set to $V_{\mathrm{T}} = -2.46$ V and $(V_{\mathrm{T,L}}, V_{\mathrm{T,R}}) = (-1.835, -1.805)$ V for Figs. 7.19 and 7.20 respectively. At $V_{\mathrm{TG}} = -0.6$ V, many more conductance features were present relative to $V_{\mathrm{TG}} = -1$ V [Fig. 7.19(a) compared with Fig. 7.11(a)], consistent with more modes present in the junction. In contrast, only few modes were visible at $V_{\mathrm{TG}} = -1.4$ V [Fig. 7.20(a)]. No $B_{\perp}$-dependent conductance features were observed for top-gate voltages $V_{\mathrm{TG}} < -1.4$ V. For increasing in-plane magnetic field $B_{\parallel}$, superconductivity in the tunnel probe was suppressed [Figs. 7.19(b) and 7.20(b)] and $B_{\perp}$-dependent conductance features moved closer to $V_{\mathrm{SD}} = 0$ [Figs. 7.19(c) and 7.20(c)]. At $B_{\parallel} = 0.6$ T, the superconducting gap was suppressed at both top-gate voltages and conductance features had very weak $B_{\perp}$-dependence close to $V_{\mathrm{SD}} = 0$ [Figs. 7.19(d) and 7.20(d)]. For larger in-plane fields, some phase-dependence appeared to recover although this was difficult to distinguish due to the poor visibility of conductance features corresponding to individual ABSs [Figs. 7.19(e, f) and 7.20(e, f)].

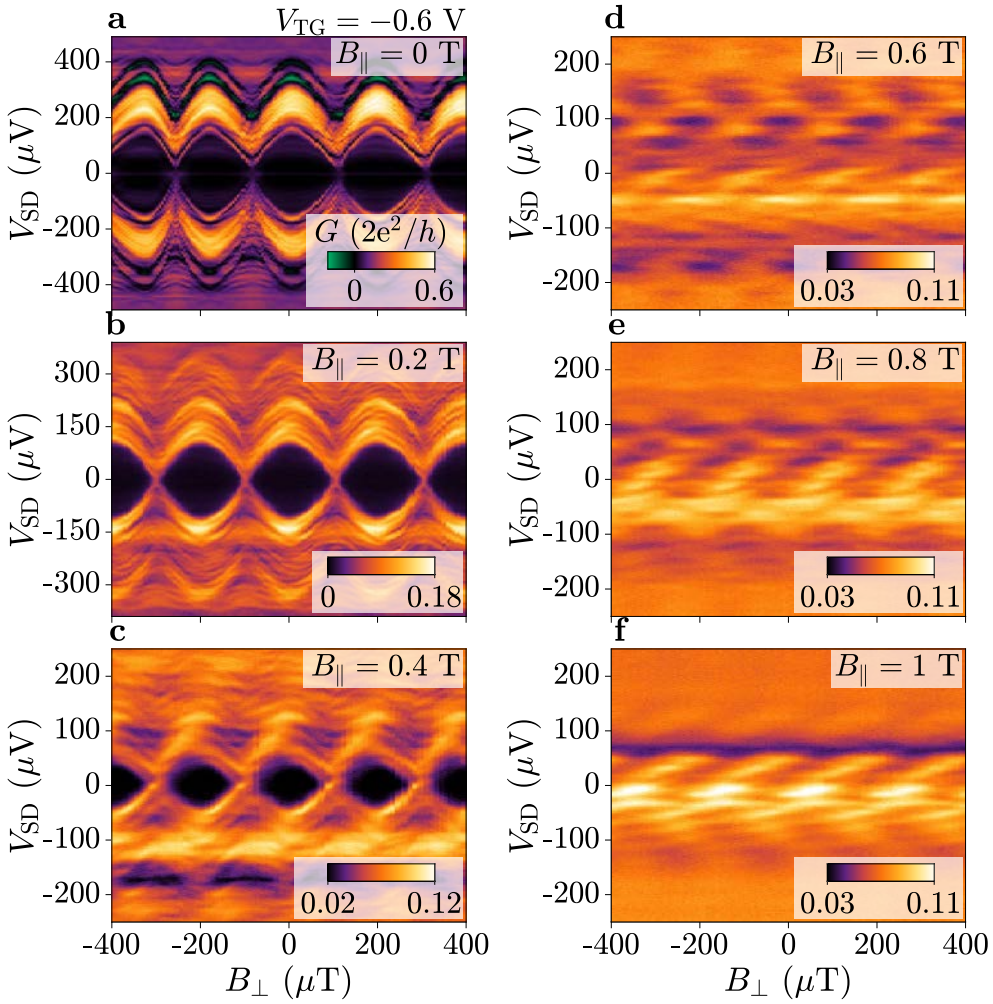

Figure 7.19. Tunnelling spectroscopy of Device 1 at $V_{TG} = -0.6$ V. Differential conductance G as a function of source-drain bias V_{SD} and perpendicular magnetic field $B_\perp$, for different values of in-plane magnetic field $B_\parallel$. Taken at a top-gate voltage of $V_{TG} = -0.6$ V and tunnel-gate voltage $V_T = -2.46$ V.

The superconducting gap was suppressed at $B_\parallel = 0.6$ T at all measured top-gate voltages. This is consistent with current-biased measurements [see Fig. 7.4(a)], where the minimum in the switching current occurred at $B_\parallel = 0.6$ T independent of top-gate voltage V_{TG}. These results suggest that the cause of gap closure is independent of the properties of the normal region of the junction. Since orbital effects depend only on the properties of the superconducting leads, these findings are consistent with gap closure induced by orbital effects.

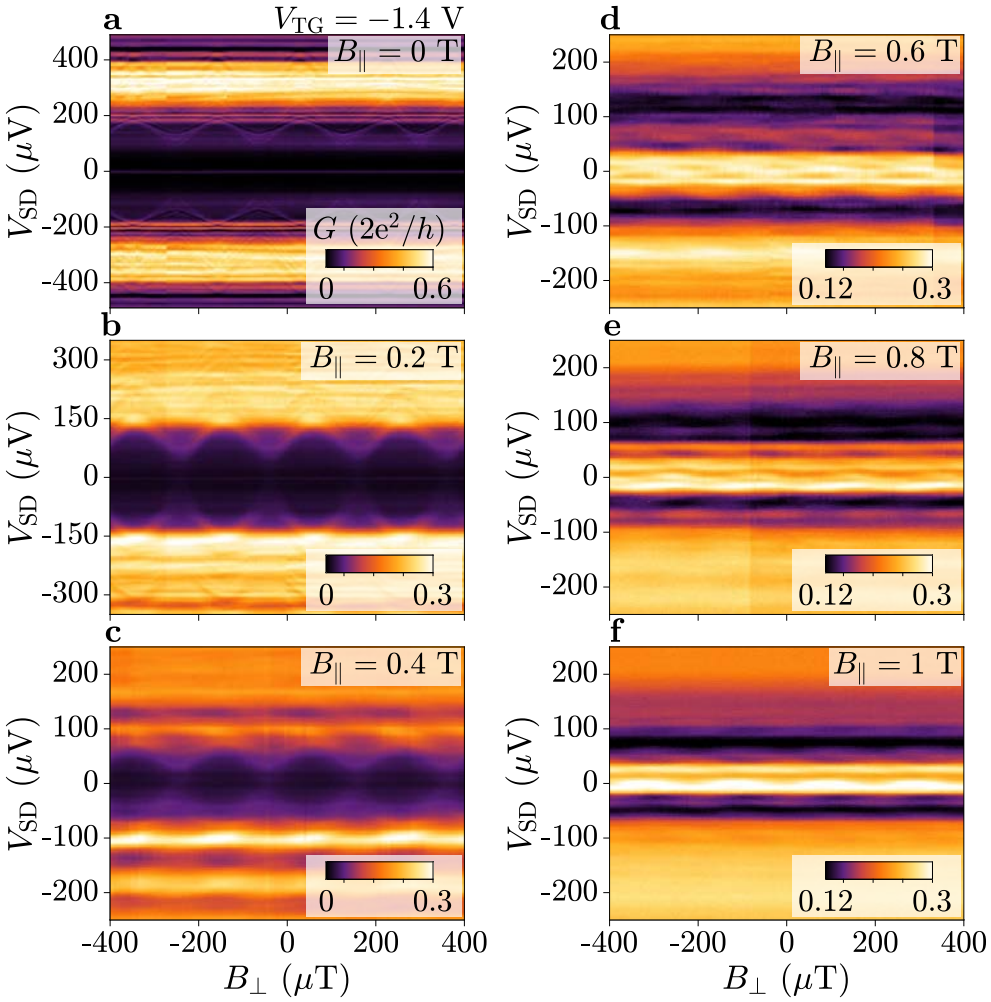

Figure 7.20. Tunnelling spectroscopy of Device 1 at $V_{TG} = -1.4$ V. Differential conductance G as a function of source-drain bias V_{SD} and perpendicular magnetic field $B_\perp$, for different values of in-plane magnetic field $B_\parallel$. Taken at a top-gate voltage of $V_{TG} = -1.4$ V and tunnel-gate voltages $(V_{T,L}, V_{T,R}) = (-1.835, -1.805)$ V.

7.11.2. Tunnelling Spectroscopy in Device 5

Tunnelling spectroscopy was performed in an additional device, which was identical to Device 1 in all aspects other than the length of the superconducting leads $L_{SC} = 400$ nm. The superconducting loop in this device, Device 5, was identical to that of Device 2 [Figs. 7.11(a, b)], where the switching current was measured. Conductance maps for different values of in-plane magnetic field $B_\parallel$ are shown in Figs. 7.21 and 7.22, for $V_{TG} = 0.8$ V and $V_{TG} = 0.2$ V respectively. These gate voltages correspond to the situation of a large [Fig. 7.21(a)] or small [Fig. 7.22(a)] number of modes, similar to Figs. 7.19 and 7.20 for Device 1. On increasing $B_\parallel$, the superconducting gap in the tunnel

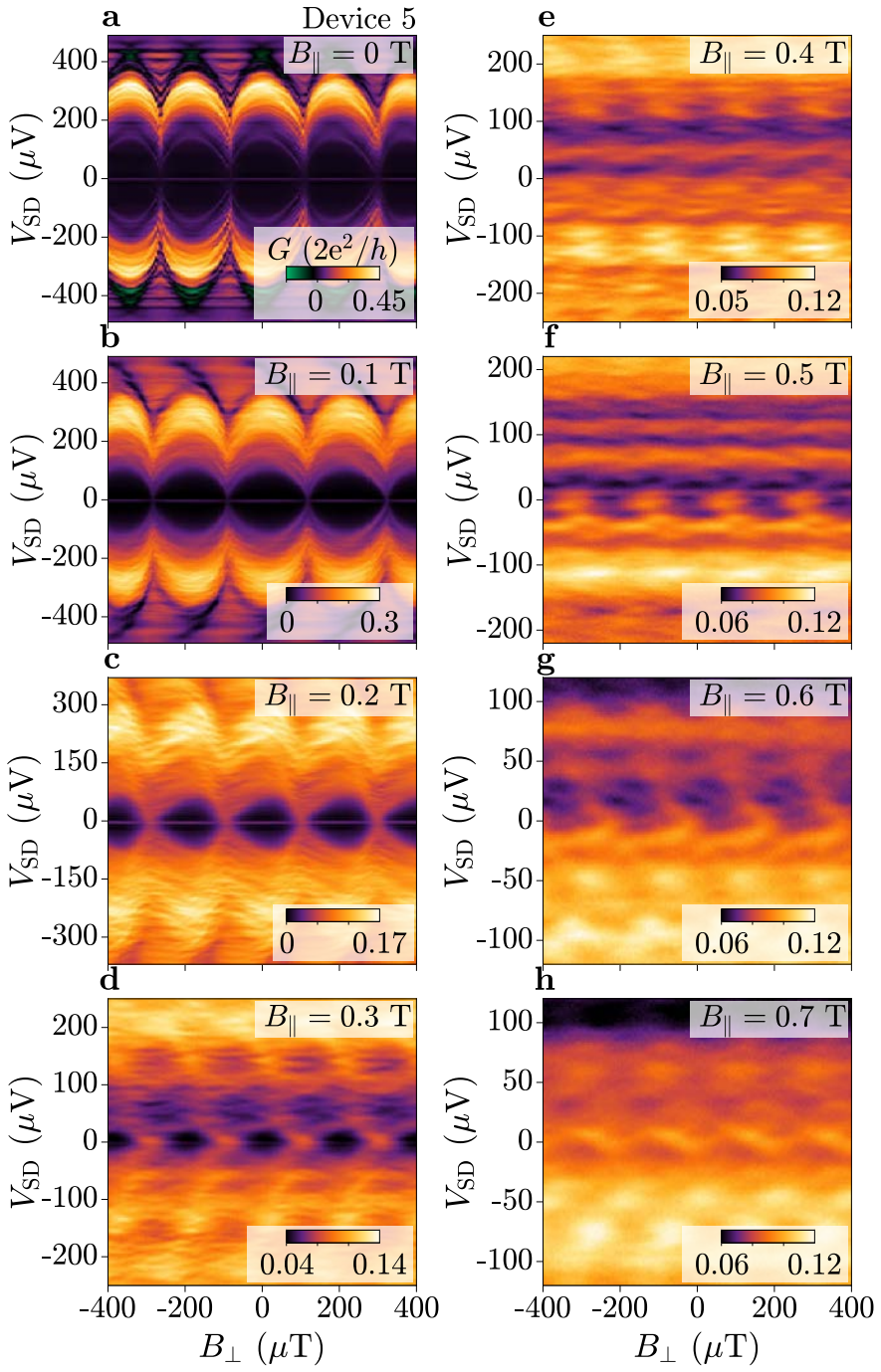

Figure 7.21. Tunnelling spectroscopy of Device 5 at $V_{TG} = 0.8$ V. Differential conductance G of Device 5, which was identical to Device 1 other than the superconducting lead length, which was $L_{SC} = 400$ nm. Conductance maps for different in-plane magnetic fields $B_\parallel$, taken at a top-gate voltage $V_{TG} = 0.8$ V.

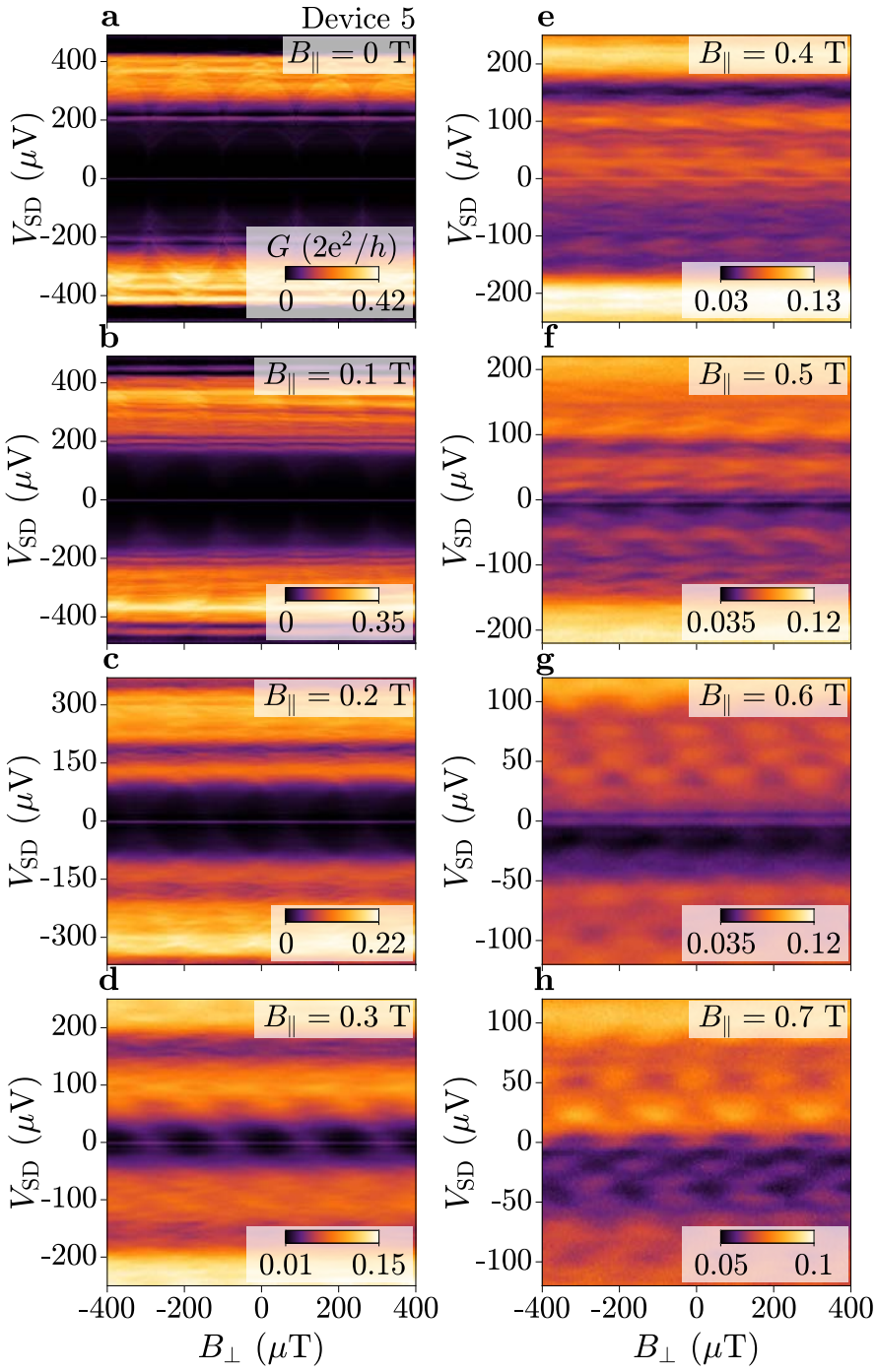

Figure 7.22. Tunnelling spectroscopy of Device 5 at $V_{TG} = 0.2$ V. Differential conductance G of Device 5 at different in-plane magnetic fields $B_\parallel$, for $V_{TG} = 0.2$ V.

probe was softened [Figs. 7.21(b) and 7.22(b)] and conductance features moved closer to $V_{\mathrm{SD}} = 0$ [Figs. 7.21(c, d) and 7.22(c, d)] until the gap between conductance features was closed at $B_{\parallel} = 0.4$ T [Figs. 7.21(e) and 7.22(e)]. For larger $B_{\parallel}$, the gap between conductance features reopened and there was a stronger $B_{\perp}$-dependence [Figs. 7.21(f, g) and 7.22(f, g)]. At $B_{\parallel} = 0.7$ T, the gap closed again and superconducting features were suppressed [Figs. 7.21(h) and 7.22(h)].

Closure of the superconducting gap was shown to occur at $B_{\parallel} = 0.4$ T in Device 5, for two top-gate voltages. This is consistent with the minimum in the switching current of Device 2, which had an identical SQUID loop, Al constriction and SNS junction. Tunnelling spectroscopy showed a reopening of the gap between conductance features at larger in-plane fields, where a reentrant supercurrent was measured in current-biased experiments. The closure of the superconducting gap and minimum in the switching current both occurred at $B_{\parallel} \approx 0.4$ T, the expected in-plane field at which one flux quantum threads the area underneath the superconducting leads. This supports the conclusion that gap closure in these devices was induced by orbital effects in the superconducting leads.

7.12. Supporting Information: Type A Shifts

7.12.1. Type A Phase Shifts in the Current-Phase Relation

Gate-dependent Type A phase shifts were observed in all devices, for in-plane fields $|B_{\parallel}| \lesssim |B_{\parallel}^{\Phi}|$, where $B_{\parallel}^{\Phi}$ is the field at which the supercurrent was minimum. The results for Devices 1–4 are summarised in Figs. 7.23 and 7.24. The perpendicular field offset relative to the most negative gate voltage, ΔB_0, was linear with in-plane field $B_{\parallel}$ with steeper gradient β for more positive top-gate voltage V_{TG} [Fig. 7.23, colours defined in Fig. 7.24]. The data (circles) are fitted with a linear curve (lines) to extract the gradient β, which is plotted in Fig. 7.24 (filled circles) for Devices 1–4. The maximum switching current I_0 at $B_{\parallel} = 0$ is also plotted as a function of top-gate voltage V_{TG} (empty squares). The trend of β with V_{TG} is similar to that of the maximum switching current I_0.

At the maximum V_{TG}, where I_0 was large, the gradient was $\beta \gtrsim 100$ μT/T for all devices independent of the superconducting lead length L_{SC}. The size of the gradient β is compared with the switching current at $B_{\parallel} = 0$, which is linked to the electron sheet density in the junction; at lower densities there are fewer transverse modes to carry the supercurrent [249]. The maximum switching current can therefore be used to compare density regimes in the different devices, despite that the gate voltages differ between devices due to local disorder, inhomogeneous material properties and fabrication imperfections. For decreasing V_{TG}, the carrier density decreases causing both I_0 and β to decrease [Fig. 7.24]. This follows a trend consistent with that of Refs. [136, 232], which directly measured the spin-orbit coupling strength as a function of carrier density in similar InAs quantum wells.

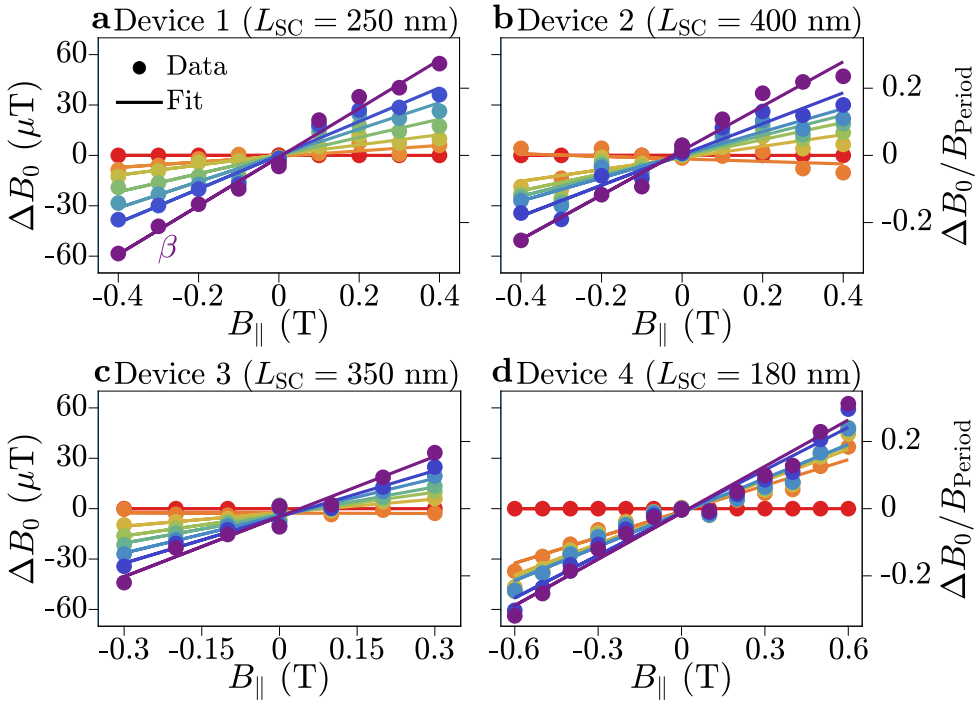

Figure 7.23. Type A phase shifts in Devices 1-4. Perpendicular field offset ΔB_0 relative to the most negative top-gate voltage, as a function of in-plane magnetic field $B_\parallel$ for different top-gate voltages V_{TG} [indicated by the colour, defined in Fig. 7.24], for Devices 1-4 respectively. Data (circles) is fitted with a linear curve at each V_{TG} (lines), giving the gradient β.

7.12.2. Phase Shifts due to Loop Inductance

Switching current measurements were performed by applying large bias currents to the SQUID device. Since the epitaxial Al was very thin, the superconducting film had an appreciable kinetic inductance L_K, which generates a flux $\Phi_K = L_K(I_{cons.} - I_{SNS})/2$, where $I_{cons.}$ and I_{SNS} are the currents flowing in the Al constriction and SNS junction, respectively. The kinetic inductance of the loop is estimated as $L_K = N_\square L_{\square,K} \approx 66$ pH, where $N_\square = 38$ is the number of squares in the superconducting loop and $L_{\square,K} \approx 1.7$ pH is the kinetic inductance per square calculated from Eq. 3.2. [198]. This gives a shift of $\Delta B_{Kin.} \approx 110$ μT, for typical currents $(I_{cons.} - I_{SNS})$ in the SQUID loop. The measured shift $\Delta B_{Kin.}$ between positive and negative currents is shown in Fig. 7.25. No top-gate dependence was observed, so points were averaged over all top-gate voltages. The field shift $\Delta B_{Kin.}$ increased for increasing magnitude of in-plane magnetic field, consistent with an increasing kinetic inductance due to quasiparticle generation in the superconducting loop. The values of $\Delta B_{Kin.}$ in Fig. 7.25 are consistent with the field shift estimated from the kinetic inductance L_K.

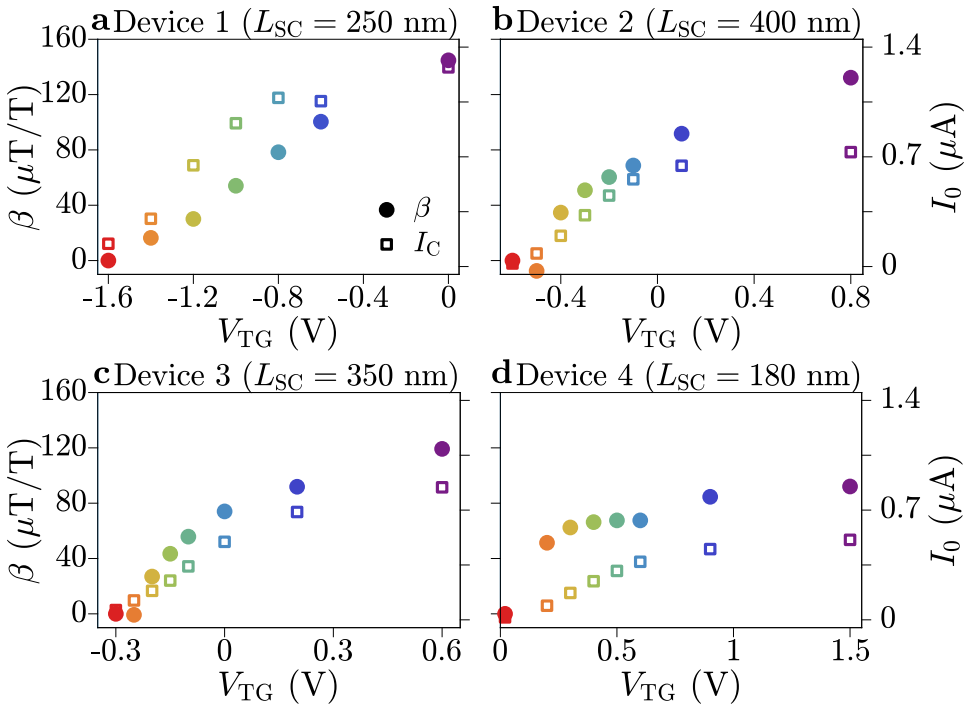

Figure 7.24. Comparing the size of Type A phase shifts to the maximum switching current. Gradient β extracted from Fig. 7.23 plotted as a function of top-gate voltage (filled circles, left axis). The maximum switching current as a function of top-gate voltage is also plotted for each Device (empty squares, right axis).

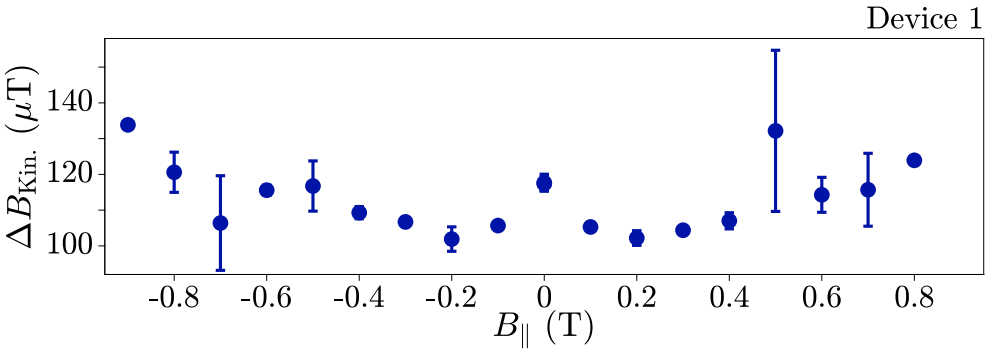

Figure 7.25. Phase shifts due to kinetic inductance. Shift in perpendicular field between current-phase relation traces measured with positive and negative bias currents, $\Delta B_{\mathrm{Kin.}}$. Points are plotted as an average over all top-gate voltages V_{TG}, with errorbars indicating the standard deviation of all V_{TG} values.

8 Conclusions and Outlook

In this thesis, we have presented a detailed study of planar Josephson junctions (JJs) in an InAs/Al heterostructure containing highly transmissive Andreev bound states (ABSs). Here, we summarise the main findings and outline avenues of research to be explored in the future.

In Chapters 4 and 5 we studied the **phase dynamics of planar JJs**, in isolation and in a superconducting quantum interference device (SQUID). We found that the switching current from the superconducting to resistive state was strongly affected by phase fluctuations, such that switching events occurred at bias currents much lower than the critical current (Section 4.2). The relative dominance of macroscopic quantum tunnelling and phase diffusion was tuned via gate voltages and magnetic fields (Section 4.3), and changes to the device geometry gave rise to thermal activation processes (Section 4.4). The effect of large phase fluctuations on a small JJ was partially alleviated by incorporating it into an asymmetric SQUID, leading to an increase in the switching current of the small junction by more than a factor of two (Section 5.1). The phase escape dynamics were further tuned via a magnetic flux threading the superconducting loop (Section 5.2). The remarkable discrepancy between the switching and critical currents in these devices has significant implications for understanding device performance (Section 3.1.2) and inferring the properties of ABSs. The effect of large shunt capacitances on phase dynamics could be studied in future experiments, to further understand the phase escape mechanisms and to guide towards optimised device designs.

In Chapter 6 we presented tunnelling spectroscopy measurements on a planar JJ, and investigated the **conductance response to microwave irradiation**. Replicas in the conductance spectrum were shown to originate from photon assisted tunnelling (PAT) between the probe and the junction density of states (Section 6.2). In addition, the current-phase relation (CPR) showed distortions for large microwave field amplitudes, consistent with a non-thermal occupation of ABSs (Section 6.3). Careful tests of the microwave coupling strength, using gate-tunability and supercurrent measurements, showed that PAT was the dominant mechanism for conductance replicas and ruled out interpretations of Floquet-Andreev states in our devices. We demonstrated that the emergence of conductance replicas under microwave irradiation is not sufficient to claim a change in the eigenstates of the junction due to light-matter coupling (i.e. the emergence of Floquet-Andreev states). More efficient microwave coupling schemes, such as via fast signals to gate electrodes, could enable the emergence of Floquet states at large drive powers. Signatures of Floquet states should depend on the Fermi

energy in the system and lead to avoided crossings in the energy spectrum, and future experiments might control the polarisation of the electromagnetic radiation. The techniques employed here can be readily implemented to generic systems where Floquet states might occur, to distinguish them from effects arising due to PAT.

In Chapter 7, we reported **phase shifts in planar JJs subjected to large in-plane magnetic fields**. Gate-dependent phase shifts emerged in the CPR for fields directed perpendicular to the current flow (Section 7.2), consistent with a φ_0-junction with Rashba spin-orbit coupling. Phase shifts in the ABS spectrum matched those of the CPR (Section 7.5), implying that ABSs with high transmission make a significant contribution to φ_0-shifts. Distinct phase shifts at larger magnetic fields were concomitant to a minimum in the switching current (Section 7.2) and depended on the superconducting lead length (Section 7.3), suggesting an orbital origin. Tunnelling spectroscopy revealed closure and reopening of the superconducting gap correlated to the phase shift and switching current minimum (Section 7.4), mimicking signatures of a topological transition. Our results show the importance of orbital effects in planar devices, and their interplay with Zeeman and spin-orbit effects. We have established a new baseline understanding of InAs/Al JJs subject to in-plane magnetic fields, which guides towards a more complete understanding of anomalous phase shifts and topological transitions in planar JJs. Further experiments could investigate the dependence of φ_0-shifts on the number and transmission distribution of ABSs, by varying the junction width and length. By implementing spectroscopic probes on both ends of the JJ, future studies could establish the influence of magnetic vector potentials on phase shifts [302], identify non-local effects [292] or relate non-reciprocal currents to asymmetries in the ABS spectrum [101, 103, 303].

This thesis presented a thorough investigation of planar JJs, giving an improved understanding towards gate-tunable qubits, superconducting circuit elements and novel Andreev bandstructures. In addition to the specific proposals made for each experiment, we also comment on these areas of interest in hybrid superconductor-semiconductor devices. For qubit technologies, device manipulation must be performed with high energy resolution on fast timescales. This is possible with radio frequency techniques [304, 305], which have recently been integrated with **planar JJs in low-loss architectures** [301, 306–308]. This is a crucial step towards realising advanced gate-tunable qubits. In superconducting electronics, tunable φ_0-junctions as those in Chapter 7 require large in-plane magnetic fields, which could be detrimental to complex superconducting circuits. A possible solution is the **Andreev molecule** [309–316]: two coupled JJs which produce a large, tunable φ_0-shift at zero magnetic field [317, 318]. Finally, an exciting opportunity to generate complex Andreev energies is to move beyond two-terminal JJs to **multi-terminal devices**, which are expected to exhibit large spin-splitting at zero magnetic field [319, 320], ground state parity transitions [319, 320] and topological phases of matter [321–325].

A Full Fabrication Process

Here we give a detailed description of the fabrication process, from receiving the wafer to loading devices into the dilution refrigerator. Fabrication was performed in the Binnig and Rohrer Nanotechnology Center.

A.1. Chip Preparation

Material heterostructures were grown on 2 inch wafers, and stored in vacuum or an Ar atmosphere until ready to be processed. Devices were patterned on 5×5 $(\text{mm})^2$ chips, to conserve material and to be compatible with the measurement sample space. Straight edges and precise dimensions were necessary for good alignment in subsequent lithography steps, so material was diced to the appropriate size.

The wafer was protected with optical resist before dicing. A 1 μm thick layer of MicroChemicals AZ 1512 positive photoresist was spin coated on the chip at a speed of 4000 rpm for 40 s. The resist was hardened by baking on a hot plate at 110°C for 60 s.

The material was diced into 5 $(\text{mm})^2$ pieces. Those closest to the wafer centre were preferentially chosen. Before beginning chip fabrication, the photoresist was stripped by rinsing in solvents. Chips were first rinsed on a cleanroom towel before transferring to a beaker, to avoid contamination from InP dust. Chips were rinsed first in acetone for 2 minutes to remove organic residues, then in isopropanol (IPA) for 2 minutes as a more gentle clean and to prevent residues from drying acetone. The chip was dried with a nitrogen gun.

A.2. Lithography Step I: Mesa Etch

The first lithography step was to define mesa structures onto which the devices will be patterned, by etching into the III-V material. The etch must be sufficiently deep that there is no parallel conduction between devices. Alignment markers are also defined in this step.

Device structures are patterned with electron beam lithography, using a positive polymethyl methacrylate (PMMA) resist. A single layer of AllResist-Positive (AR-P) 672.03 resist was spin-coated at 6000 rpm to give a 100 nm thick film covering the chip. The resist was hardened by baking at 120°C for ~ 5 minutes.

The exposed chip was developed using a mixture of Methyl Isobuthyl Ketone (MIBK) and IPA, in a ratio of 1:2. After developing for 70 s with some agitation, the chip was

rinsed in IPA for 30 s to stop the development. The chip was then dried with a nitrogen gun. Small residues of resist were removed after development by exposing the chip to an oxygen plasma with 200 W of power, for 30 s.

The first step of the etching process was to remove the top Al layer, which was done using a 25 s etch in Transene D Al etchant at 40°C. The etch was stopped by rinsing in hot deionised (DI) water for 10 s, and then cold DI water for $\sim$ 1 minute.

The second step was to etch the III-V, which was done with a $H_2O : C_6H_8O_7 : H_3PO_4 : H_2O_2$ solution with the concentration ratio 220 : 55 : 3 : 3. Importantly, this step was performed at room temperature, using a magnetic stirrer. An etch of approximately 9 minutes gave an etch depth of $\sim$ 350 nm into the III-V heterostructure, which was measured for each chip using a profilometer. Shallower etch depths were shown to give parallel conduction between devices in some cases, after deposition of the dielectric layer.

The III-V etch was approximately isotropic, meaning that there was lateral etching underneath the predefined areas. For high quality Al films, some portion of the Al film remained continuous over the mesa edge. This could prevent a uniform coverage of the dielectric layer, such that the gate layers might be connected to the Al layers in some spots. The overhanging Al was therefore etched in Transene D Al etchant, for 25 s at 40°C.

Finally, the PMMA resist was stripped by rinsing in acetone and IPA for 2 minutes each.

A.3. Lithography Step II: Aluminium Etch

The second lithography step was to define the superconducting features of the device, by selectively etching the Al on top of the mesa structures. This defines the superconducting loop, probe contacts and junction regions. As such, it is the most sensitive step in the process.

A 100 nm film of PMMA AR-P 672.03 resist was spin-coated at a rate of 6000 rpm, and then baked at 120°C for 5 minutes. As for the first lithography step, structures were patterned in the resist using electron beam lithography.

After exposure, the PMMA was developed in an MIBK:IPA solution (ratio 1:2) for 60 s, before being rinsed in IPA for 30 s and dried with a nitrogen gun. Small portions of resist were removed by exposing the chip to an oxygen plasma of 100 W power for 3 s.

The Al was etched in Transene D Al etchant at 50°C, for an etch time of 4 s. The chip was immediately rinsed in hot DI water for 10 s and cold DI water for $\sim$ 1 minute. The PMMA resist was stripped in acetone and IPA, for 2 minutes each, before drying with a nitrogen gun.

After drying the chip, it was immediately transferred to the atomic layer deposition (ALD) machine for deposition of the dielectric layer. The chip was exposed to air for less than 2 minutes, to limit the potential contamination of the surface III-V layer in the junction region.

A first dielectric layer of Al_2O_3 was deposited using thermal ALD, at a temperature

of 110°C. A 30 cycle deposition gave a layer thickness of approximately 3 nm. The thermal ALD step was used to limit the exposure of the thin Al film to an oxygen plasma (in earlier steps, sensitive regions were covered with resist, unlike for the dielectric deposition), since this was shown to degrade the superconducting properties of the film by thickening the surface oxide of the Al film.

A second dielectric layer of HfO_2 was deposited using plasma ALD, at a temperature of 120°C. A typical deposition of 150 cycles gave a dielectric thickness of 15–17 nm. The total deposition time was approximately one hour.

Before continuing with chip fabrication, test devices were imaged using a scanning electron microscope (SEM). A successful etch gave Al features which were $\sim$ 10 nm constricted relative to the design, consistent with an isotropic etch of the 10 nm film. Hence, fabricated Josephson junctions had a length which was $\sim$ 20 nm longer than that of the design. Reported junction dimensions were taken from the design values.

A.4. Lithography Step III: Inner Gate Deposition

The third lithography step was to define fine gate features on top of the dielectric layer. To allow high resolution of patterned features, thin resist and metallic layers were used.

A double layer of resist was used for this step. The resist AR-P 669.04 was spin-coated at a rate of 6000 rpm to give a nominally 200 nm layer coating the chip. This was baked on a hot plate set to 120°C for 5 minutes. A second resist layer of AR-P 672.02 was then spin-coated on top, at a rate of 6000 rpm to give a 50 nm thick top layer.

After features were written into the resist using exposure to the electron beam, the resist was developed in a MIBK:IPA (1:2 ratio) mixture for 60 s. The development was stopped by rinsing in IPA for 30 s. After drying with the nitrogen gun, the chip was exposed to an oxygen plasma at 200 W for 15 s to remove excess resist.

Metallic layers of Ti (5 nm) and Au (20 nm) were deposited onto the developed chip using electron beam evaporation. After the metal deposition, the resist was "lifted-off" by placing the chip into an already-hot beaker of dimethylsulfoxide (DMSO) solvent at 120°C. The chip was left in the beaker for at least 10 minutes. After this time, the chip was repeatedly sprayed with acetone and IPA to remove any residual gold flakes. This procedure of spraying with acetone and IPA was repeated up to 4 times. Without letting the chip dry, it was then thoroughly rinsed in acetone and IPA, for 2 minutes each.

A.5. Lithography Step IV: Outer Gate Deposition

The final lithography step consisted of depositing thick metal gate leads to connect the fine gate features on top of the mesa plateau to bonding pads far from the device, which were defined in the same step.

A thick double layer resist was used. The first layer of methylacrylate (MA) resist AR-P 617.08 was spin-coated at 300 rpm to give a nominally 586 nm thick layer. This

was baked at 120°C for 5 minutes. The second layer consisted of AR-P 672.03 resist, spin-coated at 6000 rpm to be 100 nm thick.

After exposure, the chip was developed in an MIBK:IPA (1:2 ratio) mixture for 120 s, before rinsing in IPA for 60 s and drying with a nitrogen gun. Exposure to an oxygen plasma of 200 W for 30 s was used to remove residual resist.

Thick metallic layers were deposited across the chip using an electron beam evaporator. A 10 nm adhesion layer of Ti was deposited first, and then a $>$ 400 nm layer of Al. As for the inner gate step, lift-off of the resist was done by rinsing the chip in DMSO at 120°C for $>$ 10 minutes, before repeatedly spraying with acetone and IPA. The chip was not dried until all metallic flakes had been removed, which typically required multiple solvent rinsing steps.

Before preparing the chip for measurement, test devices were imaged in the SEM. Potential failure of the gate deposition step could be identified at this stage, before measurement of devices. Successful processing resulted in fine gate features separated by $\gtrsim$ 40 nm.

A.6. Wire Bonding

Finally, the chip was prepared for measurement by gluing to a QDevil printed circuit board (PCB) and making wire bond connections between the PCB pads and the bonding pads on the device. Bonding pads were $\gtrsim 100 \times 100$ $(\mu\text{m})^2$.

The chip was glued to the PCB using PMMA resist. A droplet of resist was placed in the centre of the sample space, and then the PCB was placed on a hot plate at 110°C. As the resist began to harden, the chip was placed onto the resist such that it was fixed in place.

The PCB was connected to a large Al block, such that all electrical pads were connected together. During bonding, the Al block was also connected to the ground of the bonding machine, to limit static discharge. Bonds were made first to the PCB, and then to the device.

Bonds were made to multiple devices. Typically, two pads on the PCB were also bonded together to measure the line resistance and to confirm good electrical contact after loading into the dilution refrigerator. An additional bond was often made to the cavity of the PCB (the metallic region onto which the device was glued) or onto the frame of Al at the edge of the chip. The line connected to this bond was left grounded during all experiments. After bonding, the PCB was transferred to the measurement system and loaded into the dilution refrigerator as soon as possible.

B Potential Barrier in Junctions with Large Transparency

Theoretical analysis presented in this section was done by Clemens Müller. D.Z.H. performed the fitting of the non-sinusoidal potential, outlined in the final paragraph.

Throughout this work, analysis of phase escape has been based on equations derived for Josephson junctions with a sinusoidal current-phase relation (CPR). However, the presence of highly transmissive modes in the planar Josephson junctions measured here give a non-sinusoidal CPR. In the absence of a theory for phase escape in junctions with a non-sinusoidal CPR, the existing theory was used. In this section, we address differences between the washboard potential in the two cases and justify the use of a sinusoidal theory for phase escape.

A Josephson junction with a non-sinusoidal CPR can be modelled as a junction containing N modes with identical effective transmission τ (see Eq. 6.5). This equation can be integrated to arrive at the potential energy, which under a current bias I_b gives

$$U(\varphi) = -2\sqrt{2}I_0\sqrt{2-\tau(1-\cos\varphi)} - I_\mathrm{b}\varphi \tag{B.1}$$

as the form of the washboard potential in reduced units. The potential barrier can be found analytically in this case, and gives the result

$$\begin{aligned}\Delta U(I_\mathrm{b}) = \frac{1}{\tau}[&I_\mathrm{C}\sqrt{B_- - 8(\tau-2)} - I_\mathrm{C}\sqrt{-B_+ - 8(\tau-2)} + \\ &+ I_\mathrm{b}\tau\arccos(B_-/8\tau) - I_\mathrm{b}\tau\arccos(-B_+/8\tau)],\end{aligned} \tag{B.2}$$

where $I_\mathrm{C} = I_0\tau$ and

$$A = \sqrt{16I_\mathrm{C}^4 + 8I_\mathrm{b}^2I_\mathrm{C}^2(\tau-2) + I_\mathrm{b}^4\tau^2}, \tag{B.3}$$

$$B_\pm = 2\tau\left(A \pm I_\mathrm{b}^2\tau\right)/I_\mathrm{C}^2. \tag{B.4}$$

The general dependence of the potential barrier used in the sinusoidal formalism is

$$\Delta U(I_\mathrm{b}) = 2I_\mathrm{C}\left(1 - \frac{I_\mathrm{b}}{I_\mathrm{C}}\right)^n, \tag{B.5}$$

with $n = 3/2$.

To evaluate how the bias-dependence of the non-sinusoidal potential, we fit Eq. B.2 with Eq. B.5 for different values of τ. The fit took two free variables in Eq. B.5: I_C and

n. For a fixed I_0, the fitted and exact result for I_C were identical. The values of n were 1.5 for $\tau \sim 0$, and increased to 1.54 for $\tau \to 1$. This demonstrates that the dependence on the potential barrier is almost identical in the sinusoidal and non-sinusoidal case, where the critical current is defined as the maximum value of the CPR. However, this approach does not account for differences in the shape of the potential, which could give rise to differences in the equation for macroscopic quantum tunnelling.

C Andreev Bound States in Zeeman Fields

In this section, we extend on the discussion in Section 2.6.1 describing Andreev bound states (ABSs) in magnetic fields.

As discussed in Section 2.6.1, a magnetic field B introduces a Zeeman energy term $E_\mathrm{Z} = |g^*\mu_\mathrm{B}B|/2$ which couples to the spin of charge carriers in the junction. For charge carriers at energies close to the Fermi level, $|E| \ll E_\mathrm{F}$, we consider a linear dispersion relation. Hence, a spin-dependent shift in the wavevector is proportional to E_Z; for spin $\sigma = \pm 1$, $k_\pm^> = k_\mathrm{F} + (E \pm E_\mathrm{Z})/(\hbar v_\mathrm{F})$ for $k > 0$ and $k_\pm^< = -k_\mathrm{F} - (E \pm E_\mathrm{Z})/(\hbar v_\mathrm{F})$ for $k < 0$.

As we saw in Section 2.2, energy solutions for ABSs consist of two branches, one with $k > 0$ and one with $k < 0$, which couple in the presence of normal scattering. This is illustrated in Fig. C.1 as the solid (dashed) black lines for $\tau = 0.9$ ($\tau = 1$). Since $k^> \neq k^<$, a round trip of a junction with length L results in a phase shift between the two branches given by

$$\theta_\mathrm{B} = \frac{|g^*|\mu_\mathrm{B}BL}{\hbar v_\mathrm{F}} = \frac{\pi}{2}\frac{E_\mathrm{Z}}{E_\mathrm{Th}}, \tag{C.1}$$

where $E_\mathrm{Th} = \pi\hbar v_\mathrm{F}/(2L)$ is the Thouless energy for a ballistic system. This phase shift is illustrated with the blue dashed lines Fig. C.1(a), for $\sigma = +1$. The two branches still intersect at $\varphi = \pi$, but at lower energy such that ABSs with $\sigma = +1$ are shifted down in energy. This is illustrated by the solid blue line in Fig. C.1(a), which is the case for normal scattering. The phase shift is reversed for $\sigma = -1$, so ABSs move up in energy [see Fig. C.1(b)].

This spin-splitting was shown in Fig. 2.15, ultimately resulting in a phase transition from an energy minimum at $\varphi = 0$ to $\varphi = \pi$. In the absence of spin-orbit interaction, a transition can occur for a magnetic field applied in an arbitrary direction since the spin is well defined with respect to the field direction. Rashba spin-orbit interaction introduces a preferential direction, such that the external magnetic field couples to the spin via the Rashba term Eq. 2.1. The spin is no longer a good quantum number since spin states are mixed by the spin-orbit interaction. In this case, a $0 - \pi$ transition can lead to a Fulde–Ferrell–Larkin–Ovchinnikov (FFLO) phase, in which Cooper pairs have a nonzero momentum and a spatially non-uniform pairing potential [100, 299, 300]. These transitions also have implications for topological phases in planar Josephson junctions, where it has been proposed that a topological transition would occur for non-degenerate zero-energy solutions [120]. The junction would be topological for the values of φ between crossings, at fields much lower than given by Eq. 2.59. It was subsequently shown that

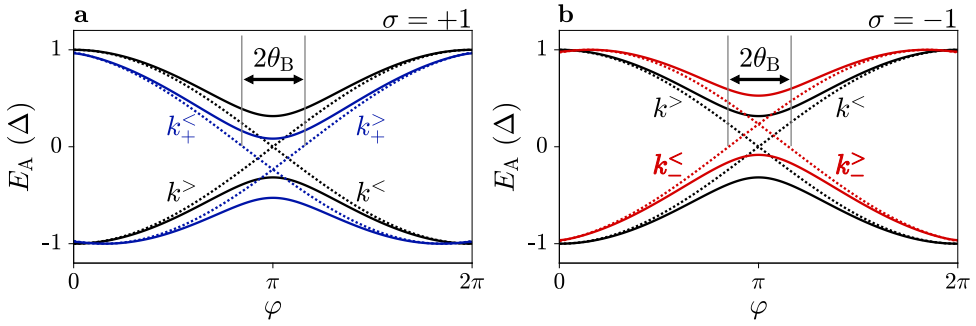

Figure C.1. Spin-splitting of Andreev bound states (ABSs) in a Zeeman field B. a Energy of a $\sigma = +1$ ABS at $B = 0$ (black solid lines) and $B > 0$ (blue solid lines). Dashed lines indicate the $\tau = 1$ case for reference. The wavevector shift $k_+^>$ relative to $k^>$ at zero field (and the symmetric shift for $k_+^<$) gives a phase shift of $2\theta_B$, resulting in a decrease in the ABS energy. **b** Same as (a) for $\sigma = -1$, resulting in an increase in the ABS energy. The ABSs are plotted with Eq. 2.57 for $\tau = 0.9$ and $\theta_B = 0.2\pi$.

for junctions where the length of the superconducting leads is smaller than the coherence length, a phase transition of this type would not necessarily signal a topological phase transition, which instead would sensitively depend on the chemical potential [326].

D Additional Data for Chapter 4

D.1. Characterisation of JJ1 and JJ2

Initial characterisation was performed by standard lock-in techniques. An AC current of $I_{\mathrm{AC}} = 2$ nA was applied to the source contact of the SQUID device, with a frequency of 233 Hz. The four-terminal differential voltage V_{AC} across the SQUID was measured at this frequency, via a differential voltage amplifier with 1000 times gain. The differential resistance $R = V_{\mathrm{AC}}/I_{\mathrm{AC}}$ was measured as a function of the applied DC current I_{DC}.

In addition to the $B_{\perp}$-dependent measurements presented in Fig. 4.1, we show temperature- and gate-dependent measurements of JJ1 and JJ2. In Figs. D.1(a) and (b), for JJ1 and JJ2 respectively, we show the differential resistance R as a function of I_{DC}, swept from negative to positive currents. The colour denotes the temperature, which ranges from 20 mK to 1.6 K, at which point both JJs are fully resistive. We offset the vertical axis by 200 Ω between each temperature trace, to highlight the zero-resistance state at low bias currents.

As we increase I_{DC} from -2 μA, each junction undergoes a transition from the resistive to superconducting state at the retrapping current I_{R}. At positive bias, the superconducting-to-resistive transition occurs at the switching current I_{SW}. The difference between the two, most notable in JJ1, indicates the underdamped JJ behaviour. At high temperatures the superconducting state softens, leading to a finite resistance at bias values below I_{SW}. This is expected from phase diffusive JJs at high temperatures, but makes determination of I_{SW} less reliable; hence we do not present SPDs at temperatures $T > 1$ K, where this effect is significant.

Figures D.1(c) and (d) show the gate dependence of the differential resistance R across JJ1 and JJ2, respectively. The normal state resistances for JJ1 and JJ2 are $R_{N,1} = 150\ \Omega$ and $R_{N,2} = 540\ \Omega$, respectively. At a small negative gate voltage, the switching current reaches its maximum. The peak occurs at $V_{\mathrm{G1}} = -180$ mV for JJ1 and $V_{\mathrm{G2}} = -140$ mV for JJ2. These define the operating points for each junction in Figs. 4.1, 4.2 and 4.6. Each JJ can be tuned to the completely resistive state with sufficiently negative gate voltages, as seen in Figs. D.1(c) and (d) for JJ1 and JJ2 respectively. To measure a single junction in isolation, we apply $V_G < -400$ mV to the other junction so that no supercurrent flows there, as in Figs. 4.1, 4.2 and 4.6. In Fig. D.1(c), we observe large fluctuations in the switching current for $V_{\mathrm{G1}} > -200$ mV. This is indicative of large quantum fluctuations when the critical current is large.

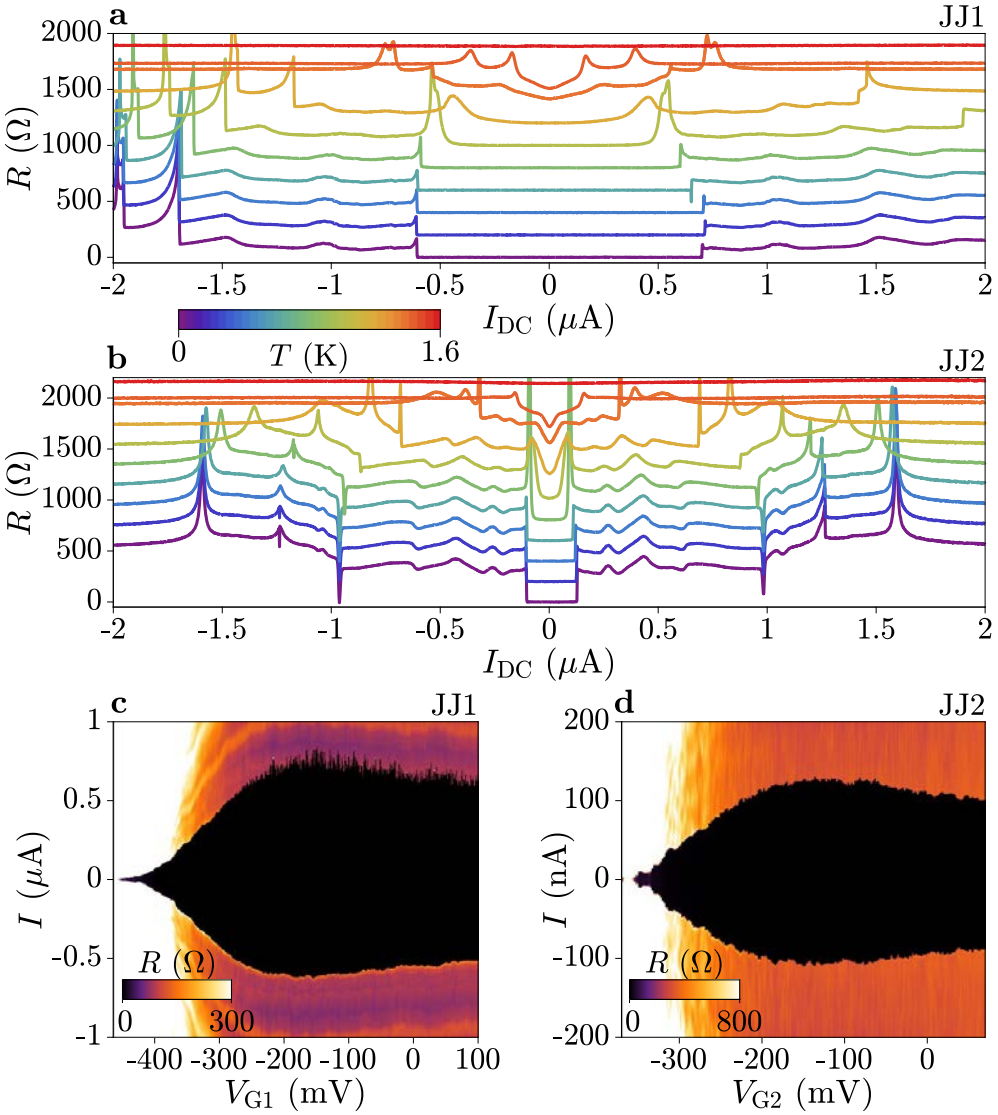

Figure D.1. Characterisation of JJ1 and JJ2. **a** Current-biased measurement of differential resistance R of JJ1 with an applied bias of I_{DC}, in the positive sweep direction. **b** Same as (a) for JJ2. **c** Differential resistance R of JJ1 as a function of gate voltage V_{G1}. The junction goes from fully open to fully closed in the gate voltage range. **d** Same as (c) for JJ2. Note that the colour scale in (c) and (d) is saturated to highlight the normal state resistance R_N close to zero gate voltage.

D.2. Additional Insights on Phase Escape Dynamics

We now consider the impact of temperature on the switching current in the macroscopic quantum tunnelling (MQT) regime. In Fig. D.2 we calculate the switching probability distribution (SPD) as a function of temperature using the same fit parameters as Fig. 4.3, but considering only MQT escape without the presence of phase diffusion (PD) ($\Gamma_R = 0$). This is instructive to see the impact of the temperature dependence of I_C and Q on SPDs at low T. In particular, we see that the mean switching current $I_{M,1}$ decreases with increasing temperature [Fig. D.2(a)]. This is due to the low T_C of Al, which causes a change in I_C even at the lowest temperature of our experiment. This is evident in Fig. D.2(b) (dashed line). The experimental data for $I_{M,1}$ (squares) aligns with the simulated result for MQT in the absence of PD (solid line) up to $T \sim T^*$. This is indicative of the dominance of MQT over PD up to $T \sim T^*$ in the experimental data. In

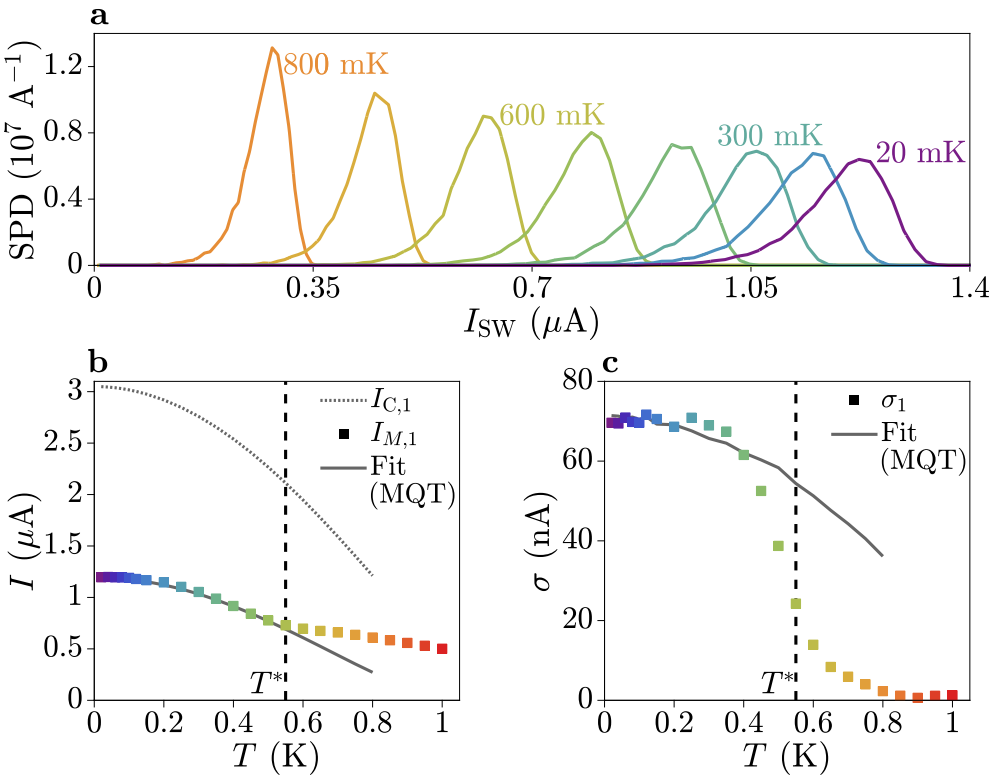

Figure D.2. Monte Carlo simulations with only macroscopic quantum tunnelling (MQT). a Switching probability distributions (SPDs) obtained from a Monte Carlo simulation considering only escape by quantum tunnelling (MQT), as a function of temperature. Calculated using the parameters $I_C = 3$ μA, $C = 1$ fF and $Q_0 = 7$. **b** Temperature dependence of critical current $I_{C,1}$ (dashed line), JJ1 switching current $I_{M,1}$ (squares) and MQT-only fit (solid line). **c** Temperature dependence of standard deviation in JJ1 (squares) and MQT-only fit (line).

Fig. D.2(c) we show the experimental standard deviation σ_1 (squares) and the modelled standard deviation in the case of pure MQT (line). The slight temperature dependence of the fit result is due to the temperature dependence of Q, again a consequence of the low T_C in Al.

Further to the standard deviation, as shown in Fig. 4.2(d), the skewness of SPDs is indicative of the phase escape mechanism. Phase escape unhindered by retrapping leads to a negative skewness close to -1 [255]. On entering the PD regime, the SPDs become more symmetric and the skewness tends towards zero. This is shown in Figs. D.3(a-c), where SPDs of JJ1 are plotted on a linear scale for $T = 20$ mK, 550 mK and 900 mK respectively. The trend in skewness is consistent with the interpretation above. At low temperature the SPD has large negative skewness, indicating that no phase diffusion is present. At higher temperatures, the SPDs are more symmetric with a skewness of zero at $T = 900$ mK. The skewness of JJ1 as a function of temperature (circles) is plotted in Fig. D.3(d), alongside the Monte Carlo fit result (grey line). Both the data and the Monte Carlo fit are negative at low temperature, and increase towards zero for higher temperatures where phase diffusion becomes dominant.

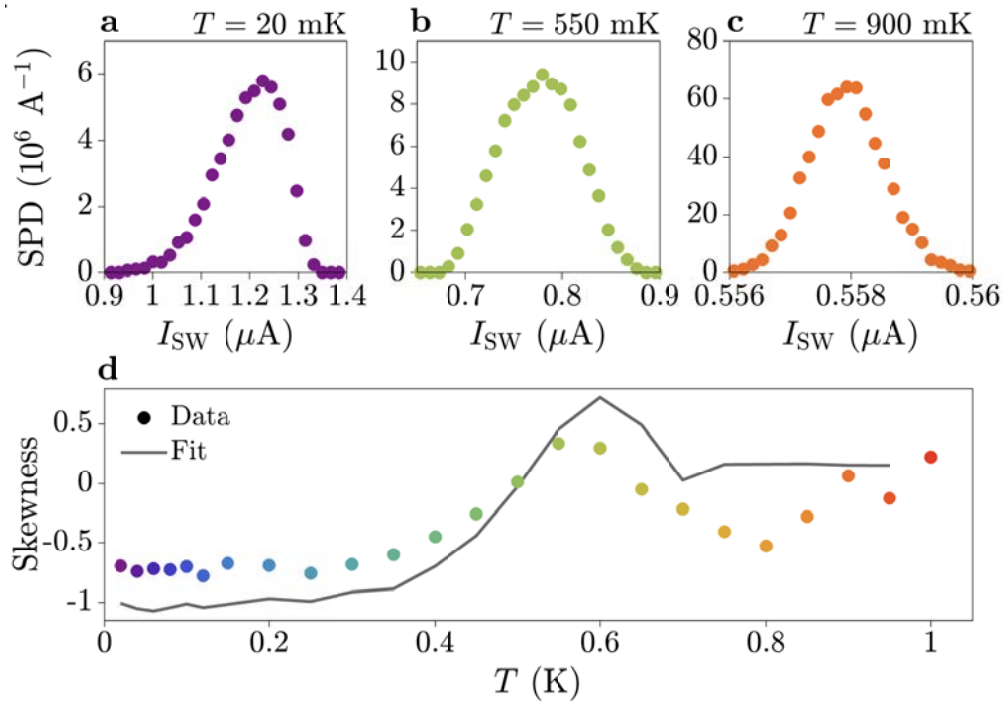

Figure D.3. Investigation of the skewness of switching probability distributions (SPDs). **a** Switching probability distribution (SPD) of JJ1 at $T = 20$ mK, plotted on a linear scale. Large negative skewness, consistent with a lack of phase diffusion at low temperature. **b** SPD at $T = 550$ mK, where skewness is positive. **c** Symmetric SPD at $T = 900$ mK. **d** Skewness of SPDs (circles) as a function of temperature, as indicated by the colour. This is compared with the result from the Monte Carlo fit (grey curve).

E Additional Data for Chapter 5

Complete datasets for Chapter 5 are presented, for different top-gate voltages applied to JJ1. The standard deviation as a function of flux is plotted for each regime in Fig. 5.6.

For $V_{G1} = -300$ mV, the SQUID undergoes direct transitions between macroscopic quantum tunnelling (MQT) and phase diffusion (PD) depending on $B_\perp$. The full dataset is shown in Fig. E.1 for 20 mK to 900 mK: the mean switching current $I_{M,S}$ in (a), the standard deviation in (b) and the oscillation amplitude $\Delta I_{M,S}/2$ in (c). The enhancement in switching current at low temperatures is again observed, where quantum tunnelling is dominant. We also observe the characteristic kink in $\Delta I_{M,S}/2$, in this case at $T \approx 0.52$ K concomitant with the lower transition temperature to the phase diffusive regime.

At $T = 20$ mK, we observe a large variation in the standard deviation σ_S depending on the field $B_\perp$. At the maximum of $I_{M,S}$ (diamond), σ_S is large at low temperature. This is consistent with quantum tunnelling as the dominant mechanism of phase escape. Instead, $\sigma_S = 20$ nA at the minimum (triangle), indicating that phase diffusive effects are strong. The traces in σ_S at these field values are shown in Fig. E.1(d) by their respective markers. The large difference in σ_S is evident at low temperatures, as indicated by the blue shading, where the external magnetic field determines the extent of phase diffusion in the SQUID. On increasing T towards the transition temperature, the difference in σ_S reduces until the SQUID is fully phase-diffusive at all values of $B_\perp$.

Figures E.2 and E.3 show the datasets for $V_{G1} = -350$ mV and $V_{G1} = -375$ mV, respectively. While still asymmetric for $V_{G1} = -350$ mV, the critical current of JJ1 is no longer much larger than that of JJ2. The much lower critical current of JJ1 means that quantum tunnelling is only dominant close to the maximum of the SQUID oscillations. This is highlighted in Fig. E.2(b). At the minima, the SQUID is fully phase diffusive with $\sigma_S < 5$ nA. The oscillation amplitude $\Delta I_{M,S}/2$ in Fig. E.2(c) shows a kink at $T \approx 0.42$ K, which is consistent with the average transition temperature between MQT and PD regimes. Figure E.2(d) shows σ_S at flux values corresponding to the maximum (diamonds) and minimum (triangles) of the $I_{M,S}$ oscillations. The divergence for $T < T^*$ is evident, as in Fig. E.1(d). We note that at some values of $B_\perp$ in the low-temperature curve the switching current went above the signal amplitude, artificially truncating the SPD and rendering its standard deviation unphysical: these points have been removed from the trace. On further decrease in V_{G1} to -375 mV, the SQUID is almost symmetric. In this case, a magnetic-field dependence is still observable in the standard deviation [see Fig. E.3(b)] but the SQUID is phase diffusive at $T = 20$ mK for all values of $B_\perp$. The corresponding oscillation amplitude, while no longer representative of the switching current of JJ2, again shows the kink in $\Delta I_{M,S}/2$ at the low transition temperature of

$T \approx 0.35$ K. Figure E.3(d) shows σ_S at the maxima (diamonds) and minima (triangles) of $I_{M,S}$, and while some divergence emerges for $T < T^*$, phase diffusion is dominant for all values of $B_\perp$.

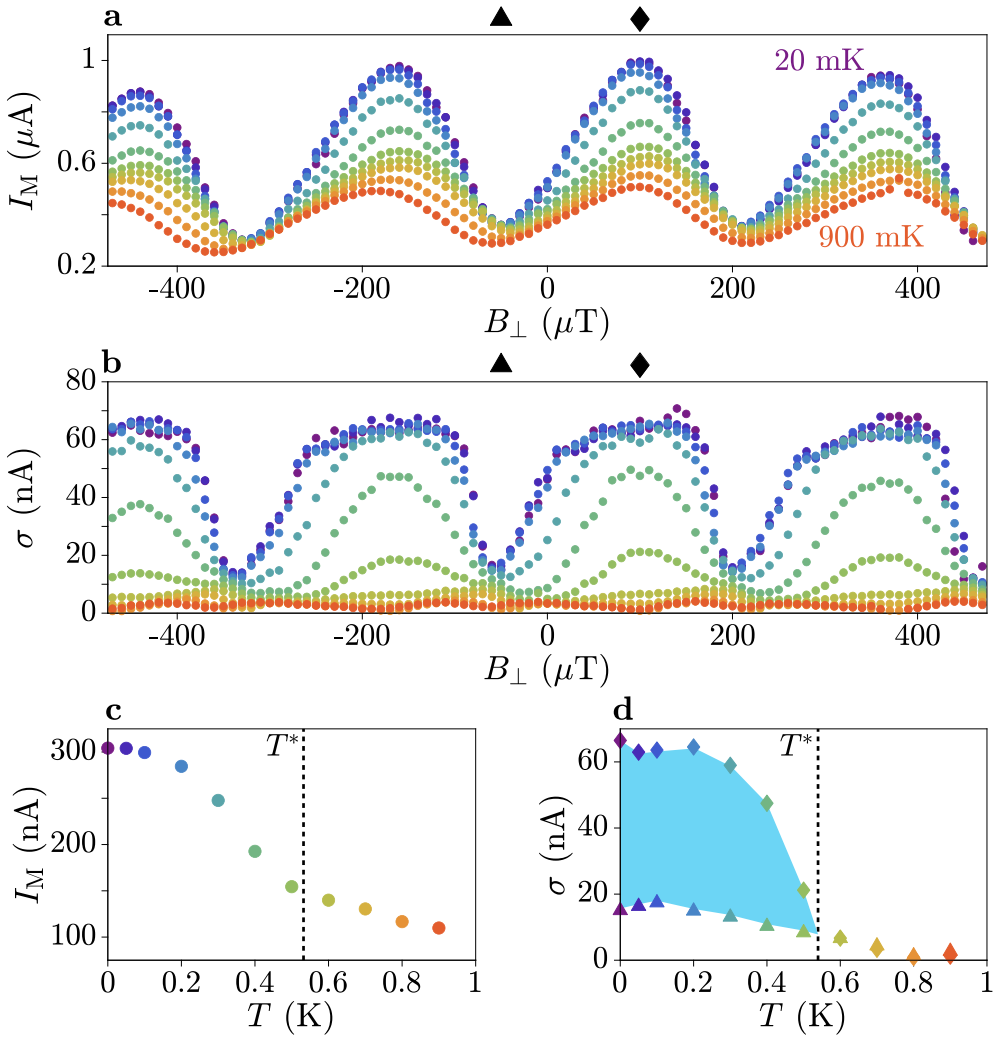

Figure E.1. Switching current measurements at $V_{G1} = -300$ mV and $V_{G2} = -140$ mV. **a** Mean switching current $I_{M,S}$ for the SQUID configuration as a function of $B_\perp$. Field traces are taken at temperatures ranging from 20 mK up to 900 mK. The maximum (diamond) and minimum (triangle) of the $I_{M,S}$ oscillations are marked. **b** Standard deviation σ_S in this SQUID configuration, for temperatures 20 mK to 900 mK. **c** Oscillation amplitude of $I_{M,S}$, $\Delta I_{M,S}/2$ as a function of temperature. A kink in $\Delta I_{M,S}/2$ occurs at the transition temperature of $T^* \approx 0.52$ K. **d** Standard deviation σ_S at values of $B_\perp$ corresponding to the $I_{M,S}$ maximum (diamonds) and minimum (triangles) respectively. The large difference at $T < T^*$ is indicated.

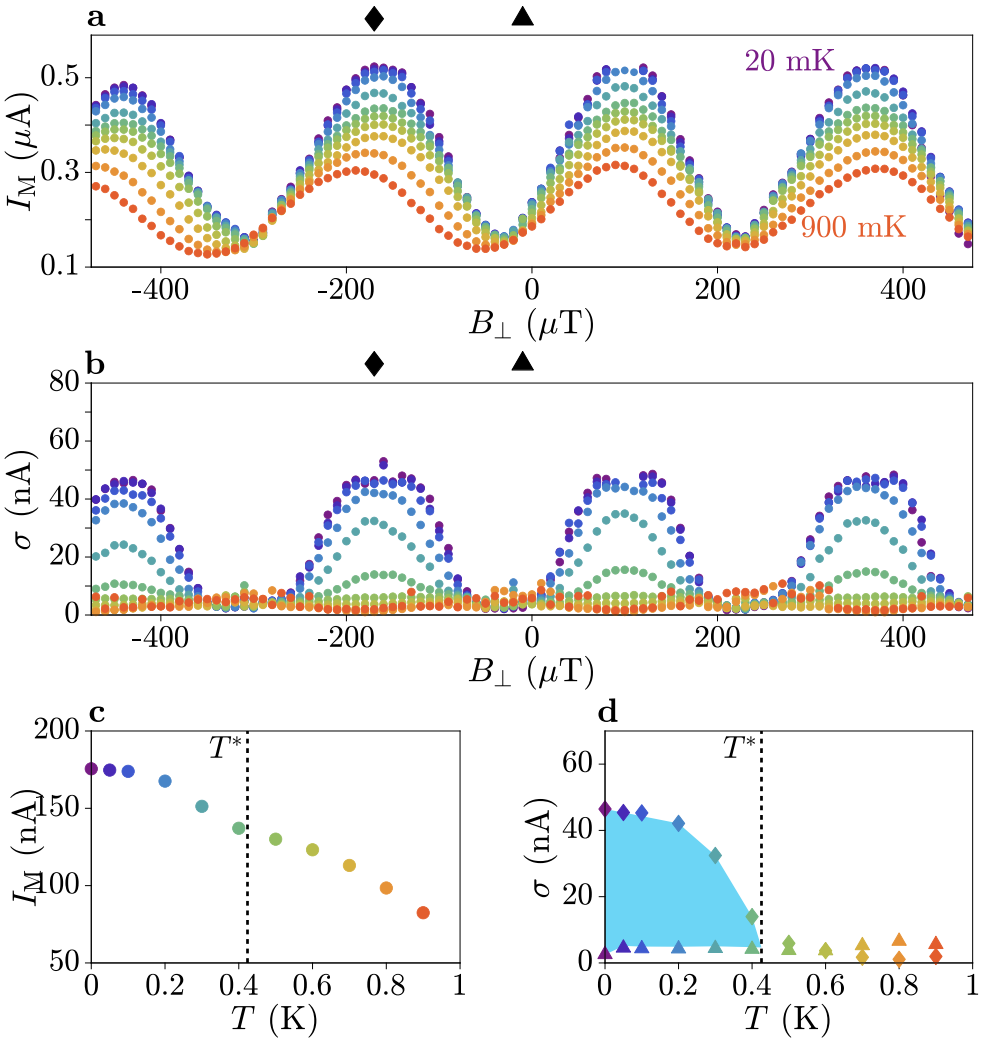

Figure E.2. Switching current measurements at $V_{G1} = -350$ mV and $V_{G2} = -140$ mV. **a** Mean switching current $I_{M,S}$ for the SQUID configuration as a function of $B_\perp$. Field traces are taken at temperatures ranging from 20 mK up to 900 mK. The maximum (diamond) and minimum (triangle) of the $I_{M,S}$ oscillations are marked. **b** Standard deviation σ_S in this SQUID configuration, for temperatures 20 mK to 900 mK. **c** Oscillation amplitude of $I_{M,S}$, $\Delta I_{M,S}/2$ as a function of temperature. A kink in $\Delta I_{M,S}/2$ occurs at the transition temperature of $T^* \approx 0.42$ K. **d** Standard deviation σ_S at values of $B_\perp$ corresponding to the $I_{M,S}$ maximum (diamonds) and minimum (triangles) respectively. The large difference at $T < T^*$ is indicated.

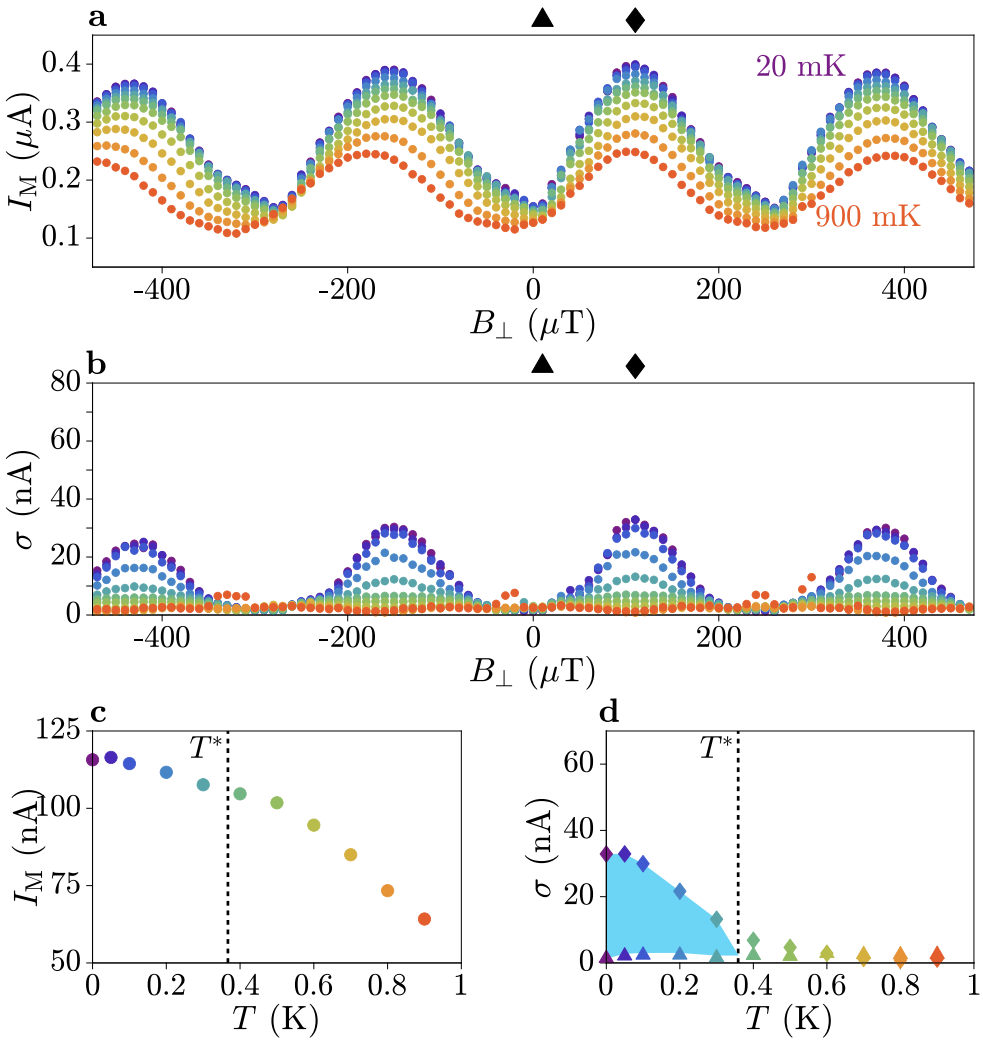

Figure E.3. Switching current measurements at $V_{G1} = -375$ mV and $V_{G2} = -140$ mV. **a** Mean switching current $I_{M,S}$ for the SQUID configuration as a function of $B_\perp$. Field traces are taken at temperatures ranging from 20 mK up to 900 mK. The maximum (diamond) and minimum (triangle) of the $I_{M,S}$ oscillations are marked. **b** Standard deviation σ_S in this SQUID configuration, for temperatures 20 mK to 900 mK. **c** Oscillation amplitude of $I_{M,S}$, $\Delta I_{M,S}/2$ as a function of temperature. A kink in $\Delta I_{M,S}/2$ occurs at the transition temperature of $T^* \approx 0.35$ K. **d** Standard deviation σ_S at values of $B_\perp$ corresponding to the $I_{M,S}$ maximum (diamonds) and minimum (triangles) respectively. The large difference at $T < T^*$ is indicated.

F Additional Data for Chapter 6

F.1. Further Data on Conductance Replicas

F.1.1. Frequency Dependence of Conductance Response

The microwave response of the device was first investigated as a function of microwave (MW) irradiation with frequency f, in the low barrier transparency regime ($V_T = -2.11$ V). Figure F.1 shows the differential conductance G as a function of source-drain bias V_{SD} for increasing frequency from 500 MHz to 12.7 GHz, with an applied power $P = 20$ dBm. The conductance was unaffected by the applied signal for frequencies up to 1.8 GHz. At frequencies $f > 1.8$ GHz, the conductance was altered by the applied microwaves and in some cases we observed a non-zero conductance at $V_{SD} = 0$. The conductance response to irradiation frequency was non-monotonic, suggesting that the coupling strength of the antenna to the device was frequency-dependent. This was due to the method of applying microwaves by an exposed antenna within the sample space. The results shown in Figs. 6.3, 6.4 and 6.5 were measured at frequencies labelled by the coloured markers. These frequencies were chosen where the response of the conductance was strongest based on Fig. F.1, such that a full power dependence was possible.

Replication of conductance features were evident at both positive and negative bias. These followed a linear dependence on frequency, as highlighted by the white dashed

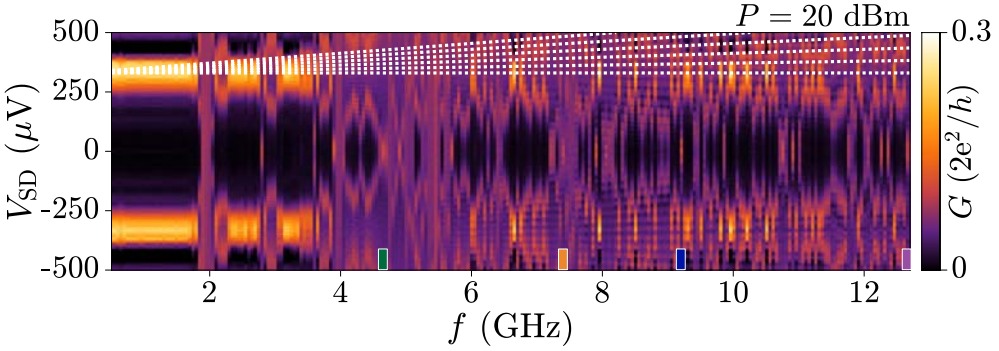

Figure F.1. Frequency dependence of conductance G as a function of source-drain bias V_{SD}, at a fixed microwave power $P = 20$ dBm. Conductance replicas are schematically indicated by the dashed white lines, $\Delta V_{SD} = nhf/e$. Frequencies shown in Figs.6.3, 6.4 and 6.5 are indicated by coloured markers.

lines at positive bias. Conductance replicas follow the relation $V_{SD} = nhf/e$, where n is an integer. Hence, the separation of conductance replicas of $\Delta V_{SD} = hf/e$ was consistent across a wide frequency range.

F.1.2. Spectroscopy at an In-Plane Magnetic Field

Results shown so far were performed at an in-plane magnetic field $B_{\parallel} = 0$. Both the Josephson junction and the probe were in the superconducting state (S), meaning that tunnelling across the insulating barrier (I) corresponded to an SIS geometry [as shown in Fig. 6.1(a)]. At an in-plane magnetic field of $B_{\parallel} = 0.2$ T, superconductivity in the probe was suppressed such that there was a finite density of states within the superconducting gap of the probe. The differential conductance G therefore showed features at bias values proportional to the density of states in the Josephson junction.

Figure F.2 shows bias spectroscopy at an in-plane magnetic field of $B_{\parallel} = 0.2$ T as a function of power P, for different frequencies f of applied radiation. The device configuration was identical to the open regime [$V_T = -2.08$ V, as in Figs. 6.3(a-c) and 6.4(a-c)]. The conductance G as a function of source-drain voltage V_{SD} shows a superconducting gap at low bias. Conductance values increased to a maximum close to $|V_{SD}| = 200$ μV. A small conductance peak was visible at $V_{SD} = 0$, from a small residual supercurrent which flowed across the tunnel barrier despite the softened superconducting gap in the probe. On increasing microwave power P, replicas in conductance features emerged at both high and low bias. High-bias conductance replicas had separation $\Delta V_{SD} = hf/e$. Furthermore, the power dependence was similar to that at $B_{\parallel} = 0$.

Conductance replicas were present under microwave irradiation when superconductivity was suppressed in the probe. This is consistent with photon assisted tunnelling (PAT) into Andreev bound states (ABSs) of charges in the probe at the Fermi energy. While the probe was not truly normal, PAT signatures also occur in superconductor-insulator-normal junctions [327, 328]. Since high bias conductance replicas are present both in the case of PAT and Floquet-Andreev states, using a normal density of states to probe the junction does not allow the two mechanisms to be distinguished.

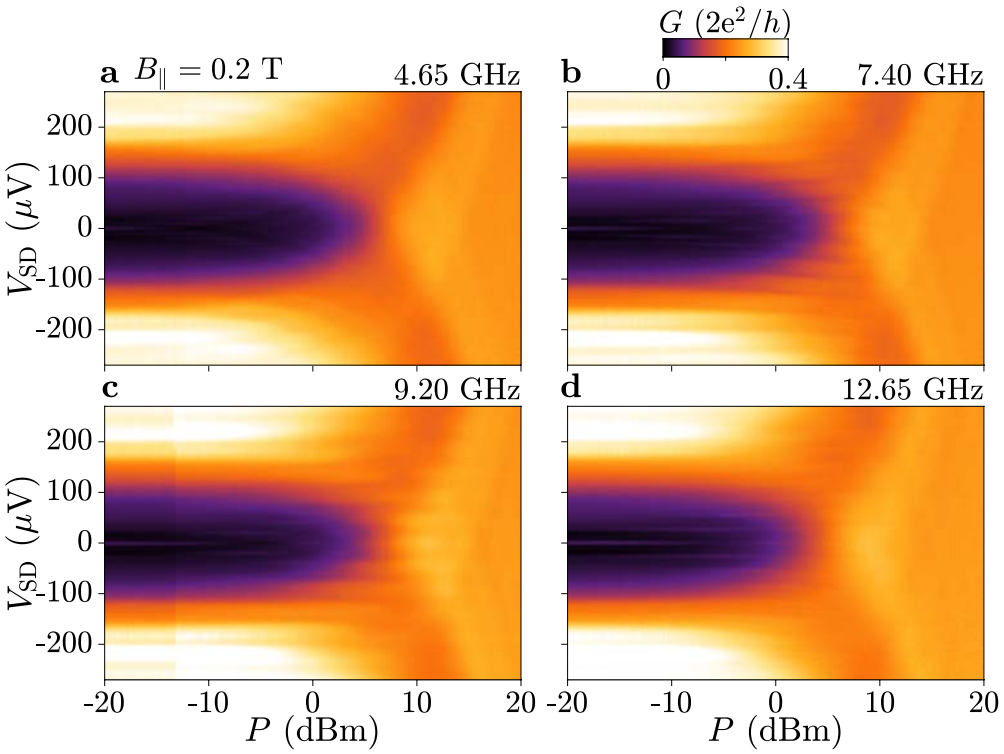

Figure F.2. Conductance replicas for an elevated in-plane magnetic field. Power dependence of conductance G as a function of bias V_{SD}, at an in-plane magnetic field $B_{\parallel} = 0.2$ T for different irradiation frequencies $f = \{4.65,\ 7.40,\ 9.20,\ 12.65\}$ GHz.

F.1.3. $B_{\perp}$-Dependence in Spectroscopy

Selected conductance maps as a function of perpendicular magnetic field $B_{\perp}$ are shown in Figs. 6.6(a-c). The full dataset is shown in Fig. F.3, for no applied microwaves [Fig. F.3(a)] and applied powers ranging from $P = -10$ dBm [Fig. F.3(b)] to $P = 10$ dBm [Fig. F.3(f)]. Some conductance features were periodic in $B_{\perp}$; these corresponded to ABSs in the SNS junction, which were dependent on the phase difference across the junction. Field-independent features corresponded to the superconducting gap edge at $V_{\mathrm{SD}} = 2\Delta/\mathrm{e}$, and conductance resonances in the tunnelling probe. For increasing microwave power, additional field-periodic features appeared in the conductance map. The magnitude of the conductance at a given bias decreased, as it was distributed across more conductance peaks. This is consistent with current conservation in the PAT process.

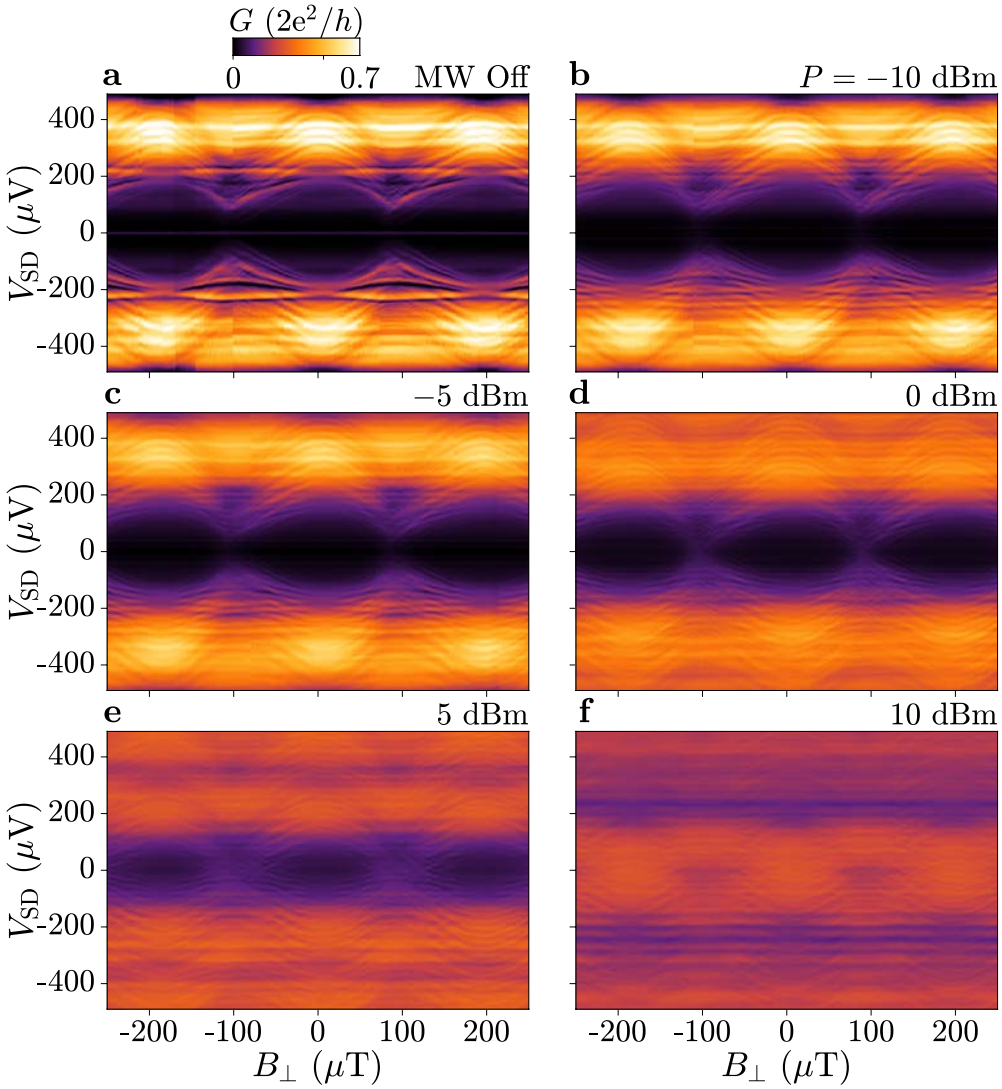

Figure F.3. Conductance as a function of perpendicular magnetic field $B_\perp$. a Conductance G as a function of $B_\perp$ with no microwave field applied.**b-f** Conductance G as a function of $B_\perp$ under microwave irradiation at frequency $f = 9.20$ GHz. Applied microwave powers of $P = \{-10,\ -5,\ 0,\ 5,\ 10\}$ dBm$d\varphi$, respectively. Same gate configuration as Fig. 6.6.

F.2. Results for $V_{TG} = -1.4$ V

A complete set of data is presented for a top-gate voltage $V_{TG} = -1.4$ V, for different tunnel gate voltages V_T. These data sets are complementary to Fig. 6.14.

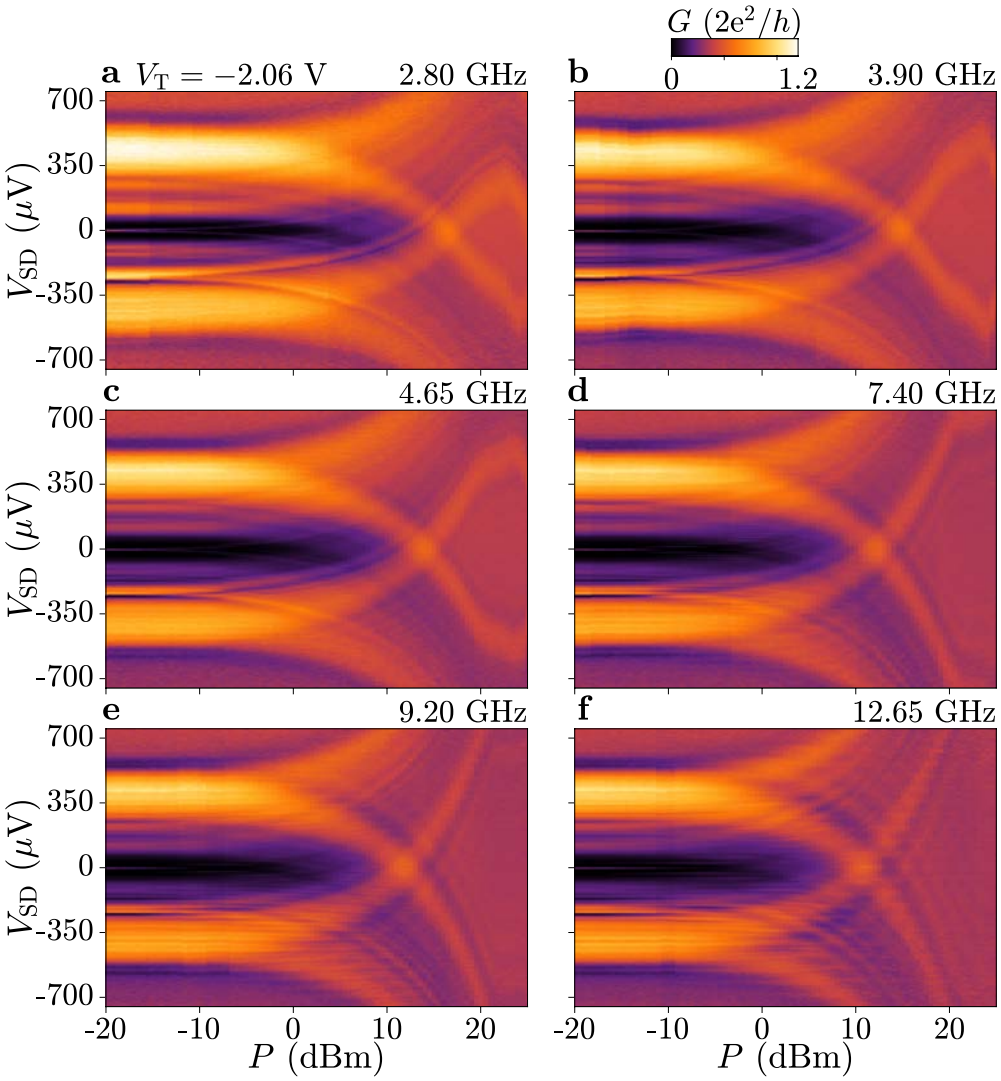

Figure F.4. Power dependence at $V_{\mathrm{TG}} = -1.4$ V and $V_{\mathrm{T}} = -2.06$ V. Conductance G as a function of source-drain bias V_{SD} and power P, for frequencies $f = \{2.80,\ 3.90,\ 4.65,\ 7.40,\ 9.20,\ 12.65\}$ GHz. Mean separation of replicated supercurrent features is shown in Fig. 6.5(b) (full grey squares).

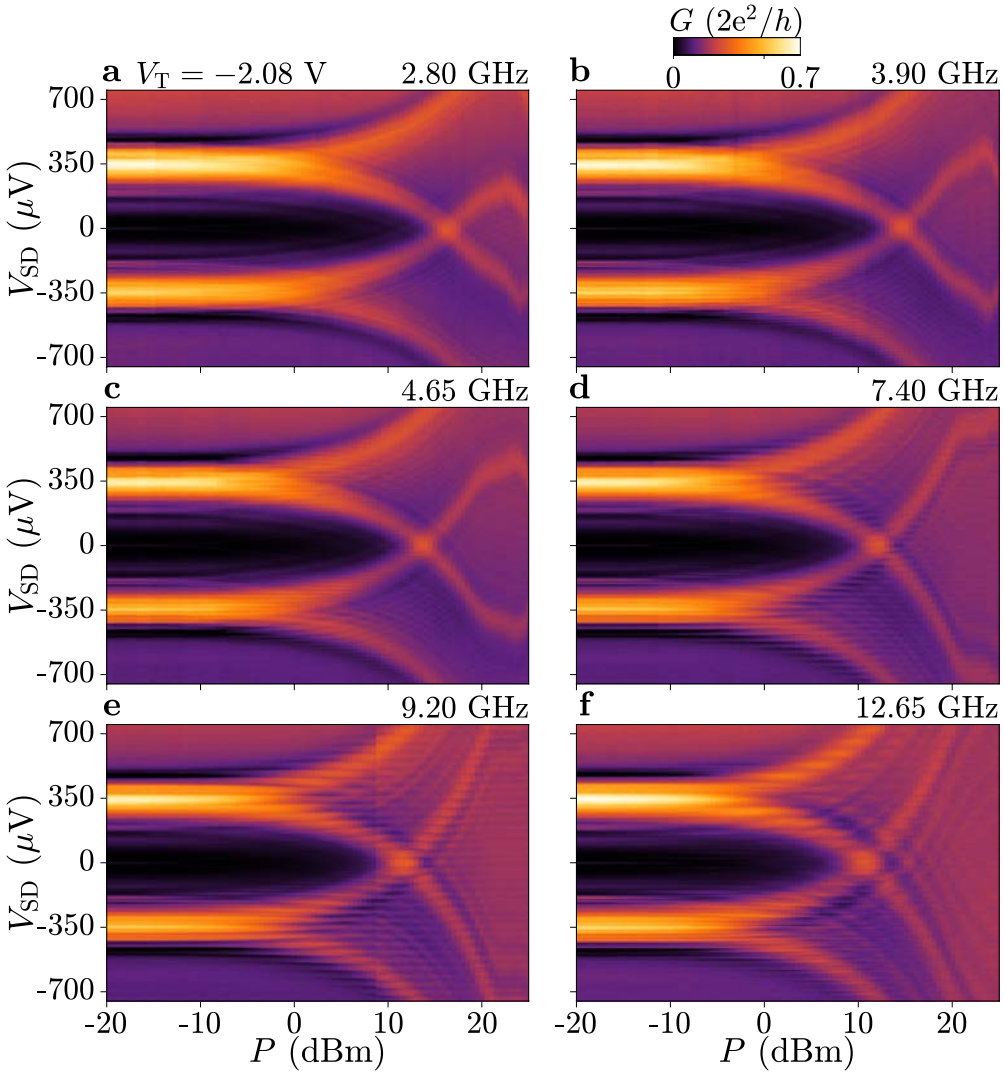

Figure F.5. Same as F.4 for $V_T = -2.08$ V.

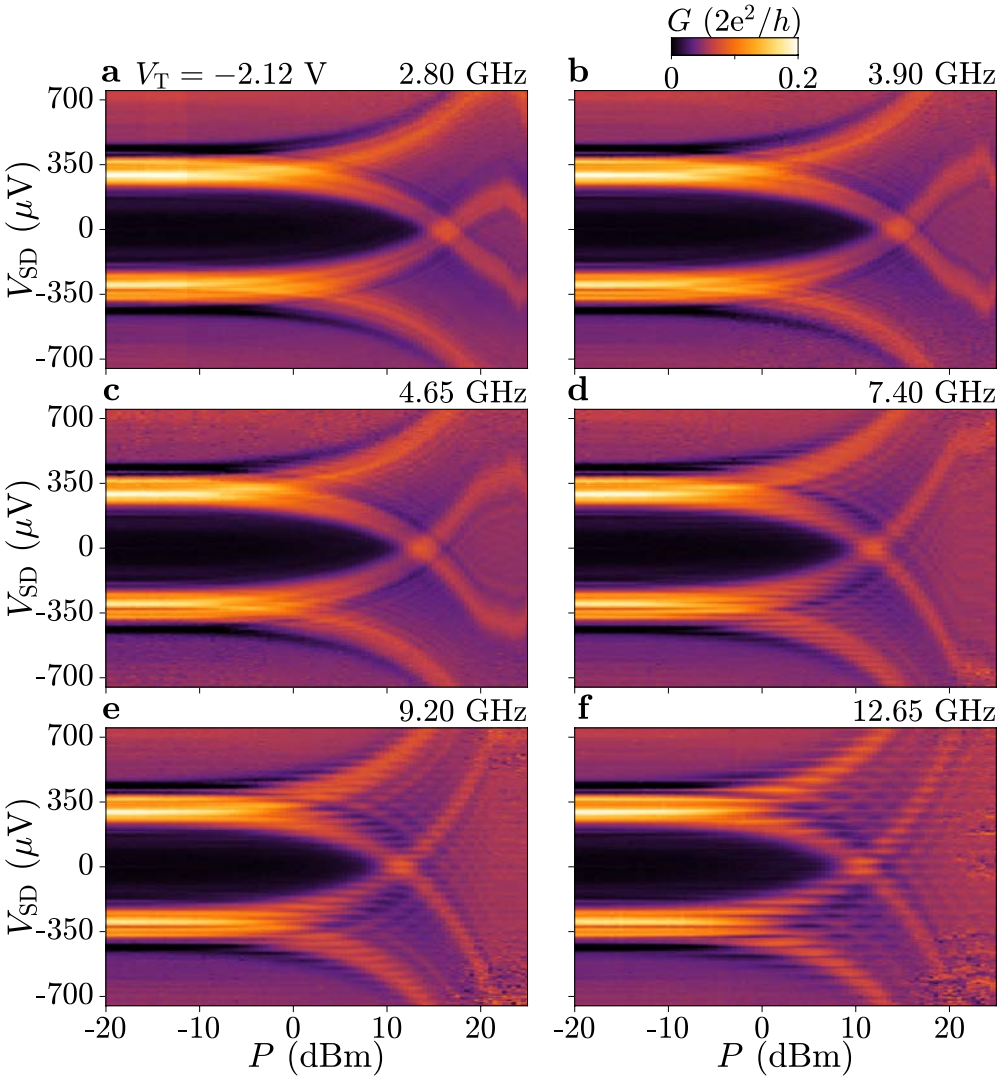

Figure F.6. Same as F.4 for $V_\mathrm{T} = -2.12$ V.

F.3. Conductance Replicas in a Second Device

Measurements were performed on a second device, fabricated on the same chip and lithographically similar to the first except for the width of the SNS junction, which was 500 nm rather than 2.5 μm for Device 1. Measurements are shown for tunnel gate voltages $V_\mathrm{T} = -0.768$ V a top gate voltage $V_\mathrm{TG} = 0$ V, kept constant throughout the measurements. Figure F.7 shows the frequency response of Device 2 to microwave irradiation at an applied power of $P = 20$ dBm. The frequency response was similar to that of Device 1 [see Fig. D.1], showing conductance replicas with separation $\Delta V_\mathrm{SD} = hf/\mathrm{e}$ indicated by the white dashed lines. Frequencies $f = 4.70$ GHz, 6.85 GHz, 9.45 GHz and 11.90 GHz are indicated by the coloured markers, where many replicas are evident. Figure F.8 shows

the conductance response to microwave irradiation at these frequencies, for increasing microwave power P. Conductance replicas emerged with separation $\Delta V_{\mathrm{SD}} = hf/\mathrm{e}$, shown as empty grey circles in Fig. 6.5(b). Figure F.9 shows the conductance as a function of perpendicular magnetic field $B_{\perp}$, for increasing microwave power. Field-periodic conductance features were replicated, with more replicas emerging for increasing applied power.

Figure F.10 shows the differential conductance as a function of applied power when the transparency of the tunnel barrier was significantly reduced, by setting tunnel gate voltages to $(V_{\mathrm{T,L}},\ V_{\mathrm{T,R}}) = (-0.911,\ -0.875)$ V. Conductance replicas emerge up to large applied powers, as in Fig. F.8.

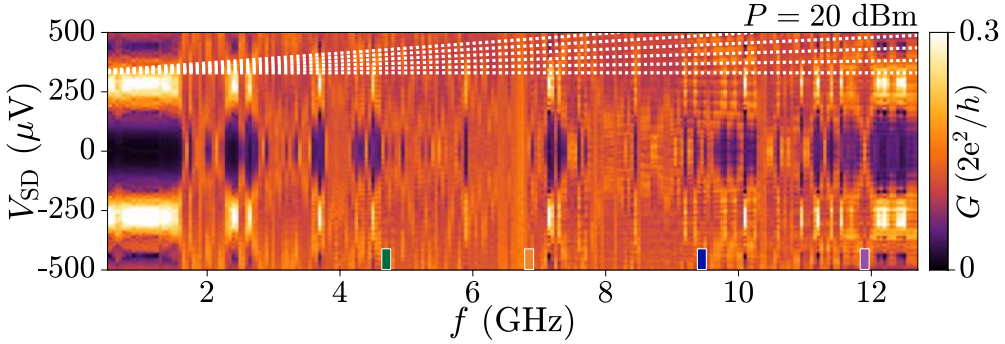

Figure F.7. Frequency dependence of conductance G as a function of source-drain bias V_{SD} in Device 2, at fixed power $P = 20$ dBm. Conductance replicas are schematically indicated by the dashed white line, $\Delta V_{\mathrm{SD}} = hf/\mathrm{e}$. Coloured markers indicate the frequencies used in Figs. F.8 and F.9.

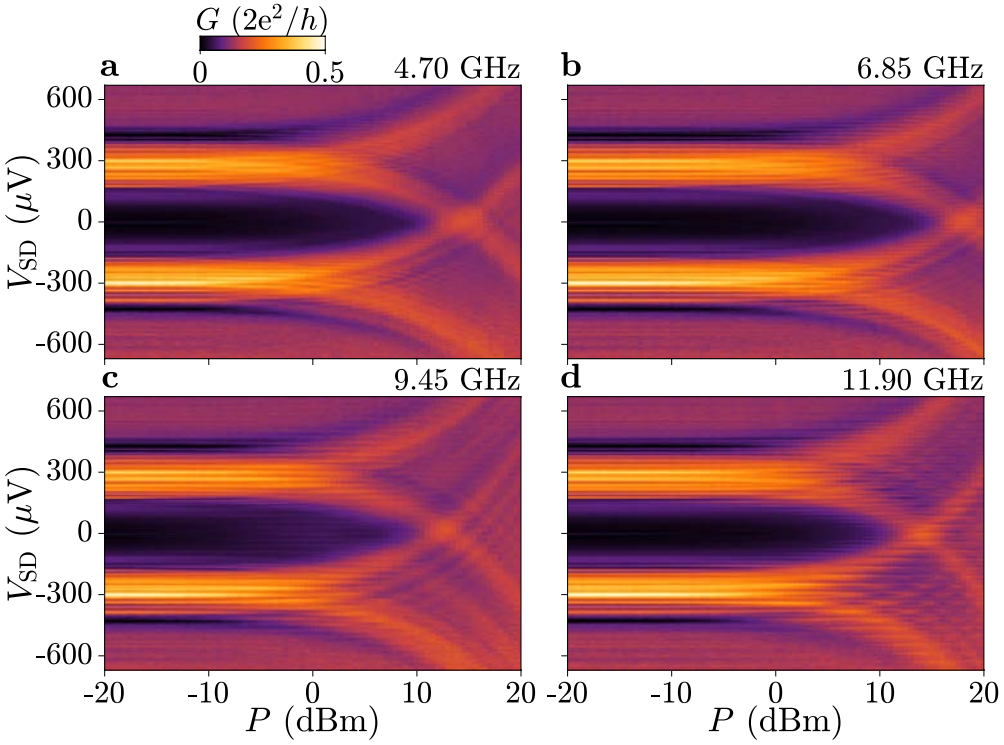

Figure F.8. Conductance of Device 2 as a function of applied microwave power P, for frequencies $f = \{4.70,\ 6.85,\ 9.45,\ 11.90\}$ GHz in (a-d) respectively.

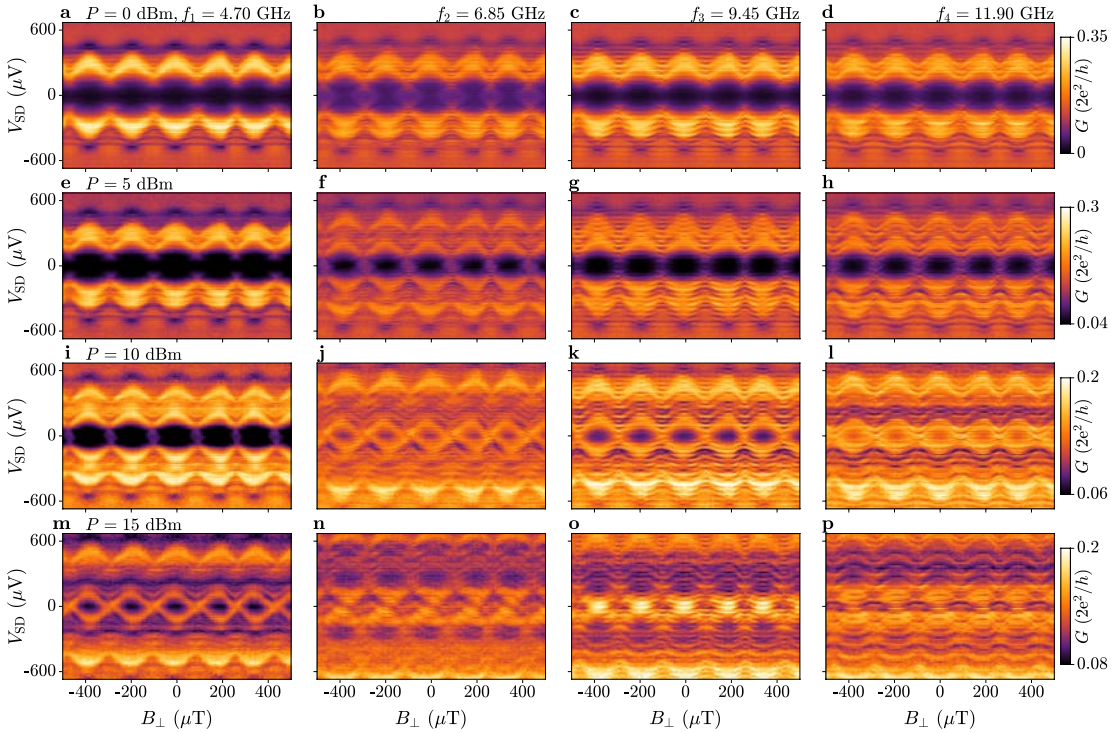

Figure F.9. Conductance of Device 2 as a function of perpendicular magnetic field $B_\perp$ for different frequencies f and powers P. **a-d** $B_\perp$ dependence of conductance response at $P = 0$ dBm for frequencies $f = \{4.70,\ 6.85,\ 9.45,\ 11.90\}$ GHz, respectively. **e-h** Same as (a-d) for $P = 5$ dBm. **i-l** Same as (a-d) for $P = 10$ dBm. **m-p** Same as (a-d) for $P = 15$ dBm.

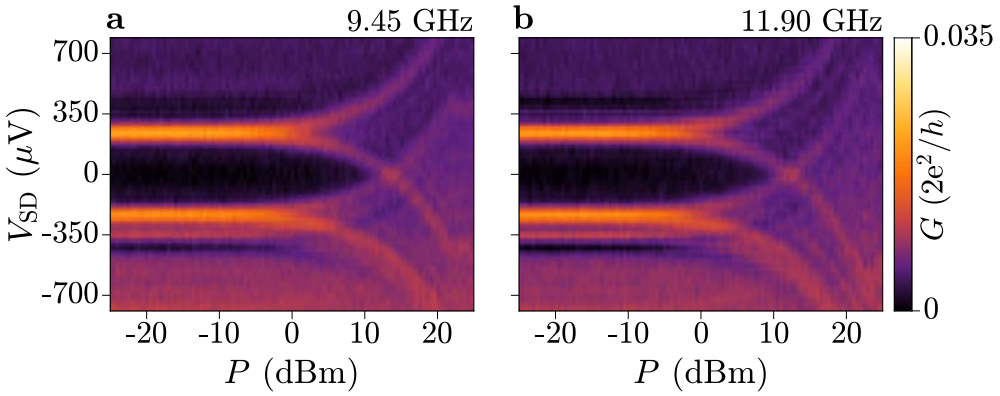

Figure F.10. Conductance replicas in Device 2 at low tunnel-barrier transparency $(V_{T,L},\ V_{T,R}) = (-0.911,\ -0.875)$ V, for frequencies 9.45 GHz and 11.90 GHz in (a, b) respectively.

G Additional Data for Chapter 7

G.1. Type A Phase Shifts in the Current-Phase Relation

Gate-dependent phase shifts in the current-phase relation (CPR) were compared with tunnelling spectroscopy, at $B_{\parallel} = 0.2$ T and 0.4 T [see Fig. 7.12]. The CPR traces at these in-plane fields are plotted in Figs. G.1 and G.2 respectively, alongside the Reference Device at that $B_{\parallel}$. Comparing the two values of $B_{\parallel}$, the amplitude and skewness of the CPR trace at each V_{TG} was reduced for $B_{\parallel} = 0.4$ T compared with $B_{\parallel} = 0.2$ T. For a given $B_{\parallel}$, there was good alignment between the Reference Device and the CPR of the junction at $V_{\mathrm{TG}} = -1.6$ V ($B_{\perp} = 0$, vertical grey dashed line). When the top-gate voltage was set to more positive values, the phase shift between the junction CPR and the Reference increased [orange shaded area]. This phase shift was larger for $B_{\parallel} = 0.4$ T [Fig. G.2(b)] than $B_{\parallel} = 0.2$ T [Fig. G.1(b)].

Type B phase shifts were also observed in devices with different superconducting lead length, L_{SC}. Figure G.3 shows the switching current I as a function of perpendicular magnetic field $B_{\perp}$ and top-gate voltage V_{TG} for Devices 3 [Figs. G.3(a, b)] and 4 [Figs. G.3(c-f)], after subtracting the background current corresponding to the Al constriction. Measurements were performed at a finite in-plane field $B_{\parallel}$, such that a gate dependent shift was observed. For positive in-plane fields [$B_{\parallel} > 0$, Figs. G.3(a, c, e)], the zero-current position shifts to more positive $B_{\perp}$. This is reversed on reversal of $B_{\parallel}$ [Figs. G.3(b, d, f)]. The maximum switching current I_0 and perpendicular field shift ΔB_0 of the data in Fig. G.3 is extracted by performing a fit to Eq. 7.2 at each V_{TG} [see Fig. G.4]. Full (empty) markers indicate positive (negative) $B_{\parallel}$, while the color denotes the size of $B_{\parallel}$: blue for $|B_{\parallel}| = 0.3$ T and yellow for $|B_{\parallel}| = 0.5$ T. For the most negative top-gate voltages, where $I_0 \lesssim 20$ nA, the fit did not reliably converge so these data points have been removed. Data in Figs. G.4(c, d) are plotted with respect to the most negative V_{TG} at which a reliable fit was obtained. The shift ΔB_0 increased in magnitude for more positive V_{TG}, and was symmetric with respect to reversal of $B_{\parallel}$. The shift ΔB_0 for Device 4 was larger for $|B_{\parallel}| = 0.5$ T, for all V_{TG}.

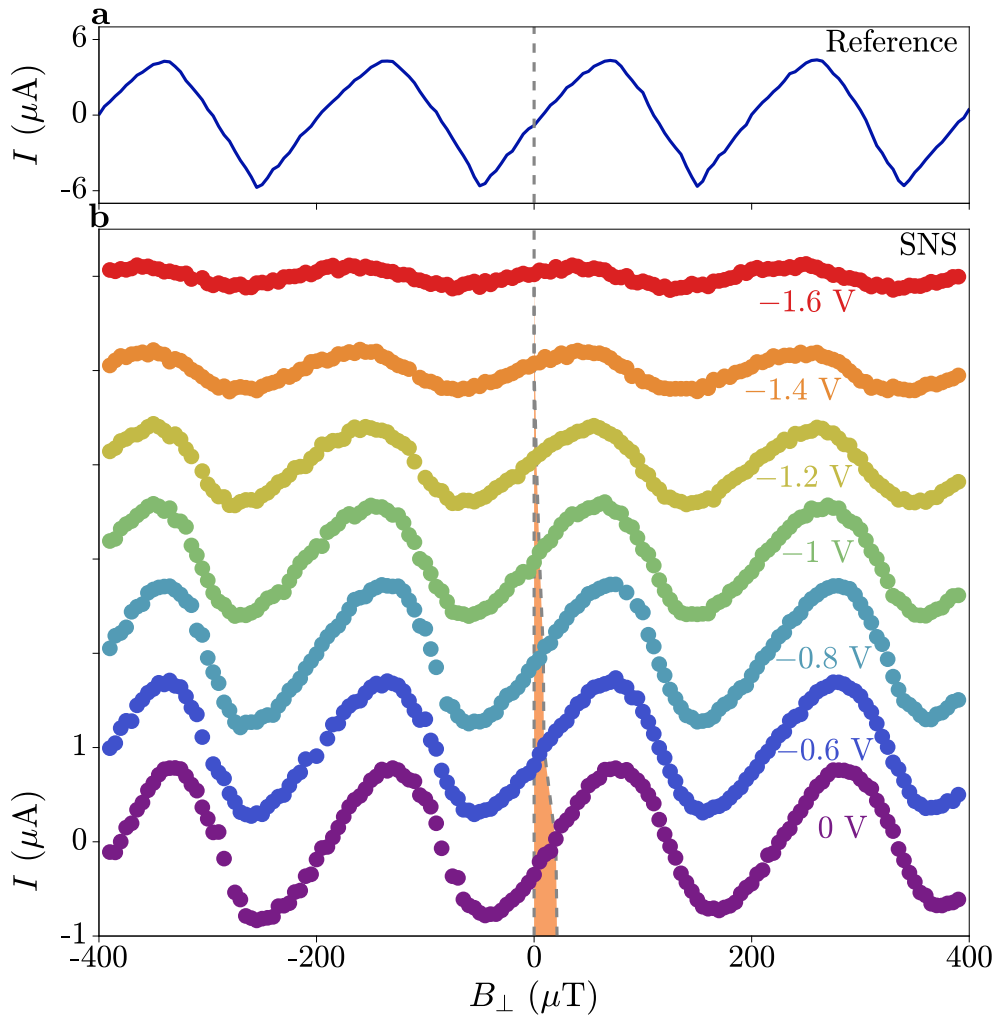

Figure G.1. Summary of Type A phase shifts at $B_{\parallel} = 0.2$ T. a Switching current of the Reference Device at $B_{\parallel} = 0.2$ T, plotted such that the zero-current position is at $B_{\perp} = 0$ (indicated by the dashed grey line). **b** Current-phase relation of Device 1 at $B_{\parallel} = 0.2$ T, for different top-gate voltages V_{TG} (indicated by the colours). Traces are plotted relative to the Reference Device. A gate-dependent phase shift is indicated by deviation of the zero-current positions (star markers) from the Reference Device (dashed grey line).

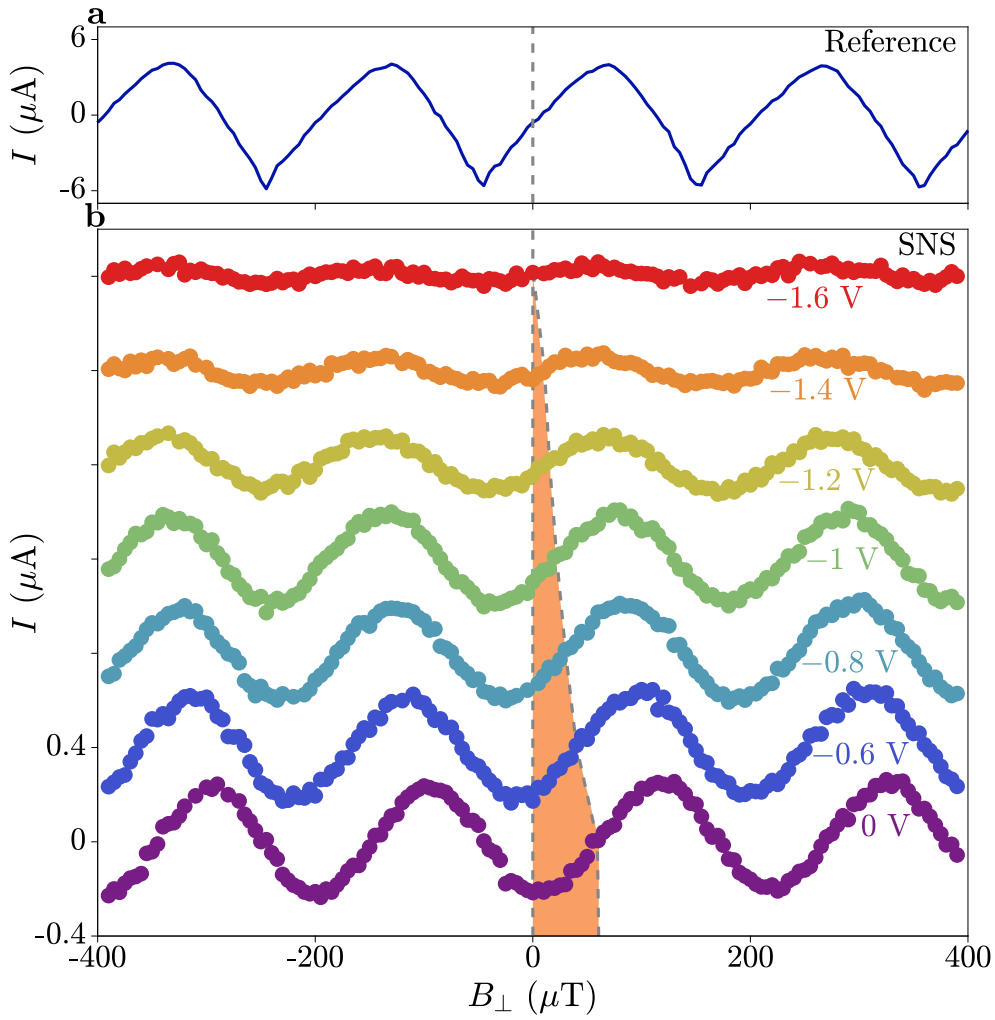

Figure G.2. Summary of Type A phase shifts at $B_{\parallel} = 0.4$ T. a Switching current of the Reference Device at $B_{\parallel} = 0.4$ T, plotted such that the zero-current position is at $B_{\perp} = 0$ (indicated by the dashed grey line). **b** Current-phase relation of Device 1 at $B_{\parallel} = 0.4$ T, for different top-gate voltages V_{TG} (indicated by the colours). Traces are plotted relative to the Reference Device. A gate-dependent phase shift is indicated by deviation of the zero-current positions (star markers) from the Reference Device (dashed grey line).

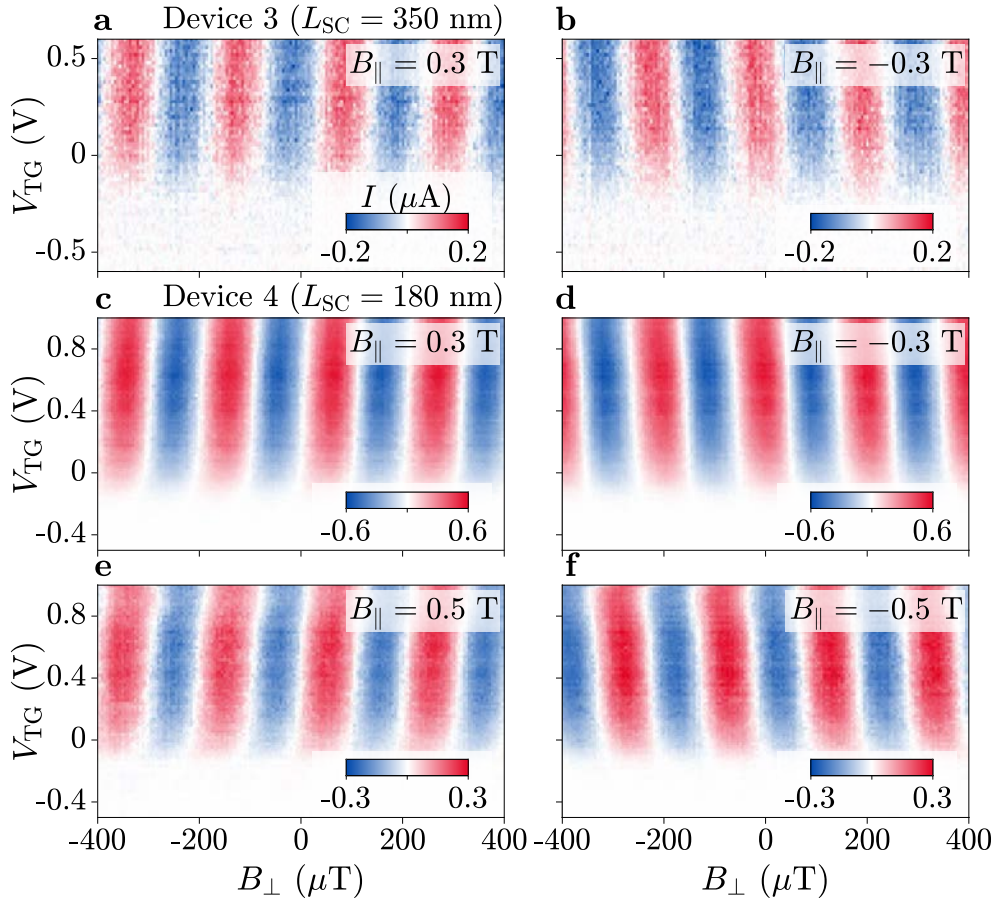

Figure G.3. Type A phase shifts as a function of gate voltage. **a, b** Switching current I of Device 3, after subtraction of a constant background corresponding to the Al constriction, as a function of perpendicular magnetic field $B_\perp$ and top-gate voltage V_{TG}, for $B_\parallel = 0.3$ T and $B_\parallel = -0.3$ T respectively. A gate-dependent shift in the zero-current position is indicated by the dashed line. **c, d** Same as (a, b) for Device 4. (e, f) Same as (c, d) for a larger in-plane field magnitude of $|B_\parallel| = 0.5$ T.

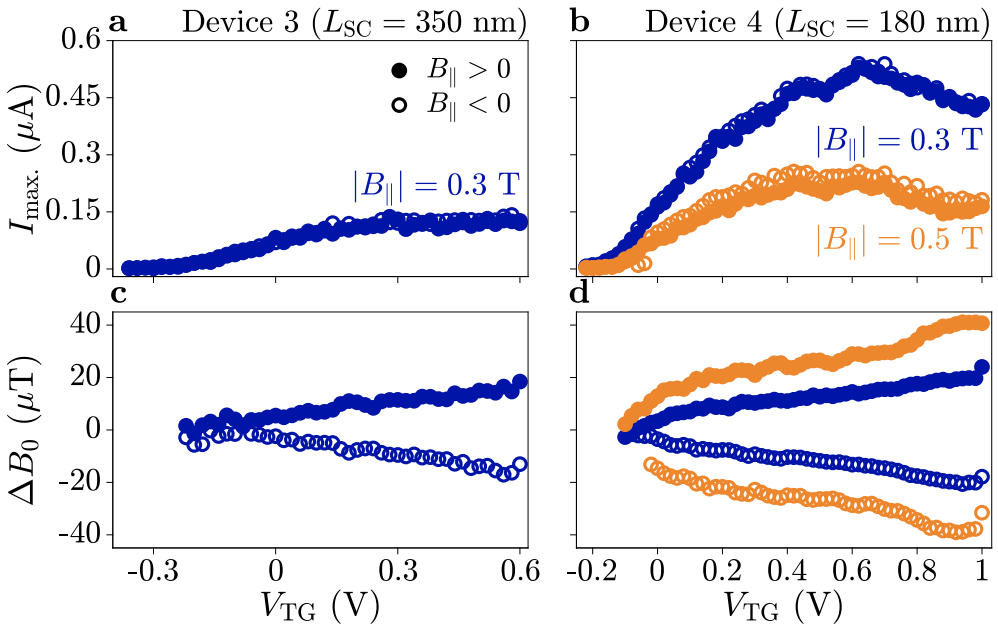

Figure G.4. Analysis of gate-dependent Type A phase shifts. a, b Switching current obtained by fitting the data in Fig. G.3, for Devices 3 and 4 respectively. Positive (negative) in-plane fields $B_\parallel$ are indicated by the full (empty) circles, with blue (yellow) colour indicating the in-plane field magnitude of $|B_\parallel| = 0.3$ T ($|B_\parallel| = 0.5$ T). **c, d** Perpendicular field offset B_0, relative to that of the most negative top-gate voltage at which oscillations were observed. This corresponds to $V_{TG} = -0.25$ V and $V_{TG} = -0.15$ V, for Devices 3 and 4 respectively.

Bibliography

[1] B. Josephson, Physics Letters **1**, 251 (1962).

[2] P. W. Anderson and J. M. Rowell, Physical Review Letters **10**, 230 (1963).

[3] J. M. Rowell, Physical Review Letters **11**, 200 (1963).

[4] I. Giaever, Physical Review Letters **14**, 904 (1965).

[5] W. Anacker, IEEE Transactions on Magnetics **5**, 968 (1969).

[6] H. Zappe, IEEE Transactions on Magnetics **13**, 41 (1977).

[7] S. Anders, M. Blamire, F.-I. Buchholz, D.-G. Crété, R. Cristiano, P. Febvre, L. Fritzsch, A. Herr, E. Il'ichev, J. Kohlmann, J. Kunert, H.-G. Meyer, J. Niemeyer, T. Ortlepp, H. Rogalla, T. Schurig, M. Siegel, R. Stolz, E. Tarte, H. ter Brake, H. Toepfer, J.-C. Villegier, A. Zagoskin, and A. Zorin, Physica C: Superconductivity **470**, 2079 (2010).

[8] K. Likharev and V. Semenov, IEEE Transactions on Applied Superconductivity **1**, 3 (1991).

[9] K. K. Likharev, Czechoslovak Journal of Physics **46**, 3331 (1996).

[10] T. Gheewala, IEEE Transactions on Electron Devices **27**, 1857 (1980).

[11] T. D. Clark, R. J. Prance, and A. D. C. Grassie, Journal of Applied Physics **51**, 2736 (1980).

[12] A. Kleinsasser and T. Jackson, IEEE Transactions on Magnetics **25**, 1274 (1989).

[13] F. Wen, J. Yuan, K. S. Wickramasinghe, W. Mayer, J. Shabani, and E. Tutuc, IEEE Transactions on Electron Devices **68**, 1524 (2021).

[14] R. Giffard, J. Gallop, and B. Petley, Progress in Quantum Electronics **4**, 301 (1976).

[15] S. J. Swithenby, Journal of Physics E: Scientific Instruments **13**, 801 (1980).

[16] J. Clarke, in *Superconducting Electronics* (Springer Berlin Heidelberg, 1989) pp. 87–148.

[17] R. L. Fagaly, Review of Scientific Instruments **77**, 101101 (2006).

[18] H. Tolner, C. Andriesse, and H. Schaeffer, Infrared Physics **16**, 213 (1976).

[19] G. Oelsner, L. S. Revin, E. Il'ichev, A. L. Pankratov, H.-G. Meyer, L. Grönberg, J. Hassel, and L. S. Kuzmin, Applied Physics Letters **103**, 142605 (2013).

[20] A. Vystavkin, V. Gubankov, L. Kuzmin, K. Likharev, V. Migulin, and V. Semenov, Revue de Physique Appliquée **9**, 79 (1974).

[21] V. A. Kulikov and K. K. Likharev, Radiofizika **19**, 543 (1976).

[22] B. Ulrich, Infrared Physics **17**, 467 (1977).

[23] P. L. Richards, T. M. Shen, R. E. Harris, and F. L. Lloyd, Applied Physics Letters **34**, 345 (1979).

[24] G. J. Dolan, T. G. Phillips, and D. P. Woody, Applied Physics Letters **34**, 347 (1979).

[25] J. Tucker, IEEE Journal of Quantum Electronics **15**, 1234 (1979).

[26] J. R. Tucker, Applied Physics Letters **36**, 477 (1980).

[27] T.-M. Shen, P. L. Richards, R. E. Harris, and F. L. Lloyd, Applied Physics Letters **36**, 777 (1980).

[28] J. R. Tucker and M. J. Feldman, Reviews of Modern Physics **57**, 1055 (1985).

[29] M. T. Levinsen, R. Y. Chiao, M. J. Feldman, and B. A. Tucker, Applied Physics Letters **31**, 776 (1977).

[30] J. Niemeyer, J. H. Hinken, and R. L. Kautz, Applied Physics Letters **45**, 478 (1984).

[31] B. Jeanneret and S. P. Benz, The European Physical Journal Special Topics **172**, 181 (2009).

[32] P. Krantz, M. Kjaergaard, F. Yan, T. P. Orlando, S. Gustavsson, and W. D. Oliver, Applied Physics Reviews **6**, 021318 (2019).

[33] J. E. Mooij, T. P. Orlando, L. Levitov, L. Tian, C. H. van der Wal, and S. Lloyd, Science **285**, 1036 (1999).

[34] T. P. Orlando, J. E. Mooij, L. Tian, C. H. van der Wal, L. S. Levitov, S. Lloyd, and J. J. Mazo, Physical Review B **60**, 15398 (1999).

[35] F. Yan, S. Gustavsson, A. Kamal, J. Birenbaum, A. P. Sears, D. Hover, T. J. Gudmundsen, D. Rosenberg, G. Samach, S. Weber, J. L. Yoder, T. P. Orlando, J. Clarke, A. J. Kerman, and W. D. Oliver, Nature Communications **7**, 12964 (2016).

[36] V. E. Manucharyan, J. Koch, L. I. Glazman, and M. H. Devoret, Science **326**, 113 (2009).

[37] L. B. Nguyen, Y.-H. Lin, A. Somoroff, R. Mencia, N. Grabon, and V. E. Manucharyan, Physical Review X **9**, 041041 (2019).

[38] P. Brooks, A. Kitaev, and J. Preskill, Physical Review A **87**, 052306 (2013).

[39] A. Gyenis, P. S. Mundada, A. D. Paolo, T. M. Hazard, X. You, D. I. Schuster, J. Koch, A. Blais, and A. A. Houck, PRX Quantum **2** (2021).

[40] A. Gyenis, A. D. Paolo, J. Koch, A. Blais, A. A. Houck, and D. I. Schuster, PRX Quantum **2**, 010339 (2021).

[41] J. Koch, T. M. Yu, J. Gambetta, A. A. Houck, D. I. Schuster, J. Majer, A. Blais, M. H. Devoret, S. M. Girvin, and R. J. Schoelkopf, Physical Review A **76**, 042319 (2007).

[42] F. Arute, K. Arya, R. Babbush, D. Bacon, J. C. Bardin, R. Barends, R. Biswas, S. Boixo, F. G. S. L. Brandao, D. A. Buell, B. Burkett, Y. Chen, Z. Chen, B. Chiaro, R. Collins, W. Courtney, A. Dunsworth, E. Farhi, B. Foxen, A. Fowler, C. Gidney, M. Giustina, R. Graff, K. Guerin, S. Habegger, M. P. Harrigan, M. J. Hartmann, A. Ho, M. Hoffmann, T. Huang, T. S. Humble, S. V. Isakov, E. Jeffrey, Z. Jiang, D. Kafri, K. Kechedzhi, J. Kelly, P. V. Klimov, S. Knysh, A. Korotkov, F. Kostritsa, D. Landhuis, M. Lindmark, E. Lucero, D. Lyakh, S. Mandrà, J. R. McClean, M. McEwen, A. Megrant, X. Mi, K. Michielsen, M. Mohseni, J. Mutus, O. Naaman, M. Neeley, C. Neill, M. Y. Niu, E. Ostby, A. Petukhov, J. C. Platt, C. Quintana, E. G. Rieffel, P. Roushan, N. C. Rubin, D. Sank, K. J. Satzinger, V. Smelyanskiy, K. J. Sung, M. D. Trevithick, A. Vainsencher, B. Villalonga, T. White, Z. J. Yao, P. Yeh, A. Zalcman, H. Neven, and J. M. Martinis, Nature **574**, 505 (2019).

[43] Y. Kim, A. Eddins, S. Anand, K. X. Wei, E. van den Berg, S. Rosenblatt, H. Nayfeh, Y. Wu, M. Zaletel, K. Temme, and A. Kandala, Nature **618**, 500 (2023).

[44] R. C. Jaklevic, J. Lambe, A. H. Silver, and J. E. Mercereau, Physical Review Letters **12**, 159 (1964).

[45] A. H. Silver and J. E. Zimmerman, Physical Review **157**, 317 (1967).

[46] C. L. Huang and T. V. Duzer, Applied Physics Letters **25**, 753 (1974).

[47] H. Takayanagi and T. Kawakami, Physical Review Letters **54**, 2449 (1985).

[48] P. Krogstrup, N. L. B. Ziino, W. Chang, S. M. Albrecht, M. H. Madsen, E. Johnson, J. Nygård, C. Marcus, and T. S. Jespersen, Nature Materials **14**, 400 (2015).

[49] W. Chang, S. M. Albrecht, T. S. Jespersen, F. Kuemmeth, P. Krogstrup, J. Nygård, and C. M. Marcus, Nature Nanotechnology **10**, 232 (2015).

[50] J. Shabani, M. Kjaergaard, H. J. Suominen, Y. Kim, F. Nichele, K. Pakrouski, T. Stankevic, R. M. Lutchyn, P. Krogstrup, R. Feidenhans'l, S. Kraemer, C. Nayak, M. Troyer, C. M. Marcus, and C. J. Palmstrøm, Physical Review B **93**, 155402 (2016).

[51] T. Larsen, K. Petersson, F. Kuemmeth, T. Jespersen, P. Krogstrup, J. Nygård, and C. Marcus, Physical Review Letters **115**, 127001 (2015).

[52] G. de Lange, B. van Heck, A. Bruno, D. van Woerkom, A. Geresdi, S. Plissard, E. Bakkers, A. Akhmerov, and L. DiCarlo, Physical Review Letters **115**, 127002 (2015).

[53] L. Casparis, M. R. Connolly, M. Kjaergaard, N. J. Pearson, A. Kringhøj, T. W. Larsen, F. Kuemmeth, T. Wang, C. Thomas, S. Gronin, G. C. Gardner, M. J. Manfra, C. M. Marcus, and K. D. Petersson, Nature Nanotechnology **13**, 915 (2018).

[54] J. I.-J. Wang, D. Rodan-Legrain, L. Bretheau, D. L. Campbell, B. Kannan, D. Kim, M. Kjaergaard, P. Krantz, G. O. Samach, F. Yan, J. L. Yoder, K. Watanabe, T. Taniguchi, T. P. Orlando, S. Gustavsson, P. Jarillo-Herrero, and W. D. Oliver, Nature Nanotechnology **14**, 120 (2018).

[55] S. J. Weber, Nature Nanotechnology **13**, 877 (2018).

[56] Z. Qi, H.-Y. Xie, J. Shabani, V. E. Manucharyan, A. Levchenko, and M. G. Vavilov, Physical Review B **97**, 134518 (2018).

[57] R. Aguado, Applied Physics Letters **117**, 240501 (2020).

[58] A. Hertel, M. Eichinger, L. O. Andersen, D. M. van Zanten, S. Kallatt, P. Scarlino, A. Kringhøj, J. M. Chavez-Garcia, G. C. Gardner, S. Gronin, M. J. Manfra, A. Gyenis, M. Kjaergaard, C. M. Marcus, and K. D. Petersson, Physical Review Applied **18**, 034042 (2022).

[59] J. G. Kroll, W. Uilhoorn, K. L. van der Enden, D. de Jong, K. Watanabe, T. Taniguchi, S. Goswami, M. C. Cassidy, and L. P. Kouwenhoven, Nature Communications **9**, 4615 (2018).

[60] F. Luthi, T. Stavenga, O. Enzing, A. Bruno, C. Dickel, N. Langford, M. Rol, T. Jespersen, J. Nygård, P. Krogstrup, and L. DiCarlo, Physical Review Letters **120**, 100502 (2018).

[61] M. Pita-Vidal, A. Bargerbos, C.-K. Yang, D. J. van Woerkom, W. Pfaff, N. Haider, P. Krogstrup, L. P. Kouwenhoven, G. de Lange, and A. Kou, Physical Review Applied **14**, 064038 (2020).

[62] D. Sabonis, O. Erlandsson, A. Kringhøj, B. van Heck, T. W. Larsen, I. Petkovic, P. Krogstrup, K. D. Petersson, and C. M. Marcus, Physical Review Letters **125**, 156804 (2020).

[63] T. Larsen, M. Gershenson, L. Casparis, A. Kringhøj, N. Pearson, R. McNeil, F. Kuemmeth, P. Krogstrup, K. Petersson, and C. Marcus, Physical Review Letters **125**, 056801 (2020).

[64] J. Danon, A. Chatterjee, A. Gyenis, and F. Kuemmeth, Applied Physics Letters **119**, 260502 (2021).

[65] C. Schrade, C. M. Marcus, and A. Gyenis, PRX Quantum **3**, 030303 (2022).

[66] C. Ciaccia, R. Haller, A. C. C. Drachmann, T. Lindemann, M. J. Manfra, C. Schrade, and C. Schönenberger, (2023), arXiv:2306.05467 .

[67] A. F. Andreev, Soviet Journal of Experimental and Theoretical Physics **46**, 1823 (1964).

[68] M. A. Despósito and A. Levy Yeyati, Physical Review B **64**, 140511 (2001).

[69] A. Zazunov, V. S. Shumeiko, E. N. Bratus', J. Lantz, and G. Wendin, Physical Review Letters **90**, 087003 (2003).

[70] L. Bretheau, Ç. O. Girit, H. Pothier, D. Esteve, and C. Urbina, Nature **499**, 312 (2013).

[71] C. Janvier, L. Tosi, L. Bretheau, C. O. Girit, M. Stern, P. Bertet, P. Joyez, D. Vion, D. Esteve, M. F. Goffman, H. Pothier, and C. Urbina, Science **349**, 1199 (2015).

[72] M. Hays, G. de Lange, K. Serniak, D. J. van Woerkom, D. Bouman, P. Krogstrup, J. Nygård, A. Geresdi, and M. H. Devoret, Physical Review Letters **121**, 047001 (2018).

[73] N. M. Chtchelkatchev and Y. V. Nazarov, Physical Review Letters **90**, 226806 (2003).

[74] C. Padurariu and Y. V. Nazarov, Physical Review B **81**, 144519 (2010).

[75] C. Padurariu and Y. V. Nazarov, Europhysics Letters **100**, 57006 (2012).

[76] L. Tosi, C. Metzger, M. F. Goffman, C. Urbina, H. Pothier, S. Park, A. L. Yeyati, J. Nygård, and P. Krogstrup, Physical Review X **9**, 011010 (2019).

[77] M. Hays, V. Fatemi, K. Serniak, D. Bouman, S. Diamond, G. de Lange, P. Krogstrup, J. Nygård, A. Geresdi, and M. H. Devoret, Nature Physics **16**, 1103 (2020).

[78] M. Hays, V. Fatemi, D. Bouman, J. Cerrillo, S. Diamond, K. Serniak, T. Connolly, P. Krogstrup, J. Nygård, A. L. Yeyati, A. Geresdi, and M. H. Devoret, Science **373**, 430 (2021).

[79] M. Hays, *Realizing an Andreev Spin Qubit* (Springer International Publishing, 2021).

[80] M. Pita-Vidal, A. Bargerbos, R. Žitko, L. J. Splitthoff, L. Grünhaupt, J. J. Wesdorp, Y. Liu, L. P. Kouwenhoven, R. Aguado, B. van Heck, A. Kou, and C. K. Andersen, Nature Physics **8**, 1110 (2023).

[81] V. V. Ryazanov, V. A. Oboznov, A. Y. Rusanov, A. V. Veretennikov, A. A. Golubov, and J. Aarts, Physical Review Letters **86**, 2427 (2001).

[82] T. Kontos, M. Aprili, J. Lesueur, F. Genêt, B. Stephanidis, and R. Boursier, Physical Review Letters **89**, 137007 (2002).

[83] A. Bauer, J. Bentner, M. Aprili, M. L. D. Rocca, M. Reinwald, W. Wegscheider, and C. Strunk, Physical Review Letters **92** (2004).

[84] E. C. Gingrich, B. M. Niedzielski, J. A. Glick, Y. Wang, D. L. Miller, R. Loloee, W. P. P. Jr, and N. O. Birge, Nature Physics **12**, 564 (2016).

[85] T. Yamashita, S. Kim, H. Kato, W. Qiu, K. Semba, A. Fujimaki, and H. Terai, Scientific Reports **10**, 13687 (2020).

[86] S. Vaitiekėnas, Y. Liu, P. Krogstrup, and C. M. Marcus, Nature Physics **17**, 43 (2020).

[87] T. Yokoyama, M. Eto, and Y. V. Nazarov, Physcial Review B **89**, 195407 (2014).

[88] A. Murani, A. Kasumov, S. Sengupta, Y. A. Kasumov, V. T. Volkov, I. I. Khodos, F. Brisset, R. Delagrange, A. Chepelianskii, R. Deblock, H. Bouchiat, and S. Guéron, Nature Communications **8**, 15941 (2017).

[89] C. Li, J. C. de Boer, B. de Ronde, S. V. Ramankutty, E. van Heumen, Y. Huang, A. de Visser, A. A. Golubov, M. S. Golden, and A. Brinkman, Nature Materials **17**, 875 (2018).

[90] C. Li, B. de Ronde, J. de Boer, J. Ridderbos, F. Zwanenburg, Y. Huang, A. Golubov, and A. Brinkman, Physical Review Letters **123**, 026802 (2019).

[91] T. V. Duzer and S. Kumar, Cryogenics **30**, 1014 (1990).

[92] E. Terzioglu and M. Beasley, IEEE Transactions on Applied Superconductivity **8**, 48 (1998).

[93] A. V. Ustinov and V. K. Kaplunenko, Journal of Applied Physics **94**, 5405 (2003).

[94] A. K. Feofanov, V. A. Oboznov, V. V. Bol'ginov, J. Lisenfeld, S. Poletto, V. V. Ryazanov, A. N. Rossolenko, M. Khabipov, D. Balashov, A. B. Zorin, P. N. Dmitriev, V. P. Koshelets, and A. V. Ustinov, Nature Physics **6**, 593 (2010).

[95] T. Yamashita and H. Terai, IEEJ Transactions on Fundamentals and Materials **136**, 728 (2016).

[96] A. A. Maksimovskaya, V. I. Ruzhickiy, N. V. Klenov, S. V. Bakurskiy, M. Y. Kupriyanov, and I. I. Soloviev, Journal of Experimental and Theoretical Physics Letters **115**, 735 (2022).

[97] I. Žutić, J. Fabian, and S. Das Sarma, Reviews of Modern Physics **76**, 323 (2004).

[98] B. Béri, J. H. Bardarson, and C. W. J. Beenakker, Physical Review B **77**, 045311 (2008).

[99] J. Linder and J. W. A. Robinson, Nature Physics **11**, 307 (2015).

[100] S. Hart, H. Ren, M. Kosowsky, G. Ben-Shach, P. Leubner, C. Brüne, H. Buhmann, L. W. Molenkamp, B. I. Halperin, and A. Yacoby, Nature Physics **13**, 87 (2017).

[101] C. Baumgartner, L. Fuchs, A. Costa, S. Reinhardt, S. Gronin, G. C. Gardner, T. Lindemann, M. J. Manfra, P. E. Faria Junior, D. Kochan, J. Fabian, N. Paradiso, and C. Strunk, Nature Nanotechnology **17**, 39 (2022).

[102] A. Costa, C. Baumgartner, S. Reinhardt, J. Berger, S. Gronin, G. C. Gardner, T. Lindemann, M. J. Manfra, J. Fabian, D. Kochan, N. Paradiso, and C. Strunk, Nature Nanotechnology (2023).

[103] C. Baumgartner, L. Fuchs, A. Costa, J. Picó-Cortés, S. Reinhardt, S. Gronin, G. C. Gardner, T. Lindemann, M. J. Manfra, P. E. F. Junior, D. Kochan, J. Fabian, N. Paradiso, and C. Strunk, Journal of Physics: Condensed Matter **34**, 154005 (2022).

[104] H. Sickinger, A. Lipman, M. Weides, R. G. Mints, H. Kohlstedt, D. Koelle, R. Kleiner, and E. Goldobin, Physical Review Letters **109**, 107002 (2012).

[105] F. Konschelle, I. V. Tokatly, and F. S. Bergeret, Physical Review B **92**, 125443 (2015).

[106] D. B. Szombati, S. Nadj-Perge, D. Car, S. R. Plissard, E. P. A. M. Bakkers, and L. P. Kouwenhoven, Nature Physics **12**, 568 (2016).

[107] E. M. Spanton, M. Deng, S. Vaitiekėnas, P. Krogstrup, J. Nygård, C. M. Marcus, and K. A. Moler, Nature Physics **13**, 1177 (2017).

[108] A. Assouline, C. Feuillet-Palma, N. Bergeal, T. Zhang, A. Mottaghizadeh, A. Zimmers, E. Lhuillier, M. Eddrie, P. Atkinson, M. Aprili, and H. Aubin, Nature Communications **10**, 126 (2019).

[109] W. Mayer, M. C. Dartiailh, J. Yuan, K. S. Wickramasinghe, E. Rossi, and J. Shabani, Nature Communications **11**, 212 (2020).

[110] T. Oka and H. Aoki, Physical Review B **79**, 081406 (2009).

[111] T. Oka and S. Kitamura, Annual Review of Condensed Matter Physics **10**, 387 (2019).

[112] J. W. McIver, B. Schulte, F.-U. Stein, T. Matsuyama, G. Jotzu, G. Meier, and A. Cavalleri, Nature Physics **16**, 38 (2020).

[113] M. S. Rudner and N. H. Lindner, Nature Reviews Physics **2**, 229 (2020).

[114] S. Park, W. Lee, S. Jang, Y.-B. Choi, J. Park, W. Jung, K. Watanabe, T. Taniguchi, G. Y. Cho, and G.-H. Lee, Nature **603**, 421 (2022).

[115] L. Fu and C. L. Kane, Physical Review Letters **100**, 096407 (2008).

[116] J. D. Sau, R. M. Lutchyn, S. Tewari, and S. D. Sarma, Physical Review Letters **104**, 040502 (2010).

[117] J. Alicea, Physical Review B **81**, 125318 (2010).

[118] Y. Oreg, G. Refael, and F. von Oppen, Physical Review Letters **105**, 177002 (2010).

[119] R. M. Lutchyn, J. D. Sau, and S. D. Sarma, Physical Review Letters **105**, 077001 (2010).

[120] F. Pientka, A. Keselman, E. Berg, A. Yacoby, A. Stern, and B. I. Halperin, Physical Review X **7**, 021032 (2017).

[121] M. Hell, M. Leijnse, and K. Flensberg, Physical Review Letters **118**, 107701 (2017).

[122] A. Fornieri, A. M. Whiticar, F. Setiawan, E. Portolés, A. C. C. Drachmann, A. Keselman, S. Gronin, C. Thomas, T. Wang, R. Kallaher, G. C. Gardner, E. Berg, M. J. Manfra, A. Stern, C. M. Marcus, and F. Nichele, Nature **569**, 89 (2019).

[123] H. Ren, F. Pientka, S. Hart, A. T. Pierce, M. Kosowsky, L. Lunczer, R. Schlereth, B. Scharf, E. M. Hankiewicz, L. W. Molenkamp, B. I. Halperin, and A. Yacoby, Nature **569**, 93 (2019).

[124] M. C. Dartiailh, W. Mayer, J. Yuan, K. S. Wickramasinghe, A. Matos-Abiague, I. Žutić, and J. Shabani, Physcial Review Letters **126**, 036802 (2021).

[125] A. Kitaev, Annals of Physics **303**, 2 (2003).

[126] C. Nayak, S. H. Simon, A. Stern, M. Freedman, and S. D. Sarma, Reviews of Modern Physics **80**, 1083 (2008).

[127] R. M. Lutchyn, E. P. A. M. Bakkers, L. P. Kouwenhoven, P. Krogstrup, C. M. Marcus, and Y. Oreg, Nature Reviews Materials **3**, 52 (2018).

[128] T. Zhou, M. C. Dartiailh, W. Mayer, J. E. Han, A. Matos-Abiague, J. Shabani, and I. Žutić, Physical Review Letters **124**, 137001 (2020).

[129] T. Zhou, M. C. Dartiailh, K. Sardashti, J. E. Han, A. Matos-Abiague, J. Shabani, and I. Žutić, Nature Communications **13**, 1738 (2022).

[130] T. Schäpers, *Superconductor/Semiconductor Junctions* (Springer Berlin Heidelberg, 2001).

[131] T. Ihn, *Semiconductor Nanostructures: Quantum states and electronic transport* (Oxford University Press, 2010).

[132] L. Esaki, in *Electronic Properties of Multilayers and Low-Dimensional Semiconductor Structures* (Springer US, 1990) pp. 1–24.

[133] D. C. Tsui, Physical Review Letters **24**, 303 (1970).

[134] E. Yamaguchi, Physical Review B **32**, 5280 (1985).

[135] C. Klauber and R. S. C. Smart, in *Springer Series in Surface Sciences* (Springer Berlin Heidelberg, 1992) pp. 3–65.

[136] K. S. Wickramasinghe, W. Mayer, J. Yuan, T. Nguyen, L. Jiao, V. Manucharyan, and J. Shabani, Applied Physics Letters **113**, 262104 (2018).

[137] C. Kittel, *Introduction to Solid State Physics* (John Wiley & Sons, Ltd, 2004).

[138] R. Winkler, *Spin-orbit Coupling Effects in Two-Dimensional Electron and Hole Systems* (Springer Berlin Heidelberg, 2003).

[139] G. Dresselhaus, A. F. Kip, and C. Kittel, Physical Review **95**, 568 (1954).

[140] R. H. Parmenter, Physical Review **100**, 573 (1955).

[141] G. Dresselhaus, Physical Review **100**, 580 (1955).

[142] F. J. Ohkawa, Journal of the Physical Society of Japan **41**, 122 (1976).

[143] Y. A. Bychkov and E. I. Rashba, Journal of Physics C: Solid State Physics **17**, 6039 (1984).

[144] H. K. Onnes, Leiden Communications **120b** (1911).

[145] L. N. Cooper, Physical Review **104**, 1189 (1956).

[146] J. Bardeen, L. N. Cooper, and J. R. Schrieffer, Physical Review **108**, 1175 (1957).

[147] M. Tinkham, *Introduction to Superconductivity: Second Edition* (Dover Publications, 2004).

[148] P. G. D. Gennes, *Superconductivity of Metals and Alloys* (CRC Press, 2018).

[149] V. L. Ginzburg and L. D. Landau, in *Collected Papers of L.D. Landau* (Elsevier, 1965) pp. 217–225.

[150] I. Giaever, Physical Review Letters **5**, 464 (1960).

[151] M. Büttiker, Y. Imry, R. Landauer, and S. Pinhas, Physical Review B **31**, 6207 (1985).

[152] C. W. J. Beenakker, Reviews of Modern Physics **69**, 731 (1997).

[153] F. Nichele, E. Portolés, A. Fornieri, A. M. Whiticar, A. C. C. Drachmann, S. Gronin, T. Wang, G. C. Gardner, C. Thomas, A. T. Hatke, M. J. Manfra, and C. M. Marcus, Physical Review Letters **124**, 226801 (2020).

[154] G. E. Blonder, M. Tinkham, and T. M. Klapwijk, Physical Review B **25**, 4515 (1982).

[155] A. V. Zaitsev, Soviet Journal of Experimental and Theoretical Physics **86**, 1742 (1984).

[156] G. B. Arnold, Journal of Low Temperature Physics **59**, 143 (1985).

[157] G. E. Blonder and M. Tinkham, Physical Review B **27**, 112 (1983).

[158] T. M. Klapwijk, Journal of Superconductivity **17**, 593 (2004).

[159] R. Parks, *Superconductivity*, edited by R. D. Parks (Routledge, 2018).

[160] A. A. Golubov, in *SPIE Proceedings*, edited by I. Bozovic (SPIE, 1994).

[161] B. Pannetier and H. Courtois, Journal of Low Temperature Physics **118**, 599 (2000).

[162] J. Clarke, Le Journal de Physique Colloques **29**, C2 (1968).

[163] M. Y. Kupriyanov and V. F. Lukichev, Soviet Journal of Experimental and Theoretical Physics **94**, 139 (1988).

[164] G. Eilenberger, Zeitschrift für Physik A Hadrons and nuclei **214**, 195 (1968).

[165] P. G. de Gennes, Reviews of Modern Physics **36**, 225 (1964).

[166] A. F. Andreev, Journal of Experimental and Theoretical Physics **49**, 655 (1966).

[167] I. O. Kulik, Soviet Journal of Experimental and Theoretical Physics **57**, 1745 (1969).

[168] C. Ishii, Progress of Theoretical Physics **44**, 1525 (1970).

[169] J. Bardeen and J. L. Johnson, Physical Review B **5**, 72 (1972).

[170] P. Dubos, H. Courtois, B. Pannetier, F. K. Wilhelm, A. D. Zaikin, and G. Schön, Physical Review B **63**, 064502 (2001).

[171] C. W. J. Beenakker and H. van Houten, Physical Review Letters **66**, 3056 (1991).

[172] A. Furusaki and M. Tsukada, Physical Review B **43**, 10164 (1991).

[173] J. H. Bardarson, Journal of Physics A: Mathematical and Theoretical **41**, 405203 (2008).

[174] S. Artemenko, A. Volkov, and A. Zaitsev, Solid State Communications **30**, 771 (1979).

[175] J. C. Cuevas, J. Hammer, J. Kopu, J. K. Viljas, and M. Eschrig, Physical Review B **73**, 184505 (2006).

[176] G. Niebler, G. Cuniberti, and T. Novotný, Superconductor Science and Technology **22**, 085016 (2009).

[177] Y. V. Nazarov and Y. M. Blanter, *Quantum Transport* (Cambridge University Press, 2009).

[178] O. Dorokhov, Solid State Communications **51**, 381 (1984).

[179] K. M. Schep and G. E. W. Bauer, Physical Review B **56**, 15860 (1997).

[180] K. K. Likharev, Reviews of Modern Physics **51**, 101 (1979).

[181] A. A. Golubov, M. Y. Kupriyanov, and E. Il'ichev, Reviews of Modern Physics **76**, 411 (2004).

[182] J. M. Martinis, M. H. Devoret, and J. Clarke, Physical Review B **35**, 4682 (1987).

[183] W. C. Stewart, Applied Physics Letters **12**, 277 (1968).

[184] D. E. McCumber, Journal of Applied Physics **39**, 3113 (1968).

[185] T. A. Fulton and L. N. Dunkleberger, Physical Review B **9**, 4760 (1974).

[186] A. Bezryadin, Stochastic premature switching and Kurkijärvi theory, in *Superconductivity in Nanowires* (John Wiley & Sons, Ltd, 2012) Chap. 8, pp. 131–162.

[187] E. Ben-Jacob, D. J. Bergman, B. J. Matkowsky, and Z. Schuss, Physical Review A **26**, 2805 (1982).

[188] H. Grabert, P. Olschowski, and U. Weiss, Physical Review B **36**, 1931 (1987).

[189] D. Massarotti, L. Longobardi, L. Galletti, D. Stornaiuolo, D. Montemurro, G. Pepe, G. Rotoli, A. Barone, and F. Tafuri, Low Temperature Physics **38**, 263 (2012).

[190] S. Washburn, R. A. Webb, R. F. Voss, and S. M. Faris, Physical Review Letters **54**, 2712 (1985).

[191] E. Turlot, D. Esteve, C. Urbina, J. M. Martinis, M. H. Devoret, S. Linkwitz, and H. Grabert, Physical Review Letters **62**, 1788 (1989).

[192] F. London and H. London, Proceedings of the Royal Society of London. Series A - Mathematical and Physical Sciences **149**, 71 (1935).

[193] B. S. Deaver and W. M. Fairbank, Physical Review Letters **7**, 43 (1961).

[194] J. H. Lee, G.-H. Lee, J. Park, J. Lee, S.-G. Nam, Y.-S. Shin, J. S. Kim, and H.-J. Lee, Nano Letters **14**, 5029 (2014).

[195] B. H. Elfeky, N. Lotfizadeh, W. F. Schiela, W. M. Strickland, M. Dartiailh, K. Sardashti, M. Hatefipour, P. Yu, N. Pankratova, H. Lee, V. E. Manucharyan, and J. Shabani, Nano Letters **21**, 8274 (2021).

[196] H. J. Suominen, J. Danon, M. Kjaergaard, K. Flensberg, J. Shabani, C. J. Palmstrøm, F. Nichele, and C. M. Marcus, Physical Review B **95**, 035307 (2017).

[197] A. C. C. Drachmann, R. E. Diaz, C. Thomas, H. J. Suominen, A. M. Whiticar, A. Fornieri, S. Gronin, T. Wang, G. C. Gardner, A. R. Hamilton, F. Nichele, M. J. Manfra, and C. M. Marcus, Physical Review Materials **5**, 013805 (2021).

[198] A. J. Annunziata, D. F. Santavicca, L. Frunzio, G. Catelani, M. J. Rooks, A. Frydman, and D. E. Prober, Nanotechnology **21**, 445202 (2010).

[199] I. Babich, A. Kudriashov, D. Baranov, and V. S. Stolyarov, Nano Letters **23**, 6713 (2023).

[200] S. Shapiro, Physical Review Letters **11**, 80 (1963).

[201] P. K. Tien and J. P. Gordon, Physical Review **129**, 647 (1963).

[202] R. Gross and A. Marx, Lecture notes in applied superconductivity: Josephson effect and superconducting electronics (2005).

[203] G. Falci, V. Bubanja, and G. Schön, Zeitschrift für Physik B Condensed Matter **85**, 451 (1991).

[204] A. Roychowdhury, M. Dreyer, J. R. Anderson, C. J. Lobb, and F. C. Wellstood, Physical Review Applied **4**, 034011 (2015).

[205] H. Grabert, Physical Review B **92**, 245433 (2015).

[206] O. Peters, N. Bogdanoff, S. Acero González, L. Melischek, J. R. Simon, G. Reecht, C. B. Winkelmann, F. von Oppen, and K. J. Franke, Nature Physics **16**, 1222 (2020).

[207] P. Kot, R. Drost, M. Uhl, J. Ankerhold, J. C. Cuevas, and C. R. Ast, Physical Review B **101**, 134507 (2020).

[208] J. Bardeen, Physical Review Letters **6**, 57 (1961).

[209] N. H. Lindner, G. Refael, and V. Galitski, Nature Physics **7**, 490 (2011).

[210] L. Jiang, T. Kitagawa, J. Alicea, A. R. Akhmerov, D. Pekker, G. Refael, J. I. Cirac, E. Demler, M. D. Lukin, and P. Zoller, Physical Review Letters **106**, 220402 (2011).

[211] T. Kitagawa, T. Oka, A. Brataas, L. Fu, and E. Demler, Physical Review B **84**, 235108 (2011).

[212] A. G. Grushin, A. Gómez-León, and T. Neupert, Physical Review Letters **112**, 156801 (2014).

[213] M. Bukov, L. D'Alessio, and A. Polkovnikov, Advances in Physics **64**, 139 (2015).

[214] J. Koski, A. Landig, A. Pályi, P. Scarlino, C. Reichl, W. Wegscheider, G. Burkard, A. Wallraff, K. Ensslin, and T. Ihn, Physical Review Letters **121**, 043603 (2018).

[215] B. Bauer, T. Pereg-Barnea, T. Karzig, M.-T. Rieder, G. Refael, E. Berg, and Y. Oreg, Physical Review B **100**, 041102 (2019).

[216] J. H. Shirley, Physical Review **138**, B979 (1965).

[217] H. Sambe, Physical Review A **7**, 2203 (1973).

[218] F. H. M. Faisal and J. Z. Kamiński, Physical Review A **56**, 748 (1997).

[219] G. Platero and R. Aguado, Physics Reports **395**, 1 (2004).

[220] M. S. Rudner and N. H. Lindner, (2020), 2003.08252 .

[221] Y. H. Wang, H. Steinberg, P. Jarillo-Herrero, and N. Gedik, Science **342**, 453 (2013).

[222] F. Mahmood, C.-K. Chan, Z. Alpichshev, D. Gardner, Y. Lee, P. A. Lee, and N. Gedik, Nature Physics **12**, 306 (2016).

[223] A. Eckardt, Reviews of Modern Physics **89**, 011004 (2017).

[224] L. W. Clark, N. Jia, N. Schine, C. Baum, A. Georgakopoulos, and J. Simon, Nature **571**, 532 (2019).

[225] K. Wintersperger, C. Braun, F. N. Ünal, A. Eckardt, M. D. Liberto, N. Goldman, I. Bloch, and M. Aidelsburger, Nature Physics **16**, 1058 (2020).

[226] T. Yokoyama, M. Eto, and Y. V. Nazarov, Journal of Physics: Conference Series **568**, 052035 (2014).

[227] J. Cayao, A. M. Black-Schaffer, E. Prada, and R. Aguado, Beilstein Journal of Nanotechnology **9**, 1339 (2018).

[228] T. Schäpers, *Semiconductor Spintronics* (De Gruyter, 2021).

[229] A. Buzdin, Physical Review Letters **101**, 107005 (2008).

[230] W. Mayer, J. Yuan, K. S. Wickramasinghe, T. Nguyen, M. C. Dartiailh, and J. Shabani, Applied Physics Letters **114**, 103104 (2019).

[231] S. J. Pauka, J. D. S. Witt, C. N. Allen, B. Harlech-Jones, A. Jouan, G. C. Gardner, S. Gronin, T. Wang, C. Thomas, M. J. Manfra, J. Gukelberger, J. Gamble, D. J. Reilly, and M. C. Cassidy, Journal of Applied Physics **128**, 114301 (2020).

[232] S. M. Farzaneh, M. Hatefipour, W. F. Schiela, N. Lotfizadeh, P. Yu, B. H. Elfeky, W. M. Strickland, A. Matos-Abiague, and J. Shabani, (2022), arXiv:2208.06050 .

[233] P. M. Tedrow and R. Meservey, Physical Review B **25**, 171 (1982).

[234] H. J. Suominen, M. Kjaergaard, A. R. Hamilton, J. Shabani, C. J. Palmstrøm, C. M. Marcus, and F. Nichele, Physical Review Letters **119**, 176805 (2017).

[235] F. Nichele, A. C. C. Drachmann, A. M. Whiticar, E. C. T. O'Farrell, H. J. Suominen, A. Fornieri, T. Wang, G. C. Gardner, C. Thomas, A. T. Hatke, P. Krogstrup, M. J. Manfra, K. Flensberg, and C. M. Marcus, Physical Review Letters **119**, 136803 (2017).

[236] T. D. Stanescu and S. Das Sarma, Physical Review B **87**, 180504 (2013).

[237] S. Takei, B. M. Fregoso, H.-Y. Hui, A. M. Lobos, and S. Das Sarma, Physical Review Letters **110**, 186803 (2013).

[238] A. E. Mikkelsen, P. Kotetes, P. Krogstrup, and K. Flensberg, Physical Review X **8**, 031040 (2018).

[239] W. L. Sarney, S. P. Svensson, A. C. Leff, W. F. Schiela, J. O. Yuan, M. C. Dartiailh, W. Mayer, K. S. Wickramasinghe, and J. Shabani, Journal of Vacuum Science **38**, 032212 (2020).

[240] E. Cheah, D. Z. Haxell, R. Schott, P. Zeng, E. Paysen, S. C. ten Kate, M. Coraiola, M. Landstetter, A. B. Zadeh, A. Trampert, M. Sousa, H. Riel, F. Nichele, W. Wegscheider, and F. Krizek, Physical Review Materials **7**, 073403 (2023).

[241] V. Umansky, R. de Picciotto, and M. Heiblum, Applied Physics Letters **71**, 683 (1997).

[242] H. Fu, K. V. Reich, and B. I. Shklovskii, Physical Review B **93**, 235312 (2016).

[243] J. D. S. Witt, S. J. Pauka, G. C. Gardner, S. Gronin, T. Wang, C. Thomas, M. J. Manfra, D. J. Reilly, and M. C. Cassidy, Applied Physics Letters **122**, 083101 (2023).

[244] T. Klapwijk, G. Blonder, and M. Tinkham, Physica B+C **109-110**, 1657 (1982).

[245] M. Octavio, M. Tinkham, G. E. Blonder, and T. M. Klapwijk, Physical Review B **27**, 6739 (1983).

[246] E. N. Bratus', V. S. Shumeiko, and G. Wendin, Physical Review Letters **74**, 2110 (1995).

[247] I. O. Kulik and A. N. Omelyanchuk, Soviet Journal of Low Temperature Physics **3**, 459 (1977).

[248] I. O. Kulik and A. N. Omelyanchuk, Journal of Experimental and Theoretical Physics Letters **21**, 96 (1975).

[249] M. Kjaergaard, H. J. Suominen, M. P. Nowak, A. R. Akhmerov, J. Shabani, C. J. Palmstrøm, F. Nichele, and C. M. Marcus, Physical Review Applied **7**, 034029 (2017).

[250] G. Kurizki, P. Bertet, Y. Kubo, K. Mølmer, D. Petrosyan, P. Rabl, and J. Schmiedmayer, Proceedings of the National Academy of Sciences **112**, 3866 (2015).

[251] D. Haxell, E. Cheah, F. Křížek, R. Schott, M. Ritter, M. Hinderling, W. Belzig, C. Bruder, W. Wegscheider, H. Riel, and F. Nichele, Physical Review Letters **130**, 8 (2023).

[252] P. Silvestrini, S. Pagano, R. Cristiano, O. Liengme, and K. E. Gray, Physical Review Letters **60**, 844 (1988).

[253] V. M. Krasnov, T. Bauch, S. Intiso, E. Hürfeld, T. Akazaki, H. Takayanagi, and P. Delsing, Physical Review Letters **95**, 157002 (2005).

[254] G.-H. Lee, D. Jeong, J.-H. Choi, Y.-J. Doh, and H.-J. Lee, Physical Review Letters **107**, 146605 (2011).

[255] A. Murphy, P. Weinberg, T. Aref, U. C. Coskun, V. Vakaryuk, A. Levchenko, and A. Bezryadin, Physical Review Letters **110**, 247001 (2013).

[256] B.-K. Kim and Y.-J. Doh, Journal of the Korean Physical Society **69**, 349 (2016).

[257] J. Kim, B.-K. Kim, H.-S. Kim, A. Hwang, B. Kim, and Y.-J. Doh, Nano Letters **17**, 6997 (2017).

[258] M. Sahu, M.-H. Bae, A. Rogachev, D. Pekker, T.-C. Wei, N. Shah, P. M. Goldbart, and A. Bezryadin, Nature Physics **5**, 503 (2009).

[259] P. Li, P. M. Wu, Y. Bomze, I. V. Borzenets, G. Finkelstein, and A. M. Chang, Physical Review Letters **107**, 137004 (2011).

[260] T. Aref, A. Levchenko, V. Vakaryuk, and A. Bezryadin, Physical Review B **86**, 024507 (2012).

[261] V. Lefevre-Seguin, E. Turlot, C. Urbina, D. Esteve, and M. H. Devoret, Physical Review B **46**, 5507 (1992).

[262] S.-X. Li, Y. Yu, Y. Zhang, W. Qiu, S. Han, and Z. Wang, Physical Review Letters **89**, 098301 (2002).

[263] F. Balestro, J. Claudon, J. P. Pekola, and O. Buisson, Physical Review Letters **91**, 158301 (2003).

[264] D. F. Sullivan, S. K. Dutta, M. Dreyer, M. A. Gubrud, A. Roychowdhury, J. R. Anderson, C. J. Lobb, and F. C. Wellstood, Journal of Applied Physics **113**, 183905 (2013).

[265] S. Butz, A. K. Feofanov, K. G. Fedorov, H. Rotzinger, A. U. Thomann, B. Mackrodt, R. Dolata, V. B. Geshkenbein, G. Blatter, and A. V. Ustinov, Physical Review Letters **113**, 247005 (2014).

[266] L. Longobardi, D. Massarotti, D. Stornaiuolo, L. Galletti, G. Rotoli, F. Lombardi, and F. Tafuri, Physical Review Letters **109**, 050601 (2012).

[267] J. C. Fenton and P. A. Warburton, Physical Review B **78**, 054526 (2008).

[268] L. Longobardi, D. Massarotti, G. Rotoli, D. Stornaiuolo, G. Papari, A. Kawakami, G. Piero Pepe, A. Barone, and F. Tafuri, Applied Physics Letters **99**, 062510 (2011).

[269] L. Longobardi, D. Massarotti, G. Rotoli, D. Stornaiuolo, G. Papari, A. Kawakami, G. P. Pepe, A. Barone, and F. Tafuri, Physical Review B **84**, 184504 (2011).

[270] J. M. Martinis and R. L. Kautz, Physical Review Letters **63**, 1507 (1989).

[271] M. Iansiti, A. T. Johnson, W. F. Smith, H. Rogalla, C. J. Lobb, and M. Tinkham, Physical Review Letters **59**, 489 (1987).

[272] M. Iansiti, M. Tinkham, A. T. Johnson, W. F. Smith, and C. J. Lobb, Physical Review B **39**, 6465 (1989).

[273] C. R. Paul, *Analysis of Multiconductor Transmission Lines* (Wiley-IEEE Press, 2008) pp. 160–239.

[274] M. H. Devoret, J. M. Martinis, and J. Clarke, Physical Review Letters **55**, 1908 (1985).

[275] R. L. Kautz and J. M. Martinis, Physical Review B **42**, 9903 (1990).

[276] K. Gloos and F. Anders, Journal of Low Temperature Physics **116**, 21 (1999).

[277] Y. Yoon, S. Gasparinetti, M. Möttönen, and J. P. Pekola, Journal of Low Temperature Physics **163**, 164 (2011).

[278] J.-D. Pillet, C. H. L. Quay, P. Morfin, C. Bena, A. L. Yeyati, and P. Joyez, Nature Physics **6**, 965 (2010).

[279] L. P. Rokhinson, X. Liu, and J. K. Furdyna, Nature Physics **8**, 795 (2012).

[280] D. Z. Haxell, M. Coraiola, D. Sabonis, M. Hinderling, S. C. ten Kate, E. Cheah, F. Krizek, R. Schott, W. Wegscheider, W. Belzig, J. C. Cuevas, and F. Nichele, Nature Communications **14**, 6798 (2023).

[281] W. C. Danchi, F. Habbal, and M. Tinkham, Applied Physics Letters **41**, 883 (1982).

[282] D. M. T. van Zanten, D. Sabonis, J. Suter, J. I. Väyrynen, T. Karzig, D. I. Pikulin, E. C. T. O'Farrell, D. Razmadze, K. D. Petersson, P. Krogstrup, and C. M. Marcus, Nature Physics **16**, 663 (2020).

[283] D. J. Carrad, L. Stampfer, D. Olsteins, C. E. N. Petersen, S. A. Khan, P. Krogstrup, and T. S. Jespersen, Nano Letters **22**, 6262 (2022).

[284] Z. Su, A. Zarassi, J.-F. Hsu, P. San-Jose, E. Prada, R. Aguado, E. J. H. Lee, S. Gazibegovic, R. L. M. Op het Veld, D. Car, S. R. Plissard, M. Hocevar, M. Pendharkar, J. S. Lee, J. A. Logan, C. J. Palmstrøm, E. P. A. M. Bakkers, and S. M. Frolov, Physical Review Letters **121**, 127705 (2018).

[285] D. T. Liu, J. Shabani, and A. Mitra, Physical Review B **99**, 094303 (2019).

[286] F. S. Bergeret, P. Virtanen, A. Ozaeta, T. T. Heikkilä, and J. C. Cuevas, Physical Review B **84**, 054504 (2011).

[287] Z. Dou, T. Wakamura, P. Virtanen, N.-J. Wu, R. Deblock, S. Autier-Laurent, K. Watanabe, T. Taniguchi, S. Guéron, H. Bouchiat, and M. Ferrier, Physical Review Research **3**, 032009 (2021).

[288] P. Virtanen, T. T. Heikkilä, F. S. Bergeret, and J. C. Cuevas, Physical Review Letters **104**, 247003 (2010).

[289] M. Fuechsle, J. Bentner, D. A. Ryndyk, M. Reinwald, W. Wegscheider, and C. Strunk, Physical Review Letters **102**, 127001 (2009).

[290] J. T. Peltonen, J. T. Muhonen, M. Meschke, N. B. Kopnin, and J. P. Pekola, Physical Review B **84**, 220502 (2011).

[291] A. Barone and G. Paternò, in *Physics and Applications of the Josephson Effect* (John Wiley & Sons, Ltd, 1982) pp. 291–353.

[292] A. Banerjee, O. Lesser, M. A. Rahman, C. Thomas, T. Wang, M. J. Manfra, E. Berg, Y. Oreg, A. Stern, and C. M. Marcus, Physical Review Letters **130**, 096202 (2023).

[293] R. Hess, H. F. Legg, D. Loss, and J. Klinovaja, Physical Review Letters **130**, 207001 (2023).

[294] D. Z. Haxell, M. Coraiola, D. Sabonis, M. Hinderling, S. C. ten Kate, E. Cheah, F. Krizek, R. Schott, W. Wegscheider, and F. Nichele, ACS Nano **17**, 18139 (2023).

[295] Y. Chen, Y.-H. Lin, S. D. Snyder, and A. M. Goldman, Physical Review B **83**, 054505 (2011).

[296] E. V. Bezuglyi, A. S. Rozhavsky, I. D. Vagner, and P. Wyder, Physical Review B **66**, 052508 (2002).

[297] J.-F. Liu and K. S. Chan, Physical Review B **82**, 125305 (2010).

[298] F. S. Bergeret and I. V. Tokatly, Europhysics Letters **110**, 57005 (2015).

[299] P. Fulde and R. A. Ferrell, Physical Review **135**, A550 (1964).

[300] A. I. Larkin and Y. N. Ovchinnikov, Soviet Journal of Experimental and Theoretical Physics **47**, 1136 (1964).

[301] M. Hinderling, D. Sabonis, S. Paredes, D. Haxell, M. Coraiola, S. ten Kate, E. Cheah, F. Krizek, R. Schott, W. Wegscheider, and F. Nichele, Physical Review Applied **19**, 054026 (2023).

[302] C. M. Moehle, P. K. Rout, N. A. Jainandunsing, D. Kuiri, C. T. Ke, D. Xiao, C. Thomas, M. J. Manfra, M. P. Nowak, and S. Goswami, Nano Letters **22**, 8601 (2022).

[303] C. Ciaccia, R. Haller, A. C. C. Drachmann, T. Lindemann, M. J. Manfra, C. Schrade, and C. Schönenberger, Physical Review Research **5**, 033131 (2023).

[304] A. Blais, S. M. Girvin, and W. D. Oliver, Nature Physics **16**, 247 (2020).

[305] A. Blais, A. L. Grimsmo, S. Girvin, and A. Wallraff, Reviews of Modern Physics **93**, 025005 (2021).

[306] R. Haller, G. Fülöp, D. Indolese, J. Ridderbos, R. Kraft, L. Y. Cheung, J. H. Ungerer, K. Watanabe, T. Taniguchi, D. Beckmann, R. Danneau, P. Virtanen, and C. Schönenberger, Physical Review Research **4** (2022).

[307] P. Zellekens, R. S. Deacon, P. Perla, D. Grützmacher, M. I. Lepsa, T. Schäpers, and K. Ishibashi, Communications Physics **5**, 267 (2022).

[308] M. Hinderling, S. C. t. Kate, D. Z. Haxell, M. Coraiola, S. Paredes, E. Cheah, F. Krizek, R. Schott, W. Wegscheider, D. Sabonis, and F. Nichele, (2023), arXiv:2307.06718 .

[309] J.-D. Pillet, V. Benzoni, J. Griesmar, J.-L. Smirr, and Ç. O. Girit, Nano Letters **19**, 7138 (2019).

[310] V. Kornich, H. S. Barakov, and Y. V. Nazarov, Physical Review Research **1**, 033004 (2019).

[311] V. Kornich, H. S. Barakov, and Y. V. Nazarov, Physical Review B **101**, 195430 (2020).

[312] J.-D. Pillet, V. Benzoni, J. Griesmar, J.-L. Smirr, and Ç. Girit, SciPost Physics Core **2**, 009 (2020).

[313] C. Jünger, S. Lehmann, K. A. Dick, C. Thelander, C. Schönenberger, and A. Baumgartner, Communications Physics **6**, 190 (2023).

[314] O. Kürtössy, Z. Scherübl, G. Fülöp, I. E. Lukács, T. Kanne, J. Nygård, P. Makk, and S. Csonka, Nano Letters **21**, 7929 (2021).

[315] S. Matsuo, T. Imoto, T. Yokoyama, Y. Sato, T. Lindemann, S. Gronin, G. C. Gardner, S. Nakosai, Y. Tanaka, M. J. Manfra, and S. Tarucha, (2023), arXiv:2303.10540 .

[316] M. Coraiola, D. Z. Haxell, D. Sabonis, H. Weisbrich, A. E. Svetogorov, M. Hinderling, S. C. ten Kate, E. Cheah, F. Krizek, R. Schott, W. Wegscheider, J. C. Cuevas, W. Belzig, and F. Nichele, Nature Communications **14**, 6784 (2023).

[317] S. Matsuo, T. Imoto, T. Yokoyama, Y. Sato, T. Lindemann, S. Gronin, G. C. Gardner, M. J. Manfra, and S. Tarucha, (2023), arXiv:2305.06596 .

[318] D. Z. Haxell, M. Coraiola, M. Hinderling, S. C. ten Kate, D. Sabonis, A. E. Svetogorov, W. Belzig, E. Cheah, F. Krizek, R. Schott, W. Wegscheider, and F. Nichele, Nano Letters **23**, 7532 (2023).

[319] B. van Heck, S. Mi, and A. R. Akhmerov, Physical Review B **90**, 155450 (2014).

[320] M. Coraiola, D. Z. Haxell, D. Sabonis, M. Hinderling, S. C. t. Kate, E. Cheah, F. Krizek, R. Schott, W. Wegscheider, and F. Nichele, (2023), arXiv:2307.06715 .

[321] T. Yokoyama and Y. V. Nazarov, Physical Review B **92**, 155437 (2015).

[322] R.-P. Riwar, M. Houzet, J. S. Meyer, and Y. V. Nazarov, Nature Communications **7**, 11167 (2016).

[323] E. Eriksson, R.-P. Riwar, M. Houzet, J. S. Meyer, and Y. V. Nazarov, Physical Review B **95**, 075417 (2017).

[324] J. S. Meyer and M. Houzet, Physical Review Letters **119**, 136807 (2017).

[325] H.-Y. Xie, M. G. Vavilov, and A. Levchenko, Physical Review B **96**, 161406 (2017).

[326] F. Setiawan, A. Stern, and E. Berg, Physical Review B **99**, 220506 (2019).

[327] R. van der Heijden, J. Stoelinga, H. Swartjes, and P. Wyder, Solid State Communications **39**, 133 (1981).

[328] D. Bonnet and H. Rabenhorst, Physics Letters A **26**, 174 (1968).

Acknowledgments

During my PhD, I have had the pleasure to work with many hard-working and talented people. Without their guidance and support, the work presented in this thesis would not have been possible. I would like to take this opportunity to thank those colleagues and friends who have been integral to work and life throughout my PhD.

First of all, I am deeply grateful to **Dr. Fabrizio Nichele** for his supervision and guidance, from the first week deciding where to put the fridge in the lab, to the last planning the publication of our exciting recent results. Thank you for sharing your knowledge and expertise; I have learned more from you than I could have possibly imagined on beginning the PhD. Most of all, thank you for your dedication to our work together, for your continual support and the motivation that you give to the team.

I am grateful to **Prof. Dr. Klaus Ensslin** for his academic supervision, for taking time for long discussions on my project, for giving me the opportunity to present my work on multiple occasions, and for his guidance on both my academic and personal development as a researcher.
I would like to thank **Prof. Dr. Werner Wegscheider**, first and foremost for providing the excellent material on which this thesis is built – without this contribution, none of the results shown in this thesis would have been possible. I am also grateful for our fortnightly meetings, which were integral to developing working devices in the first years of my project, and for evaluating this thesis.
I would like to thank **Prof. Dr. Christian Schönenberger** for his interesting discussions, at conferences and during visits to Basel, for evaluating this thesis and for acting as an external expert on my examination committee.

I am grateful to **Dr. Heike Riel** for offering me the opportunity to work at IBM Research, and for her active involvement in my project through its challenges and successes. Thank you to **Dr. Walter Riess** for his continuous support, and for instilling the importance of valuing and effectively communicating my work.

I am grateful to my colleagues at IBM for their support throughout my PhD. Thank you to the **Alternative Qubits Team**, for their useful advice and interesting discussions.
In particular, I would like to thank **Stephan Paredes** for his invaluable support in setting up our lab, which was an almost empty room on my arrival, and for fixing and maintaining the dilution fridge so that it could stay running almost continuously during my time at IBM.
Thank you to **Marilyne Sousa** for performing and assisting in TEM sessions, which were crucial to the development of our material.
I am also grateful to **Heinz Schmid** for his support in the early stages of my project, in the then-unfamiliar topics of growth and fabrication.
Thank you to **Dr. Bernd Gotsmann** for the interesting discussions on topics as varied as superconductivity, being a researcher and life in general.

A very big thank you goes to the **members of the BRNC cleanroom operations team**,

who operate and maintain an excellent clean room facility from which I am lucky to have profited. The smooth running of machines, especially during times of lockdown or reduced lab access, was integral to developing my PhD from a stage of fabrication to measurements. In particular, I would like to thank **Dr. Antonis Olziersky** for his tireless operation of the ebeam and for going out of his way to solve exposure problems. Thank you very much to **Ute Drechsler** for sharing her immeasurable expertise and for always being available to answer questions. Thank you to **Daniele Caimi** for his technical support and maintenance of the SEM.

I would like to thank all of the **members of the Ensslin Nanophysics Group** at ETH Zurich, past and present, for making me feel welcome in their team and for their enthusiasm and interest in my work. I am particularly thankful for our successes on the football pitch — I am very happy to graduate having been part of an amazing Boltzmann Cup winning team.

A special thanks goes to **Prof. Dr. Christoph Bruder** for his support in helping me to understand phase dynamics. I am very grateful for our weekly meetings on a Thursday afternoon, for his incomparable proof-reading abilities and for his invitation to Basel so that I could present my work. I would like to thank **Prof. Dr. Wolfgang Belzig** for his valued insights into Floquet and ABS physics, and his experience and guidance in preparing our work for publication. Thank you to **Prof. Dr. Juan Carlos Cuevas** for his simulations of nonequilibrium ABS distributions, and his enthusiasm and support in preparing our work for publication.

I am deeply grateful to the **members of the Advanced Semiconductor Quantum Materials group** at ETH Zurich, for their support and collaboration in providing the material on which this thesis is built.
A special thank you to **Erik Cheah** for his hard work and commitment in leading the growth effort. I am grateful for his diligence in searching for solutions, his drive to grow high quality material, and his discretion during our regular exchanges of semiconductor wafers at Hauptbahnhof.
Thank you to **Dr. Filip Krizek** for sharing his wealth of expertise to improve the growth and fabrication, which, thanks to his valuable inputs, ultimately led to working devices. I am grateful for his countless TEM sessions, for his insightful comments on my manuscripts and for the lively discussions during his visits to IBM.
I would like to thank **Dr. Rüdiger Schott** for his continuous maintenance of the MBE, which allowed a steady supply of high quality material.
I am grateful to **Christoph Adam** for his thorough material analysis and careful transport measurements, which were crucial to finding a working growth and fabrication recipe.
Thank you to **Clemens Todt**, **Sjoerd Telkamp** and **Dr. Tommaso Antonelli** for their contributions to fortnightly meetings, their tours of the MBE system and interesting discussions during visits to ETH.

A very special thank you to the **past, present and honorary members of office W222** for being the best office-mates a PhD student could ask for. Thanks for the late-night support sessions, whether by the lake, at the pub or still in the lab, and for making work and life at IBM a special experience which I will never forget; I am grateful to have shared the PhD experience with so many wonderful PreDocs. While I have no doubt that the bike tours, pub trips and royal comments will continue long after the PhD, I hope that a small part of our time will remain on *The Wall*.

I am of course enormously grateful to the former and current members of our Topological Matter/Alternative Qubits/Andreev-mon team. It was a pleasure to work with you, and none of this would have been possible without your support!
Thank you very much to **Dr. Markus Ritter** for teaching me everything I needed to know when I arrived at IBM, for sharing with the (many) challenges but also the highlights, for training me as a cyclist and a table-football player, and for guiding me through the PhD.
Thank you **Manuel Hinderling** for sharing your insights into device fabrication, for the interesting "five-minute" discussions and brainstorming sessions, and for carefully proofreading this thesis.
Thank you **Marco Coraiola** for your support with device fabrication and late-night measurements, for physics discussions which have greatly improved my understanding, and for thoroughly proofreading of this thesis.
Thank you **Dr. Deividas Sabonis** for the fascinating discussions on all things physics, for your support over a range of projects and for carefully proofreading everything that I have written in our time together at IBM.
Thank you **Fieke ten Kate** for the interesting discussions, for your support and input on measurement results, and for your nice conversations in the morning in the office – I will have more to report on Monday mornings soon!

A very special thank you to **Nele Harnack**, for your constant and immovable support throughout challenging times and your joy and celebration in the happy ones. Your thoughtfulness and encouragement, particularly over these last months, have been a daily reminder for how incredibly lucky I am to have you.

Last but not least, I am deeply grateful to my family for their love and support; without you, none of this would have been possible. I am truly thankful to have such a caring and devoted family, who I can always count on in times of need. Thank you!

Publications

Measurements of Phase Dynamics in Planar Josephson Junctions and SQUIDs
D. Z. Haxell, E. Cheah, F. Krizek, R. Schott, M. F. Ritter, M. Hinderling, C. Bruder, W. Wegscheider, H. Riel, F. Nichele
Physical Review Letters **130**, 087002 (2023).

Microwave-Induced Conductance Replicas in Hybrid Josephson Junctions without Floquet-Andreev States
D. Z. Haxell, M. Coraiola, D. Sabonis, M. Hinderling, S. C. ten Kate, E. Cheah, F. Krizek, R. Schott, W. Wegscheider, W. Belzig, J. C. Cuevas, F. Nichele
Nature Communications **14**, 6798 (2023).

Zeeman- and Orbital-Driven Phase Shifts in Planar Josephson Junctions
D. Z. Haxell, M. Coraiola, D. Sabonis, M. Hinderling, S. C. ten Kate, E. Cheah, F. Krizek, R. Schott, W. Wegscheider, F. Nichele
ACS Nano **18**, 18139 (2023).

Demonstration of the Nonlocal Josephson Effect in Andreev Molecules
D. Z. Haxell*, M. Coraiola*, M. Hinderling, S. C. ten Kate, D. Sabonis, A. E. Svetogorov, W. Belzig, E. Cheah, F. Krizek, R. Schott, W. Wegscheider, F. Nichele
Nano Letters **23**, 7532 (2023).
* *These authors made equal contributions.*

A Superconducting Switch Actuated by Injection of High-Energy Electrons
M. F. Ritter, A. Fuhrer, D. Z. Haxell, S. Hart, P. Gumann, H. Riel, F. Nichele
Nature Communications **12**, 1266 (2021).

Semiconductor Epitaxy in Superconducting Templates
M. F. Ritter, H. Schmid, M. Sousa, P. Staudinger, D. Z. Haxell, M. A. Mueed, B. Madon, A. Pushp, H. Riel, F. Nichele
Nano Letters **21**, 9922 (2021).

Out-of-Equilibrium Phonons in Gated Superconducting Switches
M. F. Ritter, N. Crescini, D. Z. Haxell, M. Hinderling, H. Riel, C. Bruder, A. Fuhrer, F. Nichele
Nature Electronics **5**, 71-77 (2022).

Ubiquitous Superconducting Diode effect in Superconductor Thin Films
Y. Hou, F. Nichele, H. Chi, A. Lodesani, Y. Wu, M. F. Ritter, D. Z. Haxell, M. Davydova, S. Ilić, O. Glezakou-Elbert, A. Varambally, F. S. Bergeret, A. Kamra, L. Fu, P. A. Lee, J. S. Moodera
Physical Review Letters **131** 027001 (2023).

Flip-Chip-Based Microwave Spectroscopy of Andreev Bound States in a Planar Josephson Junction
M. Hinderling, D. Sabonis, S. Paredes, D. Z. Haxell, M. Coraiola, S. C. ten Kate, E. Cheah, F. Krizek, R. Schott, W. Wegscheider, F. Nichele
Physical Review Applied **19** 054026 (2023).

Control over Epitaxy and the Role of the InAs/Al Interface in Hybrid Two-Dimensional Electron Gas Systems
E. Cheah, D. Z. Haxell, R. Schott, P. Zeng, E. Paysen, S. C. ten Kate, M. Coraiola, M. Landstetter, A. B. Zadeh, A. Trampert, M. Sousa, H. Riel, F. Nichele, W. Wegscheider, F. Krizek
Physical Review Materials **7** 073403 (2023).

Phase-Engineering the Andreev Bandstructure of a Three-Terminal Josephson Junction
M. Coraiola, D. Z. Haxell, D. Sabonis, H. Weisbrich, A. E. Svetogorov, M. Hinderling, S. C. ten Kate, E. Cheah, F. Krizek, R. Schott, W. Wegscheider, J. C. Cuevas, W. Belzig, F. Nichele
Nature Communications **14**, 6784 (2023).

Spin-degeneracy Breaking and Parity Transitions in Three-Terminal Josephson Junctions
M. Coraiola, D. Z. Haxell, D. Sabonis, M. Hinderling, S. C. ten Kate, E. Cheah, F. Krizek, R. Schott, W. Wegscheider, F. Nichele
arXiv Preprint 2307.06715 (2023).

Flip-chip-based Fast Inductive Parity Readout of a Planar Superconducting Island
M. Hinderling, S. C. ten Kate, D. Z. Haxell, M. Coraiola, S. Paredes, E. Cheah, F. Krizek, R. Schott, W. Wegscheider, D. Sabonis, F. Nichele
arXiv Preprint 2307.06718 (2023).